Dissertation
submitted to the
Combined Faculties for the Natural Sciences and for Mathematics
of the Ruperto-Carola University of Heidelberg, Germany
for the degree of
Doctor of Natural Sciences

presented by

Diplom-Physiker   Dietrich Foethke

born in: Göttingen

oral examination: . . . .

Forces Are Able To Set
Position And Timing Of
Microtubule Catastrophes In Fission Yeast

Referees: PD Dr. Karsten Rippe

Dr. Eric Karsenti

Abstract

In the fission yeast *Schizosaccharomyces pombe*, interphase microtubules switch to depolymerization almost exclusively at the poles of the cylindrical cell. Proper localization of these events is crucial for morphogenesis, and is thought to depend on factors preferentially localized at the cell poles. Using computer simulations we analyzed five different models of how microtubule dynamic instability might be regulated in order to reproduce the organization of microtubules observed *in vivo*. To evaluate the simulations we compared their output to nine traits of interphase cells. Using the simulation we could show that the shape of fission yeast induces forces on microtubule plus ends specifically at the cell poles. We found that the effect of these forces on microtubule dynamics was sufficient to reproduce the nine traits without the requirement of pole-specific factors. *In vivo* experiments with mutant cells confirmed that cell shape is essential for the proper organization of microtubules in fission yeast which indicates that force might also be relevant in living cells.

We furthermore applied the simulation to study the organization of microtubules in mutant cells that were deleted of the microtubule tip tracking proteins Mal3 and Tip1. This lead to the proposal of a novel hypothesis how Tip1 might function *in vivo* to assist force in the discrimination of the cell poles from central parts of the cell cortex.

Zusammenfassung

In Interphase depolymerisieren die Mikrotubuli der Hefe *Schizosaccharomyces pombe* fast ausschließlich an den Polen der zylindrischen Zelle. Die genaue Positionierung dieser Vorgänge ist entscheidend für die Morphogenese der Zelle und es wird angenommen, dass Faktoren am Zellende dafür verantwortlich sind. Mit Hilfe von Computer-Simulationen wurden in dieser Arbeit fünf verschiedene Modelle für die Regulierung der Dynamischen Instabilität von Mikrotubuli daraufhin untersucht wie gut sie die Organisation von Mikrotubuli in Wildtyp-Zellen reproduzieren. Zur Auswertung wurden die Ergebnisse der Simulationen mit neun charakteristischen Eigenschaften von Wildtyp-Zellen verglichen. Wir konnten zeigen, dass aufgrund der zylindrischen Form von *S. pombe* Kräfte auf die Mikrotubuli wirken, die vor allem an den Polen der Zelle auftreten. Simulationen, die den Einfluss dieser Kräfte auf die Dynamische Instabilität von Mikrotubuli berücksichtigten, stimmten mit den neun gemessenen Eigenschaften von Wildtyp-Zellen überein. Weitere Faktoren an den Polen der Zelle wurden nicht benötigt. *In vivo* Experimente mit Mutanten bestätigten, dass die Form der Zelle von entscheidender Bedeutung für die Organisation der Mikrotubuli ist. Dies deutet darauf hin, dass Kräfte auf Mikrotubuli auch in lebenden Zellen relevant sind.

Die Simulation wurde weiterhin verwendet, um die Organisation von Mikrotubuli in Mutanten zu untersuchen, in denen die Gene für die Proteine Mal3 und Tip1 ausgeschaltet wurden. Unsere Ergebnisse geben Hinweise darauf wie Tip1, zusätzlich zur Kraft, an der Regulierung der Dynamischen Instabilität von Mikrotubuli beteiligt sein könnte.

Contents

Chapter 1

Introduction

Polarization and morphogenesis of cells are often intertwined with the organization of the cytoskeleton. After a general overview in section 1.1 this chapter therefore describes the different elements of the cytoskeleton that are involved in these processes (Sec. 1.2). In the present work we investigated how microtubules are organized in the fission yeast *Schizosaccharomyces pombe*. Special emphasis was therefore placed on a general discussion of microtubule assembly, their dynamics and on the effects of microtubule associated proteins on dynamic instability (Sec. 1.2.4). *S. pombe* is introduced in section 1.3 together with the specific properties of microtubules and their relevance for morphogenesis in this model organism. The chapter closes by introducing the combined approach involving computer simulations and experiments that was applied in this study (Sec. 1.4).

1.1 Polarization and Morphogenesis

Almost all living cells, whether they are eucaryotes or procaryotes, are polarized. In general, polarization refers to cell shape as well as to the internal structure of the cytoplasmic volume. Shape is usually adapted to the specific function and to the environment of a cell. Bacteria and archaebacteria for example are found in many distinct shapes that range from spherical cocci over rod-shaped bacilli to spirals (Fig. 1.1). With respect to shape, all of these cells are highly polarized apart from the cocci whose shape is perfectly symmetric. Many procaryotes are furthermore able to move in a directed manner, like *Escherichia coli* which has a helical flagellum at one end to propel itself forward. Such an extension clearly discriminates one end of the cell from the other. However, the internal structure of procaryotes is usually very simple. They consist of only a single cytoplasmic compartment that contains all the molecules needed for life. This compartment appears as an unpolarized matrix without any discernible organized internal structure in the electron microscope (Fig. 1.2A). Even the DNA is distributed throughout the cytoplasm which is the reason why bacteria were often referred to as being unpolarized. More recent results illustrated however, that some bacteria utilize a cytoskeleton to separate their DNA upon cell division (Garner et al., 2004) and thus create order inside the cytoplasm.

In contrast, the internal configuration of eucaryotic cells is much more elaborate. Having a volume which is about 1000 times larger, eucaryotic cells enclose their DNA within the nucleus which is confined by a double layer of membrane. Various other compartments are separated from the cytoplasm in a similar way to carry out specialized tasks, many of which are related to digestion and secretion. These organelles are positioned within the three dimensional cell volume depending on the cell type and on the progression through the cell cycle (Fig. 1.2B). Protein complexes are enriched at specific locations, and gradients within the cytoplasm spatially control the intensity of biochemical reactions

([Caudron et al., 2005](#)). All these processes generate order and thus polarize the cell, yet this organization is not static. Cells are able to reorganize their structure during the cell cycle or in response to external signals. They might even change their shape or start to move. The changing polarization of cells in space and time is the basis for many fundamental cellular processes such as growth, division, migration and differentiation.
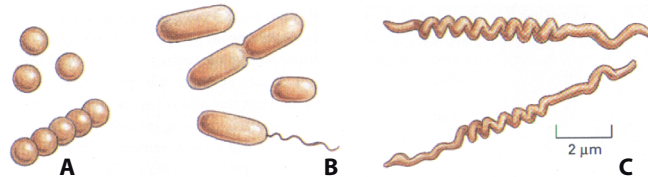
Figure 1.1: Shapes and sizes of some bacteria. Most bacteria come in one of three basic shapes: they are either (A) spherical, e.g. *Streptococcus*, (B) rod shaped, e.g. *Escherichia coli*, or (C) spirals, e.g. *Treponema pallidum* (adapted from [Alberts et al. (2002)](#)).

The internal polarization of a cell is often intertwined with morphogenesis. On the one hand, cell shape can be influenced by the environment, for example through mechanical shear forces or by spatial confinements that limit cell growth. The resulting morphological changes most certainly generate structural rearrangements inside the cytoplasm that affect the internal polarization. The influence of shape was demonstrated *in vitro* for the positioning of microtubule asters in microfabricated chambers of different geometries ([Holy et al., 1997](#)). Conversely, signalling from the inside or outside of the cell can induce the reorganization of the cytoplasm in the first place, which then causes the cell to migrate or to redirect its growth machinery to specific sites a the plasma membrane. Striking examples are the guidance of mating or migrating cells by chemotaxis or the directed growth of axons and dendrites in neurons. A feedback loop is established if the internal polarization of a cell determines its morphology and if at the same time morphological restrictions affect its polarization as it is the case in fission yeast (explained in more detail in section [1.3](#)).

The connection between morphogenesis and the internal organization of the cytoplasm is mediated by the various elements of the cytoskeleton (Sec. [1.2](#)). It consists of a system of highly dynamic protein filaments together with their associated proteins. These filaments provide a mechanical scaffold and serve as tracks for motor proteins that transport material to specific regions of the cell. Cells that do not have a stiff cell wall can directly be shaped by actin filaments like for example red blood cells. In contrast, the shape of fission yeast cells is maintained by a rigid cell wall. Nevertheless, microtubules and actin filaments are involved in fission yeast morphogenesis because they deliver parts of the growth machinery and cell wall components to the cortex. By contacting the cortex only at specific regions of the cell, microtubules determine the position of growth sites in fission yeast and therefore also determine the orientation of the long cell axis. The organization of the cytoskeleton is therefore essential for cell polarity and morphogenesis.

At the same time, the orientation of microtubules in fission is partly determined by cell shape because microtubules that contact the cortex are deflected and thus grow along the cell axis towards the cell poles where they again deposit elements of the growth machinery. Microtubules are therefore part of the positive feedback mentioned above. This loop is further enhanced by the transport of proteins that influence the dynamics of cytoskeletal filaments. The localized activity of such regulatory factors affects the organization of the cytoskeleton which again determines the positioning of these factors.

In order to understand the establishment of cell polarity one has to understand how cytoskeletal
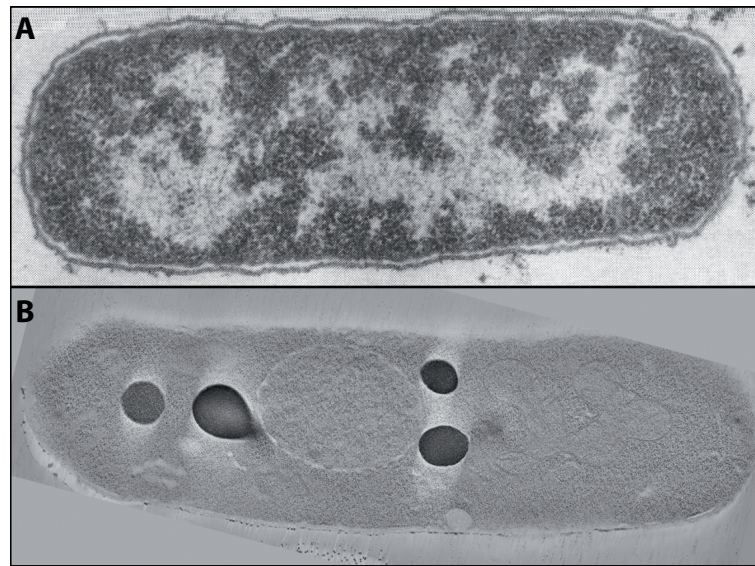
Figure 1.2: The internal structure of a bacterium compared to a fission yeast cell. (A) Transmission electron micrograph of the bacterium *Escherichia coli*. Dark spots (electron dense areas) represent the location of ribosomes while the DNA is located in the lightly stained (ribosome free) regions (Alberts et al., 2002). (B) Projection of a few slices from an electron tomogram of a fission yeast cell. The big round structure at the cell center represents the nucleus. The four dark spherical objects are vacuoles filled with electron dense material. Mitochondria are visible on the right side of the nucleus close to some microtubules at the bottom of the cell. Image kindly provided by Johanna Höög, EMBL.

filaments are organized, i.e. how their dynamics are locally regulated. To achieve this it is necessary to unravel the mysteries of the positive feedbacks described above. Due to its simple shape and cytoskeleton, fission yeast is ideally suited for this task. In the present work we investigated how microtubule dynamics is regulated in interphase fission yeast cells using an approach that combined computer simulations and experiments. Computer simulations proved to be useful, since they opened up the possibility to reconstitute the system step by step and to identify the important regulatory elements. They furthermore allowed us to test different models of microtubule dynamic instability and to investigate how well each model could reproduce the organization of microtubules observed *in vivo*. We found that forces generated at the cell poles are sufficient to properly organize microtubules in the cylindrical geometry of fission yeast, and thus to initiate a positive feedback. These results were supported by experiments with mutant cells that were unable to maintain a cylindrical cell shape.

1.2 The Cytoskeleton

The cytoskeleton is a system of protein filaments which is responsible for many structural and mechanical functions inside eucaryotic cells. Apart from guiding the intracellular transport of proteins and organelles as described above, it provides physical support for the plasma membrane and thus often determines cell shape. It enables some cell types to crawl or swim by extending lamellipodia and filopodia or by the beating of cilia and flagella. At mitosis it pulls the chromosomes apart and it separates the two daughter cells at cytokinesis.

Three major types of filaments are distinguished that carry out this diverse set of tasks: actin fila-

ments, microtubules and intermediate filaments. Each of them has different physical properties and is therefore suited for different functions. Yet, all types of filaments have in common that they are composed of small molecular subunits which are assembled in repetitive patterns to form larger polymeric structures. The individual protein molecules are held together by weak, noncovalent interactions and can diffuse quickly in the cytosol in their unpolymerized state. This enables the cell to rapidly assemble and disassemble the filaments if necessary and to quickly reorganize its internal structure. For actin filaments and microtubules this property is further enhanced by the ability to bind and hydrolyze nucleoside triphospates, which leads to phenomena such as dynamic instability and treadmilling (Sec. 1.2.1).

To combine strength with adaptability, cytoskeletal polymers are built out of multiple protofilaments. A protofilament is a long linear string of subunits that are joined end to end. The longitudinal bonds between the subunits are relatively weak in order to allow the quick reorganization of the polymer. As a consequence, a single protofilament could barely withstand the thermal fluctuations inside the cell without breakage. Yet, if the subunits were more tightly bound to their neighbors, the filament could not be disassembled quickly and would therefore be less adaptable. By associating several protofilaments laterally, both features can be combined. Subunits at the ends of the polymer can still be added and removed easily, while subunits in the core of the polymer are fixed by multiple longitudinal and lateral bonds inside the polymer lattice, thus providing strength to the filament. This type of assembly also has consequences for the *de novo* formation of cytoskeletal filaments. Short oligomers can assemble spontaneously, but unless they reach a certain critical size and shape where single subunits are bound to several neighboring subunits, they are unstable and depolymerize again rapidly. The instability of such small aggregates leads to a time lag in the polymerization process: subunits have to form an initial nucleus before they can elongate, a process which is called nucleation. This lag phase can be eliminated if the filaments are nucleated from preformed templates, such as chemically stabilized filament fragments. Living cells utilize this mechanism to control the location, time and amount of new filament nucleation.

Cells furthermore use a great variety of associated proteins to regulate the spatial distribution and dynamic behavior of cytoskeletal filaments. These accessory proteins determine where filaments are nucleated, they sequester subunits to reduce the pool of unpolymerized protein or to pre-form building blocks for faster assembly, and they directly affect the kinetics of assembly and disassembly. They can crosslink filaments to form bundles or mechanically robust scaffoldings, or they link filaments to other cellular structures such as organelles. Together, these proteins enable a eucaryotic cell to re-use the same building blocks to produce very different structures. For example, microtubules in the axons and dendrites of neurons are stabilized and bundled by the microtubule associated protein Tau (see Sec. 1.2.4.4). In the longest human axons these bundles extend from the base of the spinal cord to the tip of the big toe, reaching up to one meter in length. In contrast, the microtubules in the highly dynamic mitotic spindle are destabilized by members of the kinesin 13 family (see Sec. 1.2.4.6) and are only stabilized if they are in contact with the chromosomes. In this way the associated proteins enable the cell to build and maintain highly organized but very flexible polymer networks.

Microtubules and actin filaments are intrinsically polar because of the asymmetric conformation of their subunits and the fact that they always assemble in the same directional manner. Subunits can be added or removed at both ends of the filament, but due to the structural asymmetry of the monomers the rates of polymerization and depolymerization differ. In general, the rate of subunit addition per second, $k_{on}C$, is proportional to the concentration of monomers, C, while the rate of subunit loss, k_{off}, is independent of C. The system is in equilibrium if the two rates are equal, i.e. if $k_{on}C = k_{off}$ and the average (macroscopic) length of the filament does not change. The corresponding concentration, $C_{crit} = k_{off}/k_{on}$, is called the critical or equilibrium concentration. Since the same bonds are made

or broken if a subunit is added or removed at either end, the change of the Gibbs free energy ΔG and therefore also the critical concentration must be the same. This implies that if one end of the filament elongates much faster than the other one, it must also shrink faster as soon as the monomer concentration drops below the critical concentration, i.e. $k_{on}^+/k_{on}^- = k_{off}^+/k_{off}^-$. The more dynamic side is usually called the "plus end" and the other one the "minus end". In contrast to actin filaments and microtubules, the subunits of intermediate filaments do not show any structural polarity, but they are still highly dynamic.

Although the cytoskeleton is mainly studied in eucaryotic cells, all three types of cytoskeletal filaments can also be found in procaryotes (Shih and Rothfield, 2006). The tubulin homolog FtsZ which is present in virtually all bacteria and archaebacteria forms the Z-ring at the future site of cytokinesis and is essential for cell division. Many bacteria also contain actin homologs like MreB, ParM or MamK which are involved in morphogenesis and the segregation of DNA-plasmids (Carballido-López, 2006). The only procaryotic homolog of intermediate filaments identified so far is crescentin, which was found in the comma-shaped cells of *Caulobacter crescentus* and is essential for cell morphology (Ausmees et al., 2003). There is even one new group of cytoskeletal filaments including MinD and ParA that is not present in eucaryotic cells at all.

1.2.1 Dynamic Instability and Treadmilling

The Addition of subunits at the tips of a polymer is a reversible process, as long as no energy is consumed or released. The polymerization reaction proceeds such that the Gibbs free energy of the whole system (the filament plus the free soluble subunits) is minimized. If the concentration of free subunits is above the equilibrium concentration, C_c, both ends of the filament grow, and if the concentration is below C_c both ends shrink. However, the speed of polymerization and depolymerization can be different at the two ends if the filament is intrinsically polar. Once the equilibrium concentration is reached, the length of such a polymer stays more or less constant, fluctuating only little about the equilibrium value.

Actin filaments and microtubules show a different dynamic behavior. Actin filaments typically grow at the plus end and simultaneously shrink at the minus end, a behavior that is called treadmilling. At steady state, the amount of subunits added at one end is balanced by the loss of subunits at the opposite end, such that the length of the treadmilling filament stays constant. This steady state treadmilling is a nonequilibrium process that consumes energy gained from the hydrolysis of ATP. First experimental evidence for this kind of actin polymerization was obtained *in vitro* (Wegner, 1976) followed by the discovery of treadmilling in the lamellipodium of fibroblasts almost ten years later (Wang, 1985). Today, treadmilling is thought to be essential for cell motility (Pantaloni et al., 2001). Microtubules usually do not undergo treadmilling but exhibit dynamic instability, a behavior in which individual microtubules alternate stochastically between prolonged phases of growth and shrinkage (Mitchison and Kirschner, 1984). Compared to the equilibrium fluctuations of a reversible polymer the excursions in microtubule length are large, and single microtubules never maintain a steady state length. A population of microtubules however, can still exhibit a bulk steady state in which the total length of polymerized tubulin stays constant, while individual microtubules permanently polymerize or depolymerize utilizing energy from GTP hydrolysis. This behavior was first deduced from the discovery that the average length of fixed microtubule populations varies even at steady state where the total length is constant (Mitchison and Kirschner, 1984), and was later also shown directly by video light microscopy of individual dynamic microtubules (Walker et al., 1988).

Dynamic instability and treadmilling are nonequilibrium processes which consume energy, even in steady state. The subunits of actin filaments and microtubules, G-actin molecules and tubulin

dimers (see Sec. 1.2.2 & 1.2.4), are enzymes that have the ability to bind and hydrolyze a nucleoside triphosphate (NTP), ATP and GTP respectively. Since the only available source of energy is the hydrolysis of the bound NTP, it is safe to assume that this drives both processes. Two models will be discussed that try to explain the detailed mechanisms of how nucleotide hydrolysis might lead to treadmilling and dynamic instability. The first model is called the NTP-cap model and is built on the assumption that there is a time lag between the incorporation of subunits into the polymer and the hydrolysis of the nucleotide. This model is believed to explain most aspects of the treadmilling of actin filaments while its relevance for dynamic instability is less evident (Carlier, 1990; Desai and Mitchison, 1997). The second model is mainly discussed with regard to microtubule dynamic instability, and is based on the observation that the conformation of growing microtubule tips is very different from shrinking ones (Chrétien et al., 1995). Both models have in common, that the ends of growing filaments are thought to be protected by a special structure which is different from the rest of the filament, either chemically because of the bound nucleotide or due to its structural conformation. The two models are not mutually exclusive and it is very well possible that only a combination of both aspects, a GTP cap together with the conformational differences between growing and shrinking ends, explains microtubule dynamic instability.

1.2.1.1   The NTP-cap model

The kinetics of the assembly and disassembly of actin filaments and microtubules strongly depend on the nucleotide bound to the subunits (Cooke, 1975; Desai and Mitchison, 1997). Under certain conditions that will be discussed below, filaments containing NTP exhibit net growth, while at the same time filaments containing NDP tend to shrink. In the NTP-cap model, the tip of a growing polymer is assumed to be capped by a layer of NTP bound subunits, while the core of the filament has already hydrolyzed its nucleotides. One prerequisite for this model is that new subunits binding to the filament ends contain NTP rather than nucleoside diphosphates (NDP). Indeed, most free G-actin molecules and tubulin dimers in living cells contain NTP, since ATP and GTP are constantly synthesized and are present in high concentrations in the cytoplasm (Gao et al., 2005; Burbank and Mitchison, 2006). The hydrolysis of the bound nucleotide furthermore proceeds very slowly for free subunits, but is accelerated when a subunit is incorporated into a filament (Pardee and Spudich, 1982; Desai and Mitchison, 1997). For newly bound subunits, hydrolysis is believed to occur in two major steps subsequent to the polymerization reaction: cleavage of the inorganic phosphate (Pi) from NTP is followed by the release of the Pi while NDP remains bound to the subunit. Timing of these events is crucial for the NTP-cap model and differs between actin and microtubules.

In the case of actin, cleavage of ATP is thought to be fast, i.e. in the order of seconds (Blanchoin and Pollard, 2002), while the release of the γ-phosphate is much slower (Korn et al., 1987). In vitro measurements with purified G-actin resulted in a half-time of $\sim 350s$ (Melki et al., 1996) for the release of the phosphate. Actin filaments are therefore no homogeneous polymers but contain a core of older subunits bound to ADP, followed by subunits containing ADP plus the cleaved γ-phosphate and finally subunits that did not yet hydrolyze their ATP (Carlier, 1990) (Fig. 1.3). The grade of heterogeneity varies with the rate of growth and therefore with the free subunit concentration. It was shown that it is the release of the phosphate rather than its cleavage from ATP which causes the change of the kinetic rate constants, by polymerizing actin in the presence of high concentrations of soluble Pi (Carlier and Pantaloni, 1988; Carlier, 1990). For actin filaments the NTP-cap therefore effectively consists of the newly added ATP subunits together with the subunits that did not yet release the phosphate but contain ADP-Pi.

In the case of microtubules the situation is less clear. Microtubules are not stabilized by the

A

B
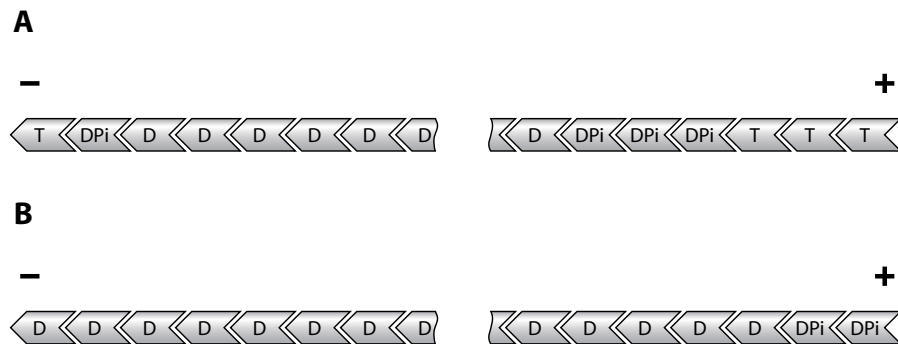
Figure 1.3: Polymerization scheme for ATP-actin. The ATP is hydrolyzed after the addition of an ATP bound subunit to the end of the filament. Filamentous actin therefore incorporates three species of subunits: older subunits bound to ADP and newly added subunits transiently bound to ATP and ADP-Pi. Two situations are illustrated: (A) At high monomer concentration the rate of association is faster than ATP hydrolysis. Terminal ATP and ADP-Pi subunits are present at both ends. (B) At steady state and in a regime of slow growth, terminal ADP-Pi subunits are present at the plus end, while ADP subunits are present at the minus end (adapted from Carlier (1990)).

addition of high concentrations of phosphate and it is therefore still controversial if GDP-Pi bound tubulin contributes to the stabilizing GTP-cap (Caplow et al., 1989). Whether the stabilizing effect is mediated by GTP or GDP-Pi subunits, the important question is if there is a delay between the incorporation of free subunits into the filament and nucleotide hydrolysis, since this is a requirement for the NTP-cap model. A number of contradicting measurements exist for the time lag and the size of the GTP/GDP-Pi cap at physiological concentrations of free tubulin which are discussed in detail in Erickson and O'Brien (1992); Desai and Mitchison (1997). However, the latest measurements indicate that there is indeed a time lag between assembly and the release of the Pi, but that the phosphate is released very quickly compared to actin, i.e. about 50 times faster (Melki et al., 1996).

The question remains how the nucleotides bound to G-actin and tubulin influence the kinetic rates of assembly and disassembly. In both cases, hydrolysis of the bound nucleotide occurs when the subunit is incorporated into the filament. Interestingly, the energy gained from hydrolysis is not consumed by the polymerization reaction. It is rather used to destabilize the polymer later on. Evidence for this was obtained from the polymerization of actin-filaments and microtubules from subunits bound to nonhydrolyzable analogs of ATP and GTP, AMPPNP and GMPCPP respectively. It was found that the polymerization rates with AMPPNP and GMPCPP are very similar to those obtained in the presence of ATP and GTP, which indicates that hydrolysis is not needed for the polymerization reaction (Cooke, 1975; Hyman et al., 1992). Instead, microtubules assembled from GMPCPP-tubulin depolymerize about $5 \cdot 10^3$ times slower than microtubules formed with GTP and they do not exhibit dynamic instability (Hyman et al., 1992). In the case of actin it was shown later that the off rate of G-actin monomers is increased upon release of the inorganic phosphate (Carlier, 1990) (in contradiction to earlier results (Cooke, 1975) that indicated that the off rate was not affected by ATP hydrolysis).

For both types of filament, the off rate of NDP subunits is higher than the off rate of NTP subunits. The explanation lies in the three dimensional conformation of the subunits. It is thought that the release of the γ-phosphate leads to a structural change which renders incorporation into the filament less favorable. For tubulin dimers containing GMPCPP this structural change cannot occur, since the nucleotide cannot be hydrolyzed. It was proposed that tubulin dimers are straight when they contain GTP and become curved when they are in a GDP-bound state (Mandelkow et al., 1991; Howard and

Timasheff, 1986). Indeed, it was found that tubulin oligomers containing GDP have a greater curvature than oligomers built from GMPCPP-tubulin (Müller-Reichert et al., 1998; Nogales and Wang, 2006). The structure of single tubulin dimers however, could until now only be determined for the GDP bound state (Nogales et al., 1998; Ravelli et al., 2004) (Fig: 1.9) while the structure of single GTP or GMPCPP bound dimers is still unknown (Nogales and Wang, 2006). A conformational change also seems to occur in the case of actin, as indicated by the crystal structures of single monomers containing either ADP (Otterbein et al., 2001) or ATP (Graceffa and Dominguez, 2003), although for actin the precise nature of these changes is still controversial (Rould et al., 2006).

For the subunits implemented in the core of the polymer the conformational change cannot occur immediately when the phosphate is released, because of constraints induced by the polymer lattice. In the case of microtubules, tubulin dimers bound to GDP are thought to be forced into an intermediate conformation imposed by their neighboring subunits (Krebs et al., 2005). Filaments that have a core of NDP subunits therefore cannot disintegrate spontaneously, but subunits can only be added or removed from the ends where the structure of the polymer is weak. Meanwhile, the energy gained from nucleotide hydrolysis is stored in the lattice (Caplow et al., 1994) in the form of mechanical strain. This strain is released when a subunit is removed from the end of the filament and is allowed to adopt its preferred conformation. Consequently the free energy change upon dissociation of NDP bound subunits is higher than for NTP subunits (Mitchison and Kirschner, 1984; Carlier, 1990) and the critical concentration of NDP subunits is larger than for NTP subunits, i.e. $C_c(D) > C_c(T)$ (Cooke, 1975; Olmsted and Borisy, 1975). Microtubules at physiological concentrations of free tubulin dimers only assemble if the subunits contain GTP (Hyman et al., 1992), which means that in living cells $C_c(D) > C > C_c(T)$.

Taking nucleotide hydrolysis into account, the rate of subunit addition, $k_{on} \cdot C$, becomes a critical parameter for the formation of the NTP cap. The longer the time that a subunit has been incorporated into the polymer, the more likely it is to have hydrolyzed its bound nucleotide. Whether the subunits at the end of the filament contain NTP or NDP depends on the relative rates of hydrolysis and subunit addition. If the addition of subunits occurs faster than nucleotide hydrolysis, i.e. the filament is growing rapidly, the tip of the polymer forms a cap of subunits containing NTP (Mitchison and Kirschner, 1984). If the addition of subunits is slow, all nucleotides are hydrolyzed before the next subunit can be added. In this case the tip of the polymer consists of subunits containing NDP.

Since the two ends of a polar filament polymerize with different rates, it is possible that they contain different nucleotides, i.e. NTP at the fast growing plus end and NDP at the minus end (Fig. 1.3). According to the NTP-cap model this might lead to treadmilling under the following conditions: if the free subunit concentration is such that subunit addition is faster than nucleotide hydrolysis at the plus end, but slower than nucleotide hydrolysis at the minus end, the plus end will be capped by NTP subunits, while the minus end subunits will contain NDP. If furthermore the concentration of free subunits is higher than the critical concentration of NTP subunits for the plus end, but lower than the critical concentration of NDP subunits for the minus end, the filament will grow at the plus end and shrink at the minus end, i.e. the filament is treadmilling.

The occurrence of dynamic instability can be explained in a similar way. To understand the principle of dynamic instability it is not necessary to distinguish between plus and minus end. Addition of subunits and nucleotide hydrolysis at either end are random processes that occur with average frequencies given by their kinetic rate constants. If these two rates are in the same order of magnitude, random fluctuations can lead to transitions between the NTP type and the NDP type of filament. Hydrolysis might catch up with the addition of subunits to transform a NTP cap to NDP and vice versa. Whether the filament is growing or shrinking then depends on the concentration of free subunits. The situation is trivial, if the concentration of free subunits is above the critical concentration for NDP
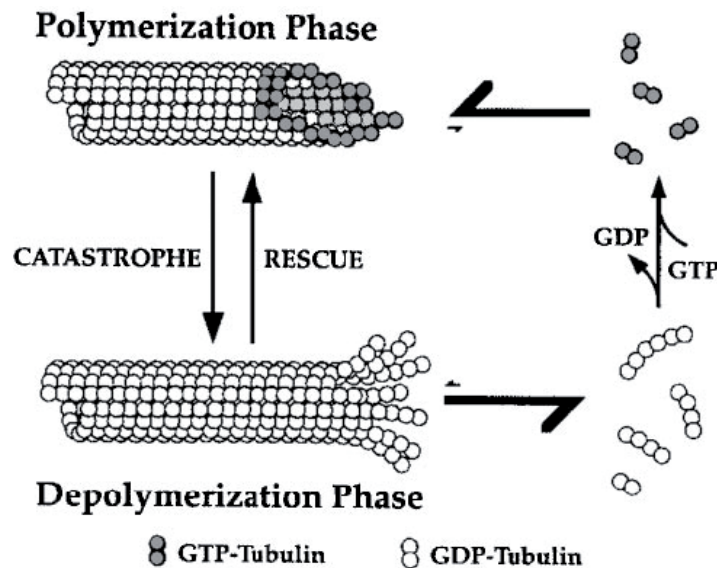
Figure 1.4: Microtubule dynamic instability. GTP-tubulin is incorporated at polymerizing microtubule ends. During or soon after polymerization the bound GTP is hydrolyzed and the Pi is subsequently released. Consequently, the microtubule lattice is predominantly composed of GDP-tubulin. Polymerizing microtubules infrequently switch to depolymerization (catastrophe). Depolymerization is characterized by the very rapid loss of GDP-tubulin subunits and oligomers from the microtubule end. Depolymerizing microtubules can also switch back to polymerization (rescue). The figure incorporates the notions of a small GTP/GDP-Pi cap acting as a stabilizing structure at polymerizing ends (NTP-cap model) as well as different conformational configurations at polymerizing and depolymerizing ends (structural model), both of which are discussed in the text (adapted from Desai and Mitchison (1997))

type filaments. In this case the filament exhibits net growth, no matter which nucleotide is bound at its ends. Similarly the filament shrinks if $C < C_c(T)$, even if the ends of the filament contain NTP. In these two cases, transitions between the NTP and NDP type filaments only have minor effects, possibly changing the speed of filament growth or shrinkage.

Dynamic instability can arise from randomly changing types of nucleotides, if the concentration of free subunits is an intermediate between $C_c(D)$ and $C_c(T)$. Filaments that have an NTP cap will grow while NDP type filaments will shrink (Desai and Mitchison, 1997; Mitchison and Kirschner, 1984) (Fig. 1.4). A filament that loses its NTP cap will switch from growth to shrinkage, because the core of the filament mostly consists of NDP subunits which have a high off rate. Such behavior was indeed observed when growing microtubules were severed with a UV-microbeam (Walker et al., 1989), thereby creating short filaments that depolymerize rapidly. Growth can be resumed, if depolymerization reaches a part of the filament that still contains NTP or if new NTP subunits are added to the tip of the filament to form a new cap. At such intermediate free subunit concentrations therefore two populations of filaments exist, the ones that have a NTP cap and grow, and the ones that consist of NDP subunits and shrink. Individual filaments switch randomly between these two populations. Filaments undergoing dynamic instability can therefore be characterized by four parameters, namely the rates of filament polymerization and depolymerization, and the rates of switching between these two states (Desai and Mitchison, 1997). A switch from growth to shrinkage is termed a "catastrophe" and the resuming of growth a "rescue" (Walker et al., 1988). These four parameters were also used in this study to describe microtubule dynamic instability for interphasic *S. pombe* cells with independent

dynamics (see Sec. 4.1; since rescues were ignored, only three parameters remained, see appendix A.8.4). In the simulation it is assumed that catastrophe events occur randomly and are independent of filament history. Consequently the occurrence of catastrophes is described as a Poissonian process with an average rate c (see simulation methods, Sec. 2.2.7).

The rates of catastrophe and rescue are usually low compared to subunit loss and addition, which leads to a broad distribution of microtubule length (Mitchison and Kirschner, 1984). Dynamic instability enables the cell to quickly reorganize parts of its cytoskeleton, which is thought to be essential for many processes like cell motility or the capture of chromosomes (Sec. 1.2.2,1.2.4).

1.2.1.2   Structural Model for Microtubule Dynamic Instability

There are some observations that cannot be explained by the NTP-cap model. For example, the relationship between the occurrence of catastrophes and the rate of filament growth is possibly more complex, as indicated by a microtubule polymerization essay in the presence of magnesium (O'Brien et al., 1990). An increase of the Mg concentration from 0.25 to $6mM$ enhanced microtubule growth up to twofold, yet the rate of catastrophes remained the same at all Mg concentrations investigated. In the GTP-cap model, the growth rate is related to the size of the cap and should therefore influence the catastrophe rate. Apart from that, microtubules sometimes pause without further polymerization or depolymerization (Walker et al., 1988) and resume growth after some time. Such a behavior cannot be explained by the presence of a GTP-cap, which should be hydrolyzed if a microtubule ceases to grow, leading to immediate catastrophe and shrinkage. Individual microtubules furthermore exhibit significant variability in the rate of polymerization and depolymerization during their life time (O'Brien et al., 1990).

Observation of microtubules by cryo-electron microscopy revealed that growing microtubule ends have a gently curved, sheet-like structure of varying length (Chrétien et al., 1995; Arnal et al., 2000), and it was shown that faster polymerization rates produce longer sheets. Depolymerizing microtubules shrink by peeling off curled protofilaments, which renders the structures of growing and shrinking ends considerably different. The sheets are thought to consist of a few protofilaments that elongate and eventually close to form a tube. The zippering of this tube might happen along the seam of the lattice (see 1.2.4) and is possibly assisted *in vivo* by accessory proteins as indicated by recent electron microscopy studies of the fission yeast EB1 homolog Mal3 (Sandblad et al., 2006). These *in vitro* findings suggest that Mal3 specifically binds and stabilizes the lattice seam, which is supported by the *in vivo* observation that Mal3Δ cells exhibit shorter microtubules with a significantly higher catastrophe rate (Busch and Brunner, 2004).

In this model, sheet closure might lead to structural changes of the microtubule tip which finally could cause the catastrophe (Chrétien et al., 1995). Pausing microtubules could represent an intermediate state where the sheet was closed, possibly with the help of accessory proteins like Mal3, but did not yet switch to catastrophe or resumed polymerization. The sheets might therefore represent a structural cap that stabilizes growing microtubule ends.

Another caveat of the NTP-cap model is that the concentration of free subunits required for treadmilling is similar to the concentration at which dynamic instability occurs. So how is it decided which kind of dynamics is displayed by the filament? Treadmilling is preferentially observed for actin filaments, whereas microtubules usually exhibit dynamic instability, but microtubules can be tricked into treadmilling by the addition of associated proteins *in vitro* (Hotani and Horio, 1988). Still, it was long believed that treadmilling of microtubules does not occur in living cells until it was observed in the fragments of fish melanophores (Rodionov and Borisy, 1997). Recently, treadmilling was also found in mutant fission yeast cells that carried a deletion of *mto2*, which is involved in microtubule nucle-

ation and bundling (Janson et al., 2005). Treadmilling furthermore seems to be a general feature of microtubules found in the two dimensional cortical arrays in plant cells. In plant cells one can indeed find a hybrid treadmilling mechanism, where the minus end is shrinking while the plus end exhibits dynamic instability biased towards net growth (Ehrhardt and Shaw, 2006).

The varying dynamic behavior of microtubule plus ends might be due to the changing structure of the growing ends. In this case only a combination of the structural and the NTP-cap model might be able to explain this behavior. 13 tubulin dimers are required to extend a microtubule by $8nm$ (see microtubule structure, Sec. 1.2.4). If a microtubule grows by extending a protofilament sheet, less subunits would effectively be needed to form a GTP-cap at the tip of the sheet. Consequently, the structure of the filament end might be important for the formation of the NTP-cap and thus for its dynamic behavior. Accessory proteins might influence the dynamic behavior of the filament end by modifying the cap structure and thus provoke a switch from dynamic instability to treadmilling.

1.2.2 Actin

Actin filaments (F-actin) are assembled by polymerization of globular protein monomers named G-actin. As described above, the structure of G-actin is not symmetric and monomers always bind in the same direction thereby creating an intrinsically polar filament with different dynamics at the two ends. Polymerization and depolymerization rates are faster at the plus end (barbed end) than at the minus end (pointed end). G-actin is an ATPase which has a nucleotide (ATP or ADP) bound inside a deep cleft in the center of the molecule (Fig. 1.5). The hydrolysis of ATP and the subsequent conformational change of the G-actin molecule give rise to dynamic instability and treadmilling (Sec. 1.2.1).
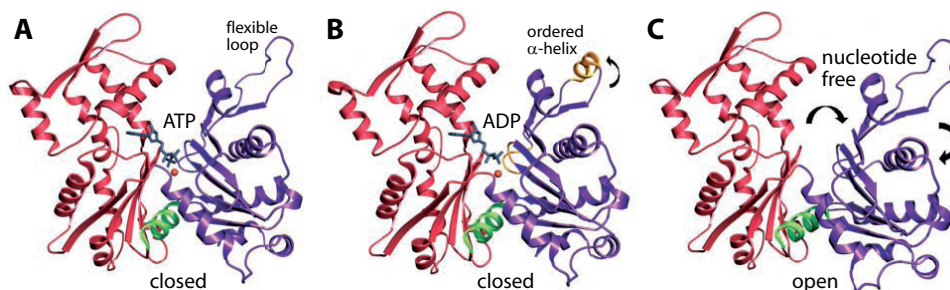
Figure 1.5: The structure of G-actin. Three conformational states of actin are shown. The two major actin domains on each side of the nucleotide are colored purple and red, respectively. (A) Actin conformation in the ATP state as derived from the structure of AMPPNP-actin. (B) Actin conformation in the ADP state. The major changes upon Pi release occur in the three regions shown in yellow. There is also a small rotation of a subdomain in a direction perpendicular to that of the plane of the figure (shown by an arrow). (C) Model of nucleotide-free actin built by homology with Arp3. See Graceffa and Dominguez (2003) for a detailed discussion of these structures.

Each filament consists of two intertwined helical strands forming a right handed helix with a diameter of $5-9nm$ and a repeat of $37nm$. These filaments are very flexible with a persistence length of $\sim 17\mu m$ (Ott et al., 1993; Gittes et al., 1993) and can be organized into a variety of structures, including linear bundles, two-dimensional networks and three-dimensional gels, each of which have different mechanical properties. Actin can be found in any eucaryotic cell but is most abundant in muscle cells where it forms so called thin filaments. Inside of the sarcomere, which is the smallest contractile unit of a muscle cell, thin actin filaments alternate with thick filaments composed of the

motor protein myosin II. When the muscle contracts, myosin II molecules hydrolyze ATP to pull on the thin filaments to shorten the sarcomere. In other types of cells, most actin filaments are nucleated within a thin layer near the plasma membrane and are responsible for cell shape and the elasticity of the cortex (e.g. in erythrocytes). The polymerization forces of actin can push on the plasma membrane to extend lamellipodia and filopodia (see below) and are responsible for the rapid movements of keratocytes. Actin stress fibers and actin cables traverse the cell to transport cargo with the help of myosin motor proteins. Actin furthermore has important functions in exo- and endocytosis and is essential for the contraction of the cytokinetic ring in cell division.

Several accessory proteins associated with actin regulate filament organization, length, location and dynamic behavior. Individual filaments can be cross-linked by bundling proteins or gel forming proteins which either form parallel arrays or connect the filaments at a large angle to each other to build loose meshworks. Bundling proteins like fimbrin, α-actinin or villin have two actin binding domains and establish straight, mechanically stiff connections between two filaments. Fimbrin is thought to be responsible for the tight, parallel bundling of F-actin in filopodia, which are thin, spike like projections of the plasma membrane that allow the cell to explore its environment. As in the case of villin which is found in microvilli, the two actin binding sites are very close together on a single polypeptide chain, such that myosin II cannot participate into the assembly of the bundle. Therefore filopodia and microvilli are not contractile. On the other hand, actin bundles formed by α-actinin are less densely packed and contain filaments oriented in both directions which allows myosin molecules to enter. α-actinin is concentrated in stress fibers which are contractable actin bundles crossing the cell body. In contrast to the accessory proteins involved in actin bundle formation, proteins that form actin webs or gels have either a flexible or a stiff, bent connection between their two binding domains. In erythrocytes, the cross-linking protein spectrin forms a two dimensional web together with actin just beneath the plasma membrane and thus enables the cell to elastically restore its shape after deformation. Actin gels formed by filamin are required to extend thin sheet-like membrane projections called lamellipodia which allow cells to crawl.

The nucleation of branched actin networks is catalyzed by the Arp2/3 complex (actin related protein 2 & 3) which induces filament growth from the minus end. The complex can attach to the side of already existing actin filaments which enhances its nucleation efficiency. While the new filament elongates at the plus end, the complex stays attached to the minus end and to the original filament, thereby creating a branch at an angle of $70°$. Unbranched actin bundles in filopodia are thought to be nucleated by formins, which are also involved in the formation of the contractile ring in cytokinesis (Wallar and Alberts, 2003). In the budding yeast *S. cerevisiae* and in the fission yeast *S. pombe* the formins Bni1 and For3 are necessary for the nucleation of actin cables (Pruyne et al., 2002; Martin and Chang, 2006) which are bundles of short actin filaments involved in cell polarity (Fig. 1.6). In contrast to the Arp2/3 complex individual filaments within these cables are nucleated from the plus end. Formins can remain associated to the fast-growing plus end of the newly nucleated filament and even increase the rate of assembly, but they can also cap the filament and thus inhibit further growth at the plus end. Actin patches containing the Arp2/3 complex are a general marker of growth sites in fission yeast (see Sec. 1.3.2.1) and were used in this study to analyze mutant cells that are deficient in polarized growth (see Sec. 5.2).

Length and dynamics of actin filaments are controlled by a great variety of accessory proteins using different strategies. The rate of filament elongation for example is modified by proteins that bind and sequester actin monomers, one of which is the very abundant protein thymosin. G-actin molecules bound to thymosin are in a locked state and cannot associate with either end of an actin filament. This enables the cell to keep a large supply of unpolymerized G-actin that can be released by the activation of another G-actin binding protein called profilin. Thymosin competes with profilin for
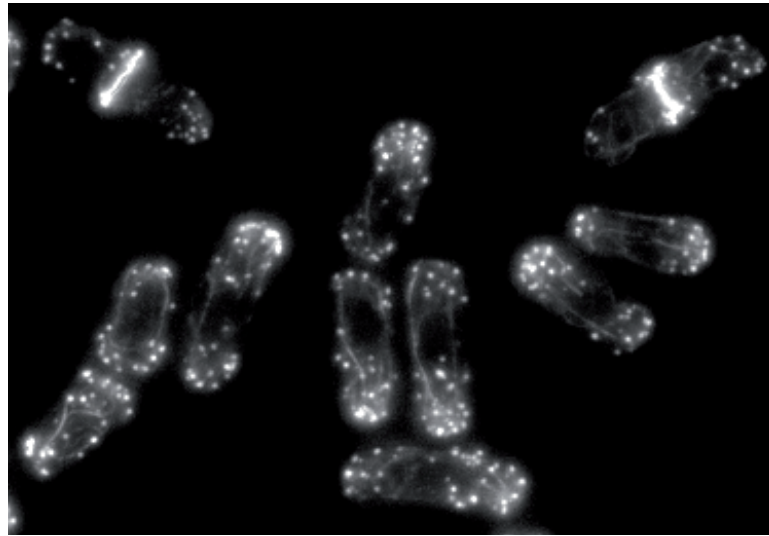
Figure 1.6: Actin patches and cables in *S. pombe*. Actin cables in *S. pombe* are composed of small actin filaments which are organized with their plus ends facing the cell poles. They are nucleated by the formin For3 which is enriched at the poles and is transported inwards together with the growing cables (Martin and Chang, 2006). Actin patches are concentrated at the sites of polarized growth at the cell poles and at the septum during cytokinesis and serve as a marker for cell polarity. The correlation with regions of active cell growth indicates that the patches may have a function in cell growth. Patches contain the Arp2/3 complex and can move in a directed manner along actin cables (Pelham and Chang, 2001) (see also Sec. 1.3.2.1)

the binding of monomers, but unlike monomers sequestered by thymosin, G-actin molecules bound to profilin can specifically be added to the plus ends of actin filaments. Local activation of profilin can therefore lead to bursts of polarized actin polymerization, particularly at the plasma membrane where profilin can be activated by extracellular signals.

Instead of sequestering G-actin molecules the proteins cofilin and tropomyosin bind to F-actin. Tropomyosin simultaneously binds to seven actin subunits and thereby stabilizes the filament while cofilin has a destabilizing effect by inducing mechanical stress that weakens the contacts between the filaments' subunits. Cofilin preferentially binds to ADP containing filaments and thus dismantles older actin structures in the cell where the ATP was already hydrolyzed. To stabilize actin filaments and to prevent further growth or depolymerization, filaments can be capped by proteins that bind preferentially to their plus or minus ends. Local regulation of such capping proteins enables the cell to assemble and dismantle specific parts of their actin cytoskeleton. The phospholipid PIP_2 for example uncaps plus ends at the plasma membrane making them available for further elongation. In muscle cells, where actin filaments are exceptionally long-lived, the filaments are capped at both ends, i.e. by the protein CapZ at the plus end and by tropomodulin at the minus end. Another important function is fulfilled by the protein gelsolin which severs actin filaments and then remains bound to the new plus end, acting as a capping protein. Severing one long filament can create many short ones, each with an uncapped plus and minus end, which under some conditions can serve as nucleation seeds for new actin structures, a process which is particularly important e.g. for the activation of blood platelets. Under other conditions severing can speed up the depolymerization of old filaments. Furthermore, severing can alter the mechanical properties of actin gels and networks, which become less stiff when filaments are cut.

Many of the accessory proteins mentioned above can be regulated by external signals triggered by cell-surface receptors. Although there are many different receptors all the regulation seems to be mediated by GTPases that are members of the Rho protein family, namely Rho, Rac and Cdc42. Each of these GTPases has numerous downstream targets that affect actin organization and dynamics. The activation of Cdc42 triggers the formation of filopodia while the activation of Rac promotes the formation of sheet like lamellipodia and membrane ruffles. Some targets for both GTPases are members of the WASp protein family which in their active state can enhance the nucleation efficiency of the Arp2/3 complex. The activation of Rho leads to the bundling of actin filaments with myosin II into stress fibers and the formation of focal adhesions.

Actin fibers can attach to such adhesion sites at the plasma membrane and thereby connect the internal structure of the cell to neighboring cells or to the extracellular matrix. Special adaptor proteins from the ERM family of proteins mediate the connection e.g. between actin stress fibers and and transmembrane proteins like integrins or cadherins. Such connections serve to stiffen or change the shape of the plasma membrane, to sense forces and stresses or to relate signals from and to the extracellular matrix and other cells.

1.2.3   Intermediate Filaments

Intermediate filaments (IFs) are rope-like fibers with a diameter of $10 - 12nm$. They can easily be deformed but are able to withstand large stresses and strains without rupture, and are therefore well suited to maintain cell integrity. Recent measurements by atomic force microscopy indicate that IFs have a persistence length of only $1\mu m$ (Mücke et al., 2004) and are highly extensible with a maximum stretch of $\sim 250\%$ before rupture (Kreplak et al., 2005).

The subunits of IFs constitute a large and heterogeneous family of filamentous proteins with more than 67 functional members in humans (Chang and Goldman, 2004). All IF proteins have a conserved substructure consisting of a highly α-helical central rod domain that is necessary for their self-assembly into IFs. This domain is flanked by non-α-helical head and tail domains at the N and C-terminus that exhibit considerable differences with respect to their amino acid sequences (Parry and Steinert, 1999). These differences of the head and tail domains account for the variability of intermediate filaments and are thought to be involved in regulating the interactions with other proteins.

According to their sequence identity and tissue specific expression patterns IFs have been divided into five distinct types. Recently they were furthermore sorted into three assembly groups depending on how they (co-)polymerize (Chang and Goldman, 2004). The first two types are constituted by type I (acidic) and type II (basic) keratins. Basic and acidic keratins form heterodimeric IFs which are found in all epithelial cells as well as in hair and nails. Since type I and II IF proteins copolymerize, they are categorized together into assembly group one. By contrast, type III intermediate filament proteins usually form homopolymers. They include vimentin which is often found in mesenchymal cells, desmin which is expressed in muscles, glial fibrillary acidic protein found in glial cells and peripherin expressed in neurons. However, some type III proteins can form heterodimers with the type IV proteins NF-L, NF-M and NF-H which are the building blocks of neurofilaments. Therefore type III and IV IF proteins are joined together in assembly group two. Neurofilaments usually form heteropolymers composed of NF-L plus NF-M or NF-H and are found in high concentrations along the axons of vertebrate neurons. The Type V proteins form assembly group three which is comprised of the nuclear lamins. Lamins line the inner membrane of the eucaryotic nucleus where they form a scaffold to stabilize the nuclear envelope and to anchor chromosomes and nuclear pores.

In contrast to microtubules and actin filaments IFs are not intrinsically polar because their subunits are arranged in a symmetrical way. Two IF monomers form a dimer with their central α-helical

domains that are intertwined in a coiled coil. A pair of dimers then associates in an antiparallel fashion to form a staggered symmetric tetramer that represents the soluble IF subunit. In the following step the tetramers associate laterally to form so called unit-length filaments (ULFs) (Strelkov et al., 2003), which have a diameter of approximately $16nm$ and a length of $60nm$. In the case of vimentin one ULF typically consists of 16 tetramers but this number may vary depending on the assembly conditions. The ULFs then anneal longitudinally to form extended filaments which shortly afterwards undergo some internal rearrangement leading to radial compaction. The filament diameter decreases to the typical $11nm$ while the length remains unchanged.

Because of the symmetry of the tetramers, the kinetics of assembly and disassembly of IFs are the same all along the filament. Studies with fluorescently labeled IF subunits demonstrated that subunit exchange is nonpolar and can occur along the entire length of polymerized IFs (Helfand et al., 2003). Because of their high stability and their role in maintaining cell structure and mechanical integrity it was long thought that IFs form static networks. However, recent studies revealed that IFs and their precursors are often very dynamic and motile. For example FRAP experiments showed that the half time of fluorescence recovery is $\sim 5min$. IFs have no known enzymatic activity, i.e. they do not hydrolyze nucleoside triphospates like ATP or GTP and therefore do not exhibit dynamic instability or treadmilling.
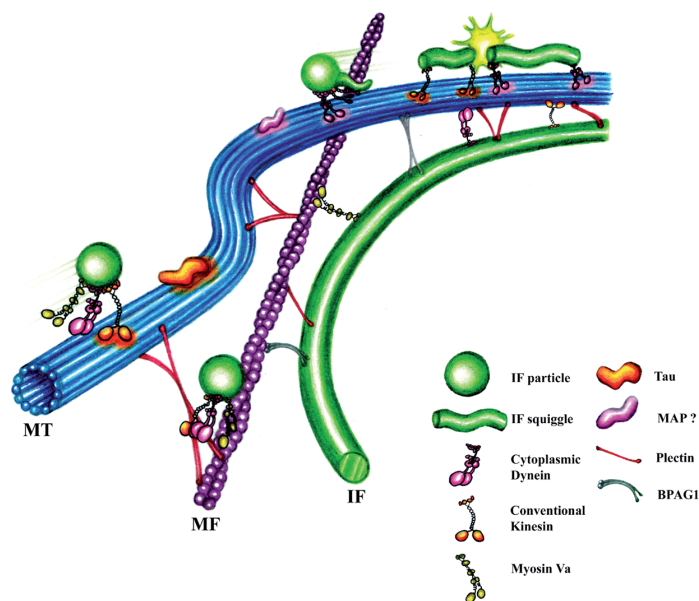
Figure 1.7: Model for intermediate filament (IF) assembly and motility. IF particles, squiggles and longer filaments are transported along microtubules (MT) and actin filaments (MF) with the help of molecular motors. Particles give rise to squiggles which join end to end to form longer filaments. IF associated proteins (IFAPs) like BPAG1 and plectin interact with the different cytoskeletal networks to stabilize long IFs and to modify the speed of IF movements. The transport of IFs along microtubules might additionally be influenced by MAPs such as Tau (see also Sec. 1.2.4.4) (Helfand et al., 2003).

Yet, IFs interact with microtubules and actin (Figs. 1.7 and 1.8). For example the organization and the motility of the vimentin network and its precursors depends to a great extend on the presence of microtubules (Yoon et al., 1998). In vivo studies revealed that vimentin forms non-filamentous particles and short filaments known as squiggles which act as precursors of longer IF filaments. These

particles and squiggles move in both directions along the microtubule network with the help of the molecular motors kinesin and dynein. Depolymerization of microtubules inhibits those movements and substantially slows down subunit exchange. Similar results were obtained for keratin (Yoon et al., 2001). Keratin squiggles move with very different speeds even in the absence of microtubules which indicates that they can also move along actin filaments. The dynamic properties of IFs are essential for the quick reorganization of cellular structures in response to morphological changes and signalling events. The control of IF motility and dynamics and the crosstalk between the three cytoskeletal networks is a growing field of future research in cell physiology.
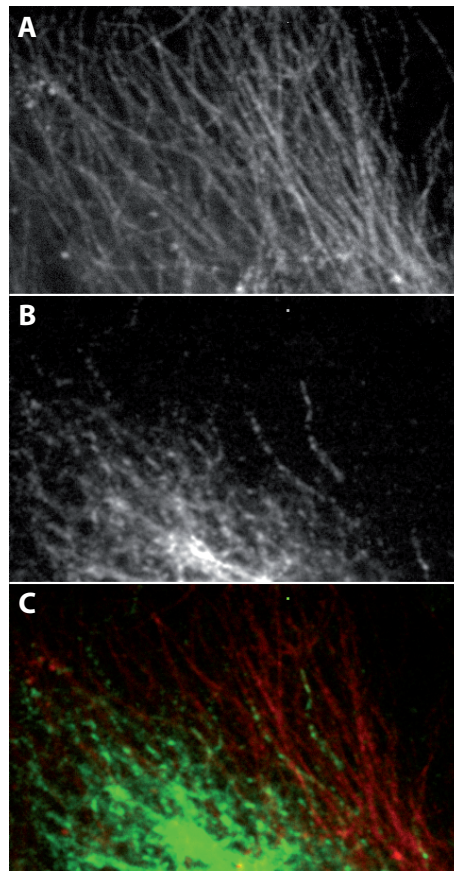
Figure 1.8: Vimentin and microtubule networks in a PTK1 cell. Cells from a stable PTK1 cell line expressing low levels of GFP-vimentin were injected with rhodamine labeled tubulin to observe the interaction between the two filament networks. The images were taken during the Physiology Course in Woods Hole, 2004.

1.2.4 Microtubules

Since microtubules are central to this work they are described in more detail in the the following sections. Microtubules are hollow cylindrical tubes with a diameter of approximately $25nm$. They can be found in almost all eucaryotic cells and are involved in a great variety of cellular processes. During cell division microtubules form the mitotic spindle, a large dynamic bipolar array which is essential for the physical segregation of sister chromatids (Gadde and Heald, 2004). In *C. elegans* the position of the spindle furthermore determines the plane of cleavage and is therefore critical for asymmetric cell division (Cowan and Hyman, 2004) - in contrast to *S. pombe*, where microtubules position the nucleus in the center of the cell to guarantee that fission yeast fissions in the middle (Tran et al., 2001). In nondividing cells, microtubules organize the interior of the cytoplasm. Apart from positioning the nucleus they are responsible for the distribution of the endoplasmatic reticulum (ER)

(Vedrenne and Hauri, 2006) and for the concentration of the Golgi apparatus close to the nucleus (Barr and Egerer, 2005) as well as for the transport of material between these two organelles (Watson et al., 2005). Microtubules are polar and serve as directional tracks for motor proteins that transport vesicles, organelles or protein complexes to specific locations inside the cell. A striking example is the transport of mitochondria and other organelles along microtubule bundles in axons (Hollenbeck and Saxton, 2005). Since almost no protein synthesis occurs in the axon, even short pieces of new microtubules have to be transported along the bundles to maintain and extend the axon (Baas et al., 2006; Ahmad et al., 2006). Apart from that, directional transport along microtubules is important for cell polarity and morphogenesis as for example in fission yeast (see Sec. 1.3.3). Microtubules are also involved in cell motility. A special arrangement of microtubules and dynein motors is responsible for the undulating motion of cilia and flagella which enables cells to swim in liquid media. But cytoskeletal components also play an important role in viral disease: microtubules and motors can be hijacked and reprogrammed by intracellular pathogens to assist the entry, assembly and egress of viral particles (Döhner et al., 2005; Radtke et al., 2006; Schepis et al., 2006).

1.2.4.1   Mechanical Properties

Microtubules are considerably more rigid than actin or intermediate filaments. Their flexural rigidity (or the persistence length) was measured in a variety of different ways which involve bending or buckling by optical tweezers (Kurachi et al., 1995) ($10-40pN\mu m^2$), thermally induced vibrations or shape fluctuations (Gittes et al., 1993) ($22pN\mu m^2$), (Mickey and Howard, 1995) ($26 - 62pN\mu m^2$), (Pampaloni et al., 2006) ($0.45 - 20pN\mu m^2$), buckling inside of vesicles (Elbaum et al., 1996) ($25pN\mu m^2$) and direct measurements by atomic force microscopy (Kis et al., 2002). The values obtained differ significantly which is explained by the observation that the flexural rigidity depends on microtubule length (Kurachi et al., 1995; Kis et al., 2002; Pampaloni et al., 2006), i.e. the stiffness increases for longer microtubules. It is thought that the length dependence is caused by the relative displacements of adjacent protofilaments (see below). Such displacements can occur easily within short filaments, but involve higher shear stresses for longer microtubules. The rigidity of microtubules is furthermore influenced by microtubule stabilizing agents (Mickey and Howard, 1995).

1.2.4.2   Microtubule Composition and Structure

Microtubules are assembled from tubulin heterodimers composed of one α- and one β-tubulin molecule. α- and β-tubulin are globular proteins of about $4nm$ diameter which results in a length of $8nm$ for the tubulin heterodimer. The two molecules share more than 40% amino-acid sequence identity (Burns, 1991) and are extremely similar with respect to tertiary structure (Nogales et al., 1998) (Fig. 1.9). Both of them furthermore bind a guanine nucleotide, but while α-tubulin binds GTP in a non-exchangeable manner at the so called N-site, β-tubulin is a GTPase that can bind and hydrolyze GTP at the exchangeable or E-site (Desai and Mitchison, 1997). The hydrolysis of GTP occurs shortly after polymerization, and the resulting GDP stays bound to the β-tubulin molecule until the microtubule depolymerizes and the dimer is removed from the lattice. In solution the nucleotide is quickly exchanged with GTP and the dimer is recycled for the next round of polymerization. Tubulin can therefore be thought of as its own GAP (GTPase Activating Protein) that accelerates hydrolysis when it contacts neighboring subunits during polymerization. The hydrolysis of the nucleotide causes conformational changes of the heterodimer (Krebs et al., 2005) which is the basis for dynamic instability and treadmilling described in section 1.2.1.

Tubulin dimers associate head to tail to form protofilaments which are joined laterally to build
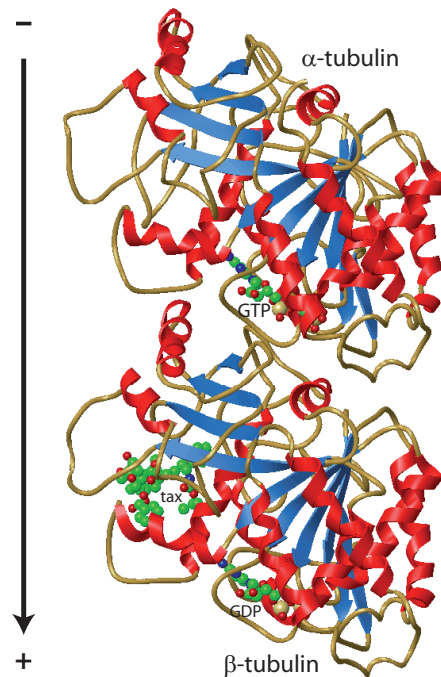
Figure 1.9: Ribbon diagram of the tubulin dimer. α-tubulin is shown on top with the bound GTP molecule. β-tubulin on the bottom contains GDP and tax-otere, an analog of taxol that stabilizes microtubules against depolymerization. The arrow indicates the direction of the protofilament and (in the case of 13 protofilaments) the direction of the microtubule. The structure was obtained by electron crystallography of zinc-induced tubulin sheets (Nogales et al., 1998).

a closed tube. The number of protofilaments per tube can vary between 10 and 17 (Chrétien and Wade, 1991) whereas microtubules *in vivo* and microtubules nucleated from centrosomes and ax-onemes predominantly consist of 13 protofilaments (Tilney et al., 1973; Desai and Mitchison, 1997). It was observed that the number of protofilaments can change abruptly along individual microtubules polymerized from purified tubulin and in *Xenopus* egg extract (Chrétien et al., 1992). Lateral protofil-ament interactions occur between tubulin monomers of different types (α-tubulin connects laterally to β-tubulin) forming a so called A-lattice, or between monomers of the same type (α-α and β-β interactions) thereby forming a B-lattice (Fig. 1.10). The nomenclature dates back to the analysis of doublet microtubules in flagella, which consist of a complete 13 protofilament A-subfiber and a partial B-subfiber which are fused together. It was thought that the two subfibers each exhibit the type of lattice named after them (Amos and Klug, 1974) but, as was found out later, both tubules consist of a B-type lattice. The monomers of neighboring protofilaments are not associated strictly horizontally but are shifted vertically by about $0.9nm$ per protofilament (Chrétien et al., 1996), such that neighbor-ing monomers describe a helix around the wall of the microtubule. After one complete turn the helix reaches a pitch of $12nm$, which matches the height of three tubulin monomers. Three such helices on top of each other would be needed to cover the whole surface of the microtubule which is therefore said to have a three-start lattice (Fig. 1.10).

It was originally postulated that microtubules have an A-type lattice (Amos and Klug, 1974) where neighboring monomers alternate between α- and β-tubulin. However, it was later shown by structural investigations of microtubules decorated with kinesin motors, that the lattice is usually of the B-type

(Song and Mandelkow, 1993, 1995). Consequently, a 13 protofilament microtubule with a three start has a seam where the monomer type changes along the helix, because after one complete turn the vertical position of the next protofilament is shifted by the height of 1.5 heterodimers (Fig. 1.10C). Recent results from electron microscopy indicate that the seam might play an important role in the regulation of microtubule dynamic instability *in vivo* (see Sec. 1.2.4.5). Microtubules that contain a different number of protofilaments can have a different start value or exhibit a supertwist (Chrétien and Wade, 1991). For example, microtubules with 10 protofilaments have a two-start, while 16 protofilament microtubules have a four-start. If there is a mismatch in the helix after one complete turn around the microtubule, the pitch created by the vertical shift between protofilaments is accommodated by a tilt of the protofilaments relative to the microtubule axis, which is called a supertwist. In microtubules that have a supertwist, the protofilaments are not straight anymore but are thought to form a helix turning around the microtubule with a very large pitch (Chrétien and Wade, 1991), in addition to the helix formed by laterally adjacent monomers. However, 13 protofilament microtubules do not exhibit a supertwist (Wade et al., 1990).
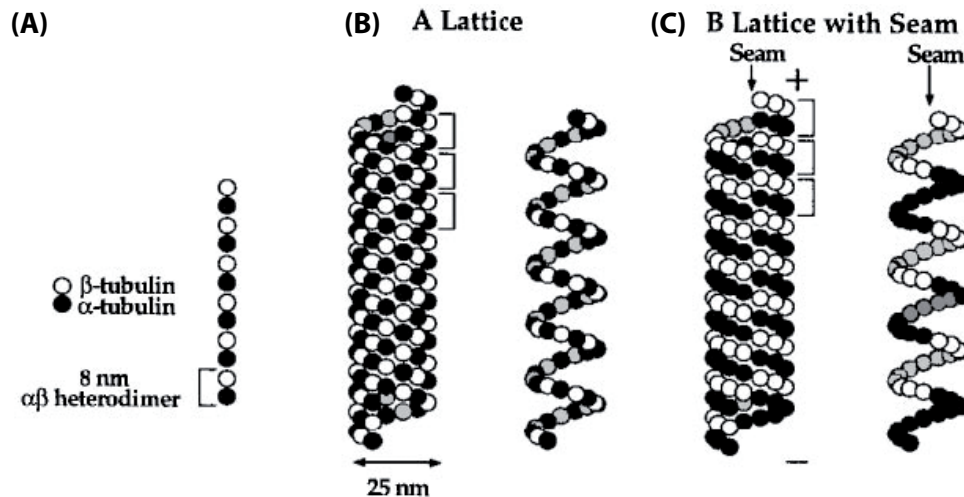
Figure 1.10: Microtubule structure and the arrangement of tubulin dimers within the lattice. (A) Head to tail interactions of α-β tubulin heterodimers form linear protofilaments. *In vivo*, usually 13 protofilaments associate laterally to form a hollow cylindrical tube of $25nm$ diameter. It should be noted however, that it is not precisely known if microtubules polymerize by association of preformed protofilaments (see text). (B) A microtubule lattice where α-tubulin laterally interacts with β-tubulin is called A-type lattice. Shown on the left is a 13 protofilament microtubule with a 3-start helix. For better visibility one of the 3-start helices that would be formed in an A-lattice is drawn on the right. This helix and the one in (C) are shown only to illustrate the helical nature of the microtubule lattice and the lateral interactions between adjacent monomers, but it does not represent a structural intermediate of microtubule assembly. (C) The image on the left shows a 13 protofilament microtubule with a B-type lattice and a seam, the accepted lattice structure for MTs. Lateral interactions between protofilaments occur between identical monomers (α-α and β-β respectively), except at the seam. The seam is formed because one turn of a 3-start helix results in a rise of 1.5 tubulin dimers (or 3 tubulin monomers). Microtubules with 11-15 protofilaments must have a seam while 10 and 16 protofilament microtubules do not have a seam and are truly helical. The protofilaments in a 13 protofilament microtubule are perfectly straight, whereas the protofilaments in microtubules with other protofilament numbers are tilted and form another helix with a very long pitch (Chrétien and Wade, 1991), which is also known as supertwist (not shown). Plus and minus signs indicate microtubule polarity and the brackets delineate dimers within the microtubule lattice (adapted from Desai and Mitchison (1997)).

1.2.4.3 Microtubule Polarity and Nucleation

Tubulin heterodimers have an intrinsic directionality because of the differences between the α and β monomers. Within a protofilament heterodimers assemble head to tail, i.e. α-tubulin alternates with β-tubulin, thereby creating a polar filament. The hydrolyzable β-tubulin monomers are exposed at the plus ends, while α-tubulin is present at the minus ends. As described in section 1.2, this leads to faster rates of polymerization and depolymerization at the plus end of the filament. The polarity of the lattice is furthermore essential for the directional transport of material via motor proteins (see below).

Microtubules are usually nucleated from the minus end by specific protein complexes containing γ-tubulin, a third member of the tubulin superfamily (Oakley and Oakley, 1989). γ-tubulin is highly conserved and is about 30% identical to α- and β-tubulin (Moritz and Agard, 2001), yet it is not assembled into the microtubule lattice but only binds to the minus ends. Although microtubules can assemble spontaneously *in vitro* from high concentrations of purified α- and β tubulin, γ-tubulin is needed at the lower tubulin concentrations in living cells (Moritz and Agard, 2001) to overcome the kinetic barrier of the lag phase (see Sec. 1.2). In all cell types examined so far, γ-tubulin associates with other proteins to form complexes that are thought to act as a template structure for the formation of new microtubules (Wiese and Zheng, 2006). These complexes have different sizes and names in different organisms such as the Tub4p-complex in budding yeast or the γ-tubulin complex (γ-TuC) in fission yeast. The γ-tubulin complex purified from *Xenopus* eggs appears ring-shaped when viewed by electron microscopy (Zheng et al., 1995) and is therefore called the γ-tubulin ring complex (γ-TuRC). Such γ-TuRCs have also been found in human and *Drosophila* cells, whereas the size of the complex in *Drosophila* depends on the lysis conditions. In *Drosophila*, γ-tubulin can also be found in a smaller complex named γ-tubulin small complex (γ-TuSC) which seems to be analogous to the Tub4p-complex in budding yeast (Wiese and Zheng, 2006).

γ-tubulin complexes can be organized further into higher structures called microtubule organizing centers (MTOCs). The shape, size and occurrence of MTOCs varies greatly between species but also within a cell during the cell cycle. In vertebrate somatic cells about 80% of the γ-tubulin is found in the cytoplasm (Schiebel, 2000) whereas the remaining 20% are associated with the centrosome, which is the most intensively studied MTOC. Centrosomes contain γ-TuRCs and nucleate microtubules in a star-like fashion in interphase while they form the two poles of the mitotic spindle during M phase. Still they are not the only source of nucleation. In interphase the number of free microtubule minus ends that are not organized by an MTOC varies widely between different cell types (Dammermann et al., 2003). In mitosis a spindle can be formed in *Xenopus* egg extract even in the absence of centrosomes from microtubules nucleated around DNA coated beads (Heald et al., 1996; Gadde and Heald, 2004). Microtubule nucleation at chromosomal DNA requires γ-TuRCs (Wilde and Zheng, 1999), but also depends on the proteins TPX2 activated by Ran-GTP (Gruss et al., 2001) and XHRAMM (Groen et al., 2004). In budding and fission yeast a structure similar to the centrosome exists which is called the spindle pole body (SPB). The SPB is embedded into the nuclear membrane and nucleates microtubules inside of the nucleus to form the mitotic spindle. However, in interphase fission yeast cells the SPB nucleates microtubules on its cytoplasmic face to form interphase microtubule arrays (see 1.3.2). Additional MTOCs are activated depending on the cell cycle. To assist cytoplasmic microtubule bundle formation, interface MTOCs (iMTOCs) nucleate microtubules at specific sites on the nuclear membrane. When the cells enter mitosis, these iMTOCs become inactive and the SPB switches from extranuclear to intranuclear nucleation. At the end of mitosis both the SPB and iMTOCs are inactive and microtubules are nucleated from the cell division cite by equatorial MTOCs (eMTOCs) (Sawin et al., 2004). But the situation is even more complicated in fission yeast: in interphase, new microtubules are also thought to be nucleated by γ-TuCs that bind and travel on existing

microtubules, and thus help to form and maintain the dynamic interphase microtubule bundles (Janson et al., 2005). A similar mechanism was found in plant cells, where microtubules are preferentially nucleated close to the cortex in two dimensional arrays (Ehrhardt and Shaw, 2006).

The example of fission yeast shows how the specific nucleation by γ-tubulin allows the cell to dynamically (re-)organize its microtubule cytoskeleton (see Sec. 1.3.2.2). The position of activated γ-TuCs determines where microtubules are nucleated throughout the cell cycle: at the cytoplasmic face of the nucleus and along existing microtubules in interphase, inside of the nucleus at the SPB in mitosis, and at the cleavage site at cell division. A common pattern in most eucaryotic cells is that the microtubule network is more dispersed in interphase when microtubules mainly serve structural and transportational purposes, while nucleation is concentrated around the chromosomes and at the SPB or centrosome in mitosis.

Apart from the creation of new microtubules from γ-tubulin complexes, short stabilized microtubule seeds can serve as templates for further elongation, as for example in the case of axonemes. The number of seeds can be rapidly increased by severing long pre-existing microtubules (Roll-Mecak and Vale, 2006). It was shown recently by electron microscopy that microtubule severing mediated by the protein katanin generates many short microtubules around meiotic chromatin in *C. elegans* (Srayko et al., 2006) and thus might assist chromatin related spindle formation.

1.2.4.4   Drugs and MAPs Regulate Microtubule Dynamics

The dynamic properties of microtubule polymerization can be affected by drugs and microtubule associated proteins (MAPs). In general there are two classes of natural toxins affecting microtubule dynamics. Microtubule destabilizing drugs usually bind free tubulin dimers and thus destabilize the microtubule lattice or prevent the incorporation of subunits into the filament. The drug colchicine from the meadow saffron for example prevents the establishment of lateral contacts between neighboring tubulin dimers in the microtubule lattice, because dimers bound to colchicine cannot adopt a straight conformation (Ravelli et al., 2004). Similarly, vinblastine binds to the longitudinal interface of tubulin molecules and forces them into a curved conformation which at high concentrations leads to microtubule depolymerization (Gigant et al., 2005). In contrast, the second class of toxins stabilizes microtubules. Taxol which was discovered in the bark of the Pacific yew tree is thought to strengthen lateral and longitudinal contacts between subunits and thereby helps maintaining a straight conformation of the tubulin dimer (Xiao et al., 2006).

In living cells dynamic instability is regulated by microtubule associated proteins (MAPs). MAPs stabilize or destabilize microtubules, alter the rates of subunit addition and removal, and mediate interactions with other cellular components. They can act globally, e.g. in response to regulatory signals during the cell cycle or locally to alter microtubule dynamics at specific locations inside the cell.

At the transition from interphase to mitosis for example, the number of catastrophes (the switch from polymerization to depolymerization) globally increases, resulting in more dynamic microtubules (Cassimeris, 1999; Wittmann et al., 2001). [1] This change of microtubule dynamics is believed to be mediated by the partial inactivation of XMAP215, a member of the XMAP215/Dis1 family of MAPs which has close homologs in many organisms ranging from yeast (Stu2) to human (TOGp). It affects

---

[1]The higher rate of catastrophe is thought to facilitate the search and capture of kinetochores by microtubules nucleated at the centrosomes (Kirschner and Mitchison, 1986). Recent studies indicate however (Odde, 2005) that the search and capture mechanism alone cannot account for the experimentally observed rate of chromosome capture, and that microtubules are additionally guided by a stabilizing gradient (Caudron et al., 2005), possibly assisted by microtubules nucleated at the chromosomes (Gadde and Heald, 2004).

microtubule dynamics in two different ways: in its active form XMAP215 speeds up microtubule plus end growth by a factor 7-10, but also increases the shortening rate about threefold (Vasquez et al., 1994). Data from electron microscopy showed that XMAP215 is an elongated molecule that can bind up to eight tubulin monomers, yet it does not affect microtubule rigidity or the curvature of protofilaments (Cassimeris et al., 2001), which suggests that it acts by enhancing the addition and removal of subunits at the microtubule plus end. The second effect of XMAP215 is related to microtubule catastrophes. XMAP215 does not change the rate of catastrophes itself but it seems to protect microtubule plus ends from the catastrophe promoting activity of another protein, namely XKCM1 (Tournebize et al., 2000). Strictly speaking, XKCM1 is not a MAP but a motor protein from the kinesin 13 family which is not processive but destabilizes microtubules at the plus end (Desai et al., 1999). At the onset of mitosis the activity of XMAP215 is downregulated by phosphorylation by cyclin-dependent kinase 1, whereas XKCM1 does not seem to be affected (Wittmann et al., 2001). This gives rise to a putative model where the phosphorylation of XMAP215 could play a central role in this change of microtubule dynamics (Heald, 2000).

However, the situation is more complicated. Although the amount of polymerized tubulin drops at prophase, possibly due to the phosphorylation of XMAP215, microtubules subsequently repolymerize to form the spindle. At this stage XMAP215 is found on the spindle but not on astral microtubules, and depletion of XMAP215 severely impairs spindle formation (Heald, 2000). These observations indicate that XMAP215 specifically stabilizes spindle microtubules and must therefore be subject to local regulation during spindle assembly.

Another example for the stabilizing activity of MAPs are the proteins from the MAP2/Tau family (Dehmelt and Halpain, 2005). Like XMAP215, MAP2 and Tau are structural MAPs with several microtubule binding domains (Al-Bassam et al., 2002). They bind longitudinally along the outer ridges of single protofilaments and thus reduce the rate of catastrophes. Both proteins are mainly found in neurons where MAP2 specifically stabilizes microtubules in dendrites while Tau is active only in the axon. Phosphorylation of MAP2/Tau can inactivate the MAP and induces dissociation from microtubules. However, hyperphosphorylation and specific mutations of Tau can promote its aggregation into helical filaments which are thought to be involved in neurodegenerative diseases such as Alzheimer's disease (Crowther and Goedert, 2000; Garcia and Cleveland, 2001). Tau furthermore competes in binding to microtubules with kinesin, and overexpression of Tau therefore inhibits the trafficking of vesicles, mitochondria and the endoplasmatic reticulum (Ebneth et al., 1998).

In contrast to MAP2 and Tau, oncoprotein 18 (Op18)/stathmin destabilizes microtubules. The name Op18 reflects the association of this MAP with several types of cancer. Overexpression of Op18/stathmin was found in leukemia as well as in breast and ovarian cancers, and the reduction of Op18/stathmin levels could reverse many of the phenotypes related to the cancer (Cassimeris, 2002). Two different mechanisms how Op18/stathmin destabilizes microtubules have been identified *in vitro* (Cassimeris, 2002): it either sequesters subunits or stimulates microtubule catastrophes. Sequestering of subunits results in a decrease of the free tubulin concentration and therefore has a dual effect on microtubule dynamics: it slows down growth and increases the catastrophe rate at both ends, as predicted by the NTP-cap model for dynamic instability (see Sec. 1.2.1). One Op18/stathmin molecule forms a complex with two tubulin dimers (T_2S) where the two tubulin dimers associate head to tail in a curved conformation (Gigant et al., 2000). Polymerization of the T_2S complex is thought to be prevented by the amino terminal tale of Op18/stathmin which binds to the interdimer interphase of the α-tubulin monomer (Wallon et al., 2000). At higher pH however, the polymerization rate of microtubules is barely affected by Op18/stathmin while the catastrophe rate is increased. The effect is furthermore limited to the plus end which suggests that the mechanism of this specific catastrophe promoting activity at high pH is indeed distinct from tubulin sequestering.

The destabilizing activity of Op18/stathmin can be switched off by phosphorylation, and is regulated during the cell cycle (Rubin and Atweh, 2004). When cells enter mitosis Op18/stathmin is phosphorylated to allow the formation of the mitotic spindle. Cells with a mutation at the phosphorylation site cannot inactivate Op18/stathmin and are arrested at the G_2/M transition (Rubin and Atweh, 2004). Later in mitosis at anaphase, Op18/stathmin is dephosphorylated again to allow separation of the sister chromatids. Thus the regulation of Op18/stathmin activity is critical not only for the formation of the spindle but also for the proper exit from mitosis. It was furthermore speculated (Cassimeris, 2002) that local deactivation of Op18/stathmin around chromatin or existing microtubules in the spindle may assist the search and capture of chromosomes by selectively stabilizing microtubules close to chromatin (see also footnote 1).

The local regulation of microtubule dynamics is not only crucial for cell division but also plays an important role in cell motility and polarity. It was shown that the dynamics of microtubules at the periphery of a cell can be very different compared to the interior (Komarova et al., 2002). In the experiments from Komarova et al. (2002), microtubule plus ends exhibited persistent growth after nucleation from the centrosome until they reached the plasma membrane, where they either paused or immediately switched to shrinking. In most cases, a catastrophe at the periphery was shortly followed by a rescue, resulting in microtubules fluctuating between growth and shrinkage close to the plasma membrane. This behavior is probably due to the direct contact of microtubule plus ends with the plasma membrane or with factors associated with it, as for example microtubule destabilizing proteins. It might enable a cell to rapidly adapt to a changing shape or to an advancing edge in the case of motile cells.

In *S. pombe* the behavior of microtubules at the cell poles is essential for the the delivery of growth factors and consequently for morphogenesis as described in section 1.3.3. In this work we investigated how dynamic instability is regulated at the poles in order to correctly organize microtubule bundles. The results of this study might also be relevant for the organization of microtubules in higher eucaryotes.

1.2.4.5   The Tip Tracking Proteins EB1 and CLIP170

A special class of microtubule associated proteins accumulates specifically at microtubule plus ends and was therefore termed +TIPs (for *plus*-end-*t*racking *p*roteins, (Schuyler and Pellman, 2001). It includes EB1, APC, Clip-170, the CLASPs and dynein as well as the fission yeast proteins Tea1 and Tea2. A comprehensive list can be found in (Carvalho et al., 2003) and (Akhmanova and Hoogenraad, 2005). The first +TIP discovered was the cytoplasmic linker protein (CLIP) Clip-170, which links endocytic vesicles to microtubules in HeLa cells (Rickard and Kreis, 1990; Pierre et al., 1992). It was later shown to stabilize microtubule plus ends and to facilitate the binding of dynein and its associated cargoes to the plus end (Wittmann and Desai, 2005). A similar function was described for the CLASPs (CLIP associated proteins) that were identified through their interaction with Clip-170 and Clip-115 (Akhmanova et al., 2001). But in contrast to Clip-170 which is found on all microtubule plus ends CLASPs are thought to specifically stabilize microtubules at the leading edge of motile cells (Akhmanova and Hoogenraad, 2005). The members of the EB1 protein family were described to promote microtubule growth, for example in *Xenopus* egg extracts and in fission yeast (Akhmanova and Hoogenraad, 2005; Busch and Brunner, 2004). Recent studies have shown that EB1 is also involved in the recruitment of protein complexes to the plus ends, including APC and other +TIPs but also motor proteins like Ncd (Vaughan, 2005; Goshima et al., 2005). Similar to CLASP, APC binds to EB1 and to microtubules directly and is specifically concentrated at the leading edge of migrating cells (Schuyler and Pellman, 2001)

In general, +TIPs are involved in a diverse set of functions which include the targeting and anchoring of specific cellular structures by microtubules, the recruiting of protein complexes to microtubule plus ends and their delivery to the cell periphery, and most important, the regulation of plus end dynamics (Carvalho et al., 2003; Galjart and Perez, 2003; Vaughan, 2005). +Tips are especially suited for the latter task since subunits are added or lost primarily at microtubule ends. Filament dynamics can therefore efficiently be regulated by a few proteins that specifically affect the state of filament ends. This is in contrast to microtubule associated proteins that bind to the sides of filaments like Tau or sequester subunits like stathmin, which have to be present at high stoichiometries to affect microtubule dynamics (for example, about one Tau for every four tubulin dimers).

The specific mechanisms how +TIPs target microtubule plus ends are still poorly defined. They can be divided into three major classes (Carvalho et al., 2003): *Treadmilling* of +TIPs (not to be confused with the treadmilling of cytoskeletal filaments) involves the recognition of specific features of growing microtubule plus ends and subsequent release from older parts of the filaments (Galjart and Perez, 2003), thereby leading to the formation of a typical comet-like structure during microtubule elongation. Association of MAPs to microtubule plus end can also be due to the protein binding to free tubulin subunits and subsequent co-polymerization. However, treadmilling and selective plus end accumulation would arise only, if co-polymerization was coupled to the rapid release of the MAP from the microtubule walls. The other two mechanisms are *hitchhiking* for proteins that bind to the microtubule via other +TIPs like for example CLASP, and the *transport* of +TIPs by plus ends directed motor proteins. Often, these mechanisms cannot clearly be separated like for example in the case of Tip1p, the fission yeast homolog of Clip-170, which is transported towards microtubule plus ends via the motor Tea2p, but can also bind to microtubules via the EB1 homolog Mal3 (Busch and Brunner, 2004). Since we used computer simulations to study the microtubule cytoskeleton in *mal3Δ* and *tip1Δ* cells, these two protein families are described in more detail below.

The EB1 Protein Family

The end binding protein 1 (EB1) was originally identified in a two-hybrid screen as a binding partner of the human tumor suppressor protein adenomatous polyposis coli (APC) (Su et al., 1995). Members of the EB1 protein family are highly conserved in eucaryotes and have a common domain structure with a single calponin homology domain (CH domain) at their N terminus, followed by a coiled coil-region and the EB1-like domain at their C-terminus which is unique to EB1 family proteins (Bu and Su, 2003). The CH domain was shown to be necessary and sufficient for the association with microtubules *in vitro* which is thought to be mediated by a combination of electrostatic and hydrophobic interactions (Hayashi and Ikura, 2003; Bu and Su, 2003). Analyzing the crystal structure of the C-terminal EB1 domain indicated that EB1 family proteins form a stable dimer with a parallel coiled coil and that dimerization is essential for the formation of the C-terminal domain (Honnappa et al., 2005). The EB1 domain is responsible for the binding of several interacting proteins like APC and p150[glued] (Bu and Su, 2003; Honnappa et al., 2005).

EB1 proteins are found to associate with microtubules through all stages of the cell cycle (Morrison et al., 1998). While EB1 binds in little amounts along the whole length of a microtubule, it is usually concentrated in comet like structures at the tips of growing microtubule plus ends. However, differences in binding exist between distinct cell types: studies in budding yeast revealed that the EB1 homolog Bim1 decorates the entire microtubule cytoskeleton when overexpressed (Schwartz et al., 1997), but is present only at microtubule tips and at the SPB at endogenous levels (Tirnauer et al., 1999; Tirnauer and Bierer, 2000). Similar results were obtained in human (Morrison et al., 1998) and fission yeast (Busch and Brunner, 2004), whereas EB1 localization varied with the cell cycle in *Xeno-*

pus egg extracts. In interphasic extracts EB1 was present all along the microtubule lattice even at low expression levels, while it formed comets at the microtubule tips in cytostatic factor (CSF) extracts (Tirnauer et al., 2002b). Apart from microtubules, EB1 is also found at the centrosome and at the SPB in yeast (Tirnauer and Bierer, 2000). The localization at MTOCs is thought to be independent of microtubules since it was not abolished by treatment with microtubule depolymerizing drugs (Rehberg and Gräf, 2002; Louie et al., 2004). In contrast, association of EB1 with kinetochores was shown to be microtubule dependent (Tirnauer et al., 2002a).
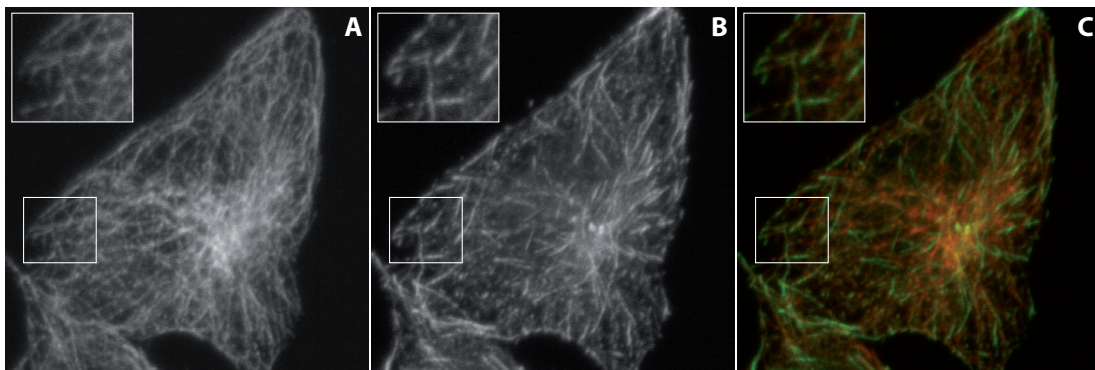
Figure 1.11: Immuno labeling of microtubules in HeLa cells expressing EB3-EGFP. HeLa cells expressing EB3-EGFP were fixed in methanol and permeabilized in TBS-0.5% TX. Microtubules (A) were labeled with anti α-tub generated in mouse and Rhodamine-anti mouse as secondary antibody. The EB3-EGFP signal is shown in (B). The inset in the upper left corner represents a magnification of the area in the white rectangle. The two color image (C) illustrates the localization of EB3 at the tips of microtubules. Images were kindly provided by Lucia Sironi, EMBL.

Why EB1 preferentially binds to growing microtubule plus ends is not precisely known, but time-lapse analysis of fluorescent EB1 speckles in *Xenopus* egg extracts indicate that it is not transported by motor proteins (Tirnauer et al., 2002b). Instead, EB1 was speculated to recognize the specific structural or chemical properties of growing microtubule ends or to copolymerize with free tubulin subunits, albeit the latter possibility seems less likely since tubulin did not immunoprecipitate together with EB1 (Tirnauer et al., 2002b). Support for the idea that EB1 recognizes growing microtubule ends comes from the recent finding that the fission yeast homolog Mal3 specifically binds to the seam of thirteen protofilament microtubules, i.e. to an A-lattice (Sandblad et al., 2006). It is thought that the sheet-like structure of growing microtubule plus ends might offer more binding sites for Mal3 than the closed surface of a thirteen protofilament tube that exhibits an A-lattice only at the seam.

The specific binding of Mal3 to the seam which is the weakest point of the microtubule lattice, furthermore sheds light on its function in regulating microtubule dynamics. By binding to the seam, EB1 is able to stabilize microtubules without blocking the remaining surface for the binding of other MAPs and motors. Indeed, EB1 stabilizes microtubule plus ends and increases their steady state length in most organisms where its function was studied. In *Xenopus* egg extracts for example, depletion of EB1 from mitotic extract caused a dramatic shortening of microtubules, whereas microtubule length in interphasic extracts was not affected (Tirnauer et al., 2002b). Live imaging of individual microtubules revealed that in both types of extract the addition of EB1 reduced the rate of catastrophes and promoted rescues. In addition to that, microtubule shrinking was slower and pausing times, where microtubules were neither growing nor shrinking, were significantly shorter. Microtubule polymerization was not affected in mitotic extracts, whereas it was increased in interphase. Altogether this

caused microtubules to be longer and more stable if EB1 was added. Similar results were obtained for the EB1 homolog Bim1 in budding yeast, where the effect of Bim1 deletion is especially prominent in G1 phase (Tirnauer et al., 1999). In *Bim1Δ* cells, microtubules were overall shorter and less dynamic due to reduced growth and shrinkage velocities and lower catastrophe and rescue rates. As in the case of *Xenopus*, pausing times were increased in cells lacking Bim1. Interestingly, the effect on the catastrophe rate was opposite to the one in *Xenopus* egg extracts. However, care has to be taken in comparing these values since the catastrophe rate was measured in a non-standard way in the study on Bim1. In fission yeast, the deletion of *Mal3* reduced microtubule growth and shrinkage only little, while the catastrophe rate was greatly increased (Busch and Brunner, 2004). The phenotype of *Mal3* deletion in fission yeast is described in more detail in Sec. 5.3.1.

The regulation of microtubule dynamics is not the only function of EB1. Through its interaction with other +TIPs and with motor proteins it is involved in a great variety of processes. In budding yeast it is thought to be implicated in the cortical capture of microtubule tips and in the positioning of the spindle by binding to Kar9, which is guided along actin cables to the bud neck (Lee et al., 2000; Liakopoulos et al., 2003). Kar9 is related to the human tumor repressing protein APC which also binds to EB1. APC has several known functions, including the degradation of β-catenin in the Wnt-signaling pathway, the regulation of microtubule dynamics and the segregation of chromosomes (Zumbrunn et al., 2001; Fodde et al., 2001; Fodde, 2003). EB1 proteins furthermore interact with p150^glued which is a part of the dynactin complex. Through this interaction, EB1 was shown to be implicated in the anchoring of microtubule minus ends at the centrosome (Bu and Su, 2003; Askham et al., 2002). Recent findings indicate that EB1 is also associated with another minus end directed motor, the kinesin Ncd in *Drosophila* S2 cells. Ncd binds to microtubules via its motor domain and via EB1 and is therefore able to crosslink microtubules. It is thought to mediate the interaction between microtubules growing from the kinetochores (K-fibers) and centrosomal microtubules (C-fibers). Computer simulations performed with the same software package used for the present study suggest that Ncd forms a complex with EB1 which is present at the tips of K-fibers, while its motor domain moves towards the spindle poles along the C-fibers and thus assists the focusing of the poles (Goshima et al., 2005).

The Clip-170 Protein Family

As described above, Clip-170 was first identified as a microtubule associated protein with a molecular weight of $170kD$ in HeLa cells (Rickard and Kreis, 1990). It was termed *C*ytoplasmic *LI*nker *P*rotein since it was thought to belong to a new class of proteins that mediates specific interactions between organelles and microtubules (Pierre et al., 1992). The protein consists of a central α-helical coiled coil domain that is flanked by two similar CAP-Gly[2] motifs at the N terminus and two metal binding motifs at the C Terminus. The CAP-Gly domains are responsible for microtubule binding *in vitro* (Pierre et al., 1992) as well as *in vivo* (Pierre et al., 1994), while the metal binding motifs are used to bind other proteins like p150^glued or LIS1. Studies using AFM and FRET furthermore indicated that the CAP-Gly domain of Clip-170 associates with the first metal binding motif of the C terminus (Lansbergen et al., 2004), thereby folding the protein back on itself. This intramolecular interaction is thought to interfere with the binding of Clip-170 to microtubule tips, as well as to p150^glued and LIS1, and its regulation might allow the cell to locally activate or inactivate Clip-170 function. The

---

[2]The CAP-Gly domain was originally defined as a glycin-rich domain (Gly) that exhibits sequence homologies between four cytoskeleton-associated proteins (CAPs). One of these four proteins was restin, an alternatively-spliced form of Clip-170 that is found in high levels in cancer (Reed-Sternberg) cells, and another one was Bik1, the budding yeast homolog of Clip-170 (Riehemann and Sorg, 1993).

central coiled coil domain mediates dimerization of Clip-170 (Scheel et al., 1999). One homodimer therefore includes four N-terminal CAP-Gly domains and four C-terminal metal binding motifs. The budding and fission yeast homologs Bik1 and Tip1 have only one CAP-Gly domain and one metal binding region per monomer (Brunner and Nurse, 2000).

The localization of Clip-170 was first analyzed in HeLa cells using antibodies. In Interphase, the protein is found in patches along the microtubule network and at the microtubule plus ends (Rickard and Kreis, 1990; Pierre et al., 1992). In mitotic cells Clip-170 localizes to the spindle but also to prometaphase kinetochores, which indicates a potential role in chromosome segregation (Dujardin et al., 1998). Live imaging with GFP-tagged Clip-170 revealed its association with growing microtubule plus ends (Perez et al., 1999), where it forms comet-like dashes that move with the growing ends. These comets become shorter if growth slows down, and are completely absent from depolymerizing microtubules. Upon rescue, new comets are acquired at growing microtubule tips.

Inhomogeneities of the fluorescence intensity within the comets were used to analyze the movements of Clip-170 along microtubules. Since such speckles of GFP-tagged Clip-170 remained immobile while the comets moved with the growing microtubule ends, it was concluded that the protein is not actively transported by motors, but rather uses treadmilling to associate with the filament tip (Perez et al., 1999). Indeed, sedimentation velocity experiments suggest that Clip-170 binds to unpolymerized tubulin and promotes the formation of tubulin oligomers (Diamantopoulos et al., 1999), and might therefore be co-polymerizing. This idea is supported by observations from electron cryo microscopy which show that the N-terminal part of Clip-170 induces the formation of tubulin rings in solution (Arnal et al., 2004). Treadmilling by co-polymerization requires that shortly after binding to the microtubule the affinity of the protein to the lattice is reduced, such that it unbinds from older parts of the filament and forms a comet at the tip. It was in fact shown that phosphorylation of Clip-170 on serine residues inhibits binding to microtubules (Rickard and Kreis, 1991). Co-polymerization and subsequent phosphorylation by a microtubule associated kinase could therefore be responsible for the treadmilling of Clip-170. Dephosphorylation of Clip-170 in the cytoplasm would then restore its ability to bind tubulin and prepare it for another round of treadmilling. However, a separate phosphorylation activity by the kinase FRAP has been identified that increases the interaction of Clip-170 with microtubules, indicating that the *in vivo* situation is more complicated and multiple kinases are involved in the regulation of Clip-170 activity.

A different mechanism of plus end tracking could be identified for Bik1 and Tip1, the budding and fission yeast homologs of Clip-170. Careful analysis in living yeast cells revealed that Bik1 and Tip1 are transported towards the plus ends by the kinesins Kip2 and Tea2 respectively (Carvalho et al., 2004; Busch et al., 2004). Interestingly, the accumulation of Tip1 at the microtubule plus ends in *S. pombe* furthermore depends on its binding to Mal3, the fission yeast homolog of EB1. Deletion of Mal3 also removes Tip1 from the plus ends (Busch and Brunner, 2004), while the presence of Bik1 at the polymer tips in budding yeast does not require Bim1, the EB1 homolog in *S. cerevisiae*. Recent findings in mammalian cells and *in vitro* indicate that CLIPs possess an intrinsic affinity for growing microtubule ends, which is enhanced by an interaction with EB1 (Komarova et al., 2005; Ligon et al., 2006)

In HeLa cells Clip-170 colocalizes with endosomes and was shown to be involved in the binding of endocytic carrier vesicles to microtubules. The preferential accumulation of Clip-170 at microtubule ends might facilitate the capture of peripheral endosomes by microtubules to allow their subsequent translocation by motor proteins. However, in fission yeast, endocytic vesicles do not seem to be associated with microtubules (Höög et al., 2007) which indicates that the binding of Clip-170 to vesicles might not be relevant in yeast. Analysis of GFP-tagged Clip-170 in living HeLa cells indicated that it might have a function in the spatial regulation of microtubule dynamics (Perez et al., 1999). Indeed it

was shown in fission yeast that Tip1 specifically prevents catastrophes of microtubules that touch the cortex in central regions of the cell, and thus allows them to reach the cell poles where Tip1 is removed from microtubule tips (Brunner and Nurse, 2000). Deletion of Tip1 results in premature catastrophes of microtubules that touch the central cortex, while the ones that happen to grow straight through the cytoplasm remain unaffected and can still reach the poles. A function of Clip-170 in regulating microtubule dynamics is also observed in budding yeast, where Bik1 deletion causes cytoplasmic microtubules to be very short or undetectable. Cells overexpressing Bik1 have abnormally short spindle microtubules and long cytoplasmic microtubules (Berlin et al., 1990). (A comprehensive review of Bik1 function in budding yeast can be found in Miller et al. (2006).) Interestingly, the premature-catastrophe-phenotype of Tip1 deletion in fission yeast is rescued by a construct that is lacking the C-terminal region of the protein containing the metal binding domain. Other phenotypes like the inability of localizing Tea1 at the cell poles remain, which indicates that only the N terminus is relevant for the regulation of microtubule dynamics but that the C terminus is essential for other functions (Brunner and Nurse, 2000). Studies in Chinese hamster ovary (CHO) cells confirmed these results. Overexpression of a dominant negative construct of Clip-170 was used to remove the endogenous CLIPs from microtubule plus ends (Komarova et al., 2002). While in wild type cells microtubules grow towards the plasma membrane where they constantly fluctuate between growth and shrinkage, the rescue rate was reduced sevenfold in the absence of CLIPs. Consequently, instead of fluctuating, microtubules exhibited periods of persistent growth and shrinkage and were overall shorter, thereby altering the distribution of microtubule plus ends.

Apart from regulating microtubule dynamics, CLIPs are involved in many processes mediated by their binding partners. The most important are the CLASPs which also play a role in the local regulation of microtubule dynamics, p150$^{\text{glued}}$, a part of the dynactin complex that helps recruiting dynein/dynactin to microtubule tips, LIS1 which is also involved in the Clip-170/dynein interaction and potentially in the localization of CLIP-170 to kinetochores, and IQGAP1. A further discussion of the functions of CLIP-170 and its binding partners can be found in Galjart (2005).

1.2.4.6   Motor Proteins

Besides the MAPs discussed in the previous sections, motor proteins also associate with microtubules and use them as linear tracks to propel themselves forward. Such molecular motors utilize the energy gained from the hydrolysis of ATP to carry out mechanical work. Their duties can be divided into three major categories: firstly, they transport cargoes like membrane enclosed organelles, proteins or mRNA along microtubules to specific locations inside the cell. Examples are the transport of Golgi stacks, the ER and mitochondria as described at the beginning of this section (1.2.4), but also the delivery of cell end factors to the poles of fission yeast (Sec. 1.3.3). Secondly, they move and organize microtubules relative to each other or relative to other organelles. Examples for microtubule structures organized by molecular motors are the mitotic spindle or the microtubule bundles in interphase fission yeast cells (Sec. 1.3.2.2). The sliding of microtubules along each other furthermore generates the movements of flagella and cilia. The third function of microtubule associated motors is to destabilize microtubule plus ends (see also the discussion of XKCM1 above 1.2.4.4), which in some cases is also thought to generate movements, e.g. during the segregation of chromosomes in the mitotic spindle (Westermann et al., 2006).

Microtubule associated motors generally bind to the microtubule lattice through a head region or motor domain that also binds and hydrolyzes ATP, while the tail of the molecule serves for the oligomerization of motors and for the binding to cargoes. The hydrolysis of the nucleotide is coupled to conformational changes of the head domain which leads to a complicated mechanochemical

cycle of filament binding, conformational changes and filament release. Motors often dimerize and thus contain two motor domains, which enables the dimer to perform processive motion along the microtubule (i.e. continuous directed movements without detaching from the microtubule). Because microtubules are polar filaments, different types of motors move into different directions along the lattice.

Dynein

Two major classes of microtubule associated motors are distinguished which are thought to be un-related to each other: dyneins and kinesins. Dyneins are minus end directed motors that were first identified in cilia and flagella (Vale, 2003). Another branch of the dynein family, the cytoplasmic dyneins, were later discovered to be responsible for minus end directed motion in nonciliated cells. Dynein forms a large complex with numerous subunits that are thought to interact with distinct protein partners to facilitate docking to different cargoes. Dynein furthermore interacts with the multisubunit complex dynactin, which seems to act as a general regulator of dynein mediated transport activity (Vale, 2003). Cytoplasmic dynein is involved in many diverse processes such as the transport and positioning of organelles, asymmetric spindle positioning and asymmetric cell division (Cowan and Hyman, 2004; McCarthy and Goldstein, 2006), the transport of intermediate filament particles (Sec. 1.2.3) and the organization of spindle poles (Fig. 1.12).

Relatively little is known about the mechanisms of dynein motility. Cytoplasmic dyneins usually form homodimers with two large motor domains as heads (Vale, 2003). A recent study shows that for cytoplasmic dynein two motor domains are needed for processivity (Reck-Peterson et al., 2006) and that it advances most frequently in $8nm$ steps corresponding to the $8nm$ repeat of the tubulin lattice. However, longer as well as side and backward steps were also observed which suggests that diffusion contributes by a considerable amount to the stepping of cytoplasmic dynein. Interestingly, a single headed axonemal dynein was shown to move processively, suggesting a mechanism other than one involving the coordination of two motor domains (Reck-Peterson et al., 2006).

Kinesin

Kinesins comprise a large and heterogeneous family of motor proteins, called the kinesin superfamily. They share many mechanistic similarities with myosin which lead to the conclusion that these two classes of motor proteins have a common evolutionary origin (Vale and Milligan, 2000). The first kinesin was isolated from squid giant axons (Vale et al., 1985), where it is involved in the plus end directed transport of membrane enclosed organelles along the axon. Subsequently, kinesins were identified in all groups of eucaryotes with six members in budding yeast (Hildebrandt and Hoyt, 2000), and 45 members in human (Miki et al., 2001). The common element of all kinesins is the head or motor domain which binds to the microtubule and hydrolyzes ATP. An early classification of kinesins was based on the position of the head in the protein sequence (Vale and Fletterick, 1997). Most kinesins have the motor domain at the N-terminus (KinN) and walk towards the microtubule plus end, while kinesins that have the motor domain at the C-terminus (KinC) walk to the minus end. A third group has the catalytic core in the middle of the molecule and was therefore referred to as M-kinesins (for middle type kinesin) or KinI (internal type) (Miki et al., 2005). However, this classification (and others with respect to function or evolutionary relatedness) lead to inconsistencies and confusion which resulted in a new nomenclature for the kinesin superfamily based on sequence similarity, so far comprising 14 families (Lawrence et al., 2004; Miki et al., 2005).

While the motor domain is conserved within the kinesin superfamily, different kinesins exhibit enormous variations with respect to composition and function. Some of them operate as monomers, others dimerize or even form trimers or tetramers mediated by the coiled-coil regions of their heavy

chains. Some move processively in a hand-over-hand mechanism (Yildiz and Selvin, 2005), while others are thought to undergo one dimensional diffusion (Hunter et al., 2003). As mentioned above they can move directionally towards either end of a microtubule to transport cargoes or to organize microtubules, or they influence microtubule dynamics by destabilizing their plus ends (Moores and Milligan, 2006).
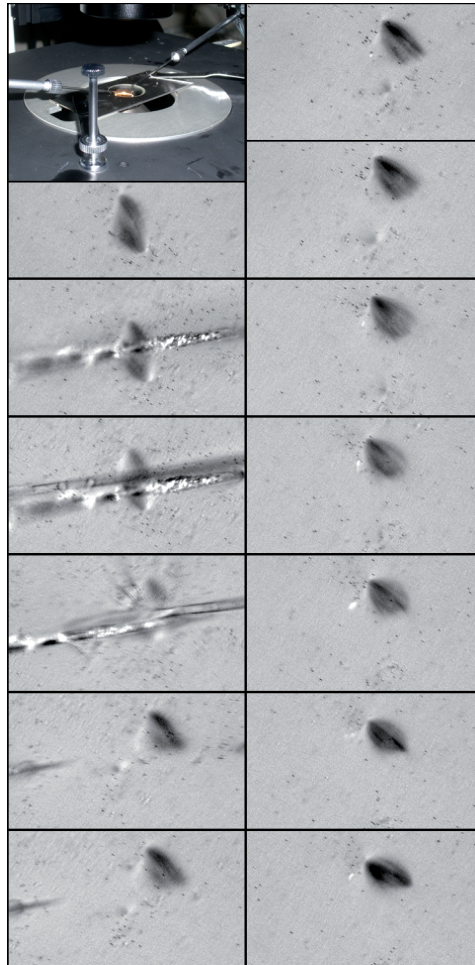
Figure 1.12: Cutting one spindle pole with a glass needle. Spindle formation in *Xenopus* egg extract was triggered by the addition of sperm nuclei, which nucleate microtubules at the associated centrosomes (see Gadde and Heald (2004)). The extract was put on a slide and covered with mineral oil to avoid drying. One pole of a spindle was severed next to the chromosomes with glass needles attached to micromanipulators. After cutting, microtubules regrew from the chromosomes and focused to reform the missing spindle pole, even in the absence of the second centrosome. The formation of a pole in the absence of centrosomes and the recruitment of many mitotic factors to the poles is thought to be mediated by cytoplasmic dynein. This experiment was performed in the Physiology Course in Woods Hole, summer 2004.

Several types of kinesins play an important role in the establishment of the mitotic spindle. Plus end directed tetrameric motors like the *Xenopus* Eg5, a member of the kinesin 5 family (previously referred to as BimC), contain four motor domains and are thought to organize microtubules relative to each other. It was proposed that in *Xenopus*, Eg5 crosslinks and bundles parallel microtubules

while microtubules pointing in opposite directions are separated (Walczak et al., 1998). By pushing apart antiparallel interpolar microtubules Eg5 might play an important role in the creation of bipolar microtubule arrays during spindle assembly. Two other kinesins are thought to be involved in the alignment of chromosomes at metaphase and their segregation at anaphase: MCAK (or XKCM1 in *Xenopus*) from the kinesin 13 family (formerly referred to as KinI) localizes to the kinetochores where it is thought to destabilize microtubule plus ends (see above and Sec 1.2.4.4) and possibly contributes to the forces that pull the chromosomes towards the spindle poles. In contrast to the kinetochores, chromosome arms are subject to a force directed away from the poles that is important for their alignment in metaphase. This polar-ejection force is thought to be mediated by plus end directed kinesins located on the chromosome arms like the *Xenopus* kinesin Xkid where the family assignment has yet to be determined. The minus end directed motor Ncd from the kinesin 14 family is thought to localize to kinetochore microtubules (K fibers) where it is involved in the focusing of spindle poles. It is furthermore found at the plus ends of centrosomal microtubules where it is implicated in the capture of K fibers (Goshima et al., 2005).

1.3   The Fission Yeast *Schizosaccharomyces pombe*

The unicellular fission yeast has become a popular model organism in molecular and cell biology. It is a rod-shaped eucaryote with a diameter of $3 - 4\mu m$ and a length of $7 - 14\mu m$ depending on how far the cell progressed through the cell cycle. Fission yeast maintains its cylindrical shape by growing exclusively at the cell poles and by dividing through medial fission, thereby producing two daughter cells of equal size. Due to its simple shape and intracellular organization it is ideally suited to study cell division and growth. Standard genetic techniques and straightforward crossing methods can be applied, which makes it relatively easy to handle experimentally. *S. pombe* was first isolated in 1893 by Lindner from East African millet beer, and its name was derived from the Swahili word "Pombe" for beer. Most strains used today trace back to cells that were isolated by A. Osterwalder from "an exceedingly over-sulfurized grape juice", originating from southern France (Egel, 2004). In the 1950s, *S. pombe* was used by Murdoch Mitchison to study the cell cycle. For unraveling the mysteries of the cell cycle in fission yeast, Paul Nurse together with Lee Hartwell and Tim Hunt were awarded the Nobel Prize for Medicine in 2001.

Because of the simple organization of its cytoskeleton (see Sec. 1.3.2) *S. pombe* is furthermore used to study the connection between morphogenesis, polarization and the regulation of the cytoskeletal network. As described in section 1.3.3, microtubules are essential for the establishment and maintenance of cell polarity in fission yeast, while at the same time microtubules are possibly guided by localized polarity markers and by cell shape. To disentangle the resulting feedback loop, we investigated what are the minimal requirements to reproduce the organization of microtubules in wild type cells, using a combined approach of computer simulations and experiments described in section 1.4.
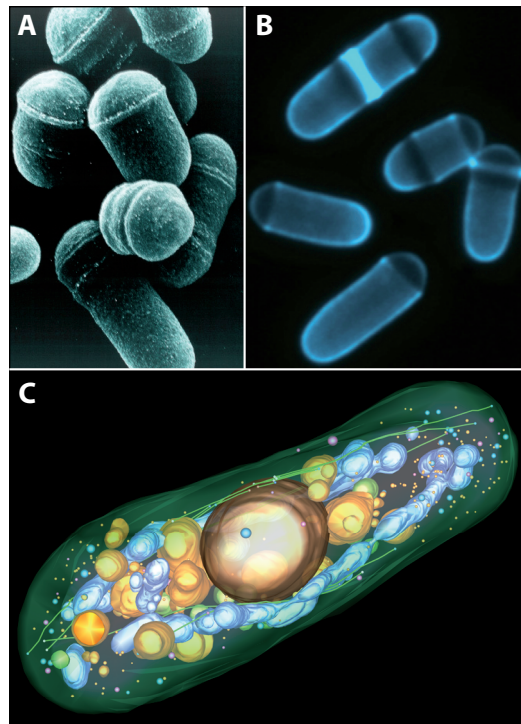
Figure 1.13: Images of *S. Pombe* obtained by different microscopy techniques. (A) Scanning electron micrograph of fission yeast cells. The rings around the cells are birth scars from the previous attachment site to the sister cell. (B) Staining of the fission yeast cell wall with the fluorescent dye calcofluor. The bright band in the dividing cell on top corresponds to a septum. (A) and (B) were kindly provided by Damian Brunner, EMBL. (C) Electron tomogram of a fission yeast cell. Microtubules are shown in green, mitochondria in light blue. Vacuoles are shown in yellow and the small spherical objects illustrate the position of vesicles. Image (C) was kindly provided by Johanna Höög, EMBL.

1.3.1 The Cell Cycle

Like other eucaryotic cells, fission yeast alternates between phases of growth and division. In interphase, wild type cells elongate exclusively at the cell poles and divide by medial fission, which is sufficient to maintain the cylindrical cell shape (see also Sec. 1.3.3). These alternating events are accompanied by a drastic reorganization of the actin and microtubule cytoskeleton (Fig. 1.14), discussed in more detail in section 1.3.2. In common with other fungi, *S. pombe* undergoes a closed mitosis where the nuclear envelope remains intact throughout M-phase. However, fission yeast is special with respect to the timing of events during the cell cycle. The chromosomal DNA is replicated fast during S-phase, which in rapidly dividing cells commences shortly after nuclear division. S-phase therefore coincides with septum formation and is basically finished when cytokinesis occurs. The newly separated daughter cells consequently emerge as G_2 cells from the start.
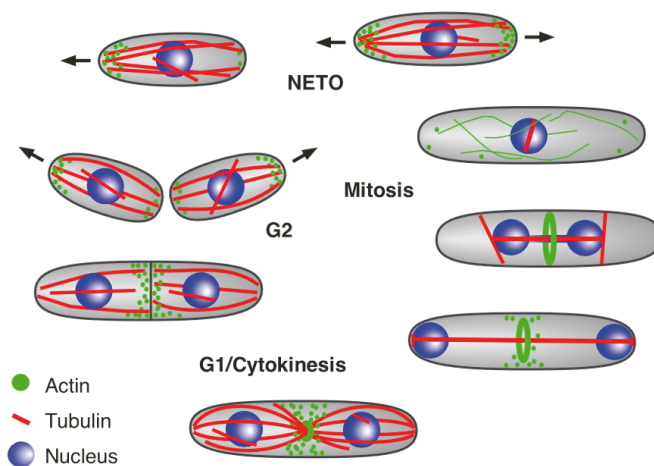
Figure 1.14: The fission yeast cell cycle. The different stages of the cell cycle are shown in clockwise order. Microtubules are drawn in red, actin patches and actin filaments in green, and the nucleus in blue.

The nuclear division cycle is tightly coordinated with the morphogenetic cycle. As cells exit from mitosis they start growing at the old end only, which already existed before cell division (see also Fig. 1.14). Growth is dependent on actin, which localizes in patches at the old pole (see Sec. 1.3.3). In interphase, microtubules form bundles that are attached to the nucleus and push at the poles to ensure that the nucleus stays centered, even as the cell grows in an asymmetric manner. Once the cell reaches a critical mass, actin patches also accumulate at the new cell end, and the cell switches from monopolar to bipolar growth. This transition occurs in G_2 and is also called new end take-off (NETO) (Mitchison and Nurse, 1985). In wild type cells, the new growth site is placed exactly opposite of the old end which ensures that cells grow straight. However, its position depends on microtubules and associated proteins like Tea1, and mutants of cytoskeletal proteins often exhibit morphological defects (see Sec. 1.3.3). After reaching a certain length, cells temporarily cease growing at the poles and enter mitosis. Actin is relocalized to the cell center where it forms a contractile ring composed of f-actin, myosin and numerous other proteins. Microtubules depolymerize in the cytoplasm and the mitotic spindle is formed inside of the nucleus. When the spindle elongates in anaphase the nucleus adopts a barbell-like shape (Fig. 1.15). During this process the two daughter nuclei are pushed into the

old cell poles and are repositioned by cytoplasmic microtubules to the new cell centers after spindle breakdown. Upon disassembly of the mitotic spindle at the end of anaphase, the actomyosin ring constricts and the septum is deposited at the cell center. Finally the cells undergo cytokinesis and resume growth at the old end to go through another cell cycle.
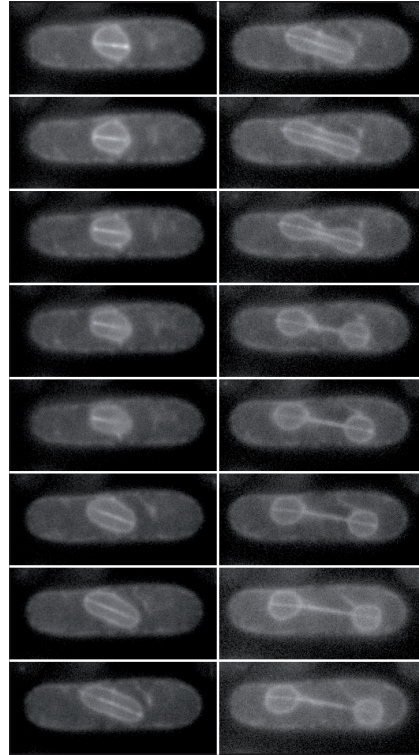
Figure 1.15: The nucleus in anaphase. Cells expressing GFP-α2tub were transformed with pD817, a plasmid encoding for GFP-cytochrome P450 reductase to label nuclear and plasma membranes. The image sequence shows how the spindle elongates at anaphase and pushes the two daughter nuclei into the cell poles.

1.3.2   The Fission Yeast Cytoskeleton

In fission yeast, actin and microtubules are both considered important regulators of cell growth and polarization. Because of the cell wall, both cytoskeletal components are not essential for maintaining cell shape in a structural sense, as it is the case in some animal cells. Yet they are involved in the positioning and regulation of growth and polarity factors, for example at the cell poles in interphase. In the following sections we therefore briefly discuss the most important aspects of the actin and microtubule cytoskeletons throughout the cell cycle. So far, none of the classical intermediate filaments (IF) were discovered in *S. pombe*, although IF-like structures have been reported in budding yeast (McConnell and Yaffe, 1993).

1.3.2.1   Actin

As described in the previous section, the distribution of actin follows the pattern of growth and cytokinesis. In interphase, patches of F-actin are localized at the regions of growth at the cell poles. When the cell starts growing at the old pole after cytokinesis, actin patches are found exclusively at the growing pole, and only become associated with the new end after NETO (Marks et al., 1986). The amount of actin patches at either end correlates with the velocity of cell growth, which is about 1.5 times faster at the old end (Mitchison and Nurse, 1985; Egel, 2004). Cables of F-actin furthermore extend along the axis of the interphase cell (Arai et al., 1998; Pelham and Chang, 2001), which are thought to be

involved in the formation of the contractile ring at the onset of mitosis (Arai and Mabuchi, 2002). At the transition to M-phase, the patches disappear from both ends and the actomyosin ring is formed at the site where the septum will be built at cytokinesis. After the cleavage of the two daughter cells, actin patches relocalize to the old ends to commence another round of cell growth.
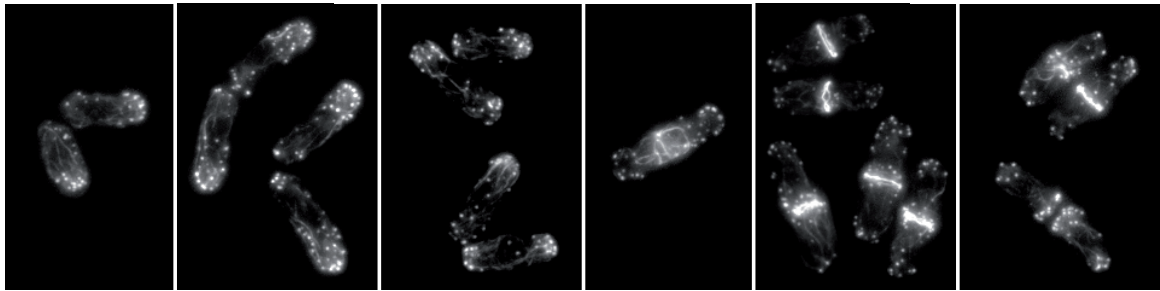
Figure 1.16: Distribution of F-actin during the cell cycle. Cells were fixed in paraformaldehyde and stained with bodipy-phallacidin. Images follow the stages of the cell cycle from left to right, i.e. from the beginning of G_2 to cytokinesis. After division actin localizes only to the old poles, and later in G_2 also accumulates at the new pole. At the onset of mitosis, actin cables are redistributed to the cell center to form the cytokinetic ring. Before the cell finally divides, secondary septa are formed at both sides of the primary septum.

Because of their correlation with active regions of cell growth, actin patches are regarded as a general marker of growth sites. They are nucleated by the Arp2/3 complex (see also Sec. 1.2.2), which colocalizes with the patches at the cell poles (McCollum et al., 1996; Morrell et al., 1999). The patches were furthermore shown to be motile using a fusion of GFP to the fission yeast homolog of coronin, Cor1-GFP. Cor1 localizes to actin patches and with less affinity also to actin cables. It was shown that the patches move in an undirected manner at the poles but also translocate along actin cables, mostly in the direction away from the cell ends (Pelham and Chang, 2001). Both types of motion are dependent on actin polymerization and are suppressed by the addition of latrunculin A. Actin patches furthermore stopped moving in mutants of Arp3 which suggests that they drive their own movement using Arp2/3 based polymerization, and that motor proteins are not involved in this process. The formation of actin cables depends on the formin For3 (Feierbach and Chang, 2001). Most actin cables in interphase are oriented with their barbed ends facing the cell poles, but reverse their direction during mitosis (Kamasaki et al., 2005). Recently it was discovered that small dots of For3 move on the cables from the cell poles towards the center, with a speed corresponding to the polymerization of F-actin (Martin and Chang, 2006). These movements are dependent on the continuous assembly of actin and on the ability of For3 to bind to the barbed end of actin with its FH2 domain. It is thought that For3 is delivered to the cell poles through association with the microtubule tip tracking protein Tea4 (Martin et al., 2005). For3 particles are then transiently anchored and activated at the poles where they assemble a short actin filament that is incorporated into a larger actin bundle. When For3 is inactivated, it occasionally remains bound to the barbed end of its filament and travels towards the cell center, moved by the polymerization of actin from active formins at the pole. While actin patches are nucleated by the Arp2/3 complex, formins appear to take over this function in cable assembly.

The polarized actin cables furthermore serve as tracks for the delivery of vesicles to the cell poles. The fission yeast myosin V, Myo4, transports secretory vesicles along the cables to the sites of growth at the poles in interphase, and to the cell center in mitosis (Motegi et al., 2001; Win et al., 2001). Interestingly, disruption of Myo4 not only results in abnormal accumulation of vesicles throughout the cytoplasm, but also causes actin patches to redistribute over the whole cortex, leading to a high num-

ber of round cells. Apart from its role in polarized cell growth and in cytokinesis, actin is furthermore important for endocytosis. Recent experiments utilizing the uptake of a fluorescent dye by endocytic vesicles demonstrated that the sites of endocytosis coincide with the location of actin patches (Gachet and Hyams, 2005). Furthermore, endocytosis was inhibited in mutants that affected actin patch integrity and by latrunculin A.

As illustrated by targeting For3 to the cell poles by microtubules, there is considerable interplay between the actin and the microtubule cytoskeletons in fission yeast. Another example is the polarity marker Tea1 (Behrens and Nurse, 2002; Sawin and Snaith, 2004), which is transported on the plus ends of microtubules and is thought to be anchored to the cortical actin cytoskeleton at the poles. The concerted action of actin and microtubules is needed for the establishment and maintenance of growth sites in fission yeast (see Sec. 1.3.3).

1.3.2.2   Microtubule Bundles in Interphase

In interphase, microtubules form 3-6 bundles that align parallel to the long axis of the cell (Hagan, 1998). Within these bundles microtubules are organized in an antiparallel way with their minus ends close to the cell center, where the bundles are attached to the nucleus (Fig. 1.17).
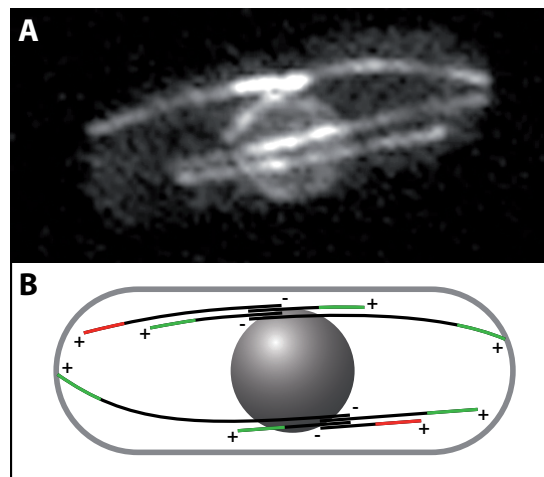
Figure 1.17: Microtubule organization in an interphase fission yeast cell. (A) A strain expressing GFP-tubulin and the nuclear pore marker Nup85-GFP. Microtubule bundles are attached to the nucleus and orient parallel to the cell axis. They position the nucleus at the cell center by pushing against the poles. (B) A simplified model of microtubule organization in interphase fission yeast. Microtubule plus ends face the cell poles while the minus ends form an antiparallel overlap region close to the nucleus. The composition of bundles is more complicated *in vivo*, where the bundles are dynamically constructed by microtubule associated nucleation, bundling factors and molecular motors (see also Fig. 1.18). Growing microtubules are shown in green, shrinking microtubules in red.

Microtubules are usually nucleated by γ-tubulin complexes (γ-TuCs) that stay attached to their minus end (see also Sec. 1.2.4.3). The minus ends are therefore stable and do not exhibit dynamic instability. In contrast, the plus ends are dynamic and grow from the nucleation site towards the nearest cell pole with an average velocity of $2 - 3\mu m/min$ (Tran et al., 2001). Microtubules that touch the cortex in the central part of the cell are deflected and continue elongating parallel to the long cell axis until they reach the cell poles (Brunner and Nurse, 2000). While they contact the poles, microtubules

grow with a reduced velocity of $\sim 1.3 \mu m/min$ (Tran et al., 2001; Loïodice et al., 2005) and often bend, but usually do not curl around the poles (Behrens and Nurse, 2002). After touching the poles for about 66 seconds on average (see Sec. 3.7), microtubules undergo catastrophe and shrink back to the cell center with a rate of $9 \mu m/min$ (Tran et al., 2001; Busch and Brunner, 2004) (see also appendix A for a discussion of measured dynamic parameters). In most cases, the midzone of the bundle, where microtubules overlap in an antiparallel way, does not depolymerize but microtubules almost immediately regrow after shrinking back to this region. In fluorescence microscopy it is difficult to follow the dynamics of single microtubules within the bundles since short microtubules are hidden within the signal of the long ones. It is therefore not clear how single microtubules behave within the bundle, but it is thought that their dynamics is mostly uncorrelated. Data from electron tomography indicates that each bundle contains between two and seven microtubules, and that the bundle associated with the SPB consists of a higher number of microtubules than the remaining ones (Höög et al., 2007).

*Dynamic Construction of Microtubule Bundles*
Several recent studies have shown that the construction of bundles from single microtubules is a highly dynamic process that results from the interplay of microtubule nucleation, antiparallel bundling and motor activity. It was long assumed that in interphase, microtubules are nucleated almost exclusively from interphase microtubule organizing centers (iMTOCs) on the surface of the nucleus (Fig. 1.17B), until it was found that nucleation along existing microtubules is essential for efficient bundle formation (Janson et al., 2005) (Fig. 1.18). This type of nucleation requires the protein Mto2 whose deletion causes severe defects in microtubule bundling.

To ensure that a newly nucleated microtubule aligns to the mother filament in an antiparallel fashion, the bundling factor Ase1 crosslinks only antiparallel microtubules (Loïodice et al., 2005; Yamashita et al., 2005). It was hypothesized that the position of the plus end of a newborn microtubule fluctuates due to Brownian motion as long as the microtubule is still short. While the minus end stays attached to the mother filament, the new microtubule could then only be fixated by Ase1 when it happens to be antiparallel (see Fig. 1.18). New microtubules can be nucleated along the whole length of pre-existing ones. To collect the microtubule minus ends at the bundle midzone close to the nucleus, new microtubules are transported towards the midzone by the minus end directed kinesin Klp2 (Carazo-Salas et al., 2005). This motor is a tip tracking protein (see also Sec. 1.2.4.5) that specifically binds to the plus ends of growing microtubules (Janson et al., 2007). Since Ase1 accumulates all along the length of antiparallel bundled microtubules, Klp2 has to work against an increasing bundling force as the new filament is growing. When it has reached a certain length, the force generated by Klp2 is not sufficient anymore to reel it in any further. Sliding and bundling forces are therefore regulated such that only short, newly nucleated, microtubules can be transported. Furthermore new microtubules stop sliding as soon as the motor reaches the minus end of the mother filament at the bundle midzone. The minus ends then remain stable at the midzone without being pushed out by parallel sliding forces. This suggests that Klp2, like Ase1, is unable to bind and slide parallel microtubules (Janson et al., 2007). For the simulation of interphase fission yeast cells we implemented a simplified model of the bundle structure as shown in Fig. 1.17. However, it turned out that the dynamic construction of microtubule bundles was important to reproduce certain characteristics of living cells (see Sec. 5.3).

Microtubule Bundles Organize the Interphase Cytoplasm
By pushing at the cell cortex microtubule bundles in interphase position the nucleus at the cell center (Tran et al., 2001; Daga et al., 2006) (see also Sec. 1.3.3). Apart from that microtubules are also involved in the spatial distribution of mitochondria throughout the cell (Yaffe et al., 1996). Mutants of
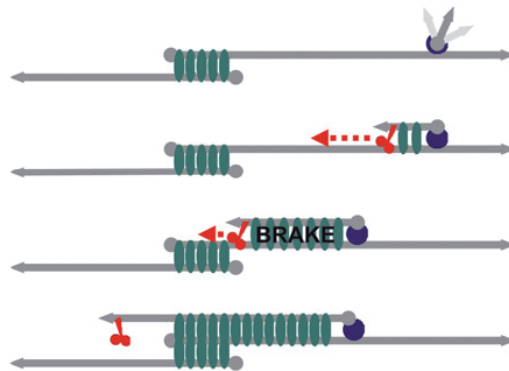
Figure 1.18: Model of microtubule bundling in fission yeast. Microtubule plus ends are indicated by arrow heads, minus ends by spheres. Microtubule nucleation along interphase bundles occurs from microtubule-bound nucleation complexes containing a γ-TuC and Mto2 (purple). After nucleation, microtubules are stabilized in an antiparallel configuration by polarity-specific Ase1 (green). The minus end directed kinesin-14 Klp2 (red) subsequently transports microtubules to the bundle midzone. As the new microtubule grows, additional Ase1 binds, increasing the friction against a length-independent number of motors at microtubule plus ends. Consequently, the speed of transport decreases and finally becomes zero when motors lose contact with antiparallel microtubules (Janson et al., 2007).

α2-tubulin and β-tubulin displayed an asymmetric aggregation of mitochondria depending on the progression of the cell cycle. The association of mitochondria with microtubule bundles was furthermore illustrated by electron tomography (see Fig. 1.13, mitochondria are shown in light blue).

1.3.2.3   The Tip-tracking Proteins Mal3 and Tip1

As in other organisms, microtubule dynamics in *S. pombe* is regulated by a number of MAPs like the EB1 homolog Mal3, the Clip-170 homolog Tip1, the motor protein Tea2 and two members from the XMap215 family, Alp14 and Dis1. The two tip tracking proteins Mal3 and Tip1 are well characterized experimentally and were therefore chosen to be analyzed further with the help of computer simulations in this study. While Mal3 globally prevents microtubule catastrophes, Tip1 is thought to be involved in the spatial organization of microtubules in interphase.

The EB1 Homolog Mal3
Mal3 was identified in a screen for mutants that have defects in chromosome segregation (Beinhauer et al., 1997). Deletion of Mal3 resulted in abnormally short cytoplasmic microtubules as seen by indirect anti tubulin immunofluorescence. As a consequence *mal3Δ* cells often exhibit abnormal morphologies like bent and T-shaped cells while cell growth itself does not seem to be impaired (see also Sec. 1.3.3). Since the microtubules are too short to push at the cell poles, the nucleus and the septum are often misplaced resulting in unequally sized daughter cells after fission. Furthermore cells lacking Mal3 show hypersensitivity to the microtubule depolymerizing drug TBZ and are cold sensitive. Overexpression of Mal3p leads to the formation of excessively long cells and compromises spindle formation and function. Interestingly human EB1 which shares about 40% percent sequence homology with Mal3 was able to rescue the *mal3Δ* phenotype which suggests that the two homologous proteins have similar functions (Beinhauer et al., 1997; Browning et al., 2003). It was furthermore

shown that the fission yeast Mal3 binds to human APC *in vitro* and that it can substitute for EB1 to promote microtubule polymerization, even though there is no APC homolog in fission yeast (Nakamura et al., 2001).

Contrary to earlier observations Mal3 is not required for the movement of the motor protein Tea2 along microtubules but for its accumulation at microtubule plus ends (Browning et al., 2003; Busch et al., 2004). Tea2 was shown to transport Tip1 to microtubule plus ends (see below), and to accumulate in bigger particles at microtubule tips. Careful imaging in living cells revealed that the absence of Mal3 does not affect the motion of Tea2/Tip1 speckles along microtubules, but it prevents the accumulation of bigger particles at the plus ends. Hence, Mal3 is thought to be required for the docking and immobilization of Tip1/Tea2 particles at microtubule plus ends, but not for the movement of the motor along the microtubule lattice. In the absence of Mal3 neither Tea2 nor Tip1 are found at microtubule plus ends (Busch et al., 2004; Busch and Brunner, 2004).

Analysis of microtubule dynamics in *mal3Δ* cells showed that Mal3 promotes the initiation of microtubule growth from the antiparallel overlap region and reduces the probability of catastrophe about twofold (see Sec. 5.3.1 for a more detailed discussion of the dynamic parameters). Studies with GFP tagged Mal3 revealed that the signal of Mal3-GFP becomes weaker about $80s$ prior to a catastrophe event for microtubules that touch the cortex at the cell poles. This indicates that Mal3 has to be removed from microtubule ends before a catastrophe can occur. Interestingly, the fading of the Mal3 signal was only observed for microtubules touching the cell poles but not for microtubules that touch the cortex in central regions of the cell (Busch and Brunner, 2004). This is different for cells that do not express Tip1. In *tip1Δ* mutants, Mal3 is also removed from microtubules that contact the cortex at the cell center, resulting in premature catastrophes. This suggests that Mal3 is essential for the binding of Tip1 to microtubule plus ends, but that in turn Tip1 is not needed to localize Mal3. Yet, Tip1 is important for the spatial regulation of Mal3 association, and therefore for the localization of catastrophes, because it prevents the removal of Mal3 from microtubule tips specifically at the cell center but not at the poles.

Recent findings using electron microscopy (Sandblad et al., 2006) suggest that Mal3 acts by stabilizing the sheet-like structures at microtubule plus ends, since it was found to associate specifically with the seam of thirteen protofilament microtubules (see section 1.2.4.5 for details and for a general discussion of the EB1 protein family).

The Clip-170 Homolog Tip1
In interphase cells Tip1 is localized in particles at the tips of growing microtubules and along the microtubule lattice (Brunner and Nurse, 2000). It furthermore associates with both cell poles in a Tea1 dependent manner (see below) and is found at the tips of astral microtubules in mitosis. Deletion of *tip1* results in cells with abnormal morphologies, including bent and branched cells, whose frequency is increased if the cells recover from starvation (Fig. 1.19). Furthermore, the polarity marker Tea1 is not anymore located at the cell poles. The observed phenotypes are believed to be caused by the changes of the microtubule cytoskeleton: in *tip1Δ* cells microtubule bundles are about $30 - 60\%$ shorter than in wild type but still mostly occur at the cell cortex. In contrast, 70% of all microtubule bundles undergo catastrophe in central regions of the cell, whereas more than 90% reach the cell poles in wild type cells. Therefore Tip1 is thought to selectively stabilize microtubules that contact the cortex at the cell center, but to allow the occurrence of catastrophe at the poles where it is removed from microtubule tips.

Binding of Tip1 to microtubules depends on the plus end directed kinesin Tea2 which transports Tip1 towards microtubule tips (Busch et al., 2004). Reaching the plus end, the presence of Mal3 is required for accumulation and tip tracking of Tip1 (see previous paragraph). The association of Tip1

with microtubules (via Tea2) is mediated by its N-terminal domain which is also sufficient to restore the wild type microtubule length and catastrophe location when it is expressed in *tip1Δ* cells (Brunner and Nurse, 2000). However, the C terminus seems to be required for the binding to the polarity marker Tea1, which is absent from the poles in *tip1Δ* cells and in cells expressing only the N-terminal domain of Tip1. In turn, Tip1 failed to accumulate at the poles in cells that were deleted of Tea1 and in cells that only express the N-terminal fragment of Tip1, even when microtubule length and dynamics were almost normal (see also the discussion of the Clip-170 protein family in section 1.2.4.5).

The morphological defects in *tip1Δ* cells are therefore thought to be caused by the aberrant localization of the polarity marker Tea1, which is discussed in section 1.3.3. Interestingly, the Tip1 homolog Bik1 in *S. cerevisiae* does not require the Mal3 homolog Bim1 to stay at microtubule plus ends (Akhmanova and Hoogenraad, 2005). Furthermore, Bik1 is also found at the ends of shrinking microtubules, while Tip1 only accumulates at growing plus ends.

Summary: The Concerted Action of Mal3, Tip1 and Tea2
According to our present knowledge, Mal3 binds to microtubule plus ends independently of Tea2 and Tip1 where it protects microtubules from catastrophes and promotes microtubule growth. Tip1 speckles are transported by Tea2 along the microtubule lattice without the help of Mal3. When such speckles reach the plus ends they are immobilized by Mal3 and thus stay bound to the microtubule tip. Without Mal3, Tip1/Tea2 speckles can still be transported along microtubules, but they cannot form particles at microtubule plus ends. Although Mal3 binds to microtubule plus ends independently of Tip1, the Clip-170 homolog is required to prevent premature removal of Mal3 from microtubules that touch the cortex in central regions of the cell. Reaching the poles, Mal3 is removed on average $80s$ before catastrophe occurs. If Tip1 is removed prior to Mal3 at the poles is unknown, because of the strong Tip1 signal which accumulates at cell ends. The polarity factor Tea1 is required to retain Tip1 at cell poles and might be involved its removal from microtubule plus ends (see following section).

1.3.3   Polarization and Morphogenesis in *S. pombe*

Due to its simple symmetric cell shape, *S. pombe* is ideally suited to study polarization and morphogenesis. Morphological mutants can be easily identified by visual screening (Snell and Nurse, 1994; Verde et al., 1995) and include spherical cells (orb mutants), bent cells (banana mutants), cells that form a branch or become T-shaped and many more (Fig. 1.19). Under normal conditions, fission yeast maintains its shape by elongating in a polarized fashion at the cell tips and by dividing through medial fission. The cytoskeleton is involved in the localization of both processes.

Positioning the Nucleus - Setting the Cell Division Site
The position of the septum depends on the position of the nucleus at the onset of mitosis (Daga and Chang, 2005). To obtain two equally sized daughter cells it is crucial that the nucleus is located at the center of the cell. This is achieved by microtubule bundles that are attached to the nucleus in interphase and push against the cell poles when they grow. The resulting forces, produced equally at both poles, keep the nucleus centered (Tran et al., 2001), and thus ensure that fission yeast fissions in the middle. When the microtubules push at the nucleus the nuclear membrane usually exhibits strong deformations (Tran et al., 2001; Daga et al., 2006), which are no longer visible if a microtubule depolymerizing drug like MBC is added. To demonstrate the ability of microtubules to center the nucleus, bundles were depolymerized by addition of MBC and the nucleus was moved into a cell pole by centrifugation. After washout of the drug new microtubules polymerized and recentered the nucleus in less than 30 minutes (Daga et al., 2006). Consequently, mutants with defects in microtubule

organization are often unable to center the nucleus, like for example cells that carry a deletion of Mto1, Mto2 or Ase1 (Sawin et al., 2004; Janson et al., 2005; Loïodice et al., 2005).

Positioning the Growth Sites - Control of Cell Polarity

The second crucial element of morphogenesis in *S. pombe* is cell growth at the poles. Both cytoskeletal networks, actin and microtubules, are involved in the positioning and in the maintenance of the growth sites. As described in section 1.3.2.1, the distribution of actin patches coincides with the sites of active growth. Furthermore, actin cables are thought to be involved in polarized growth by transporting secretory vesicles to the cell ends that can deliver membrane and components required for cell wall synthesis (Win et al., 2001). In agreement with this, mutants in the motor protein Myo52/Myo4 that is responsible for the transport of vesicles along actin cables obtain a round morphology. If the actin cables are disrupted by deleting the actin nucleator For3, cells can to some degree maintain polarized growth but often exhibit different shapes, including bent and bottle-shaped or lemon-shaped cells (Feierbach and Chang, 2001). Thus, although actin cables are not absolutely essential for polarized growth, they may function to localize polarity factors to the cell ends.
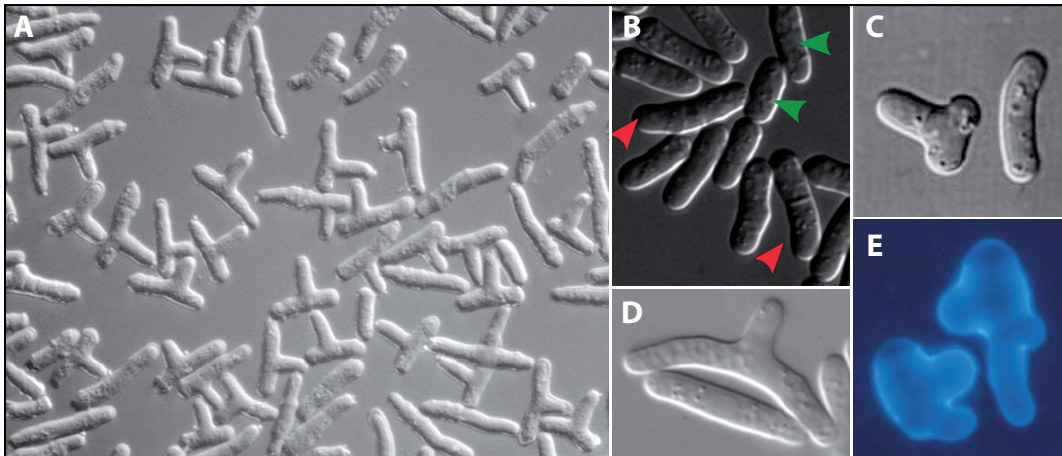

Figure 1.19: Fission yeast cells with abnormal morphologies. (A) Formation of branched cells in Cdc10-129 mutants by treatment with TBZ (Sawin and Nurse, 1998). (B) *mto2Δ* cells exhibit bent (red arrows) and wild type looking cells (green arrows) (Janson et al., 2005). (C) The deletion of *tea1* results in bent and branched cells (Behrens and Nurse, 2002). (D) Cells deleted of *tea2* (Browning et al., 2000). (E) *tip1Δ* cells 2*h* after recovery from nutritional starvation (Brunner and Nurse, 2000).

In contrast, microtubules were shown to be crucial for the determination of growth sites. Cells with abnormal microtubules and associated proteins often form bent, branched or T-shaped cells, or are unable to undergo NETO and grow at one end only (Fig. 1.19). Important insights into the underlying mechanisms came from the study of mutant cells with defects in microtubule organization and from the use of microtubule depolymerizing drugs like TBZ and MBC. Cells that were blocked in G$_1$ before the occurrence of NETO were treated with TBZ to depolymerize their microtubules. When they were released from the cell cycle block these cells often started to branch, which demonstrated that microtubules are important for the establishment of new growth sites (Sawin and Nurse, 1998). More recently it was shown that once a cell polarity axis is established, microtubules have at best a minor role in maintaining the direction of cell growth (Sawin and Snaith, 2004). Experiments with different depolymerizing drugs revealed that fission yeast cells possess a memory of the positions of growth sites that is mediated by actin. This memory allows the cell to continue growing at or near the previously established sites even in the absence of microtubules. It was found that TBZ not only

depolymerizes microtubules but also disrupts the actin cytoskeleton which explains the occurrence of branched cells in the previous experiment. The use of TBZ lead to the deletion of the actin memory and thus facilitated the establishment of new growth sites. In contrast MBC has no effect on actin, and repetition of the same experiment with MBC resulted in a much lower number of branched cells.

Tea1 Links Microtubules To Cell Polarity

But how do microtubules redirect the sites of growth? An important link between microtubules and the cell polarity machinery was identified in the protein Tea1 (for *t*ip *e*longation *a*berrant) (Snell and Nurse, 1994). Tea1 is a microtubule tip tracking protein, that localizes in dots at the ends of growing microtubules and at both cell poles (Mata and Nurse, 1997). Cells lacking Tea1 grow bent or form a new branch and become T-shaped. In wild type cells, Tea1 localizes to both poles even before NETO, regardless of whether the end is growing or not, which indicates that it plays a role as a general polarity marker that dictates the location of growth sites independent of actin patches and cables. It is important to note that Tea1 is not required for the establishment of growth zones, but it is required to place the growth zone in the correct place (Mata and Nurse, 1997). In cells where cell polarity is disrupted and actin is depolarized, the selection of a new growth site by microtubules requires Tea1, which suggests that Tea1 is crucial for coupling microtubule distribution to the regulation of cell polarity (Sawin and Snaith, 2004). This mechanism was demonstrated for example in Mto2 deleted cells where Tea1 is not symmetrically distributed but has a bias towards the upper or lower side at both poles (Janson et al., 2005). Consequently such cells grow bent as indicated in Fig. 1.20.
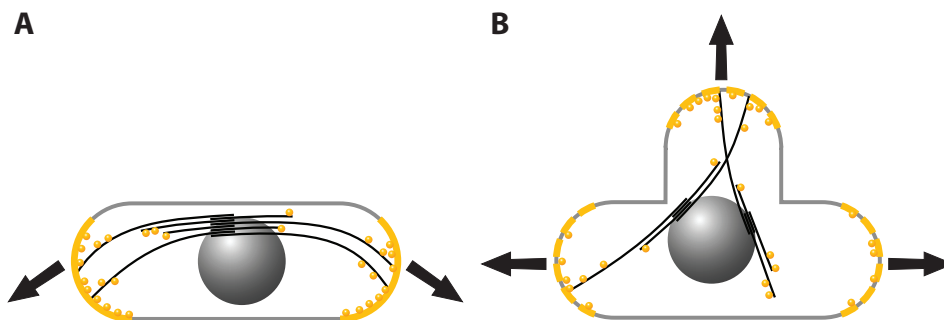
Figure 1.20: Positioning of growth sites by microtubules and Tea1. Tea1 travels on growing microtubule tips and is released and anchored at the plasma membrane where microtubules stop elongating (yellow dots and yellow regions at the cortex). Together with Tea1, other polarity factors like Bud6 and For3 are transported on microtubules or associate with Tea1 at the cortex. (A) If microtubule bundles are not symmetrically distributed, the accumulation of Tea1 is biased towards one side, resulting in cells that grow bent. This happens for example in Mto2 deleted cells that possess only one strong microtubule bundle (Janson et al., 2005). (B) If microtubules are short, for example in *tip1Δ* cells or after treatment with TBZ (Brunner and Nurse, 2000), polarity markers are delivered to central parts of the cortex and the cell starts branching.

Tea1 is required to retain other morphogenetic factors like Tip1 and Tea2 at the cell ends (Behrens and Nurse, 2002; Browning et al., 2003). In turn the tip tracking property of Tea1 does not seem to depend on these proteins. In cells deleted of Tip1 or Tea2, Tea1 still localizes to microtubule plus ends but it fails to accumulate efficiently at the cell poles. This is most likely caused by the fact that in these mutants only few microtubules extend throughout the cell to reach the poles (see also Sec. 1.3.2.3). The mechanism of how Tea1 associates with the cell ends is not precisely known. However, the localization of Tea1 is strongly reduced in the absence of the plasma membrane associated protein

Mod5, which in turn accumulates at cell poles in dependency of Tea1 (Snaith and Sawin, 2003). Furthermore, the protein Tea3 is required to anchor Tea1 especially at non-growing cell ends (Snaith et al., 2005) These results suggest that independent protein-protein interactions among Tea1, Tea3 and Mod5 collectively contribute to Tea1 anchoring at the cell poles. At the cell poles, Tea1 forms a large protein complex containing the actin-binding protein Bud6 and the formin For3 (Glynn et al., 2001; Feierbach and Chang, 2001), whose localization depends on Tea1. Tea1 might therefore guide the delivery of the actin related growth machinery to the cell poles by positioning of For3 and other polarity factors.

A Model for the Establishment of Cell Polarity -
The Importance of Microtubule Dynamics at the Poles
Based on these findings one might propose the following model for the regulation of cell polarity and the positioning of growth sites by Tea1 and microtubules : Tea1 is transported on microtubule plus ends to the poles where it is anchored at the cortex with the help of Mod5 and Tea3. At the poles it recruits other proteins like Bud6 and For3 in order to promote the formation of actin cables and patches. Myosin motors then transport vesicles containing parts of the growth machinery and cell wall components to the poles. Tea1 might furthermore be involved in the regulation of microtubule dynamics for example by removing Tip1 from microtubule tips, or by recruiting other factors that regulate microtubule dynamics to the poles. This might create a feedback on the organization of microtubule bundles which ensures that Tea1 is constantly delivered to the poles in interphase (see also Fig. 5.12).

Summarizing, microtubules play an important role in the proper positioning of the nucleus and the growth sites. For both processes it is essential that microtubules reach the cell poles but do not grow further and start curling. Microtubule dynamics must therefore be regulated at the cell poles. As described in the previous paragraph, the system might be self-sustaining once it is properly set up, but the question remains how it gets started and how it is re-established after perturbations. In wild type cells, the low polymerization rate at the poles and the long microtubule contact times seem to be perfectly adapted to deliver marker proteins like Tea1, and to exert the right amount of pushing forces. However, since cells elongate during G_2, the organization of microtubules needs to be constantly adjusted to maintain these features. To study cell polarity control, it is therefore crucial to understand how microtubule dynamic instability is regulated at the cell poles. In this work we used a combined approach of computer simulations and experiments to address these questions.

1.4 Computer Simulations and Experiments - A Combined Approach to Investigate Microtubule Dynamics

While there is increasing knowledge about how microtubules orient and target the cell poles in *S. pombe* (Brunner and Nurse, 2000; Busch et al., 2004; Busch and Brunner, 2004), little is known about how the behavior of the plus ends is controlled at the poles. It is speculated that microtubule length might be regulated by global mechanisms like for example a limiting amount of free tubulin subunits, or locally by catastrophe-inducing factors whose activity is restricted to the cell poles (Hayles and Nurse, 2001). Another hypothesis is that forces generated at the cell cortex could be involved not only in centering the nucleus (Dogterom et al., 2005; Faivre-Moskalenko and Dogterom, 2002), but also in the regulation of microtubule dynamics (Janson et al., 2003; Dogterom and Yurke, 1997). These models are not easy to discriminate experimentally because microtubule associated proteins are often involved in multiple aspects of microtubule organization. Sometimes, backup systems exist and other

proteins fill in functions of MAPs and +TIPs in cells that were genetically modified. Another problem is that to date forces cannot be selectively switched off by genetic manipulation. Consequently, the influence of force on microtubule dynamics cannot be ruled out which makes it difficult to clearly identify the important regulatory mechanisms.

We therefore chose an approach which combined computer simulations and experiments to investigate how microtubule dynamics might be regulated in fission yeast. The simulation includes microtubules and the nucleus which are confined inside the geometry of the *S. pombe* cortex. Their motion is calculated using constrained Langevin dynamics as described in section 2.2.1. The advantage of this approach is that different models can be tested easily. Distinct dynamic properties of microtubules can be switched on and off *ad libitum*, and one needs to change only a single number to make the cell twice as long (wild type pombe at $25°C$ needs about three hours to do this). This allowed us to determine the minimal set of requirements and assumptions that is able to generate the organization of microtubules observed *in vivo*. To compare the simulation with reality we chose nine characteristics of wild type fission yeast cells that were partly described in the literature or measured by ourselves. Quantitative experimental data for each of these traits was needed to allow a decision about how well the simulation reproduced the corresponding feature. On this basis we could accept or discard simulations and thus gain some insights in how microtubule dynamics might be regulated *in vivo*.

Using the simulation, we found that forces generated at the cell poles due to the cylindrical shape of *S.pombe* were sufficient to reproduce the nine *in vivo* traits without having to impose different dynamic properties for microtubules touching the poles (Chap. 5). To investigate if cell shape is also relevant *in vivo* we analyzed microtubule organization in cells carrying a temperature sensitive mutation of *pmo25*, a gene involved in the maintenance of polarized cell growth. Our results demonstrated that microtubule organization in living fission yeast cells indeed depends cell shape which indicates that forces might be important for the regulation of microtubule dynamics *in vivo* as well. We then went on to simulate microtubule dynamics in mutant cells that were deleted of Mal3 and Tip1. This allowed a thorough test of our model but also provided some insight in how these proteins might function in living fission yeast cells.
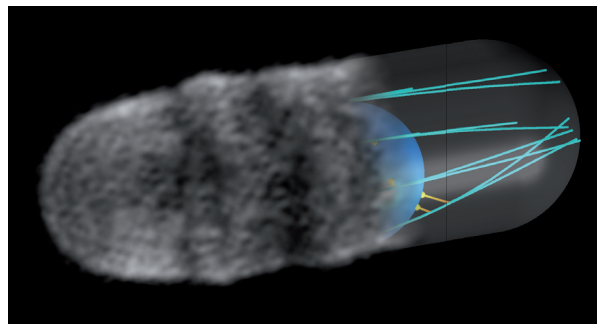
Figure 1.21: A new modeling organism: the chimera '*Schizosaccharomyces electronicus*'.

Chapter 2

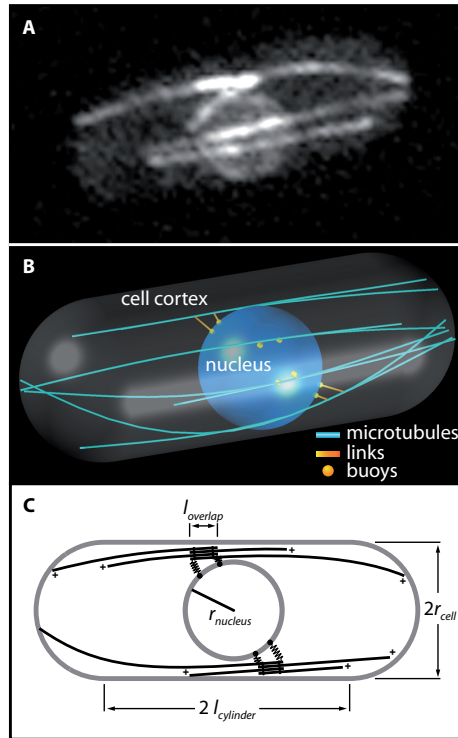# Simulating Microtubule Dynamics in *Schizosaccharomyces pombe*

In fission yeast, microtubule dynamics and spatial organization have been extensively analyzed, which allowed us to build an accurate model of the cell with well-defined parameters. The complete set of parameters and their influence on the simulation are described in detail in appendix A. In this chapter, we give an overview of the setup of the simulation (Sec. 2.1) and explain how the different components were described mathematically in order to implement them into the computer simulation (Sec. 2.2).

2.1   Setup of the Simulation

In all our simulations, the cell body is modeled as a cylinder closed by half-sphere caps (the cell poles) with a fixed size, confining the microtubules and the nucleus within a frictionless boundary (Fig. 2.1B). We simplified the interplay of nucleation and motor activity that organizes microtubules into bundles *in vivo* (see Sec. 1.3.2.2), and focused on the mechanical interactions of microtubules with the nucleus and the cortex. In the simulation microtubules are organized in four bundles containing four microtubules each. These are connected in an anti-parallel manner at the static minus ends, creating a fixed overlap-zone. Microtubule plus ends grow and shrink independently of each other. Shrinking microtubule plus ends re-grow immediately when they reach the overlap region but do not rescue (switch back to polymerization) in the cytoplasm, as rescue events have not been described *in vivo* Tran et al. (2001).

The overlap zones are attached tangentially to a non-deformable sphere representing the nucleus (Fig. 2.2). Yet, to mimic the deformations of the nuclear membrane seen *in vivo* (Tran et al., 2001; Daga et al., 2006), the attachments are mediated by soft springs. Furthermore, each bundle is anchored on two buoys that are able to move on the surface of the nucleus, which is a viscous 2D-fluid (Fig. 2.1C). The mobility of these buoys allows independent movement and rotation of microtubule bundles, which is critical to fulfill an important characteristic of living cells: bundles elongating at an angle to the cell axis are deflected by the cortex such that they can reach the cell poles. The ability of microtubule bundles to align with the cell axis was considered an important trait that simulations had to fulfill in order to reproduce the behavior of interphase cells (see T1, Sec. 3.1). In our simulations this trait was always fulfilled, except when the surface-viscosity of the nucleus was unreasonably high (see discussion of parameters, appendix A.5). Finally, our model includes a hydrodynamic effect, which results from the geometry of *S. pombe*: When the nucleus moves, it behaves like a piston, and the cytoplasm is forced to pass between the nucleus and the cortex. Lubrication theory predicts that

Figure 2.1: Setup of the simulation. (A) A Strain expressing GFP-tubulin and the nuclear pore marker Nup85-GFP. (B) The simulation calculates the motion of a spherical nucleus with attached microtubule bundles, confined in a fixed 3D-shape. Although in the simulation the nucleus is nondeformable, microtubule bundles are attached via elastic links to imitate the deformations observed *in vivo*. The nucleus has a fluid membrane to allow the attachment sites to move and diffuse on the viscous 2D surface. (C) The cell is modeled as a cylinder of half-length $l_{cylinder}$ ($3.5\mu m$) and of radius r_{cell} ($2\mu m$), closed by half-spheres. Microtubule bundles consist of 4 single microtubules, 2 pointing in each direction. They are linked near their minus ends to form a tight static anti-parallel overlap region of size $l_{overlap}$ ($1.0\mu m$). Bundles are attached to the nucleus of radius $r_{nucleus}$ ($1.5\mu m$) by springs between microtubule minus ends and nuclear "buoys".

this effect reduces the mobility of the nucleus by a factor ~ 25 compared to the motion in an infinite fluid described by Stokes's law (see Sec. 2.2.4.1).

2.2   Simulation Methods

To simulate microtubule dynamics in *S. pombe* we consider microtubules, the nucleus and their confinement inside the cell. Microtubules in the simulation do not sterically interact with each other, but are excluded from the nucleus and confined by the cell cortex. The cortex is represented as a potential which also confines the nucleus inside the cell. The dynamics of the objects are simulated by solving the equations of motion, which are set according to the laws of classical mechanics. Considering the physical scale of the problem (see 2.2.8 and 2.2.9), inertia may be neglected, but Brownian motion makes an important contribution. Accordingly, over-damped Langevin equations are used for the nucleus and microtubules to account for the multitude of thermal collisions as well as the larger scale non-stochastic interactions. The simulation automatically sets and solves these equations of motion in consecutive time steps.

The flow of the cytoplasm inside the cell is laminar (i.e. the Reynolds number is low, see 2.2.8) and viscous forces are proportional to speed. Since inertia can furthermore be neglected (Sec. 2.2.9), the motion of objects inside the cytoplasm is governed by their mobility which is the proportionality factor between force and speed (speed = mobility × force). The mobility can be calculated from the size and shape of the object and from the viscosity of the fluid as exemplified by Stokes's law, which describes the mobility of a sphere in an infinite fluid. For microtubules, we used a variant of Stokes's law describing the mobility of elongated rods. The nucleus however, occupies almost the whole diameter of the cell and when it moves, the counter-flow between the nucleus and the plasma membrane creates shearing forces which are stronger than in an infinite liquid. To account for this

effect, we implemented a formula derived from lubrication theory Bungay and Brenner (1973) (see Sec. 2.2.4.1).

Microtubules in the simulation are organized in bundles whose structure is described in detail in section 2.2.6.1. These bundles are attached tangentially to the nucleus at two points which are able to move on the nuclear surface. The mobility of the attachment sites is essential to allow microtubule bundles to orient, as observed in living cells (see Fig. 3.2). The nucleus itself is described by a rigid sphere. Yet, to mimic the deformations of the nuclear membrane observed *in vivo*, the connections between microtubule bundles and the nucleus are modeled as soft springs (see Fig. 2.2). Microtubules within a bundle grow and shrink independently and bend according to their elastic modulus which is defined by *in vitro* measurements (see appendix A.9).

Microtubules are described by continuous bending elasticity equations, which are discretized in space along the length of the fiber, and the nucleus is described by the position of its center. Thus, all objects in the simulation are represented by a set of discrete points for which we write equations of motion. These equations will be given first. In particular, we will indicate how certain properties of the objects, for example the incompressibility of the fibers, are mathematically implemented using algebraic constraints. We then discretize the equations in time, and use a semi-implicit method to integrate them. After introducing the mechanical objects themselves, we will list their interactions. Last, we will describe how the dynamic instability of microtubule plus ends is modeled by discrete stochastic transitions, and how the catastrophe rate is affected by tubulin concentration, the position of microtubule plus ends, or force.

2.2.1 Constrained Langevin Dynamics

The microtubules and nucleus are described by points, which are constrained in their motions relative to each other. The constraints are specific to the nature of each object, and are used as an alternative to methods in which springs of high stiffness impose the shape of objects. The nucleus for example is a nondeformable sphere of radius $r_{nucleus}$. Therefore, we use one point n_0 to designate the center, and several additional points $n_{i>0}$ on its surface, which must satisfy $||n_i - n_0|| = r_{nucleus}$. The nucleus is free to move as a whole (n_0 is free), but the points $n_{i>0}$ must stay on the surface of the sphere. Thus, to calculate the speed of a point n_i, the forces acting on it are projected on the directions allowed by the constraint $||n_i - n_0|| = r_{nucleus}$; *i.e.* forces on n_i are projected tangentially to the sphere.

In the simulation, the coordinates of all N points in the system are pooled in a vector $\mathbf{x}$, which is of size DN, for a simulation running in D dimensions (we used $D = 3$ for *S. pombe*). All the constraints are globally expressed as was described for the nucleus using a projection $P(\mathbf{x})$ of size $(DN)^2$. Using this formalism, the equation of motion is:

$$\frac{d\mathbf{x}}{dt} = \mu P(\mathbf{x}) \left[F(\mathbf{x}, t) + B(t) \right] \tag{2.1}$$

The vector $F(\mathbf{x}, t)$ of size DN contains the forces acting on the points at time t. $B(t)$ of size DN summarizes the random collisions leading to Brownian agitation, in the Langevin formalism (it is a non-differentiable function of time). As discussed, the transformation implemented by P maintains the radius of the nucleus, and length of the fibers. $F(\mathbf{x}, t)$ on the other hand, includes softer interactions, such as the elastic restoring forces of bent microtubules, the links between nucleus and microtubules and the confinement. The number of points in the system (and the number of equations to solve) vary as microtubules grow and shrink. However, this happens on a slow time scale compared to the motion of the objects, and thus does not impose any difficulty.

2.2.2   Numerical Integration

From an initial configuration at time $t = 0$ the future of the system is calculated by advancing small discrete time steps h. The numerical integration of the differential equation is done by finite differences with a first-order implicit scheme, which proved to be numerically stable. This allowed us to use $h = 10\,ms$, and to simulate *S. pombe* in real time on current processors (e.g. 2.2GHz Opteron).

As described later, many of the interactions are modeled by harmonic potentials, and therefore already linear. The others are linearized to allow the implicit integration. Consequently, the forces are expressed as $F(\mathbf{x}, t) = A(t)\,\mathbf{x} + D(t)$, where matrix $A(t)$ and vector $D(t)$ are sums over all the interactions present at time t. The stiffness-matrix $A(t)$ is square and symmetric. To solve the time step $[t, t+h]$, P and A are used at time t, while $\mathbf{x}$ is used implicitly at $t + h$. The following system of linear equations is thus derived from equation (2.1):

$$\frac{\mathbf{x}_{t+h} - \mathbf{x}_t}{h} \;=\; \mu P_t\left[A_t\,\mathbf{x}_{t+h} + D_t + B_t\right] \tag{2.2}$$

$$\left[I - h\mu P_t A_t\right](\mathbf{x}_{t+h} - \mathbf{x}_t) \;=\; h\mu P_t\left[A_t\,\mathbf{x}_t + D_t + B_t\right], \tag{2.3}$$

where we noted $A_t = A(t)$, $D_t = D(t)$, $P_t = P(x_t)$ to indicate that these variables are taken now at time $t = nh$, with n the iteration counter of the simulation. The "simulated Brownian force" $B_t = h^{-1}\int_t^{t+h} B(u)du$ is a vector of normally distributed random number. In the simulation, the components of B_t are generated for each time step from independent normally distributed numbers of mean zero and variance one $\theta_{t,i} \sim N(0,1)$, using $B_t = \{\beta_i\,\theta_{t,i}\}$. The factors β_i (which scale like $h^{-1/2}$) are most easily obtained by calibrating the diffusive motion[1] for the objects (see below). Equation (2.3) is solved to yield $\mathbf{x}_{t+h}$ using a sparse storage form of A_t (Press et al., 2002) and the bi-conjugate gradient stabilized iterative solver. The convergence criteria of the iterative solver is set to $\psi\,min(\beta_i)$ with $\psi = 0.1$ in this study. Thus the approximated solution of (2.3) is always close to the real one, compared to Brownian motion. To check the method and its convergence, the tolerance parameter ψ and the time-step h were systematically varied, leading to an appropriate choice for the values used (see appendix A.11).

An additional correction was necessary to implement the constraints, as the equations used are only exact to first order. For example, in the case of the nucleus, the points $n_{i>0}$ are allowed to move on the tangent plane to the sphere, which effectively moves them away from the surface. The points obtained by solving (2.3) are thus projected back on the sphere. The constraints of microtubules are similarly re-imposed at every time step, also in a straightforward operation, which accounts for a negligible fraction of the motion (Nédélec, 2002). In the following chapter, we explain how microtubules and the nucleus are modeled and discretized in space. The interactions between objects (which contribute to A_t and D_t) will be described afterwards.

2.2.3   Microtubules

Microtubules are modeled as previously described in Nédélec (2002): infinitely thin linear objects behaving like elastic, non extensible rods. Each fiber is represented by $p + 1$ equidistant points m_i, for $i \in [0, p]$, separated by a distance L/p. m_0 is the minus-end, and m_p the plus-end. The number of segments p is automatically adjusted as a function of the total length of the microtubule L. Points

---

[1]It should be noted however, that the resulting Brownian forces, B_t, do not correspond to real physical forces actually occurring in the system. The B_t are calibrated to generate Brownian displacements, $\Delta x^{1/2}$, according to the time step h. Consequently, the factors B_t scale with the time step like $h^{-1/2}$

are added or removed, in order to minimize the difference $|\rho - L/p|$, where the parameter ρ sets the desired segment length. This procedure is necessary to allow fibers of arbitrary length. We used $\rho = 0.5\mu m$ in this study, after checking that similar results were obtained for finer values of ρ (see appendix A.11).

2.2.3.1 Bending Elasticity

Microtubules in the simulation can bend under external forces and Brownian motion and resist elastically. The internal force generated under bending is linearized for any set of three consecutive points m_k, $k \in \{i-1;\ i;\ i+1\}$ by applying an effective torque $\{-F;\ 2F;\ -F\}$ to each point respectively. We use $F = \kappa_{mt}(n/L)^3(m_{i-1} - 2m_i + m_{i+1})$ as obtained by linearization around a straight configuration. κ_{mt} is the bending modulus of microtubules. The linearization is appropriate, because ρ is such that within the volume of *S. pombe*, the angles between consecutive microtubule segments remain small at any time.

2.2.3.2 Interpolation of Intermediate Points

Any intermediate point s on the fiber is interpolated from the model-points as $s = \alpha m_k + (1-\alpha)m_{k+1}$. The index k is chosen such that m_k and m_{k+1} are surrounding s on both sides. The interpolation factor $\alpha \in [0, 1]$ is calculated from the relative positions of the three points: $\alpha = \|s - m_{k+1}\| / \|m_k - m_{k+1}\|$. This gives $\alpha = 1$ if $s = m_k$ and $\alpha = 0$ if $s = m_{k+1}$ as expected. If a force f is to be applied in s, it is distributed to m_k and m_{k+1} as $f_k = \alpha f$ and $f_{k+1} = (1-\alpha)f$. This procedure preserves any linearity in the relationships between force and coordinates.

2.2.3.3 First order Constrained Dynamics

In this chapter, we calculate the projection P as derived from the constraints, for a linear incompressible fiber. We also prove that the constrained forces can be expressed linearly from the unconstrained forces, thus justifying equation (2.1). Considering a microtubule, each of the $p+1$ points m_k is subject to an *external* force f_k, which together make a force-vector $\mathbf{f}$, of dimension $3(p+1)$. The motion of the points is additionally determined by an *internal constraint* force-vector $\hat{\mathbf{f}}$, which arises from the fiber being incompressible and inextensible. The incompressibility of the fiber imposes the points to be equidistant. This is represented mathematically by a set of algebraic constraints $C_k = (m_{k+1} - m_k)^2 - (L/p)^2 = 0$ for $k \in [0, p[$. Given the coordinates x_j, $j \in [3l, 3l+1, 3l+2]$ of the fiber-point m_l, we define the $p \times 3(p+1)$ Jacobian matrix as $J_{ij} = \partial C_i / \partial x_j$. In our case:

$$J = 2 \begin{pmatrix} x_0 - x_3 & x_1 - x_4 & x_2 - x_5 & x_3 - x_0 & x_4 - x_1 & x_5 - x_2 & 0 & 0 & 0 & \cdots \\ 0 & 0 & 0 & x_3 - x_6 & x_4 - x_7 & x_5 - x_8 & x_6 - x_3 & x_7 - x_4 & x_8 - x_5 & \cdots \\ & & & & \vdots & & & & & \ddots \end{pmatrix}$$

A global motion of the points defined by a speed-vector $\mathbf{v}$ is allowed by the constraints if $J\mathbf{v} = 0$. The *internal* forces are always such that the constraints are maintained, and therefore must satisfy $J(\mathbf{f} + \hat{\mathbf{f}}) = 0$ (the mobility is the same for all the points). Furthermore, internal forces should also be *virtual*: their work should be null as not to contribute to global motion or rotation of the object. This should be true for any motion compatible with the constraints: $\hat{\mathbf{f}} \cdot \mathbf{v} = 0$ for any $\mathbf{v}$ such that $J\mathbf{v} = 0$. This implies that we can write $\hat{\mathbf{f}} = J^T \lambda$, where λ is a vector whose components are the Lagrange multipliers associated with the constraints. Hence the relation for the Lagrange multipliers:

$J(\mathbf{f} + J^T \lambda) = 0$, from which we derive $\lambda = -(JJ^T)^{-1}J\mathbf{f}$, and $\hat{\mathbf{f}} = -J^T(JJ^T)^{-1}J\mathbf{f}$, since JJ^T of size $p \times p$ is invertible in our case. The total force on each point can thus be obtained linearly from the external forces: $\mathbf{f} + \hat{\mathbf{f}} = P\mathbf{f}$, where $P = I - J^T(JJ^T)^{-1}J$ is a projector, because $PP = P$, as can be verified simply. J and thus P for each microtubule depends only on the shape of the fiber (i.e. on the coordinates in a translation-independent manner). The equations of motion for each microtubule are thus of the form described in equation (2.1). The same general procedure applies to the nucleus as well, but we will see that the different constraints lead to a simpler formulation.

2.2.3.4 Mobility of Microtubule Points

The mobility of a microtubule of length L in the cytoplasm of viscosity η_{cell} is set as:

$$\mu_{mt} = \frac{\log(L_h/0.025\mu m)}{4\pi\eta_{cell}L}$$

This includes a logarithmic correction, which accounts for the elongated shape of the fiber, which have a diameter of $25nm$. L_h is a hydrodynamic cut-off distance; we used $L_h = 2\mu m$, to roughly match to the diameter of *S. pombe*, which effectively introduce a cut-off. We further assumed that the $p + 1$ points representing the fiber all share the same mobility, which is therefore $\mu_{mt-point} = (p+1)\mu_{mt}$. In an infinite fluid, a straight rod is twofold as easy to move in the longitudinal direction than in a transverse direction. This anisotropy in the mobility could not easily be accounted for in the simulation. This is because microtubules may bend and adopt arbitrary shape and applying the formula obtained for the rigid rod would lead to inconsistent numerical behavior. Correcting for the anisotropy of the mobility requires a full hydrodynamic calculation, which was beyond the scope of this study. Because varying the bulk viscosity η_{cell} over a factor 2 or more showed little effect on the system, we are confident that neglecting these hydrodynamic factors does not invalidate our conclusions.

2.2.3.5 Brownian Motion of Microtubules

To each microtubule-coordinate corresponds a term in B_t (*cf.* equation (2.3)). This term is a random number generated for each time step, which is most simply calibrated by considering diffusion in the absence of bending or external forces. We can illustrate the idea by first considering a coordinate x which we note here as a function of time x_t. Under pure diffusion, it should satisfy:

$$\langle x_{t+h} - x_t \rangle = 0 \qquad \langle (x_{t+h} - x_t)^2 \rangle = 2k_BT\mu h \tag{2.4}$$

Where Einstein's relation $D = \mu k_BT$ was used to get the diffusion from the mobility, the Boltzmann constant k_B and the absolute temperature T. Setting $A = 0$, $D = 0$ and first assuming $P_t = I$ in equation (2.3) yields $x_{t+h} - x_t = h\mu B_t$, and should produce a similar motion. This can be achieved if B_t is normally distributed, of mean zero and variance $2k_BT/\mu h$.

For the microtubule with $p + 1$ points, we use $3(p + 1)$ random numbers, independent and all normally distributed of variance $2k_BT/h\mu_{mt-point}$. This produces the appropriate diffusion for the fiber, as well as thermally-driven deformation. For example, the translation in X of the center of gravity depends on the sum of all the terms in X, which is appropriately a random number of variance $2k_BT/\mu_{mt}h$. Numerically, normally distributed random numbers are generated by transforming pseudo random numbers equidistributed in $[0, 1]$ using a standard procedure (Press et al., 2002), and scaling by $\beta^{mt} = \sqrt{2k_BT/h\mu_{mt-point}}$.

2.2.4   The Nucleus

The nucleus is represented by a non-deformable sphere of center n_0 and radius $r_{nucleus}$ with q additional points n_i on its fluid surface. The sphere moves as a rigid body, i.e. by translation and rotation, which move both the center of the sphere, and the surface points. The surface-points in addition are dragged in the viscous surface if they are subject to forces, or simply diffuse on the surface. If f_k is the vectorial-force applied at point k, and we define $r_k = n_k - n_0$, the motion is described by:

$$\frac{dn_o}{dt} = \mu^T \left(F + B^T \right) \tag{2.5}$$

$$\frac{dr_k}{dt} = \mu^R \left(T + B^R \right) \times r_k + \mu^S P_k \left(f_k + B_k^S \right) \tag{2.6}$$

where $F = \sum_{i=0}^{q} f_i$ is the total force on the sphere, and $T = \sum_{i=1}^{q} r_i \times f_i$ is the total torque calculated from the center, and P_k the projection defined by:

$$P_k = \mathrm{I} - \frac{r_k \otimes r_k}{r_k^2} \tag{2.7}$$

P_k is simply the projection on the plane tangent to the sphere in r_k. B^R, B^T and B_k^S are the random functions of time in the Langevin equation. The motion involves three different mobility factors: μ^T is the translation mobility of the sphere as a whole, μ^R the rotational mobility and μ^S the mobility of the points in the surface.

μ^S could be calculated for a disk embedded in a fluid 2D-membrane, from the 2D-viscosity and the size of the inset (Saffman and Delbrück, 1975). However, we could estimate neither of these parameters, and the iMTOC in the cell might be further attached to structures inside the nucleus. We chose therefore to directly explore the effect of μ^S on the system by systematically varying its value (see appendix A.5).

2.2.4.1   Mobility of the Nucleus

Recent measurements indicate that the cytoplasm in *S. pombe* shows subdiffusive behavior Tolić-Nørrelykke et al. (2004). This could be caused by obstruction by cellular structures, in particular for the nucleus which is the largest object in the cell. However, for simplicity, these effects were not taken into account. Furthermore, hydrodynamic effects were ignored apart from the lubrication flow between the nucleus and the cortex. The arrangement of the $\sim 3\ \mu m$ nucleus inside *S. pombe* of diameter $\sim 4\ \mu m$ resembles a closely fitting sphere in a cylindrical tube. To move the nucleus, the cytoplasm has to flow in the opposite direction between the nucleus and the cortex. The translational and rotational mobilities, μ^T and μ^R, of a sphere in such a geometry were calculated for the case of an infinitely long tube Bungay and Brenner (1973). Assuming axial symmetry, the mobilities (expanded to lowest order in the clearance $\epsilon = (r_{cell} - r_{nucleus})/r_{nucleus}$) are:

$$\mu^T = \frac{4\epsilon^{5/2}}{9\pi^2 \sqrt{2}\eta_{cell} r_{nucleus}} \qquad \mu^R = \frac{\sqrt{\epsilon}}{2\pi^2 \sqrt{2}\eta_{cell} r_{nucleus}^3} \tag{2.8}$$

(see Tab. A.1 for an explanation of variables). For simplicity, we also used these mobilities in the transverse direction, and applied the same formulae if the nucleus was off-axis. The effect is large and results in a reduction of the translational mobility by a factor ~ 25 compared to Stokes's law for a nucleus with radius $1.5\mu m$, or even a factor ~ 50 for a radius of $1.6\mu m$. For comparison, an obstacle in the cell of similar size as the nucleus would yield a factor ~ 2. The mobilities are highly

sensitive to the radius of the nucleus, and we therefore measured this parameter in wild type cells (see appendix A.4). To check the influence of the errors associated with the theoretical determination of the mobilities, we furthermore varied η_{cell} and $r_{nucleus}$ in the simulation (see appendix A.3 and A.4).

2.2.4.2 Brownian Motion of the Nucleus

As described above, points belonging to the nucleus incorporate three different types of motion, *i.e.* translation and rotation of the sphere, and additional motion of surface-points on the sphere. A random number B_t in equation (2.3) is associated to each of these motions. The numbers are calibrated by considering diffusion in the absence of other forces. For the translational diffusion of the sphere center $n_0(t)$, denoting here x_t one of the components (X, Y or Z), we have:

$$\langle x_{t+h} - x_t \rangle = 0 \qquad \langle (x_{t+h} - x_t)^2 \rangle = 2k_BT\mu^Th \tag{2.9}$$

Setting $A = 0$ and $D = 0$ in equation (2.3) yields $x_{t+h} - x_t = h\mu^T P_t \ B_t^T$, and should produce a similar motion. Since for a pure translation $P_t = I$, this can be achieved for X, Y and Z if we use for B_t^T a vector with 3 random and independent components, normally distributed, of mean zero and variance $2k_BT/\mu^Th$.

Rotational diffusion of the sphere is calibrated in a similar manner using equation (2.6). Ignoring the second term which describes the motion of points on the surface, we denote r_t the position of one of the surface points $r_k(t)$. For pure diffusion ($T = 0$), we get $r_{t+h} - r_t = h\mu^R \ B_t^R \times r_t$. The motion of an immobile point on the sphere of radius $r_{nucleus}$ due to rotational diffusion of the sphere should follow:

$$\langle r_{t+h} - r_t \rangle = 0 \qquad \langle (r_{t+h} - r_t)^2 \rangle = 4k_BT\mu^R r_{nucleus}^2 h \tag{2.10}$$

Since $\|r_t\| = r_{nucleus}$, and neglecting the curvature of the surface, we derive that we can use for B_t^R a random vector, with three independent components normally distributed, of mean zero and variance $2k_BT/\mu^R r_{nucleus}^2 h$.

In addition to movements of the whole sphere, the surface-points diffuse on the 2D nuclear envelope. With r_t being one of the surface points $r_k(t)$, the diffusion part is described by $r_{t+h} - r_t = h \ \mu^S P_k \ B_{k,t}^S$. It must, on the other hand, be a diffusion in the tangent plane to the sphere at r_t:

$$\langle p_{t+h} - p_t \rangle = 0 \qquad \langle (p_{t+h} - p_t)^2 \rangle = 4k_BT\mu^S h, \tag{2.11}$$

where p_t is the projection of r_t on the tangent plane. Since P_k is the identity in this plane, we derive that we can use for $B_{k,t}^S$ a vector with three independent components, each a normally distributed number, of mean zero and variance $2k_BT/\mu^S h$.

2.2.5 Confinement

In the simulation, the cortex is immobile and undeformable. To represent an idealized wild type *S. pombe* cell, we used a cylinder of length $2\,l_{cylinder}$ and radius r_{cell} closed by two half-spheres (see Fig. 2.1B). Since the volume thus defined is convex, it is sufficient to confine the model points of the microtubules in order for the whole microtubule to be inside the cell. Any model-point x outside the cell volume is subject to a force $f(x) = k_{cortex}(p(x) - x)$, where $p(x)$ is the point on the cortex with the shortest distance to x, *i.e.* the orthogonal projection of x on the cortex. Because the term is included in the matrix A only if the point is mathematically outside the cell, the force is always directed inwards. Furthermore, by definition this force is always perpendicular to the cortex, and thus represents a friction-less boundary. $f(x)$ is linearized for $y \approx x$ as $\tilde{f}(y) = k_{cortex} \ e_x(e_x \cdot (p_x - y))$,

where $p_x = p(x)$ and e_x is a unit vector in the direction of $p_x - x$. This linearization effectively replaces the curved cortex by the tangent plane in p_x, and because $\|p_x - y\| \ll r_{cell}$ in our case, this is a very good approximation of $f(x)$.

As described before, the nucleus is a sphere of center n_0 and radius $r_{nucleus}$. To ensure that not only the center, but the whole sphere is properly confined, n_0 is effectively confined in a shape which has been "deflated" by $r_{nucleus}$. This reduced volume has the same general shape, and thus the procedure is similar, albeit with a radius $r_{cell} - r_{nucleus}$. This way the entire nucleus including all the surface-points are properly confined. In summary, the confinement is applied to all microtubule points considering the full volume, and for n_0, the center point of the nucleus with the reduced volume. We used a stiffness $k_{cortex} = 1000 pN/\mu m$. Since the forces are in the pico-newton range, the points are never noticeably outside the cell volume.

2.2.6 Interactions Between Simulated Objects

2.2.6.1 Microtubule Bundles

For simplicity, the structure of microtubule bundles in the simulation is static and the bundles are constructed as shown in figure 2.2. Four microtubules are crosslinked together by Hookean springs of stiffness k_{bundle}. Each connection creates an attractive force between the minus end of the i-th microtubule m_0^i, and an intermediate point x^j, at the distance $l_{overlap}$ from the minus end of the j-th microtubule. To satisfy the action-reaction principle, $f = k_{bundle}(x^j - m_0^i)$ is applied to m_0^i, while $-f$ is applied to x^j. The intermediate point x^j is interpolated as described in the microtubule section. A total of six connections in the bundle generates an antiparallel overlap region of size $l_{overlap}$ as described in Fig. 2.2. However, the exact arrangement of the links should not affect the simulation outcome, since k_{bundle} is set relatively high compared to other stiffness parameters.
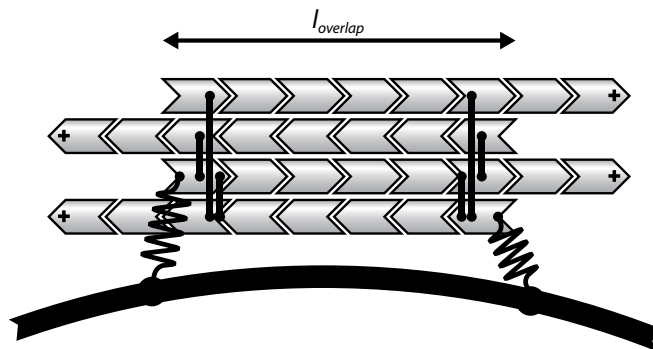
Figure 2.2: Construction of microtubule bundles and their connection to the nucleus. Each bundle in the simulation consists of four microtubules which are connected at their minus ends with stiff elastic links, shown as straight vertical lines. Microtubules within the bundle alternate in direction so as to create a balanced overlap of size $l_{overlap}(1.0\mu m)$. Furthermore, each bundle is attached to the nucleus at the edges of the overlap zone with two softer elastic links, shown as springs. The fibers in the simulation have no width, and the Hookean links of zero resting length make them overlap, unlike in this sketch.

The structure of the bundles is static, i.e. the number of microtubules per bundle stays constant over time. Outside of the overlap zone the microtubules are not connected and are therefore free to bend away from each other. However, due to their high bending stiffness, the fibers generally stay

close to each other as long as they do not touch the cortex. The influence of the bundling parameters $l_{overlap}$, $k_{bundling}$ and the number of microtubules per bundle on the outcome of the simulation is discussed in appendix A.10.

2.2.6.2   Attachment of Microtubule Bundles to the Nucleus

In interphase, microtubule bundles are mechanically linked to the nucleus Daga et al. (2006). Microtubule pushing forces on the cortex are transferred to the nucleus via these links which allows the cell to re-position the nucleus. In the simulation, each bundle is attached to the sphere at two surface-points, which are linked to the minus ends of two microtubules of the bundle (Fig. S2.2). The connection between the point m_0 at the microtubule minus end and a surface-point n_k ($k \geq 1$) on the nucleus is mediated by a spring with stiffness k_{link}. The action-reaction principle is satisfied by applying the force $k_{link}(n_k - m_0)$ to m_0, and the opposite force to n_k.

The stiffness k_{link} is chosen relatively low, to account for the elasticity of the nuclear membrane. Nevertheless, these forces orient the bundles tangentially to the nucleus. Since the nucleus surface-points behave like buoys in a fluid, the different bundles are only coupled indirectly. Strong couplings arise only when a bundle moves the entire nucleus, and not only the surface-points to which it is attached. In general, the motions of a surface point have little influence on the other points (and bundles), if they are small compared to the radius of the nucleus. As expected, however, moving a surface-point by more than $r_{nucleus}$ hauls the entire nucleus including all microtubule bundles.

2.2.6.3   Microtubule-Nucleus Steric Interactions

Microtubules are prevented from entering the nucleus by a repulsive force. If the distance between a point m_k of a microtubule and the center n_0 of the nucleus becomes smaller than $r_{nucleus}$, an interaction force f_k is added to push the two points apart: f_k is applied on m_k, and $-f_k$ on n_0. In agreement with the nature of the nucleus, we used a soft-repulsion, f_k being a Hookean spring with a resting length $r_{nucleus}$ and stiffness k_{nuc}:

$$f_k = k_{nuc} \left(\frac{r_{nucleus}}{\|m_k - n_0\|} - 1 \right) (m_k - n_0) \tag{2.12}$$

This force is linearized around $\frac{m_k - n_0}{\|m_k - n_0\|} r_{nucleus}$ and added at the right column/lines into the matrix A, for any k such that $\|m_k - n_0\| < r_{nucleus}$. Steric interaction between microtubules are not considered.

2.2.7   Dynamic Instability of Microtubules

In the simulation the dynamics of individual microtubules are not correlated within a bundle, i.e. all microtubules grow and shrink independently. Microtubule minus ends are static and stay attached to the nucleus while the plus ends are either growing or shrinking. Catastrophes occur with a rate c which is either constant (model 1: independent microtubule dynamics) or a function of the tubulin concentration (model 2: limited tubulin concentration) or position (model 3: position dependent catastrophes) or force (model 4 & 5: force dependent microtubule dynamics) (see chapter 4). According to experimental observations Tran et al. (2001) shrinking microtubules never rescue in the cytoplasm. For simplicity, we assumed that microtubules regrow immediately if they shrink into the overlap region. This leaves three parameters common to all models: the growth velocity v_g, shrinkage speed v_s and catastrophe rate c (see also chapter 4 and Tab. 4.1). The three models for dynamic instability used in this study were defined as follows:

1. **Independent microtubule dynamics (model 1)**
   The three parameters of dynamic instability are constant.

2. **Limited tubulin concentration (model 2)**
   The catastrophe rate c is constant, but the growth velocity v_g depends on the amount of tubulin available for polymerization. The tubulin concentration is measured in the equivalent length of polymerized tubulin, Σ_{MT}. To limit the tubulin concentration, we introduced a maximum for the total length of all microtubules in the simulation, denoted by Σ_{MT}^0. Microtubule growth velocity depends linearly on the fraction of Σ_{MT}^0 that is already used up by the microtubules in the simulation, i.e. $v_g = c_{tub}v_0$ where

   $$c_{tub} = 1 - \Sigma_{MT}/\Sigma_{MT}^0, \qquad c_{tub} \in [0,1]. \tag{2.13}$$

   The concentration of tubulin in fission yeast has not been measured. We therefore systematically varied Σ_{MT}^0 to test the influence of this parameter on microtubule dynamics in the simulation (see Sec. 5.1.2).

3. **Position dependent catastrophes (model 3)**
   The growth and shrinkage velocity v_g and v_s are constant, but the probability of undergoing catastrophe depends on the location of microtubule plus ends $\mathbf{m}^+ = \{x, y, z\}$. The model introduces two additional parameters: the catastrophe rate at cell poles c_{poles}, and a distance d_{cap} that defines a region of the cortex near the cell poles, where the catastrophe rate is c_{poles}. Mathematically, the catastrophe rate is c_{poles} , if $|x| \geq d_{cap}$ and if at the same time $\mathbf{m}^+$ is outside the confinement, i.e. in contact with the cortex. Anywhere else the catastrophe rate is c_0. We systematically varied d_{cap} to find the best agreement with the *in vivo* situation, which was obtained for $d_{cap} = l_{cylinder}$ (see Sec. 5.1.3).

4. **Force dependent microtubule dynamics (model 4 & 5)**
   The shrinkage velocity v_s is constant, but growth velocity and catastrophe rate depend on the force experienced by microtubule plus ends. We implemented the *in vitro* finding Dogterom and Yurke (1997) that the assembly rate of tubulin at microtubule tips is slowed down by an opposing force f:

   $$v_g(f) = v_0 \, e^{\,f/f_s} \qquad (f \leq 0) \tag{2.14}$$

   Here, v_0 is the maximum growth velocity obtained for microtubules that do not touch the cortex and are not under compression. The parameter f_s can be interpreted as the sensitivity of microtubule growth to the opposing force. The scalar f used in equation (2.14) is calculated from the projection of the force vector $\mathbf{f}$ (acting on the microtubule plus end) on the direction of microtubule growth. If $\mathbf{e}^+$ denotes the unit vector pointing in the direction of growth at the microtubule plus end, we use $f = \mathbf{f} \cdot \mathbf{e}^+$. In the simulation, forces originating from interactions with the cortex are always compressive (see Fig. 1C), and the growth speed can only be reduced ($f \leq 0$).

   In addition to slowing-down microtubule polymerization, the force increases the probability of a microtubule to undergo catastrophe. *In vitro* experiments with pure tubulin indicated that a linear relationship exists between the catastrophe time $t_{cat} = 1/c$ and the growth speed v_g of microtubule plus ends Janson et al. (2003):

   $$1/c = a + b \, v_g \tag{2.15}$$

We can relate the two constants a and b to the 'minimum' catastrophe rate c_0 obtained for microtubules growing under zero force ($v_g = v_0$), and to the 'maximum' catastrophe rate $c_{stalled}$ reached for stalled microtubules ($v_g = 0$):

$$
\begin{aligned}
1/c_{stalled} &= a \\
1/c_0 &= a + b\,v_0
\end{aligned}
\tag{2.16}
$$

We use c_0, v_0 and $c_{stalled}$ as parameters of the simulation, from which a and b are calculated using equations (2.16) (c_0 and v_0 were varied in the same range as for the other models). The growth and catastrophe rates of each microtubule are calculated using equations (2.14) and (2.15). Like the position dependent model, the force dependent model expands the independent model by introducing two additional parameters. In this case however, the sensitivity to force f_s and the catastrophe rate at speed zero $c_{stalled}$ are both set according to what has been observed *in vitro* Dogterom and Yurke (1997); Janson et al. (2003): $f_s = 1.67pN$, and $1/c_{stalled} = 24s$ (see appendix A).

5. **Extension of model 5: increased catastrophe rate at the cortex**
   Model 5 is extended by the parameter c_{cortex} that specifies the catastrophe rate for microtubules that contact the cortex. This model was used to simulate the phenotype of *tip1Δ* cells (see Sec. 5.3.2). The growth velocity and the catastrophe rate for microtubules growing in the cytoplasm is determined as in model 5, whereas for microtubules touching the cortex

$$
c = \begin{cases}
c_{cortex}, & \text{if } c_{cortex} \geq c_{stalled} \\
\frac{1}{a+bv_g}, & \text{if } c_{cortex} < c_{stalled}, \\
& \text{with } \quad 1/c_{stalled} = a \\
& \qquad\quad 1/c_{cortex} = a + b\,v_0.
\end{cases}
\tag{2.17}
$$

The additional parameter c_{cortex} was systematically varied to find the best agreement with the spatial distribution of catastrophes observed in *tip1Δ* cells (see Sec. 5.3.2).

Implementation: microtubules in the simulation grow and shrink continuously at a speed of v_g or v_s respectively. Equation (2.14) is compatible with a thermal-ratchet mechanism, but we did not model tubulin assembly stochastically. Instead, growing microtubules are elongated by $v_g h$ at their plus end in each time interval h. The time step h (0.01s) is chosen such that at a growth speed of $0.05\mu m/s$, the elongation ($0.5nm$) is small. Catastrophe events however, are rare and are modeled stochastically: To decide if a catastrophe occurred during the time interval h, the cumulative probability $P(c, h) = 1 - e^{-ch}$ is compared to a pseudo-random number θ, which is uniformly distributed in $[0, 1]$. The dynamic state of the microtubule is changed, if $\theta < P(c, h)$. This choice is made independently for all microtubules and is repeated at each time step h.

2.2.8 Life at Low Reynolds Number

The Reynolds number, Re, is a dimensionless factor that is used to determine the properties of the flow of a viscous fluid, and is often described as the ratio between viscous and inertial forces. More precisely, the Reynolds number is a factor in the dimensionless Navier-Stokes equation, that determines the weight of inertial terms relative to viscous terms. To clarify the meaning of the Reynolds number and its relevance for the motion of objects in the cytoplasm of cells, the Navier-Stokes equation will be derived in its dimensionless form.

The Navier-Stokes equation is a Newtonian equation of motion for viscous fluids and gases. Following Newton's law, the forces acting on a unit element of volume of the fluid must equal the mass of the unit element times its acceleration, a. If the density of the fluid is given by ρ, the force, f, per unit volume is

$$\rho\, a = f. \tag{2.18}$$

The force density on the right hand side can be written as a sum of two terms[2] which are the pressure gradient per unit volume $-\nabla p$ and viscous forces $\eta\Delta v$. The acceleration on the left hand side is given by the total derivative of the fluid velocity with respect to time:

$$a = \frac{dv}{dt} = (v \cdot \nabla)v + \frac{\partial v}{\partial t} \tag{2.19}$$

This includes the changes of velocity due to the fluid element moving from a position x to $x + v_x\Delta t$, i.e. $(v \cdot \nabla)v$, as well as the changes of velocity at a fixed point in space, $\frac{\partial v}{\partial t}$. For steady flow $\frac{\partial v}{\partial t} = 0$, and the streamlines of the fluid are constant in time (in this case the path of a particle in the fluid coincides with the streamlines). The Navier-Stokes equation becomes

$$\rho\left\{\frac{\partial v}{\partial t} + (v \cdot \nabla)v\right\} = -\nabla p + \eta\Delta v. \tag{2.20}$$

Together with the equation of continuity and appropriate boundary conditions this is all that is needed to completely determine the velocity field v and the pressure p. For an incompressible fluid ($\rho = $ const) the equation of continuity, $\nabla \cdot (\rho v) = -\frac{\partial \rho}{\partial t}$, simplifies to

$$\nabla \cdot v = 0 \tag{2.21}$$

Equations (2.20) and (2.21) are partial differential equations of second order for the velocity field v and the pressure p. Because of the inertial terms on the left hand side, the equations are nonlinear in v and superposition of solutions is not possible.

To investigate the influence of the different terms in the Navier-Stokes equation it is useful to introduce dimensionless variables that are scaled to the problem under investigation. For example, for the flow past an object of radius L there are four important parameters: the fluid density ρ, the viscosity η and the size L and speed V of the object. We can therefore substitute

$$x' = \frac{x}{L}, \qquad v' = \frac{v}{V}, \qquad t' = \frac{x'}{v'} = \frac{V}{L}t, \qquad p'(x') = \frac{1}{V\rho}p(x),$$

and the Navier-Stokes equation becomes

$$\frac{\partial v'}{\partial t'} + (v' \cdot \nabla')v' = -\nabla'p' + \frac{\eta}{\rho\,VL}\Delta'v'. \tag{2.22}$$

---

[2]We neglected the influence of external forces like gravity or electric fields, since we are not interested in such effects. Conservative forces with a potential ϕ per unit mass would result in an additional term, $-\rho\nabla\phi$.

The factor in front of the viscous term is the inverse of the Reynolds number, i.e.

$$Re = \frac{\rho V L}{\eta}. \tag{2.23}$$

Since equation (2.22) does not involve any parameters apart from the Reynolds number, it is solved by the same fields v' and p' for objects of different size L and speed V if the ratio $\rho V L/\eta$ stays the same. Because of this property it is possible to study small-scale models of hydrodynamic problems by choosing appropriate values for the four parameters. As mentioned above, the Reynolds number can furthermore be used to characterize the flow, since it describes the ratio of inertial and viscous terms in equation (2.22). If $Re \ll 1$, viscous forces dominate the Navier-Stokes equation. The inertial terms can be neglected and equation (2.20) simplifies to

$$\nabla p = \eta \Delta v. \tag{2.24}$$

This equation is linear in v and describes a situation with laminar flow, where layers of liquid slide along each other but do not mix. Its most important solution was calculated in the 19th century by Gabriel Stokes and describes the laminar flow past a sphere in an infinite viscous fluid. Knowing the velocity and pressure fields one can determine the resulting net force on the sphere by integrating the pressure and shear stress about the sphere surface, which leads to the well known Stokes' formula:

$$F_{drag} = 6\pi\eta L V. \tag{2.25}$$

If $Re \gg 1$, the inertial terms become important and the Navier-Stokes equation becomes nonlinear. Velocity and pressure at a fixed point in space are not constant anymore, since $\frac{\partial v}{\partial t} \neq 0$. Consequently the streamlines are changing in time and the fluid is constantly mixing. This state of flow where the velocities are very irregular is called turbulent.

Often the Reynolds number is described as the ratio of inertial forces to viscous forces. Yet is is not obvious that Re is in fact a ratio of forces. This can be understood the following way: When an object of size L is moved with speed V inside a fluid that was initially at rest, a volume of approximate size L^3 is forced to redirect around the object. This portion of the fluid therefore will have to accelerate and then decelerate again. The inertial forces involved in the acceleration of the fluid are given by $F_{inertia} = L^3\rho\frac{dv}{dt}$. For steady flow $\frac{dv}{dt} = (v \cdot \nabla)v$ (see eq. (2.19)), which can be written as $|v|\frac{dv}{ds}$ where $\frac{dv}{ds}$ is the directional derivative in the direction of a streamline, i.e. the direction of v. We assume that the fluid has to accelerate by V along the streamline on the length L, such that $\frac{dv}{ds} \approx V/L$ and $F_{inertia} = L^2\rho V^2$. Since the fluid moves with speed V on the surface of the object (the fluid is at rest relative to the sphere), the shear stress of the fluid acts on a surface of approximate size L^2. The viscous forces can be estimated from the definition of the shear stress $F_{viscous}/A = \eta\frac{dv}{ds_\perp}$, where $ds_\perp$ denotes the direction perpendicular to the streamlines. Assuming that the flow slows down to zero on a length $L_{viscous}$ along $ds_\perp$, the frictional force is $F_{viscous} = L^2\eta V/L_{viscous}$. The ratio of inertial to viscous forces is therefore given by

$$Re = \frac{F_{inertia}}{F_{viscous}} = \frac{\rho V L_{viscous}}{\eta}. \tag{2.26}$$

It should be noted that equation (2.26) involves $L_{viscous}$ and not the size L of the object. Equation (2.26) is equivalent to equation (2.23) only if we assume that $L_{viscous} \approx L$. This is not always the case: for example in a pipe we usually have $L_{viscous} \ll L$ where L is the diameter of the pipe. The switch between laminar and turbulent flow therefore occurs at higher Reynolds number ($Re \approx 2000$).

The flow around the Nucleus in S. pombe

To estimate the Reynolds number for the flow past objects in the cytoplasm of *S. pombe* we consider the nucleus which is the biggest object inside the cell. We assume that the density of the cytoplasm is similar to the densitiy of water, i.e. $\rho_{cytoplasm} = 10^3 kg/m^3$, and the viscosity is $\eta_{cell} = 0.9 pNs/\mu m^2$ (see appendix A.3). The radius of the nucleus is $r_{nucleus} = 1.5\mu m$ (see appendix A) and therefore $L = 3\mu m$. Since it is pushed by microtubules, the nucleus cannot move faster than at the speed of microtubule growth, i.e $V = 0.05\mu m/s$. This results in a Reynolds number of $Re \approx 1.7 \cdot 10^{-10}$. Consequently, the flow is laminar.

It should be noted that the Reynolds number describes only the properties of flow around the object. It does not compare the inertial forces of the object to viscous drag forces (the mass density in the Reynolds number is the density of the fluid, not of the object). However, for laminar flow the viscous drag is proportional to speed and we can easily determine the relevance of inertial forces within the cytoplasm.

2.2.9 On the Role of Inertia Within the Cytoplasm

To determine the role of inertial forces within the cytoplasm of *S. pombe* we consider the nucleus moving at an initial speed of $V = 0.05\mu m/s$, i.e. the speed of growing microtubules. If all microtubules suddenly underwent catastrophe, the nucleus would slow down due to the friction within the cytoplasm. The motion of the nucleus in such a case is described by the equation of motion

$$\frac{\partial v(t)}{\partial t} = -\frac{1}{\mu \cdot m} v(t), \tag{2.27}$$

where μ and m are the mobility and the mass of the nucleus. Integration of equation (2.27) yields

$$v(t) = v(0)\, exp^{-\frac{t}{\mu \cdot m}} \tag{2.28}$$
$$x(t) = v(0)\, \mu \cdot m \left(1 - exp^{-\frac{t}{\mu \cdot m}}\right)$$
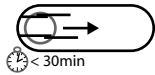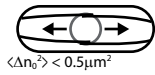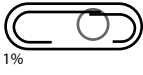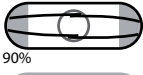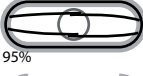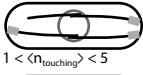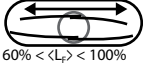
According to equation (2.8) the translational mobility of the nucleus is $\mu \approx 0.0015\mu m/pNs$. The mass of the nucleus can be estimated from a sphere with radius $r_{nucleus} = 1.5\mu m$ and the density of water, $\rho = 10^3 kg/m^3$, which gives $m \approx 4.5\pi \cdot 10^{-9} pNs^2/\mu m$. With $v(0) = 0.05\mu m/s$ we get $x(\infty) \approx 3.375 \cdot 10^{-13}\mu m$ for the maximum distance the nucleus would travel due to inertia. The half-time of the exponential slow down is $\mu \cdot m = 6.75 \cdot 10^{-12}s$. It is therefore justified to neglect the influence of inertial forces in the simulation.

Chapter 3

Nine Traits of Wild Type Interphase Fission Yeast Cells

Nine characteristics of interphase microtubules in wild type *S.pombe* (see Fig. 3.1) were chosen to quantitatively evaluate the five models of dynamic instability described in chapter 4. In the following paragraphs each trait is discussed together with its method of quantification. Experimental data for the first six traits was obtained from the literature, whereas results for the remaining traits have not been published. We therefore recorded time series of living *S.pombe* cells expressing GFP-α2tub to determine the distribution of microtubule contact times with the cell poles (T7), the number of half-bundles touching the cell poles (T8) and the distribution of microtubule bundle length (T9). Importantly, the quantification of the traits in the simulation was adjusted to match the experimental methods to be able to directly compare experiments and simulations.

T1: Microtubule bundles align along the cell axis

T2: The nucleus is actively centered within 30min
$t_3 < 30min$

T3: The nucleus fluctuates about the center with $\langle \Delta n_0^2 \rangle < 0.5 \mu m^2$
$\langle \Delta n_0^2 \rangle < 0.5 \mu m^2$

T4: Microtubules do not curl
1%

T5: Catastrophes occur at cell poles
90%

T6: Catastrophes occur at the cortex
95%

T7: The contact time of microtubules with cell poles is 66s on average
$t_3 > 66s$

T8: 50% of all microtubule half-bundles contact the cortex on average at any time
$1 < \langle n_{touching} \rangle < 5$

T9: The lenght of Microtubule bundles is 70% of the cell length on average
$60\% < \langle L_F \rangle < 100\%$

Figure 3.1: Nine traits of interphase fission yeast cells. Nine features of wild type cells that are well characterized experimentally were used to evaluate the five different models of microtubule dynamic instability presented in chapter 4. The details of the quantification of the nine traits (T1-T9) are described in the text.

3.1 T1: Alignment of Microtubule Bundles

Microtubule bundles in wild type cells are usually aligned parallel to the cell axis. However, existing bundles eventually disappear and new ones are nucleated on the nucleus. New bundles form in random directions and orient themselves as they grow longer (Fig. 3.2). Since the new bundles rotate relative to the existing ones during this period, it is thought that the bundle attachment sites are mobile on the nuclear surface. In the simulation this mobility is granted by the fluidity of the nuclear envelope (see methods, Sec. 2.2.6.2 and discussion of parameters in appendix A.5). Microtubule bundles are
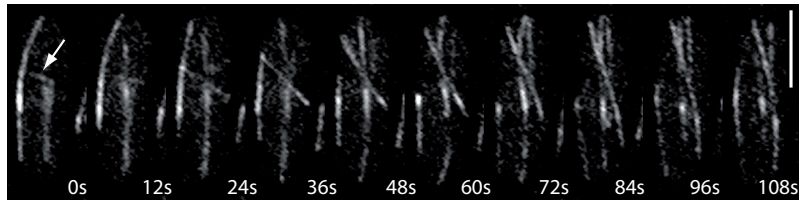
Figure 3.2: Time series of a wild type cell expressing GFP-tubulin. A microtubule bundle, newly nucleated on the nucleus (arrow) aligns itself to the cell axis. The new bundle rotates relative to the existing ones, indicating that interphase microtubule organizing centers (iMTOCs) are mobile on the nuclear surface. The images shown are maximum projections of single planes taken on a spinning disc confocal microscope with a z-spacing of $0.5\mu m$. scalebar: $5\mu m$

always able to orient, as long as they become longer than the cell diameter and the mobility of the buoys anchoring the bundles to the nucleus is high enough. The results of the systematic variation of these parameters are documented in appendix A.

3.2 T2: Active Centering of the Nucleus

Several observations have indicated that, *in vivo*, the nucleus is centered by microtubule bundles pushing on the cortex (Daga et al., 2006; Tran et al., 2001). Cells treated with microtubule depolymerizing drugs like methyl-2-benzimidazole-carbamate (MBC) or thiabendazole (TBZ) do not exhibit active displacements of the nucleus, confirming this mechanism (Tran et al., 2001). Interestingly, the nucleus is moved off-center, and repositioned at every cell cycle. During anaphase the two daughter nuclei are pushed into the cell poles by the elongating spindle. After spindle breakdown the nuclei are repositioned to the center by cytoplasmic microtubule bundles. As interphase resumes the center position is maintained, even if the cells grow only at one pole before 'new end take off' (NETO) (see also Sec. 1.3.1).

In the simulation, the center of the nucleus, n_0, was initially positioned at the edge of the central cylinder, i.e. $n_0 = l_{cylinder} = 3.5\mu m$ (see table A.1 in appendix A). T2 was considered to be fulfilled if the nucleus reached the center within $30min$, a test that most wild type cells would pass. Indeed, in cells in which the nucleus was artificially misplaced by centrifugation (Daga et al., 2006), it crossed the distance of $\sim 3\mu m$ from the pole to the center within $17 \pm 6.7min$ on average.

3.3 T3: Variance of the Nucleus Position

The equilibrium position of the nucleus at the cell center is reached before cytokinesis and is maintained until the cell progresses into mitosis. Yet, throughout interphase microtubules constantly pull

on the nuclear envelope while they are pushing at the cell ends, and the nucleus moves stochastically around the cell center by approximately $\pm 0.2 \mu m$ (Janson et al., 2005).

In the simulation we measured the variance of the nucleus center $\langle n_0^2 \rangle$, and we considered T3 to be fulfilled, if it was lower than $0.5 \mu m^2$. Since all simulations were started with the nucleus being off-centered, the beginning of the measurement was delayed until the nucleus had reached its equilibrium position at the cell center. In our model the magnitude of the deviation from the center position depends on several parameters, e.g. the viscosity of the cytoplasm η_{cell}, the size of the nucleus, the rigidity of microtubule-nucleus links k_{link} and on the dynamic parameters of microtubules (see appendix A). Together they can be used to tune the variance within a certain range. Furthermore, viscoelastic and hydrodynamic effects within the cytoplasm that were ignored are likely to affect the motion of objects within the fluid. This is particularly true for the nucleus, which is the biggest object inside the cell. Consequently, comparing nuclear motions between simulations and experiments does not provide on its own a stringent test of the different models.

3.4 T4: Microtubule Curling

Microtubules in wild type cells often bend when they push against the cortex. Yet they almost never curl around the cell poles such that the microtubule plus ends point towards the nucleus. The amount of curling microtubules in wild type cells is below 1% (Behrens and Nurse, 2002). In the simulation, we quantified the amount of curling by considering every microtubule during the course of a simulation. T4 was considered to be fulfilled, if the fraction of curling microtubules was less than 1%.

Mathematically, the test for each microtubule was based on the tangential vectors at the minus end ($\mathbf{m}$) and at the plus end ($\mathbf{p}$) (both vectors point in the direction of the plus-end, and are therefore equal if the microtubule is straight). To compute if a microtubule is curling, we first multiplied the x-components of $\mathbf{m}$ and $\mathbf{p}$ to obtain a scalar $c_1 = m_x\, p_x$, which is negative if the microtubule bends further than being perpendicular to the x-axis. However, c_1 can also be negative for short straight microtubules that happen to be perpendicular to the cell axis, because Brownian fluctuations can bend them such that $\mathbf{m}$ and $\mathbf{p}$ point in opposite left/right directions. We therefore additionally used the scalar product $c_2 = \mathbf{m} \cdot \mathbf{p}$, which is negative if the microtubule bent more than 90 degrees on itself. Only if $c_1 < 0$ and $c_2 < 0$, the microtubule was registered to be curled.

3.5 T5: Catastrophes at Cell Poles

Previous measurements revealed that more than 90% of all 'microtubule catastrophes' in wild type cells occur at the cell poles (Brunner and Nurse, 2000). However, in this study (as well as in other ones) single microtubules within a bundle could not be resolved. Hence only catastrophes of the longest microtubules within each half-bundle were recorded. Catastrophes of shorter microtubules were not detected.

In the simulation however, we distinguished between bundle and microtubule catastrophes. In order to be able to compare it to the published data, only bundle catastrophes were registered. Furthermore, only catastrophes that occurred after the nucleus reached the center were taken into account. This was done to exclude any influence of the equilibration period on the measurement of the catastrophe location. T5 was considered to be fulfilled, if more than 90% of all bundle catastrophes occured in the caps ($|x| > l_{cylinder}$, the origin being at the cell center). Apart from the dynamic parameters, the probability of a bundle reaching the cell poles in the simulation depends on the number of microtubules per bundle and on the cell length (see following section).

3.6 T6: Catastrophes at the Cortex

In wild type cells more than 95% of all bundle catastrophes were reported to occur at the cortex (Brunner and Nurse, 2000). However, due to the limited resolution of optical microscopy, all catastrophes happening within a distance of $\sim 0.5\mu m$ from the cell edge were probably scored at the cortex. To compare with the *in vivo* measurements, bundle catastrophes in the simulation were therefore also registered, if they happened closer than $0.5\mu m$ to the edge of the cell. As for T3 and T5, only events that happened after the nucleus reached the center were considered. T6 was fulfilled if the fraction of cortical bundle catastrophes represented 95% or more of all bundle catastrophes.

3.7 T7: Microtubule Contact Time at Cell Poles

Microtubules in contact with the cell poles grow with a reduced polymerization rate (Tran et al., 2001; Loïodice et al., 2005), which allows them to stay in physical contact with the cortex without curling (Tran et al., 2001; Brunner and Nurse, 2000, our own measurements Fig. 3.3). To measure the contact times with high precision *in vivo*, we acquired time-lapse movies of wild type cells expressing GFP-α2tub with a frame rate of $3s^{-1}$ and analyzed them visually using custom macros in ImageJ. Contact was defined from the moment a microtubule touched the cortex within the cell cap, to the frame at which depolymerization was detected. We found that microtubules contacted the cortex at the cell poles for about $66s$ on average before they underwent catastrophe. Strikingly, some microtubules remained at the cell poles for more than four minutes without curling (Fig. 3.3).
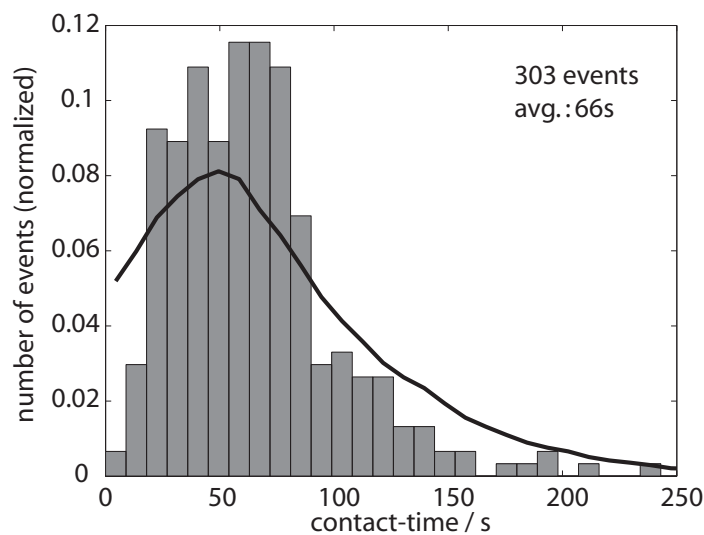
Figure 3.3: Microtubule contact times with the cortex at the cell poles. In *S. pombe*, microtubule bundles reach the cell poles $\sim 1min$ before undergoing catastrophe. The individual contact times are stochastic observables, and we measured their probability distribution to infer how catastrophes may be regulated. Bars: 303 contact times, extracted from $343min$ of live imaging. The distribution has a local maximum at $\sim 60s$. Line: distribution of contact times acquired from a simulation with force dependent microtubule dynamics (75000 events scored). The simulation was run with the standard parameter set representing a wild type cell (see appendix A).

The distribution of contacts furthermore exhibited a local maximum at $\sim 60s$ which provided a good test of the five models of dynamic instability (see chapter 4). Indeed, the experimental distribution did not fit a simple one-step stochastic (Poissonian) process as used in the model with localized catastrophes (model 3, explained in section 4.3). In simulations performed with model 3, the contact times were exponentially distributed (Fig. 3.4 D-F). However, the experimental results were consistent with simulations run with the force dependent microtubule dynamics model (model 5). This is indicated in Fig. 3.3, where the solid line represents the probability distribution estimated from a very large number of simulated events, or from Fig. 3.4 A-C, where the number of events is comparable to what we measured in vivo.
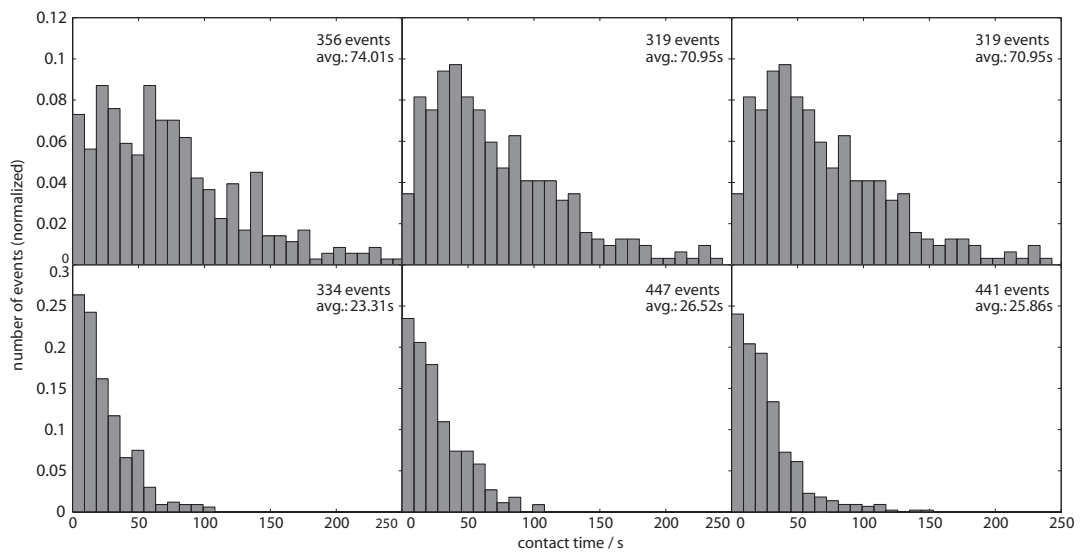
Figure 3.4: Distribution of microtubule contact times with the cell poles, determined from simulations with model 3 and 5. The number of events scored corresponds to the number of contact times measured in vivo. All simulations were run with the standard set of parameters (see appendix A). (A-C) With force dependent microtubule dynamics, the distribution has a maximum around $50s$; the average is $75s$. (D-F) In the position dependent model, contact times are exponentially distributed with an average of $25s$.

In the simulation, contacts were defined the same way as in the experiment, as the time between the encounter of a cell pole and the occurrence of catastrophe. Only events that occurred after the nucleus reached the center were recorded to avoid any influence of the centering process. If more than 1% of all microtubules curled around the cell poles, the measurement of the contact time was declared invalid, since curling microtubules usually underwent catastrophe within the cytoplasm long after they had lost contact with the poles.

3.8   T8: Number of Half-Bundles Touching the Poles

According to T5 more than 90% of all microtubule half-bundles reach the poles. The number of half-bundles touching the poles at any time depends on the growth and shrinkage velocities of the microtubules as well as on the contact time (T7). For the recently published value of 1.5 ± 0.4 (Daga et al., 2006) it was not specified which bundles were exactly scored and how many half-bundles were

observed per cell. We therefore repeated the measurement and found that the number of half-bundles touching the poles was normally distributed around the average value 3.6 ± 1.2 (Fig. 3.5).
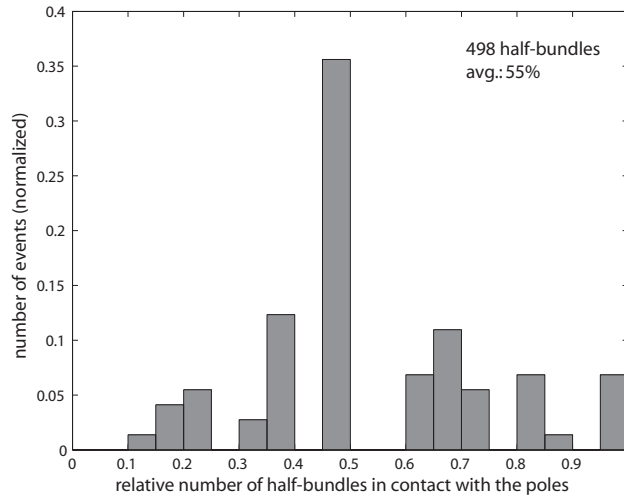
Figure 3.5: Number of half-bundles in contact with the cell poles. 498 half-bundles were scored in 73 cells. An average number of 3.6 ± 1.2 half-bundles was touching the cortex at any time. These were $55 \pm 21\%$ of the average total number of 6.8 half-bundles per cell.

The average number of half-bundles per cell was 6.8 resulting in a fraction of $55 \pm 21\%$ of all half-bundles touching the cell poles at any time. In our experiment and in the simulation, a half-bundle was considered to be touching the cell pole if it was in contact with the cortex within the curved region of the cell. Since the simulation contains eight half-bundles we regarded T8 to be fulfilled, if the number of touching half-bundles was between 1 and 5. Again, only events after the nucleus reached the center were scored.

3.9　T9: Microtubule Bundle Length

As described in section 1.3.2.2, individual microtubules within the bundles are difficult to resolve by optical microscopy and quantitative data on the length distribution of single microtubules has not yet been published. Recently, such data was obtained by electron tomography (Höög et al., 2007). However, due to the labor intensive detection method the number of microtubules measured this way is relatively low. We therefore determined the length of microtubule bundles rather than single microtubules from cells expressing GFP-α2tub. The distinction of two antiparallel half-bundles was not possible, because the positions of the microtubule minus ends could not be detected and microtubule bundles in living cells are dynamically constructed from motors and accessory proteins (see Sec. 1.3.2.2). We therefore measured the full length of microtubule bundles relative to the cell length from maximum intensity projections. We found that microtubule bundles covered 70% of the cell length on average (Fig. 3.6)

To compare the output from the simulation to the *in vivo* measurement the full bundle length in the simulation was also projected in the z-direction. It turned out however, that the difference between the z-projected and the full length was neglectable ($< 3\%$), since the bundles aligned to the cell axis
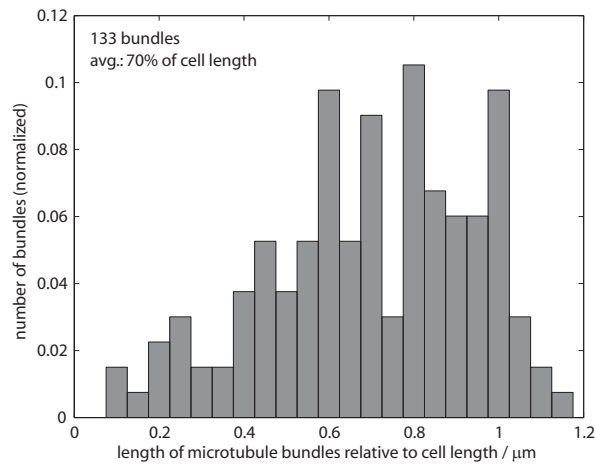
Figure 3.6: Distribution of microtubule bundle length *in vivo*. 133 bundles were scored in 36 cells. The average bundle length was $\sim$70% of the cell length, as determined from maximum intensity projections.

in the xy-plane. Trait nine was considered to be fulfilled, if the bundle length was between 60 and 100% of the cell length. A typical distribution from a simulation with force dependent microtubule dynamics (model 5) is shown in Fig. 3.7.
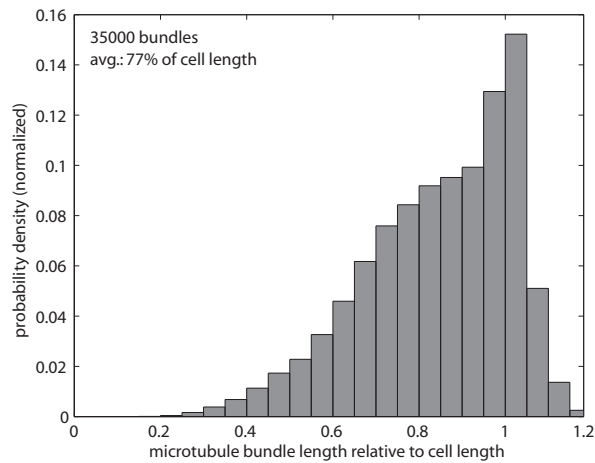
Figure 3.7: Distribution of microtubule bundle length from a simulation with force dependent microtubule dynamics. About 35000 events were scored. The average bundle length was $\sim$77% of the cell length projected on the xy-plane.

Chapter 4

Five Models for the Regulation of Microtubule Dynamic Instability

How is microtubule dynamic instability regulated in order to produce the nine characteristics (T1-T9) described in the previous chapter? Several models were suggested to answer this question, including the effects of tubulin concentration, localized regulatory factors and forces acting on microtubule plus ends. To test and compare the proposed mechanisms we implemented five different models in the computer simulation and analyzed the results with respect to the nine traits. Two of these models involve only global regulation of microtubule dynamics while the remaining three models are based on local regulation at the cell poles.

In the most simple model, microtubule dynamics is regulated globally for example by evenly distributed growth promoting or catastrophe inducing factors. The behavior of microtubules is assumed to be independent of the concentration of free tubulin subunits, the position of microtubule plus ends or the physical force exerted on microtubule tips. The parameters of microtubule dynamic instability are constant in time and space (independent dynamics, Sec. 4.1). As discussed below, such a basic model is not very likely to reproduce T1-T9 correctly since the distribution of microtubule length does not conform with the requirement that the vast majority of microtubule bundles is adjusted to match the length of the cell. However, it is still instructive to study why exactly the model fails to identify aspects of microtubule organization that have to be regulated differently. For independent dynamics, the distribution of microtubule length can furthermore be described analytically which provided a way to check the results produced by the simulation. From the theoretical analysis we could infer an upper limit for the catastrophe rate of single microtubules which was so far not measured *in vivo* (see Sec. 4.1.3).

It was suggested that the length of microtubules might be self-regulating because the amount of tubulin available for polymerization is limited within the cell. The second model therefore implements a maximum length for the sum of all microtubules in the simulation. The growth velocity of microtubules decreases linearly with the remaining available length (the amount of tubulin that is still available for polymerization) and is zero if the maximum length is reached (limited tubulin, Sec. 4.2). The competition for tubulin introduces correlations between the length of different microtubules and therefore influences the outcome of the nine characteristics. Since we assumed that diffusion is fast enough to neglect local variations of the tubulin concentration this model involves only global regulation of microtubule dynamics.

In contrast, the following three models locally affect microtubule growth and catastrophes at the cell poles. Experimental observations in mutant cells demonstrated that the catastrophe rate at the

poles is higher than in central parts of the cell. A possible mechanism involves the Clip-170 homolog Tip1 which localizes to the plus ends of growing microtubules where it is thought to protect them from catastrophes when they touch the cortex. Tip1 is removed from the plus ends of microtubules at the cell poles in dependency of Tea1 which could explain the locally increased catastrophe rate observed *in vivo* (Brunner and Nurse, 2000). Our third model therefore introduces a higher catastrophe rate for microtubules that contact the cortex at the cell poles (localized catastrophes, Sec. 4.3).

The fourth and fifth model are based on the experimental result that force influences microtubule dynamics. It was shown *in vitro* that microtubule polymerization is slowed down by forces opposing the direction of growth (Dogterom and Yurke, 1997). Albeit being a general property of microtubule plus ends at any position, this was proposed to create a local effect in the cylindrical geometry of fission yeast cells, where compressive forces primarily occur at the cell poles. To test if this is indeed sufficient to reproduce the nine characteristics measured in living cells, we implemented a force dependent growth velocity in our fourth model (force dependent growth velocity, Sec. 4.4). More recent experiments performed with pure tubulin furthermore demonstrated that slow growing microtubules generally exhibit a higher catastrophe rate. This was shown for microtubules that polymerized slowly due to an opposing force as well as for microtubules that were growing at low tubulin concentrations, which indicates that these findings reflect a general property of microtubule dynamics (Janson et al., 2003). Our fifth model therefore incorporates both force dependent microtubule growth and a catastrophe rate that depends on the growth velocity (force dependent dynamics, Sec. 4.5).

We used the simulation to study each of the five models. Our aim was to identify the simplest model that was able to reproduce the nine traits measured in living cells. The two force dependent models were the most attractive candidates because they did not rely on the inhomogeneous distribution of regulatory factors inside the cell and thus did not require any additional assumptions. Local effects were generated simply from the global physical properties of microtubules which are experimentally measured.

4.1   Model 1: Independent Microtubule Dynamics

In our first model (independent dynamics), the behavior of microtubules is completely determined by four parameters: the microtubule growth and shrinkage velocities, v_g and v_s, are constant in space and time. Transitions between the growing and the shrinking state occur randomly with average rates c for catastrophes (transition from growth to shrinkage) and r for rescues (transitions from shrinkage to growth).

4.1.1   Microtubule Length Distribution

It is assumed that the transition probabilities are independent of the filament history, i.e. that catastrophes and rescues are Poissonian processes. Consequently, the waiting times for the occurrence of the next catastrophe or rescue are exponentially distributed:

$$p_c(t) = ce^{-ct}, \qquad p_r(t) = re^{-rt} \tag{4.1}$$

Under the assumption that the minus ends are static while the plus ends exhibit dynamic instability, the distribution of microtubule length can be calculated from the probability densities to find a growing or shrinking microtubule plus end at a time t and at a location x, $p_g(t, x)$ and $p_s(t, x)$ respectively

(Dogterom and Leibler, 1993). The time evolution of these probability densities is then given by

$$
\begin{aligned}
\frac{\partial p_g}{\partial t} &= -cp_g + rp_s - v_g \frac{\partial p_g}{\partial x} \\
\frac{\partial p_s}{\partial t} &= +cp_g - rp_s + v_s \frac{\partial p_s}{\partial x}.
\end{aligned}
\tag{4.2}
$$

These partial differential equations can be solved analytically with appropriate boundary conditions (Verde et al., 1992; Dogterom and Leibler, 1993) which leads to an expression for the average growth velocity J of a population of microtubules with given parameters v_g, v_s, c and r (see appendix C.1 for an alternative way to derive this result):

$$
J = \frac{v_g r - v_s c}{c + r}
\tag{4.3}
$$

Equation (4.3) predicts two regimes for the average microtubule length of the population: If $v_g r > v_s c$, the average growth velocity, J, is positive and the average microtubule length $\langle L \rangle = Jt$ increases with time. With an unlimited supply of free tubulin, the population of microtubules would always keep elongating, which is why the case of $J > 0$ is called the regime of unlimited or unbounded growth. If $J < 0$, the average length of the population decreases, which means that microtubules disassemble completely. Yet, in reality the average microtubule length cannot become negative. Instead we assume that a certain number of microtubules is renucleated after complete disassembly such that the average length of microtubules reaches a steady state where $J = 0$. The case of $J = 0$ is called the regime of bounded growth, and the average length is well defined by the four dynamic parameters:

$$
\langle L \rangle = \frac{v_g v_s}{v_s c - v_g r}
\tag{4.4}
$$

The steady state distribution of microtubule length in the regime of bounded growth is exponential (see appendix C.2):

$$
p(l) = \lambda e^{-\lambda l}, \qquad \text{with } \lambda = \langle L \rangle^{-1}
\tag{4.5}
$$

An exponential length distribution was indeed found for microtubules nucleated from centrosomes in *Xenopus* egg extracts (Verde et al., 1992). In *S. pombe*, rescues are not observed in the cytoplasm (see appendix A.8.4). Microtubules usually shrink back to the antiparallel overlap region close to the nucleus and regrow from the nucleus or from nucleation centers that associate with existing microtubules (see 1.3.2.2). In the simulation, microtubules are renucleated only from the central overlap region (Sec. 2.1). Consequently, r is set to zero in our model and microtubule growth is always in the bounded regime. The length of microtubules is distributed according to equation (4.5) (Fig. 4.1 solid line).

4.1.2 Length Distribution of Microtubule Bundles

As described in section 1.3.2.2, microtubules in interphase fission yeast cells are bundled, and it is difficult to follow the dynamics of single microtubules within the bundles *in vivo* by optical microscopy. To be able to compare the measurements from living cells to the theoretical predictions of the independent model and to the results from the simulation, it is therefore necessary to analyze the length distribution of microtubule bundles rather than single microtubules (see also section 3.9).

The probability density for a bundle consisting of N parallel microtubules to be at length l can be easily calculated from the probability densities of the individual microtubules, if we assume that the dynamics of microtubules within a bundle are uncorrelated. The probability density for all filaments

in a half-bundle (i.e. all microtubules that point into the same direction) to have a certain length $l_i(i = 1, \ldots, N)$ is therefore simply the product of the individual probability densities:

$$p(l_1, \ldots, l_N) = \prod_{i=1}^{N} p(l_i) \tag{4.6}$$

In a half-bundle of length l the longest microtubule must have the length l while all other microtubules are shorter. The probability density for the longest microtubule to have length l is $p(l) = \lambda e^{-\lambda l}$ according to equation (4.5). This is weighted by the probability that all other microtubules are shorter, i.e by

$$P^{(N-1)}(x < l) = \left(\int_0^l \lambda e^{-\lambda l'} dl' \right)^{(N-1)} = \left(1 - e^{-\lambda l} \right)^{(N-1)}. \tag{4.7}$$

Since the microtubules within a bundle are not distinguished, there are N permutations to realize a situation where the longest microtubule has length l, and the probability density, $p_H(l)$ of a half-bundle to have length l is

$$p_H(l) = N\lambda e^{-\lambda l} \left(1 - e^{-\lambda l} \right)^{(N-1)}. \tag{4.8}$$

The length distribution of half-bundles containing two individual microtubules ($N = 2$) is illustrated by the dashed line in Fig. 4.1. For given dynamic parameters, the average length of half-bundles, $\langle L_H \rangle$, is

$$\langle L_H \rangle = \int_0^\infty l \cdot p_H(l) dl, \qquad \langle L_H \rangle_{N=2} = \frac{3}{2\lambda}. \tag{4.9}$$

Inserting $\lambda = 0.1/\mu m$ as determined from the reference set of parameters (see next section and chapter A) results in an average length of $\langle L_H \rangle_{N=2} = 15\mu m$.

However, as described in section 2.1 microtubule bundles in the simulation consist of two antiparallel half-bundles that overlap in an antiparallel way where they are attached to the nucleus. In living cells, microtubule bundles are dynamically constructed from motors and accessory proteins Janson et al. (2007) and it is therefore difficult to determine where one half-bundle stops and the other one starts. Consequently, only the length of full microtubule bundles can be measured *in vivo*, which can also be calculated from equation (4.8) in the independent model. The probability density for a full microtubule bundle, $p_F(l)$, to have length l is the integral over all possibilities to realize this length with the two half-bundles:

$$p_F(l) = \int_0^l p_H(x) p_H(l - x) dx \tag{4.10}$$

This integral is difficult to solve for arbitrary N, but in the case of $N = 2$ used for the simulations in this study, the probability density for a full microtubule bundle to have length l is (Fig. 4.1 dotted line)

$$p_F(l)_{N=2} = 4\lambda^2 e^{-\lambda l} \left(l \left(e^{-\lambda l} + 1 \right) + \frac{2}{\lambda} \left(e^{-\lambda l} - 1 \right) \right). \tag{4.11}$$

Since the two half-bundles are independent, the average full-bundle length, $\langle L_F \rangle$, is just the double of the half-length, resulting in $\langle L_F \rangle_{N=2} = 30\mu m$ for $\lambda = 0.1/\mu m$:

$$\langle L_F \rangle = \int_0^\infty l \cdot p_F(l) dl, \qquad \langle L_F \rangle_{N=2} = \frac{3}{\lambda} \tag{4.12}$$
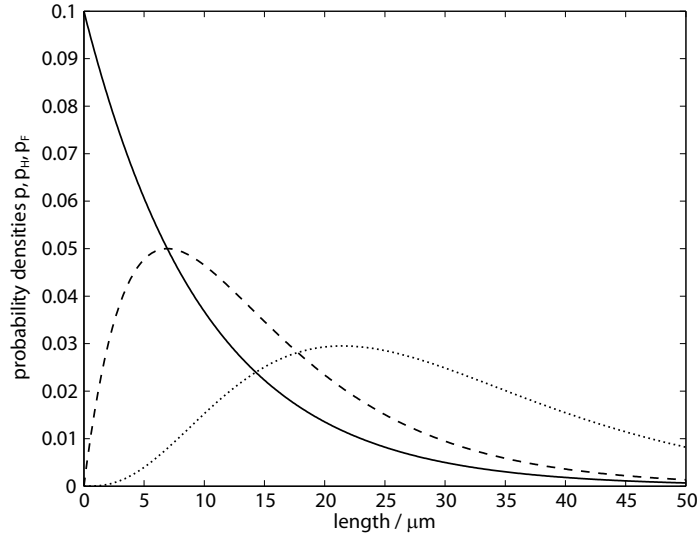
Figure 4.1: Length distribution of microtubules, microtubule half-bundles and full-bundles in the independent dynamics model. The solid line displays the exponential length distribution of single microtubules according to equation (4.5). The dashed and dotted lines show the distribution of the half- and full-bundle length calculated from equations (4.8) and (4.11) respectively, for two microtubules per half-bundle ($N = 2$). The dynamic parameters were chosen from the standard set of parameters for *S. pombe* simulations (see section 4.1.3 and Tab. A.1) The graphs illustrate that a significant fraction of microtubule bundles becomes longer than the simulated cell which has a length of $11\mu m$ Such microtubule bundles are therefore likely to curl at the cell poles and thus violate trait four (see Sec. 3.4).

4.1.3 Parameters for Simulations With Independent Dynamics

The results from the previous section can be used to determine a lower threshold for the catastrophe rate, c, of single microtubules. This value has not yet been quantified *in vivo*, due to the fact that such catastrophes are hidden within bundles and are difficult to detect. In living cells, more than 90% of all microtubule half-bundles reach the cell poles (see T5, 3.5). In the simulation, the cylindrical body of the cell has a half-length of $3.5\mu m$ and the antiparallel overlap of microtubule half-bundles is $1\mu m$ (cf. Tab. A.1). Microtubules regrow if they become shorter than the overlap width, i.e. they have a minimum length of $1\mu m$. In order to fulfill T5 in the simulation, more than 90% of all half-bundles have to become longer than $3\mu m$, assuming that the middle of the overlap region is at the center of the cell. With equation (4.8) this results in the following condition for λ:

$$0.9 < 2\lambda \int_{3}^{\infty} e^{-\lambda l} \left(1 - e^{-\lambda l}\right) = 2e^{-3\lambda} - e^{-6\lambda}, \tag{4.13}$$

which is fulfilled for $\lambda < 0.1267$. Inserting the remaining dynamic parameters measured in *S. pombe* ($v_g = 3\mu m/min$, $v_s = 9\mu m/min$ and $r=0$, see chapter A) results in a catastrophe rate of $c \approx 0.38/min$. This value represents the maximum rate at which T5 can be fulfilled. We therefore used $c = 0.3/min$ for the reference set of parameters. The boundary where λ becomes small enough, such that more than 90% of all half-bundles reach the poles, is depicted by the dashed lines in the figures in the results section (e.g. Fig. 5.1).

From these theoretical considerations we could deduce that at $v_g = 3\mu m/min$ the catastrophe rate has to be below $0.38/min$ to fulfill T5. On the other hand we know from equation (4.8) that for this value of c about 78% of all half-bundles will become longer than $5\mu m$ and will curl around the cell poles (see also Fig. 4.1). This is in contradiction with the fourth trait which states that less than 1% of all half-bundles exhibit curling in wild type cells. We can therefore conclude that a model with independent microtubule dynamics is unlikely to fulfill the nine characteristics of wild type cells (Chap. 3), since either T4 or T5 will be violated. Nevertheless we used the simulation to investigate, if there is any set of input parameters that can match T1-T9. The critical parameters with respect to the nine traits are the ones that affect the average microtubule length. As can be seen from equation (4.4) there are only two relevant parameters in the independent model: the growth velocity v_g and the catastrophe rate c. Since rescues were ignored, the shrinkage velocity has no influence on $\langle L \rangle$. We therefore varied v_g and c and analyzed how this affected the outcome of the simulation with respect to T1-T9.

These two dynamic parameters also determine the basal behavior of microtubules in the four other models of microtubule dynamic instability. On top of this, additional parameters define how microtubules behave at the cell poles or under force. Therefore v_g and c were varied for all the models in the same range, together with the additional parameters specific for each model. The results are presented in section 5.1.

4.2 Model 2: Limited Tubulin Concentration

It was proposed that the length of microtubule bundles in fission yeast cells could be regulated by the concentration of free tubulin. We therefore expanded the independent model to make the growth velocity dependent on the amount of tubulin that was still available for polymerization. As described in the introduction (Sec. 1.2), the rate of tubulin addition at microtubule plus ends is proportional to the concentration, C_{tub}, of free tubulin dimers:

$$v_g = (k_{on}C_{tub} - k_{off}) \frac{l_{dimer}}{13},\tag{4.14}$$

where $l_{dimer} = 8nm$ is the length of one tubulin subunit which is divided by thirteen for a thirteen-protofilament microtubule. In the simulation the functional dependence of the growth velocity on the free tubulin concentration is implemented as described in section 2.2.7. Essentially, the independent model is extended by one parameter which specifies the amount of available tubulin as the equivalent total length of microtubules, Σ_{MT}^0, that would be reached if all tubulin was polymerized. The current growth velocity v_g is calculated from the maximum growth velocity v_0, which is the same as in the independent model, and from the remaining amount of free tubulin as described in section 2.2.7.

We assumed that the diffusion of tubulin dimers is fast enough such that local effects can be neglected. Consequently, the remaining tubulin concentration was calculated globally for all microtubules. To validate this approach we estimated the distance that a tubulin dimer can cross by diffusion within one second: The mean square displacement $\langle \Delta x^2 \rangle = 2Dt$ of tubulin dimers within the cell can be estimated from the diffusion coefficient of tubulin in buffer which is about $D = 4.4 \cdot 10^{-11} m^2/s$ (Krouglova et al., 2004). With this $\langle \Delta x^2 \rangle \approx 88\mu m^2$ in one second, i.e. $\sqrt{\langle \Delta x^2 \rangle} \approx 9.38\mu m$. Tubulin dimers can therefore cross almost the whole length of a pombe cell by diffusion in one second. Even though the cytoplasm is probably more viscous and diffusion is hindered by inhomogeneities, this is fast enough to justify a global approach.

If there is only a finite amount of free tubulin available, the maximum length of microtubules is bounded. However, a more interesting consequence is that correlations are introduced between the

length of different microtubules. In the most extreme case all available tubulin polymerizes into a single microtubule, and the remaining microtubules cannot grow unless the first one depolymerizes and releases tubulin subunits. Because of these correlations, the length distribution of microtubules is not exponential as in the independent model. An example from a simulation with two microtubules that are limited to have a maximum length of $10\mu m$ is shown in Fig. 4.2 (dashed line). The correlation coefficients between the length of the two microtubules were 0.0043 for the simulation with independent dynamics and -0.47 for the case of limited tubulin concentration.
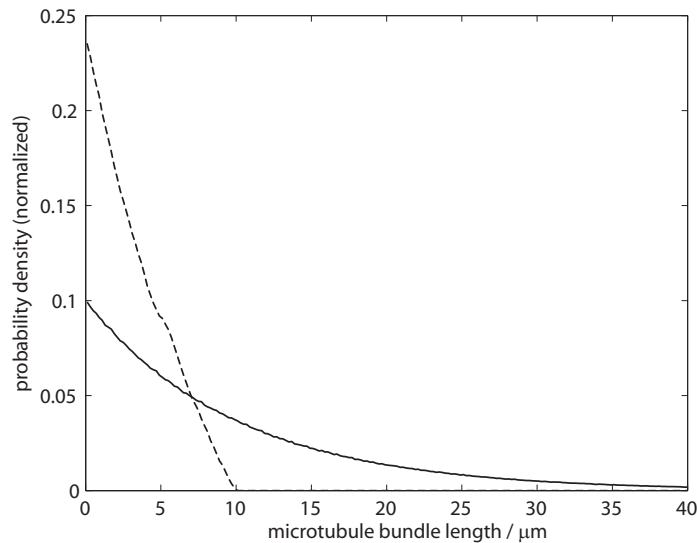
Figure 4.2: Length distribution of microtubules from a simulation with independent dynamics and with limited tubulin concentration. To illustrate how a finite amount of free tubulin affects microtubule length, two simulations were run either with independent dynamics or with limited tubulin. Both simulations contained two microtubules and had identical dynamical parameters taken from the reference set (Tab. A.1). For the simulation with limited tubulin the maximum length of both microtubules was set to $10\mu m$, and the growth velocity dropped proportionally to the amount of polymerized tubulin. As expected, the simulation with independent dynamics exhibited an exponential length distribution (solid line) while the correlations between the two microtubules altered the distribution in the limited case (dashed line).

We did not explore the additional effects of an increase of the catastrophe rate for slow growing microtubules. A higher catastrophe rate for slow growing microtubules at low tubulin concentrations was observed *in vitro* Janson et al. (2003) using pure tubulin. If was found that the inverse of the catastrophe rate, i.e. the average time a microtubule spends in the growing state, increases linearly with the tubulin concentration (see Fig. 4.7). However, we did not further explore the implications of such a model on the nine traits.

4.3 Model 3: Localized Catastrophes

Independent dynamics and the limitation of tubulin represent global strategies. However, as described by the fifth trait (T5) most microtubules in fission yeast become long enough to reach the cell poles, but they do not grow further and they do not start curling (T4). We found that such microtubule behavior

is difficult to achieve with global regulation of microtubule dynamics (see results 5.1.1, 5.1.2). It rather suggests that local regulation occurs at the poles and prevents microtubules from becoming too long. As in the global models, a prerequisite to fulfill T5 is that the general dynamic parameters allow microtubules to become long enough to reach the poles, which imposes a limit on the cytoplasmic growth and catastrophe rates (see Sec. 4.1.3). Yet, when the microtubules reach the cortex at the poles the dynamic parameters have to change locally in order to prevent microtubules from curling. This model therefore suggests that regulatory proteins are localized specifically at the cell poles to satisfy T4 (localized catastrophes).
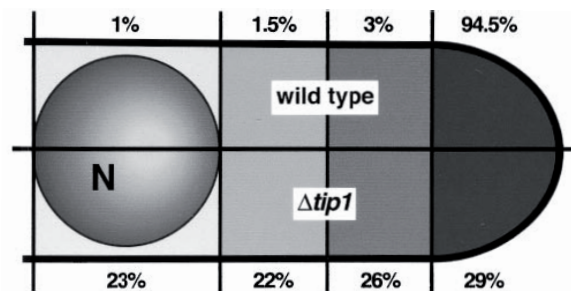

Figure 4.3: Distribution of catastrophes in wild type and *tip1Δ* cells. The schematic drawing of a partial pombe cell shows the percentage of catastrophes occurring in different regions of the cell (N denotes the nucleus at the cell center). In wild type cells (top half, 198 microtubules scored) catastrophes happen almost exclusively at the cell poles, whereas in the *tip1Δ* mutant (bottom half, 192 microtubules scored) they occur evenly distributed along the length of the cell (Brunner and Nurse, 2000).

Experimental evidence for the local regulation of microtubule dynamics in fission yeast comes from the analysis of microtubules in *tip1* deleted cells, a homolog of the human Clip170 (see 1.2.4.5). In wild type cells Tip1 binds to the plus ends of cytoplasmic microtubules which is thought to protect them from catastrophes (Brunner and Nurse, 2000). When the microtubules reach the cell poles Tip1 is removed from the plus ends by a factor localized only in the polar region of the cortex (possibly Tea1). The removal of Tip1 renders microtubules less stable when they touch the cortex at the poles and thus locally increases the probability of catastrophe. Indeed, microtubules in *tip1Δ* cells exhibit premature catastrophes all over the cortex, indicating that one function of Tip1 is to stabilize microtubule plus ends (Fig. 4.3). The localized removal of Tip1 would therefore allow the cell to discriminate the poles from other parts of the cortex.

The main effect of Tip1 removal at the cell poles is a local increase of the catastrophe rate. Our third model thus implements a different probability of catastrophe for microtubule plus ends that touch the cortex within the curved region of the poles. Two additional parameters are needed to describe microtubule dynamics in this model. One is the catastrophe rate at the poles, c_{poles}, and the other, d_{cap}, defines the size of the cortical region where c_{poles} is active. The setup of this model is illustrated in Fig. 4.4 and the details of the implementation can be found in section 2.2.7.

4.4   Model 4: Force Dependent Growth Velocity

In the previous model the catastrophe rate was assumed to be higher at the poles because of the inhomogeneous distribution of catastrophe promoting or stabilizing factors. Such a model raises the
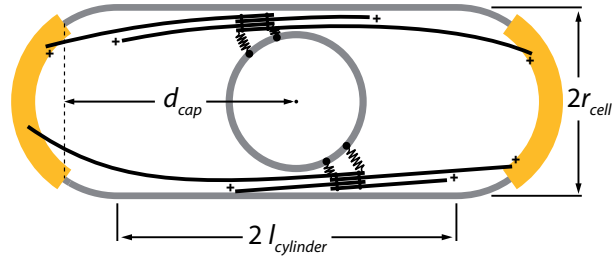
Figure 4.4: Setup of simulations with localized catastrophes. The catastrophe rate of microtubule plus ends contacting the cell poles is set to c_{poles}. The size of the region where c_{poles} is active is determined by the parameter d_{cap} which specifies the distance from the center along the x-axis where c_{poles} becomes active.

question how the position of these factors is determined. Assuming that they are transported on microtubules produces a feedback loop where the location of microtubule catastrophes is determined by factors that are in turn positioned by microtubule plus ends. But how is the loop initially started? Either microtubules have to be correctly organized from the beginning in order to transport regulatory proteins to the poles, or such factors have to be located at the poles initially in order to organize the microtubules.
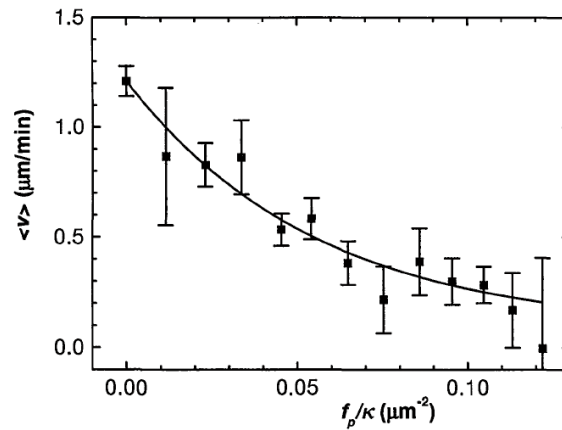
Figure 4.5: Average microtubule growth velocity as a function of force. Microtubules were attached to a substrate at one end, causing the other end to grow against a microfabricated barrier. The buckling of the microtubules was analyzed to determine their growth velocity and the force exerted on the barrier. The solid line represents the best fit to an exponential decay (Dogterom and Yurke, 1997).

An elegant way out is offered by the finding that microtubule growth is sensitive to force. *In vitro* experiments demonstrated that force opposing microtubule growth slows down tubulin assembly as

$$v_g = v_0 \, exp\left(-\frac{f}{f_s}\right), \tag{4.15}$$

where f_s is the sensitivity to force and v_0 is the unloaded polymerization speed. In the experiment the shape of buckling microtubules was fitted to the shape of homogeneous elastic rods which produced values for the force acting on the rod relative to its flexural rigidity, f/κ_{mt}. The component of this normalized force that directly opposes microtubule growth is the component that is parallel to the direction of elongation, f_p/κ_{mt}, plotted on the abscissa in Fig. 4.5. From these measurements and from the flexural rigidity chosen for the reference set of parameters, $\kappa_{mt} = 30pN\mu m^2$, we obtained $f_s = 1.67pN$ for the sensitivity parameter (see Sec. A.9.2). For the scalar force f we used the projection of the force vector on the direction of microtubule growth (see also Sec. 2.2.7 and Fig. 4.6). The results from the *in vitro* experiments fit well with a generalized Brownian ratchet model (Mogilner and Oster, 1999) that explains the slow down of microtubule growth on a molecular level.
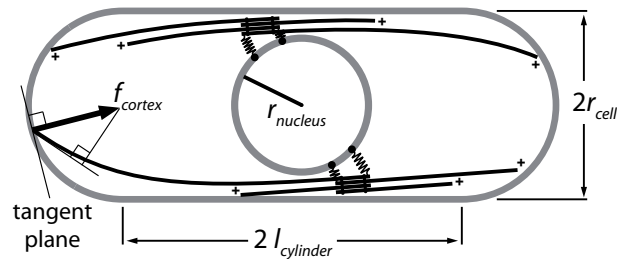
Figure 4.6: Setup of simulations with force dependent microtubule growth.
The growth velocity of microtubules is slowed down by the component of the force that is opposing the direction of microtubule growth. The forces f_{cortex} exerted by the cortex are always perpendicular to the local surface, representing a frictionless contact between microtubules and the cell wall.

The sensitivity of microtubule growth to force is a general mechanistic property of microtubule plus ends at any location. However, because of the special morphology of the *S. pombe* cortex this can produce local effects at the cell poles. Microtubules that grow perpendicular to the cell axis and touch the cortex within the cell body are usually deflected and continue growing towards the poles (see T1, Sec. 3.1). Consequently, the force on microtubule plus ends that grow within the cytoplasm or touch the cortex away from the poles is relatively low. This is different for microtubules that target the cell poles. When they touch the cortex at the poles and continue growing, they have to push on the nucleus or even against other microtubules from the same bundle touching the opposite pole. Consequently the force on growing plus ends is higher at the poles than at the remaining parts of the cortex.

4.5   Model 5: Force Dependent Microtubule Dynamics

As described before, slow growing microtubules were observed to undergo catastrophe more often than rapidly elongating microtubules *in vitro*. Interestingly, the result was the same if polymerization was slowed down due to an opposing force or because of low tubulin concentration (Janson et al., 2003). Careful evaluation revealed a linear relationship between the growth velocity and the inverse of the catastrophe rate, i.e. the time a microtubule spends growing, shown in Fig. 4.7.

The line in Fig. 4.7 can be described by the equation $1/c = a + bv_g$ where a and b are the ordinate and the slope of the line. The inverse of the ordinate provides the catastrophe rate, $c_{stalled}$, for microtubules at zero growth velocity (see also Sec. 2.2.7). *In vitro*, catastrophes occurred after $24s$ on average if microtubule growth was stalled completely. This value was independent of the tubulin

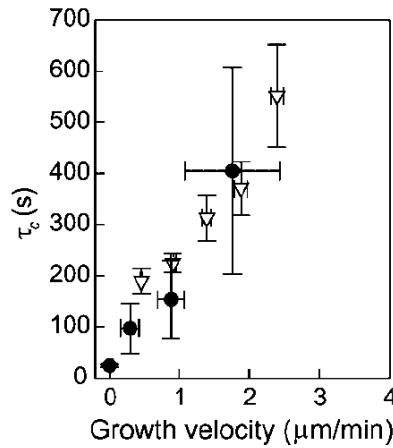**Figure 4.7: Catastrophe time as a function of microtubule growth velocity.** As for the determination of microtubule growth under force, microtubules were attached to a surface at one end while the other end polymerized against a barrier. The graph shows the duration of contact to the barrier before catastrophe occurred for different growth velocities (∇). Similar results were obtained for the lifetimes of free microtubules at different tubulin concentrations (●) (Janson et al., 2003).

concentration (Janson et al., 2003), which allowed us to use $c_{stalled} \approx 0.05s^{-1}$ for the maximum catastrophe rate, even if the tubulin concentration in *S. pombe* is unknown. The basal or minimum catastrophe rate, c_0, at the maximum growth velocity v_0 determines the slope, b, of the line in Fig. 4.7 (see Sec. 2.2.7 for more details). The value of c_0 or b may reflect the overall effect of microtubule associated proteins like for example Mal3 that are present in *S. pombe* and determine the basal catastrophe rate for microtubules growing unhindered in the cytoplasm with v_0. As for the other models c_0 and v_0 were varied to determine their influence on the nine traits. The results are presented in section 5.1.5.

4.6 Summary of Model Parameters

The parameters that determine microtubule dynamics in each model[1] are summarized in Tab. 4.1. In the model with independent dynamics (model 1, Sec. 4.1) the microtubule growth velocity and the catastrophe rate are constant, whereas in the model with limited tubulin concentration (model 2, Sec. 4.2) microtubule growth depends on the fraction of unpolymerized tubulin, c_{tub}. The model with localized catastrophes (model 3, Sec. 4.3) introduces two new parameters which are the catastrophe rate at the poles, c_{poles}, and a parameter d_{cap} that defines the size of the catastrophe promoting region. Only one parameter is added in the model with force dependent growth velocity (model 4, Sec. 4.4) which is the sensitivity to force, f_s. A default value of $1.67pN$ for f_s was determined from the *in vitro* measurements (Dogterom and Yurke, 1997) and from our choice of the flexural rigidity $\kappa_{mt} = 30pN\mu m^2$ (see appendix A.9.2).

---

[1]Since rescues were ignored in the simulation (see appendix A.8.4), the average microtubule length did not depend on the shrinkage velocity, v_s, which is therefore not listed. After we had verified that v_s did not influence the outcome of the simulation (see appendix A.8.2) this parameter was kept constant for all simulations.

Finally, in the model with force dependent growth and catastrophes (model 5, Sec. 4.5), the sensitivity to force is complemented by the catastrophe rate, $c_{stalled}$, for microtubules at zero growth velocity. In this model the current catastrophe rate, c, of each microtubule is individually set and depends on the growth velocity like $1/(a + b \cdot v_g)$. Four parameters thus determine microtubule dynamics instability in model 5: the free growth velocity, v_0, the free catastrophe rate, c_0, the sensitivity to force, f_s, and the catastrophe rate for stalled microtubules, $c_{stalled}$. Default values for the two additional parameters $f_s = 1.67pN$ and $c_{stalled} = 0.05s^{-1}$ are provided from the *in vitro* experiments.

	Equations	**Parameters that determine microtubule dynamics**
Model 1: independent dynamics	$v_g = v_0,$ (const) $c = c_0,$ (const)	v_0: growth velocity c_0: catastrophe rate
Model 2: limited tubulin concentration	$v_g = c_{tub} \cdot v_0, \ c_{tub} = \frac{\Sigma^0_{MT} - \Sigma_{MT}}{\Sigma^0_{MT}}$ $\in [0,1]$ $c = c_0,$ (const) Σ^0_{MT}: max. MT length in simulation Σ_{MT}: MT length already used	v_0: maximum growth velocity for $\Sigma_{MT} = 0$ (all tubulin available) c_0: catastrophe rate c_{tub}: tubulin concentration as fraction of MT length available for growth
Model 3: localized catastrophes	$v_g = v_0,$ (const) $c = \begin{cases} c_0 : x_{MT} \le d_{poles} \\ c_{poles} : x_{MT} > d_{poles} \end{cases}$ (x_{MT}: x-position of MT plus ends)	v_0: growth velocity c_0: cytoplasmic catastrophe rate c_{poles}: catastrophe rate at the poles d_{cap}: the distance along the x-axis from the cell center to the region where c_{poles} is active (see Fig. 4.4)
Model 4: force dependent growth velocity	$v_g = v_0 \cdot exp^{-f/f_s}$ $c = c_0,$ (const)	v_0: free growth velocity ($f = 0$) c_0: catastrophe rate f_s: microtubule sensitivity to force
Model 5: force dependent MT dynamics	$v_g = v_0 \cdot exp^{-f/f_s}$ $c = \frac{1}{a + b \cdot v_g}, \quad a = c^{-1}_{stalled}$ $b = \frac{c_{stalled} - c_0}{c_{stalled} c_0} \frac{1}{v_0}$	v_0: free growth velocity ($f = 0$) c_0: free catastrophe rate ($v_g = v_0$) f_s: microtubule sensitivity to force $c_{stalled}$: catastrophe rate for microtubules at $v_g = 0$

Table 4.1: Parameters that determine microtubule dynamics in models 1-5. Each model is listed with the equations and the parameters that are used in the simulation to calculate the microtubule (MT) growth velocity and the catastrophe rate.

Chapter 5

Results

To evaluate the five models for the regulation of dynamic instability presented in the previous chapter, we compared the results of the computer simulations to the nine traits (T1-T9) of wild type *S. pombe* defined in chapter 3. For each model we varied the parameters that control microtubule dynamics (see Tab. 4.1) to investigate how they influence the nine traits. This allowed us to identify regions in parameter space where the simulation could successfully reproduce the organization of microtubule bundles in living cells. The results of these simulations are discussed in section 5.1. The most successful model turned out to be model 5 with force dependent microtubule growth and catastrophes. To further characterize this model we systematically varied its remaining parameters and analyzed how they affected the nine traits. These additional results are discussed in appendix A.

Our simulations indicated that localized factors at the cell poles are not needed to fulfill T1-T9, but that the cylindrical shape of the cortex is crucial for the proper organization of microtubule bundles in interphase (Sec. 5.1.5). To investigate the role of cell shape *in vivo* we analyzed the organization of microtubule bundles in cells that carried a temperature sensitive mutation of *pmo25*, a gene that is involved in the maintenance of cell morphology. At the restrictive temperature the *pmo25* mutant is deficient in anchoring the growth machinery at the cell poles, and cells successively become round within a few hours. Growth factors and actin patches, which collocalize with growth sites in fission yeast, are redistributed quickly after the temperature shift. Yet, cell shape changes only gradually which allowed us to study the organization of microtubules in the absence of these polarized factors but within a normal cylindrical cell shape. As the cells gradually became round we could furthermore investigate how microtubule organization correlates with cell morphology. The results of these experiments suggested that cell shape is essential for proper microtubule organization *in vivo*. This indicates that force might also be important to organize microtubules in living cells (see Sec. 5.2).

Inspired by these findings, we varied the parameters of the simulation to investigate if we could reproduce the mutant phenotypes of *mal3Δ* and *tip1Δ* cells in the context of model 5. Our results lead us to extend the model for *tip1Δ* cells and to propose a novel mechanism how Tip1 might interact with regulatory factors located at the cell cortex to assist force in the spatial control of microtubule dynamics in living fission yeast cells (Sec. 5.3).

5.1 Analyzing Five Models for the Regulation of Dynamic Instability

For each of the five models described in the previous chapter, we investigated if the computer simulation could reproduce the nine characteristics (T1-T9) of the wild type microtubule cytoskeleton

described in chapter 3. The behavior of microtubules in each model was mainly determined by the dynamic parameters listed in Tab. 4.1. Our aim was to find a set of these parameters that fulfilled all or at least some of the nine traits. The two most relevant parameters were the growth velocity, v_0, and the catastrophe rate, c_0, since they fundamentally influence the behavior of microtubules in all the models (Tab. 4.1). As described in section 4.1.3, v_0 and c_0 determine how long microtubules become on average if microtubule dynamics is independent of tubulin concentration, the position of microtubule plus ends and of force (model 1, independent dynamics). On top of that, additional parameters affect the distribution of microtubule length in the remaining models, yet all the models fundamentally depend on v_0 and c_0.

We therefore varied v_0 and c_0 for each model in the same range around the reference values (see appendix A for the definition of the reference set of parameters), i.e. v_0 from $1 - 5\mu m/min$ and c_0 from $0 - 2/min$. The meaning of v_0 and c_0 differs between the five models as summarized in Tab. 4.1. In general, these two parameters correspond to the unbiased growth and catastrophe rates, i.e. the values that are adopted when all tubulin is available for polymerization (model 2), the plus ends do not contact the cell poles (model 3), and no force is acting on the plus ends (model 4 & 5). For models 2 to 5 we furthermore varied the additional model specific parameters, for example the sensitivity of microtubules to force, f_s, for model 4 & 5 (see Tab. 4.1), in order to investigate their influence on microtubule dynamics and on the nine traits.

	simulation characteristics	*in vivo*		**simulation characteristics**	*in vivo*
T2:	time needed to center the nucleus	$< 30 min$		variance of the position of the overlap region	-
T3:	variance of the nucleus position	$< 0.5\mu m^2$	T7:	avg. microtubule contact time with the cell poles	$> 60s$
T4:	percentage of curling microtubules	$< 1\%$		avg. bundle contact time with the cell poles	-
	effective catastrophe rate measured in the simulation	-		avg. number of microtubules touching the poles	-
	percentage of microtubule catastrophes at the poles	-	T8:	avg. number of bundles touching the poles	$1 - 5$
T5:	percentage of bundle catastrophes at the poles	$> 90\%$		avg. microtubule length projected on the z-direction	-
	percentage of microtubule catastrophes cortex	-		avg. half-bundle length projected on the z-direction	-
T6:	percentage of bundle catastrophes at the cortex	$> 95\%$	T9:	avg. full-bundle length projected on the z-direction	$60 - 100\%$ of the cell

Table 5.1: Characteristic profile generated for each simulation. The output of each simulation was processed to generate a characteristic profile containing the data shown in this table. The right column describes the conditions that a simulation had to fulfill in order to comply with the corresponding trait measured *in vivo* (see chapter 3). A hyphen indicates that this value was not yet measured in living cells, and was therefore not considered for the evaluation of simulations.

To avoid sampling artifacts the dynamic parameters were varied randomly. For the two dimensional plain spanned by v_0 and c_0 we typically generated 1000 different input files for the simulation.

From each simulation run on the computer, we then recorded the trajectory of the nucleus and of the microtubule plus and minus ends, as well as the microtubule length and the time and location of all catastrophes. Subsequently, the output was analyzed automatically with scripts written in Python to calculate a characteristic profile for each simulation. This profile included values that could directly be compared to the nine traits. The most important elements of the profile are listed in Tab. 5.1, together with the corresponding values obtained from *in vivo* measurements.

Screening the parameter space in this way, we could identify regions where simulations complied with T1-T9, and regions where some of the traits could not be fulfilled. In living fission yeast cells, some of the dynamic parameters might be affected by environmental changes, for example by temperature or by the availability of nutrients. However, *S. pombe* is able to survive and to maintain the organization of its cytoskeleton under such varying conditions. The simulation should therefore be robust in the sense that parameters that are observed to vary *in vivo* can also be changed within the corresponding range in the simulation without causing it to fail. For example, experimentally measured values for the growth velocity of microtubule bundles vary between 2 and $3.5\mu m/min$ (see appendix A.8.1). Simulations that fulfill T1-T9 should therefore not be sensitive to changes of v_0 within this range. Consequently, we rather tried to identify continuous regions where the nine traits were fulfilled, whereas isolated simulations that only worked for one specific set of parameter values were not regarded to be relevant. The range of different growth velocities measured in living cells is indicated by the gray shaded area in the figures in the next sections (for example Fig. 5.1).

In all our simulations the nucleus was initially placed at a cell pole, to test if microtubules could push it back to the center within $30min$ (T2). Furthermore all simulations were started with the same reference set of parameters (see appendix A), and only differed in the dynamic parameters that were varied, as well as in the initial orientation of microtubule bundles on the nucleus, which was chosen randomly (see Sec. 2.1).

For the model with force dependent microtubule growth and catastrophes (model 5) we furthermore systematically varied all the remaining parameters that define the configuration of the simulation, like for example the length of the cylindrical cell body, $l_{cylinder}$, and the viscosity of the cytoplasm. This allowed us to further characterize this model and to study the influence of the remaining parameters on T1-T9. Again, we tested if the simulation was robust with respect to naturally occurring parameter variations, like for example the increase of cell length that is observed as the cell grows during the cell cycle. Moreover, the variation of parameters like $l_{cylinder}$ allowed us to predict how the organization of microtubules changes together with cell length, which could now also be tested *in vivo*. The results of these systematic parameter screens are presented in appendix A.

5.1.1 Results Model 1: Independent Microtubule Dynamics

In the model with independent microtubule dynamics the distribution of microtubule length is completely determined by the growth velocity, v_0, and by the catastrophe rate, c_0. As anticipated (see Sec. 4.1), we could not find any region in parameter space where all traits were fulfilled simultaneously. Simulations were able to orient microtubule bundles (T1) and to center the nucleus (T2 & T3), but they usually failed to meet either T4 or T5. This was a direct consequence of the exponential distribution of microtubule length: if more than 90% of all microtubule half-bundles reached the cell poles (T5 fulfilled), many of them continued to grow and consequently curled around the poles (T4 failed) (see also Fig. 4.1). Conversely, if v_0 and c_0 were chosen to comply with T4, simulations failed to meet T5. With independent dynamics, the choice of parameters is therefore a tradeoff between T4 and T5.

However, the analysis of this model allowed us to investigate in more detail how the simulation

behaved for different values of the dynamic parameters and how these values affected the nine traits. We divided the parameter space into different sections according to the average length of microtubule half-bundles. These sections are confined by the lines shown in Fig. 5.1, which are passing through the origin of the coordinate system spanned by v_0 and c_0. On these lines the average half-bundle length, $\langle L_H \rangle$, is constant and is determined by the parameter λ which is the inverse of the average microtubule length[1]. According to equation (4.9) the lines can therefore be described by

$$c_0 = \frac{3}{2} \frac{v_0}{\langle L_H \rangle}, \qquad \text{for two microtubules per half-bundle.} \qquad (5.1)$$

Microtubule half-bundles on the solid line in the upper left corner of Fig. 5.1 reached an average length[2] of $\langle L_H \rangle \approx 2.8 \mu m$. Below this line, microtubules were able to orient along the cell axis (T1) and to push the nucleus to the cell center within $30 min$ (T2), whereas they were too short to do so for higher catastrophe rates or lower growth velocities[3]. Typical trajectories of the nucleus and of the microtubule plus ends for both cases are shown in Fig. 5.2 A and B respectively. Microtubules started to curl around the cell poles (T4), if the average length was only slightly longer than it was needed for centering, thereby leaving only a small region in parameter space where centering succeeded but microtubules did not curl (indicated by the yellow area in Fig. 5.1). On the dotted line in Fig. 5.1 $\langle L_H \rangle = 3.06 \mu m$ according to equation 5.1[4]. An example for a simulation with curling microtubules is shown in Fig. 5.2C.

The few remaining simulations within the yellow area satisfied T2-T4, but because the average half-bundle length was relatively short (between 2.8 and $3.06 \mu m$), only about 10% of the growing tips of microtubule bundles reached the cell poles, in contrast to more than 90% *in vivo*. Consequently, most catastrophes occurred in the cytoplasm, and simulations failed T5 as well as T6, which states that 95% of all bundle catastrophes occur at the cortex. In living cells, these two characteristics are important for the deposition of marker proteins at the poles. If the bundles do not reach the poles, regulatory factors transported along microtubules are not sufficiently enriched, which can lead to abnormal cell morphologies. This situation occurs for example in mutants of the microtubule associated proteins Tip1 and Mal3, resulting in an increased number of branched and bent cells (see Sec. 1.3.2.3).

The variance of the nucleus position was usually low enough to fulfill T3 due to the high viscosity of the cytoplasm. However, some simulations with curling microtubules failed T3 because such microtubules were not able to counteract pushing forces from the opposite pole which rendered the position of the nucleus mechanically unstable (illustrated by the trajectory of the nucleus in Fig. 5.2C). Such a situation occurred for example in the simulations in the lower left corner in Fig. 5.3 (plot of T3), at low catastrophe rates and relatively slow growth. For faster growth rates, microtubules pro-

---

[1] λ is the inverse of the average length of single microtubules (see Sec. 4.1.1). Since rescues are ignored, $\lambda = c/v_g$.

[2] This value includes $0.5 \mu m$ from the initial microtubule length. Microtubules in the simulation do not shrink beyond the width of the antiparallel overlap, but switch to growth when they become shorter than $1 \mu m$ (see simulation setup 2.1). Assuming the nucleus and the bundle overlap are at the center of the cell, $0.5 \mu m$ are added to the dynamic length of each half-bundle calculated from λ.

[3] On the solid line in Fig. 5.1 $\lambda = 0.66 \mu m^{-1}$. Since all microtubules grow and shrink independently, one might also ask for the average length of all microtubules on one side of the nucleus. The simulation contains four bundles with two microtubules per half-bundle, which results in a number of eight microtubules on each side of the nucleus. Because microtubule dynamics are uncorrelated, one can practically treat these eight microtubules as one half-bundle with $N = 8$. From equation (4.9) we get $\langle L_H \rangle_{N=8} = \frac{761}{280 \lambda}$. On the solid line in Fig. 5.1 the microtubules on one side of the nucleus therefore have an average length of $\langle L_H \rangle_{N=8} \approx 4.64 \mu m$ including $0.5 \mu m$ from the initial length (see also footnote 2).

[4] On the dotted line in Fig. 5.1 $\lambda = 0.59 \mu m^{-1}$. The average length of all microtubules on one side of the nucleus is therefore $\langle L_H \rangle_{N=8} = 5.14 \mu m$ (see also footnote 3).

duced a meshwork that effectively caused the nucleus to get stuck in one place, which again reduced the variance.
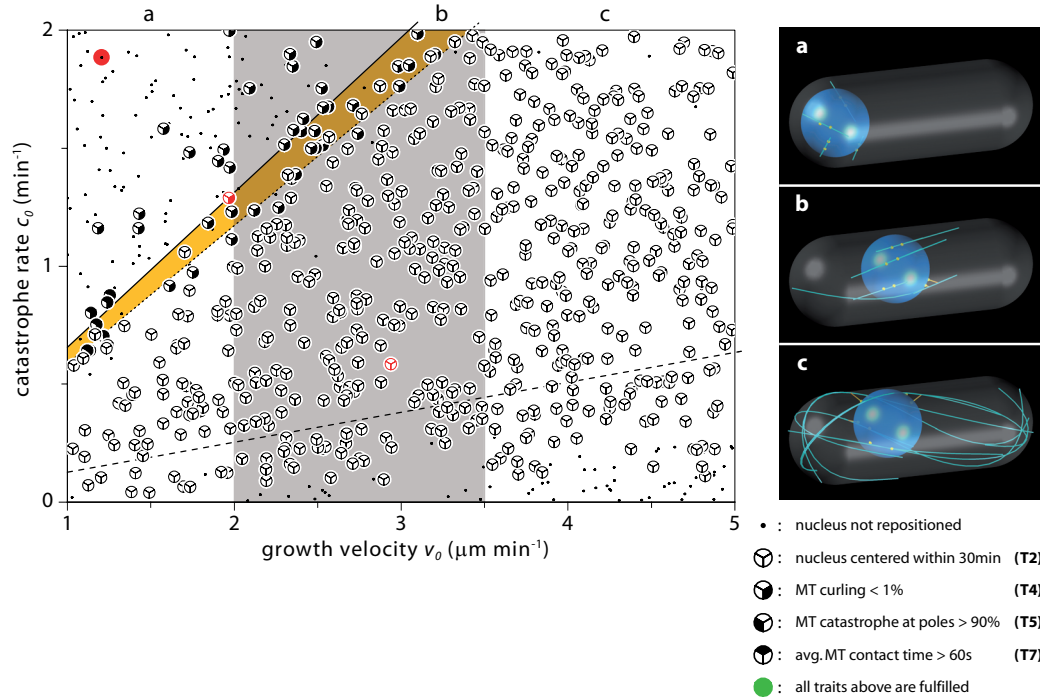

Figure 5.1: **Variation of v_0 and c_0 for independent microtubule dynamics.** Each symbol depicts the outcome of one simulation, indicating which features of wild type cells were fulfilled. Pie charts are shown if the nucleus could be repositioned to the center of the cell within 30min (trait T2), a dot ($\cdot$) is drawn otherwise. Pie-sections denote the occurrence of curling microtubules (T4, right section), the localization of catastrophes at the cell poles (T5, left section) and the average contact time of microtubules with the cell poles (T7, upper section). Pie-sections are filled if the simulation complied with the corresponding trait. Further characteristics are considered to evaluate the models, but are not represented on the graph for clarity (see Fig. 5.3). The solid line separates regions of centering and non-centering simulations. The dotted line separates curling and non-curling simulations (T4). The dashed line depicts the boundary where more than 90% of microtubule half-bundles undergo catastrophe at the cell poles (see Sec. 4.1.3). The graph exhibits a thin region between the solid and dotted lines (marked in yellow) where microtubules were long enough to reposition the nucleus (T2), but short enough to avoid curling (T4). However, in this region only a small fraction of catastrophes occurred at the cell poles, thus failing T5. Images (a-c) show examples from simulations that failed T2 (a), complied with T2 but failed T5 (b) or had curling microtubules (c). Red symbols mark the simulations shown in Fig. 5.2

According to T7, microtubules *in vivo* contact the poles for about $66s$ on average. With independent dynamics this failed for almost all simulations over the whole range of v_0 and c_0, because microtubules either contacted the poles only briefly or started to curl. The requirement not to exhibit curling microtubules finally caused the last two traits to fail. In simulations without curling, less than one half-bundle touched the poles on average which was not sufficient to fulfill T8. Furthermore, in a situation where only the longest microtubules reached the poles, the average length of full bundles was inevitably low and failed to satisfy T9. As predicted by equation (4.12), $\langle L_F \rangle \approx 5.8\mu m$ for simulations between the solid and the dotted line (including the initial length of $1\mu m$). On the other hand, simulations below the dashed line in Fig. 5.1, which denotes the boundary where microtubules

become long enough to fulfill T5, exhibited an average bundle length of more than $30\mu m$. These simulations therefore also failed T9 because the bundles became on average longer than the whole cell. The intermediate region where $\langle L_F \rangle$ met T9 did not comply with the other traits (see T9 in Fig. 5.3). Interestingly, the simulations below the dashed line also failed to fulfill T5, despite the fact that the half-bundles were long enough. The reason is that most of them grew around the poles and underwent catastrophe in the cytoplasm thus failing T5. The detailed results for traits T2-T9 are shown in Fig. 5.3.
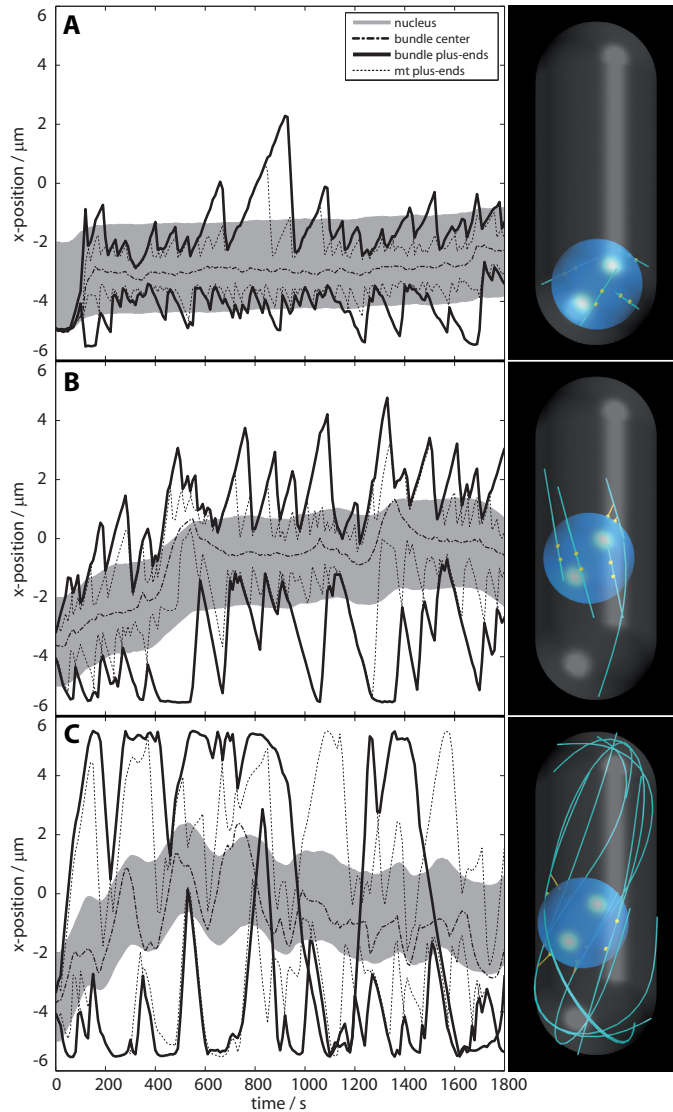
Figure 5.2: Trajectories of the nucleus and of microtubule plus ends and bundles for simulations with independent dynamics. The gray shaded area represents the nucleus. Out of the four microtubule bundles per simulation only one is included in the figure for clarity. The position of the bundle center, i.e. the middle of the overlap region, is depicted by the dashed line. Microtubule plus ends are shown as dotted lines. The longest microtubule in each half-bundle, i.e. the bundle tip, is drawn as a thick solid line. The trajectories shown here correspond to the simulations with red symbols in Fig. 5.1. (A) A simulation that did not center the nucleus and thus failed T2 with $v_0 = 1.2\mu m/min$, $c_0 = 1.9/min$, avg. half-bundle length $\langle L_H \rangle = 1.45\mu m$. Since the half-bundles were too short to effectively push at the poles, the movements of the nucleus and of the bundles were mainly caused by Brownian motion. Microtubules switched rapidly between growth and shrinkage due to the high catastrophe rate. (B) Simulation with an intermediate half-bundle length of $\langle L_H \rangle = 2.80\mu m$ at $v_0 = 2.02\mu m/min$ and $c_0 = 1.32/min$. Microtubules became long enough to center the nucleus (T2) but did not yet curl (T4) and thus fulfilled T1-T4. However, only few bundles reached the cell poles and simulations failed T5-T9. (C) At $v_0 = 2.94\mu m/min$ and $c_0 = 0.59/min$ the average half-bundle length was $\langle L_H \rangle = 7.97\mu m$, which caused microtubules to curl around the poles, failing T4. Microtubules grew around the poles and traversed the whole cell in the opposite direction. When they contacted the cell poles, microtubules exerted high forces on the nucleus. However, curling microtubules did not push on the nucleus and could not balance pushing forces from microtubules touching the opposite pole. The nucleus therefore wobbles as shown by the gray shaded area in Fig. 5.2C.
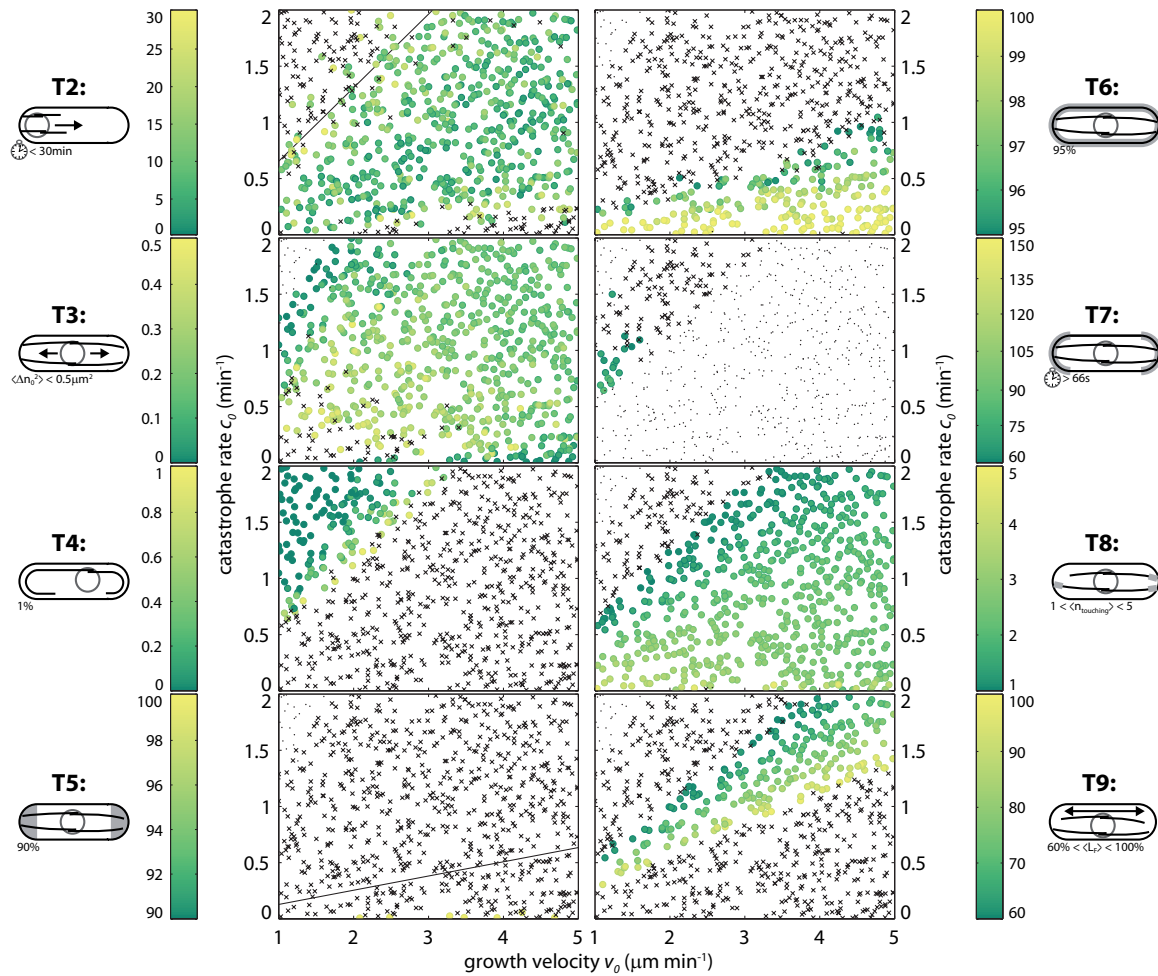
Figure 5.3: Evaluation of the traits T2-T9 for independent microtubule dynamics. Circles depict simulations that fulfilled the corresponding trait while crosses mark the ones that failed. In some cases, traits T3 and T5 - T9 could not be evaluated, since the measurement of these traits only includes values after the nucleus reached the cell center. If microtubules were not able to push the nucleus to the center within simulation time, T3 and T5 - T9 were marked by dots. Furthermore, microtubule contact times (T7) could not be determined for microtubules curling around the cell poles.

### 5.1.2 Results Model 2: Limited Tubulin Concentration

We extended our model with independent microtubule dynamics by introducing a maximum for the total length of all microtubules, Σ_{MT}^0, in the simulation (see Sec. 4.2). The microtubule growth velocity, v_g, was reduced linearly with the fraction of microtubule length that was already polymerized, Σ_{MT}, while the catastrophe rate remained unaffected (see Sec. 2.2.7). Three parameters therefore control microtubule dynamics in this model: the maximum growth velocity, v_0, the catastrophe rate, c_0, and the tubulin concentration given as the equivalent polymer length Σ_{MT}^0 (see Tab. 4.1).
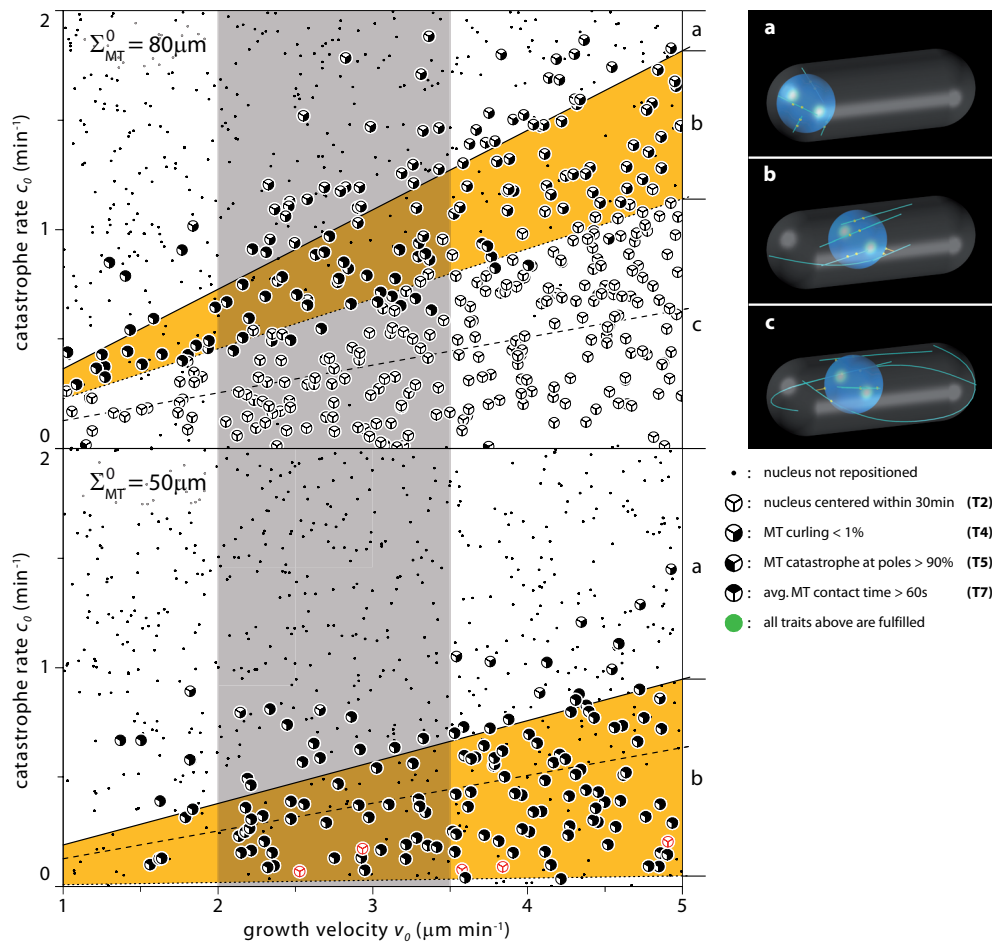
Figure 5.4: Variation of v_0 and c_0 for the model with limited tubulin concentration. The meaning of symbols and lines is explained in the text and in the caption of Fig. 5.1. Simulations in the upper graph were run with a tubulin concentration of $\Sigma_{MT}^0 = 80\mu m$ and in the lower graph with $\Sigma_{MT}^0 = 50\mu m$. The yellow area between the solid and the dotted lines represents the region where T1-T4 are fulfilled. In both cases this region is larger than for the model with independent microtubule dynamics and it is shifted further down towards the dashed line below which simulations can potentially fulfill T5. However, at $80\mu m$ of tubulin microtubules still curl below this line, whereas $50\mu m$ of tubulin are not sufficient anymore for 90% of all half-bundles to reach the poles. At both tubulin concentrations simulations therefore fail to satisfy T5, either because they curl or because they are not able to reach the poles, both of which causes microtubules to catastrophe in the cytoplasm. The red symbols highlight simulations that failed T4 even at $50\mu m$ of tubulin. Images (a-c) show examples from the indicated regions.

Again, we could not identify a region in the three dimensional parameter space where all traits were

fulfilled simultaneously. As for the independent model, simulations could satisfy T1-T4 but failed
to reproduce the correct localization of catastrophes (T5 & T6). Limiting the maximum length of
microtubules in the simulation introduced correlations between the length of different microtubules.
Yet, this did not cause catastrophes to occur at the cell poles, since this would require correlations
between the positions of microtubule plus ends and microtubule dynamics.
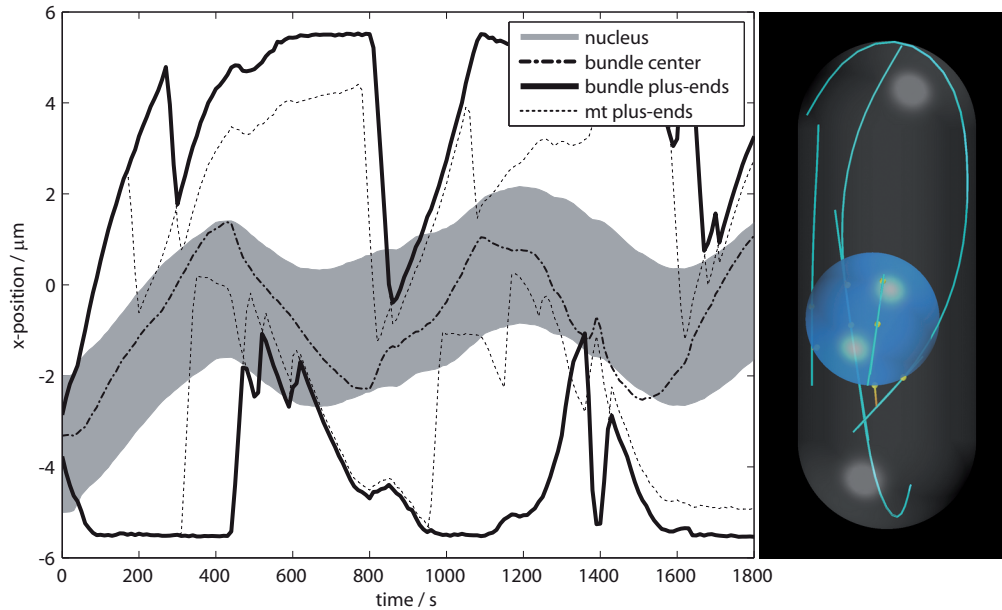
Figure 5.5: Trajectories from a simulation with limited tubulin concentration. The simulation
shown was run with the reference set of parameters (see Tab. A.1) and $\Sigma_{MT}^0 = 80 \mu m$. The slope
of the thick black lines can be interpreted as the growth velocity of the bundle tips. In contrast to the
model with independent dynamics, microtubule growth slows down if less tubulin is available, leading
to slightly curved trajectories. At ~ 1300 seconds the lower half-bundle curls around the cell pole.

However, to thoroughly test the model we first investigated in which region in parameter space the
tubulin concentration becomes relevant. While v_0 and c_0 were varied within the same ranges as for
the other models (see Sec. 5.1), Σ_{MT}^0 was varied between 30 and $300 \mu m$[5]. As expected, the influence
of the tubulin concentration on the nine traits was small for values above $160 \mu m$. In this range the
16 microtubules in the simulation were able to reach a length of $10 \mu m$ each. If the nucleus is at the
cell center, microtubules reach the cell poles already at a length of $\sim 5 \mu m$ and subsequently start
curling. We therefore needed to reduce the tubulin concentration such that curling at the cell poles
could be avoided. However, at tubulin levels around $\Sigma_{MT}^0 = 50 \mu m$ only few microtubules became
long enough to reach the cell poles and simulations therefore failed to satisfy T5 for the whole range
of growth velocities and catastrophe rates (see Fig. 5.4 lower graph). Consequently, we chose an
intermediate concentration of $80 \mu m$ which allowed microtubules to push the nucleus to the center,
but still reduced curling at the cell poles.

Using $\Sigma_{MT}^0 = 80 \mu m$ we performed a two dimensional parameter screen for v_0 and c_0 similar
to model 1. The curling of microtubules at the cell poles was indeed reduced, which increased the

---

[5]Values below $\Sigma_{MT}^0 = 30 \mu m$ are not relevant, since the 16 microtubules in the simulation cannot become long enough
to fulfill T5. For values above $300 \mu m$ microtubules could reach a length of $20 \mu m$ each, which would violate T4.

region between the solid and the dotted line (Fig. 5.4) where T1-T4 were fulfilled. At the same time this region was shifted towards lower catastrophe rates and higher growth velocities, since less microtubules became long enough to reposition the nucleus. Nevertheless, just like in the independent model the simulations in this region failed to satisfy the remaining traits, in particular the location of catastrophes (T5 and T6). T5 could not be fulfilled, since the region in parameter space was still above the dashed line, which indicates where more than 90% of all half-bundles can potentially reach the cell poles. Obviously the amount of tubulin was still too high to shift the region further down, below this line. However, reducing Σ_{MT}^0 even more resulted in simulations where only few microtubules could become long enough to fulfill T5 because of the limitation of available tubulin. Such simulations therefore failed T5 even below the dashed line (Fig. 5.4 lower graph). On the other hand, since catastrophes are random events, this did not stop some microtubules from curling in situations where the remaining microtubules were short and enough tubulin was available for polymerization. Even at $\Sigma_{MT}^0 = 50\mu m$ where T5 could not be met, some simulations therefore failed to satisfy T4 (red symbols in Fig. 5.4 lower graph). T5 and T6 failed for any value of v_0 and c_0 (see Fig. B.1 in appendix B), because microtubules either curled around the poles or they were not able to reach them, both leading to a high number of catastrophes occurring in the cytoplasm.

Typical trajectories for the nucleus and microtubule bundles with a finite amount of tubulin are shown in Fig. 5.5. The trace of the nucleus displays strong fluctuations about the equilibrium position at the cell center. Indeed, this simulation failed to fulfill T3 (see also T3 in Fig. B.1). The reason was that long microtubules pushing at one cell pole inhibited the elongation of the remaining ones, because of the correlations that are introduced between the length of different microtubules. Microtubules on one side of the nucleus therefore could not counteract the pushing forces from the opposite side, if the available amount of tubulin was already used up. The slow down of microtubule growth due to the lack of tubulin becomes apparent in the slopes of microtubule plus ends in Fig. 5.5, for example for the shorter microtubule of the upper half-bundle between 400 and $800s$ (dotted line).

5.1.3 Results Model 3: Localized Catastrophes

In living cells the majority of the growing tips of microtubule half-bundles reaches the cell poles (T5), yet they are never seen to curl (T4) because they stall and eventually undergo catastrophe. The results of the previous two models indicated that such a behavior cannot be achieved by global regulation of microtubule dynamics. In model 3 we therefore introduced an increased catastrophe rate for microtubules that touch the cortex at the cell poles as suggested from experiments with *tip1Δ* cells (see Sec. 4.3). The parameters that control the size and the activity of this catastrophe promoting region are the distance from the cell center along the x-axis, d_{cap}, and the local catastrophe rate, c_{poles} (see Fig. 4.4 and Tab. 4.1).

The local catastrophe rate and the size of the area were varied to find a range where centering succeeded without curling (T2-T4), and at the same time more than 90% of all half-bundle catastrophes occured at the cell poles (T5). From the four dimensional parameter screen we could narrow down the range of c_{poles} to $0.05 - 0.1s^{-1}$ ($3 - 6min^{-1}$). Above $0.1s^{-1}$ microtubules failed to center the nucleus (failing T2), whereas they started to curl below $0.05s^{-1}$ (failing T4). Surprisingly, there was only a small effect of the size of the area defined by d_{cap} on the ability to center the nucleus. Instead d_{cap} mainly influenced the curling of microtubules. The explanation lies in the morphology of the *S. pombe* cell and is illustrated in Fig. 5.6: growing microtubules that are attached to the nucleus usually contact the poles at the very end of the cell, but not at the sides of the poles. However, when microtubules start to curl, they do not push on the nucleus anymore but touch the sides of the poles. Consequently, the size of the catastrophe promoting region mainly affects the catastrophe rate

of microtubules that just started to curl.

The results of the two dimensional variations of v_0 and c_0 at two different values of c_{poles} and d_{cap} respectively are shown in Fig. 5.7. The best agreement with the nine traits was achieved if the catastrophe promoting activity was set to $c_{poles} \approx 0.05$ within the whole cap, i.e. for $d_{cap} = l_{cylinder}$, (Fig. 5.7D). With these settings a few simulations indeed fulfilled T1-T6. However, these simulations contacted the poles only for $\sim 25s$ on average and therefore failed T7. If the local catastrophe rate was lowered such that the contact time matched the in vivo value, the system was not able to accommodate the excess length and microtubules curled around the cell poles (T4). Furthermore, the distribution of contact times was exponential unlike the *in vivo* distribution (compare Fig. 3.4 and Fig. 3.3). Between one and two microtubule half-bundles touched the poles on average which was still enough to fulfill T8. The projected length of full microtubule bundles reached about 75% of the cell length on average which complied with T9. Detailed results of the traits T2-T9 for the simulations from Fig. 5.7D are included in appendix B, Fig. B.2[6].

A localized catastrophe promoting activity was able to fulfill all traits apart from the contact time at the poles (T7). T7 failed because the average contact time was low but also because the shape of the distribution did not match with *in vivo* measurements. Furthermore the region where the simulation complied with T1-T6 in Fig. 5.7D is rather small and intermingled with simulations that could not center the nucleus or exhibited curling microtubules. Obviously, T1-T6 were just about satisfied but the model lacked robustness with respect to variations of v_0 and c_0. The following model overcomes this problem by introducing a force dependent microtubule growth velocity.

---

[6]It might be noted that T5 is not immediately fulfilled for simulations below the dashed line. The position of this line was determined from the requirement that the integral over the microtubule length from $3\mu m$ to infinity covered more than 90% of all microtubules (see Sec. 4.1.3). In this calculation it was assumed that the distribution of microtubule length is exponential and some microtubules actually become very long. This assumption is not valid in this model, since most microtubules undergo catastrophe at the poles. Consequently, the proportion of short microtubules in the distribution is higher while long microtubules are absent, and on average the requirement for T5 is met at higher growth and lower catastrophe rates than in the other models.
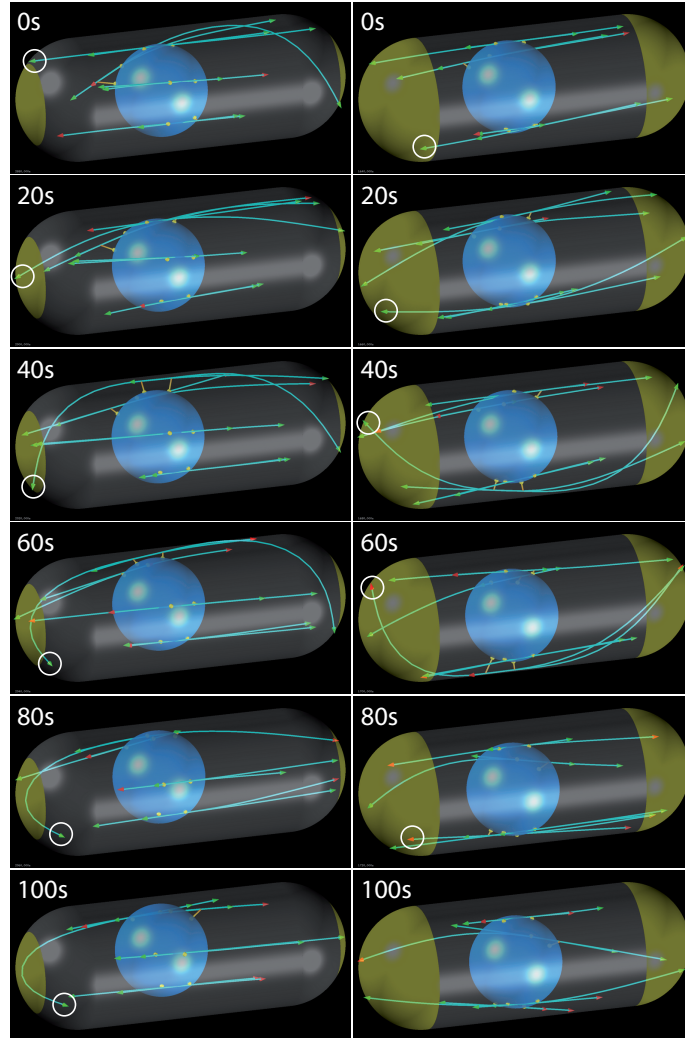
Figure 5.6: The influence of the size of the catastrophe promoting region d_{cap}. The example shows two simulations run with the reference set of parameters and $c_{poles} = 0.05s^{-1}$, while $d_{cap} = l_{cylinder} + 1.5\mu m$ on the left and $d_{cap} = l_{cylinder}$ on the right (indicated by the yellow caps). Both simulations successfully centered the nucleus (T2 & T3), but only in the simulation on the right microtubule curling is avoided (T4). To illustrate the difference between the two simulations, one microtubule is highlighted in each timecourse with a white circle. Growing microtubule plus ends are marked by a green arrow, shrinking ones are marked in red. In both simulations the growing microtubule touched the cell pole very close to the end and exerted pushing forces on the nucleus ($t = 0 - 40s$). Both microtubules ceased pushing, when they started to curl around the pole, and therefore contributed equally to the motion of the nucleus. But while the microtubule on the left side escapes the catastrophe promoting region, and grows back into the cytoplasm, the other microtubule is stopped by the catastrophe promoting activity at the side of the poles. Simulations with $d_{cap} = l_{cylinder}$ consequently can center the nucleus equally well but exhibit less microtubule curling.
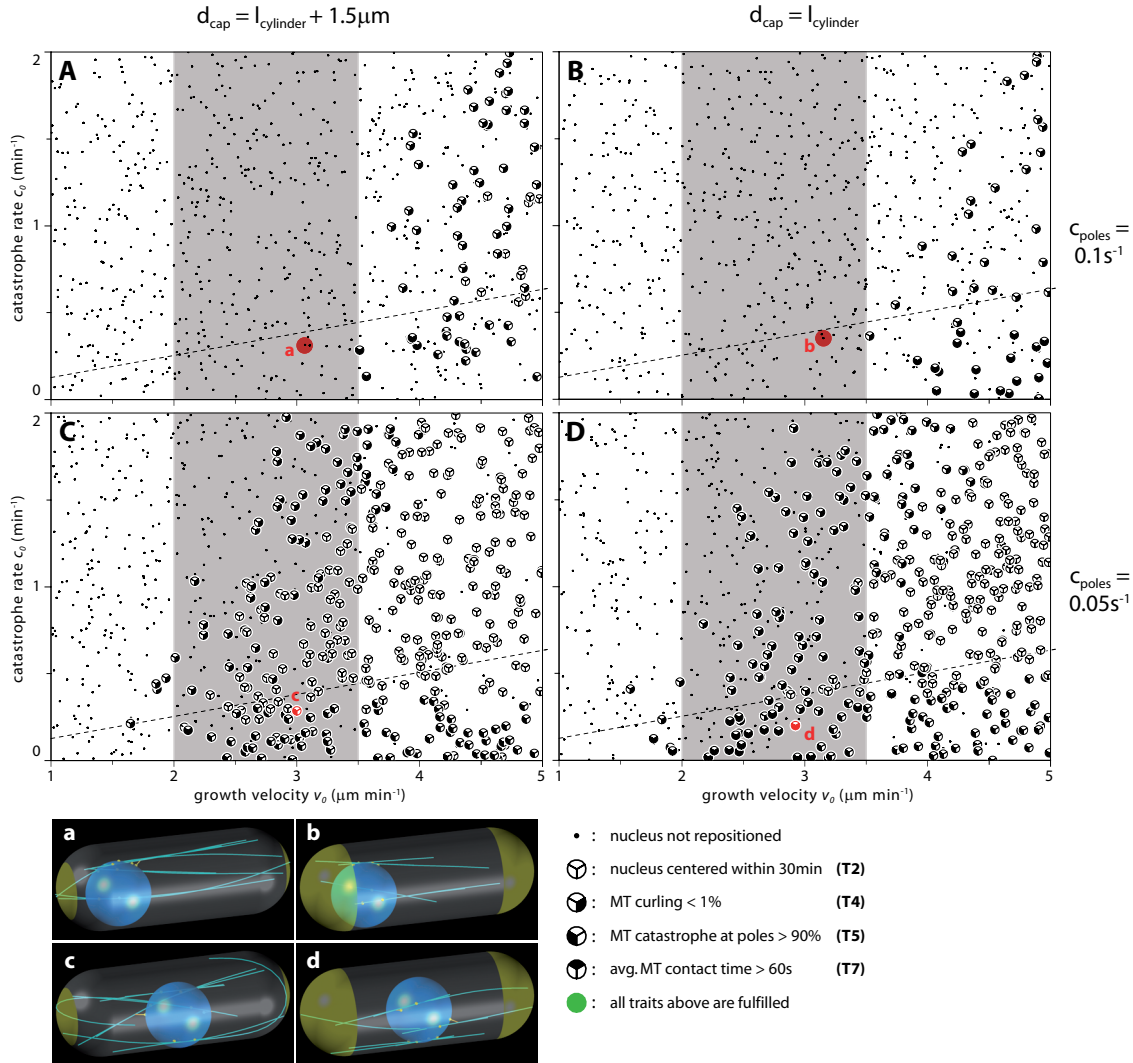
Figure 5.7: Variation of v_0 and c_0 with localized catastrophes. The meaning of symbols and lines is explained in the text and in the caption of Fig. 5.1. The four parameter screens (A-D) were preformed with a local catastrophe rate of $c_{poles} = 0.1s^{-1}$ in the upper row (A and B) and with $c_{poles} = 0.05s^{-1}$ in the lower row (C and D). The size of the catastrophe promoting region was restricted to the very end of the cell ($d_{cap} = l_{cylinder} + 1.5\mu m$) in the screens on the left side (A and C), while it covered the whole cap ($d_{cap} = l_{cylinder}$) on the right side (B and D). (A and B): Centering the nucleus (T2) did not succeed for simulations with microtubule growth velocities within the range measured *in vivo* (indicated by the gray shaded area). Increasing the size of the catastrophe promoting area (B) had little influence on centering but prevented microtubule curling for the few simulations that centered the nucleus at high growth velocities (T4). (C and D): At a lower value of c_{poles}, the nucleus could be centered successfully (T2 & T3) but microtubules curled around the poles, if the catastrophe promoting region was small (C). Some simulations fulfilled T1-T5 if the catastrophe rate was increased within the whole cap (D). However, these simulations contacted the poles only shortly and thus failed T7. (a-d): Images from simulations with v_0 and c_0 close to the reference set. The simulations were selected from the corresponding screens (A-D) and are marked in red in the plots.

5.1.4 Results Model 4: Force Dependent Growth Velocity

As described in section 4.4 microtubule polymerization *in vitro* slows down under an opposing force. In the geometry of *S. pombe* this can produce a local effect on microtubule dynamics at the cell poles without involving any localized factors. We therefore investigated if a model with force dependent growth velocity could reproduce the nine traits correctly. Force dependent growth involves only one new parameter compared to independent dynamics which is the sensitivity to force, f_s, (Tab. 4.1). We first chose $f_s = 1.67pN$ as determined from the experiments (see appendix A.9.2) and varied the free growth velocity v_0 and the catastrophe rate c in the same range as for the other models.
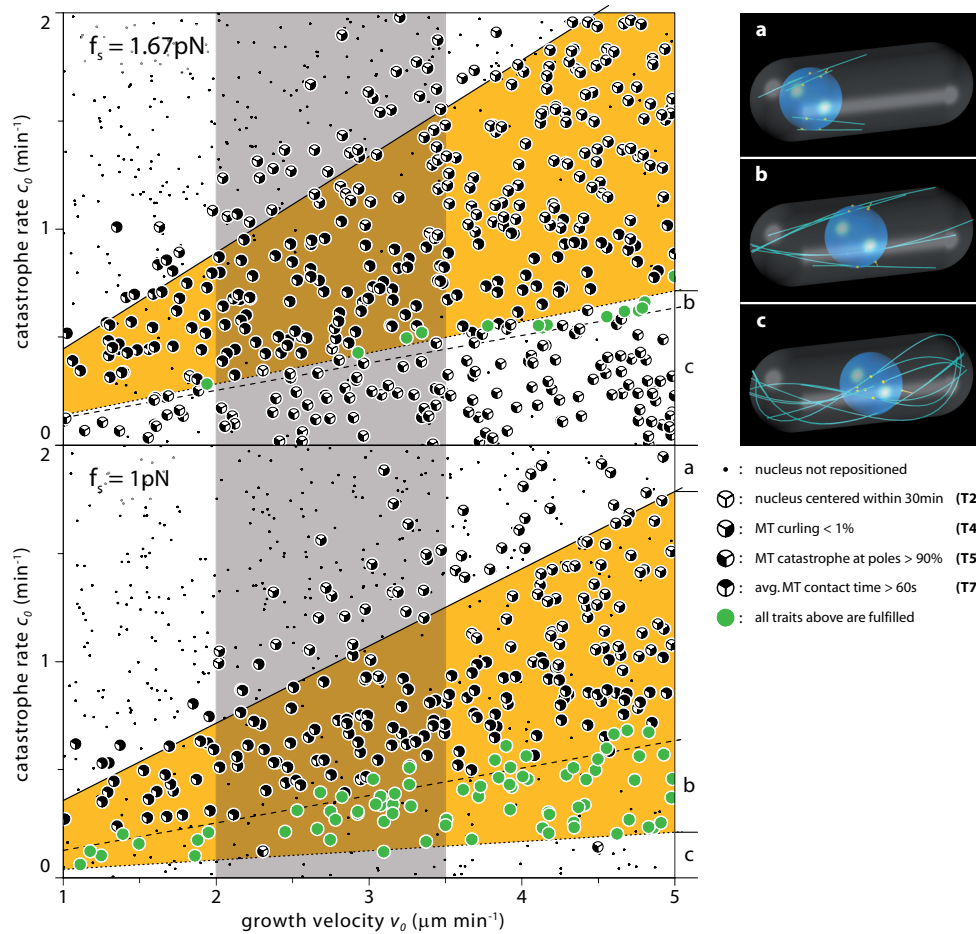
Figure 5.8: Variation of v_0 and c_0 with force dependent growth velocity. The meaning of symbols and lines is explained in the text and in the caption of Fig. 5.1. Simulations in the upper graph were run with $f_s = 1.67pN$ and in the lower graph with $f_s = 1pN$. As before, the yellow area represents the region where T1-T4 were fulfilled. With a sensitivity of 1.67pN only a few simulations additionally complied with traits T5 and T7 (green symbols in the upper graph), since the slow down of growth was not sufficient to avoid microtubule curling below the dashed line. With $f_s = 1pN$ curling was successfully prevented for a whole region of simulations that consequently fulfilled T1-T7 (green symbols in the lower graph). However, these simulations exhibited very long contact times and therefore failed T8 and T9 which were not included in this graph for clarity (see text and Fig. B.3 in appendix B). Images (a-c) show examples from the indicated regions.

For the first time we found some simulations that in addition to T1-T4 now also fulfilled T5-T7 (green symbols in Fig. 5.8A), i.e. more than 90% of all half-bundle catastrophes occurred at the cell poles, and microtubule bundles contacted the poles for more than $60s$ on average. However, only few simulations satisfied T1-T7 close to the dotted line that indicates where more than 90% of the half-bundles become long enough to reach the poles. Above that line, simulations failed to comply with T5, and below the line the slowdown of microtubule polymerization was not sufficient to prevent curling (T4). We therefore lowered the value of f_s to $1pN$ to make the microtubules slightly more sensitive to force and repeated the variation of v_0 and c_0. The results are shown in Fig. 5.8B. Indeed we found more simulations that fulfilled T1-T7 without curling. Yet, several aspects of these solutions were unsatisfying: Microtubules contacted the poles long enough to comply with T7 but in fact, the average contact time was about $200s$ which is far higher than the value measured *in vivo*. The reason was that microtubule growth was slowed down at the poles and probably almost stalled, whereas the catastrophe rate remained unchanged. This allowed microtubules to stay in contact with the poles for a long time, which is illustrated by the trajectories in Fig. 5.9.
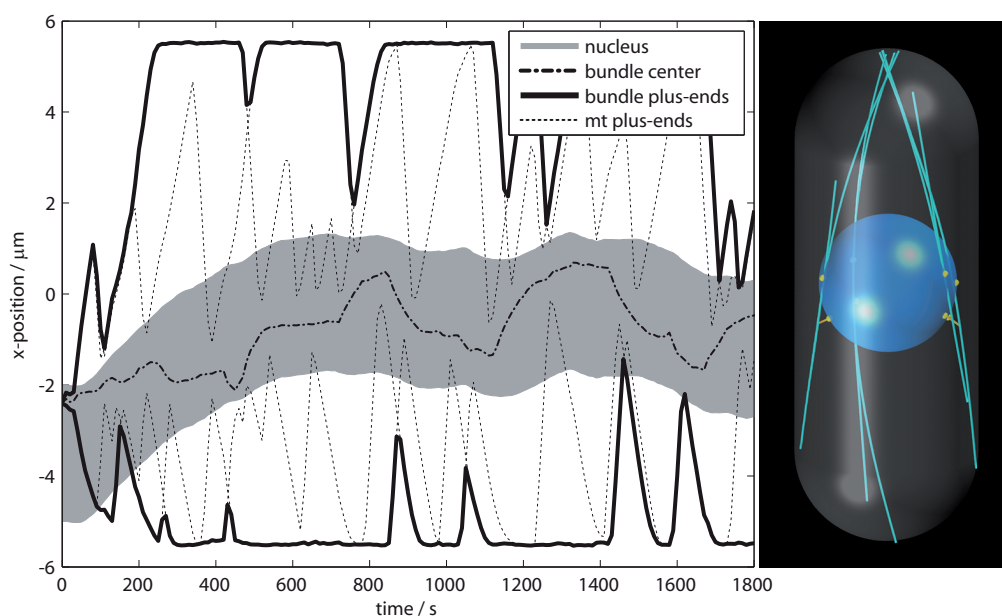
Figure 5.9: Trajectories from a simulation with force dependent growth velocity. The simulation shown was run with the reference set of parameters apart from the sensitivity to force which was set to $f_s = 1pN$ (see Tab. A.1). Microtubule plus ends contacted the poles much longer than it is observed *in vivo* which is illustrated by the dotted lines. For example, in the lower half-bundle a single microtubule touched the pole for about 6 minutes between the times 400 and $800s$. Yet, microtubules did not curl around the poles. But the trajectories of the bundle tips (thick black lines) indicate that too many microtubules contacted the poles on average (T8), and that the average bundle length was close to the cell length, i.e. about $10.9\mu m$ in this simulation. See also Fig. 5.11 for comparison with force dependent catastrophes.

As a consequence of the long contact time, most of the simulations that are marked with green symbols in Fig. 5.8B actually failed to fulfill T8 and T9, because too many half-bundles touched the poles on average, and the mean total length of microtubule bundles exceeded the length of the cell (see Fig. B.3 in appendix B for detailed results for traits T2-T9). Force dependent growth velocity

can therefore stop microtubule curling at the poles and it can at the same time satisfy T5 and T6. But instead of having a contact time which is too low, as in the model with localized catastrophes, simulations with force dependent growth suffer from very long contact times that cause T8 and T9 to fail. To render the organization of microtubules less static we added force dependent catastrophes, described in the next section.

5.1.5 Results Model 5: Force Dependent Microtubule Dynamics

The previous model with a force dependent microtubule polymerization rate complied with traits T1-T6 but suffered from a long average microtubule contact time at the poles. To overcome this problem we additionally implemented the *in vitro* result that the catastrophe rate increases for slow growing microtubules as described in section 4.5. One more parameter is needed to determine the current catastrophe rate, c, which is the catastrophe rate, $c_{stalled}$, for microtubules at zero growth (see Tab. 4.1). We set f_s and $c_{stalled}$ to the values determined from the *in vitro* measurements, i.e. $f_s = 1.67pN$ and $c_{stalled} = 0.05s^{-1}$ and varied v_0 and c_0 in the same range as for the other models.
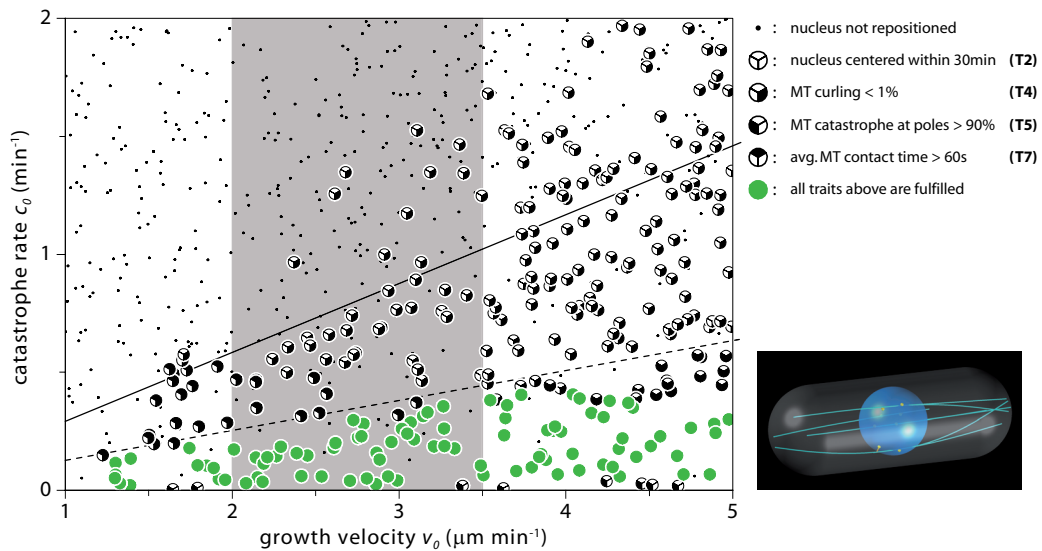
Figure 5.10: Variation of v_0 and c_0 with force dependent microtubule growth and catastrophes. The meaning of symbols and lines is explained in the text and in the caption of Fig. 5.1. Most simulations below the dashed line fulfilled T2-T5 and T7, indicated by the green symbols. These simulations also satisfied the remaining traits as illustrated in Fig. B.4 in appendix B. A whole region of working simulations can be found within the gray shaded area which defines the range of measured growth velocities *in vivo*. The image is taken from a simulation that fulfilled all traits, run with the reference set of parameters (Tab. A.1).

With force dependent microtubule dynamics we indeed found a range of simulations that fulfilled all traits (green symbols in Fig. 5.10). Importantly, this was achieved without having to change the force related parameters f_s and $c_{stalled}$ from the measured values. Moreover, a subset of these solutions covered the region corresponding to the microtubule growth speed measured under standard laboratory conditions (Fig. 5.10, shaded region). The increase of the catastrophe rate due to force lowered the contact time at the poles such that microtubules became more dynamic and the average number of half-bundles touching the poles satisfied T8. Furthermore the mean total length of mi-

crotubule bundles was about 80% of the cell length and therefore fulfilled T9. The fully compliant simulations not only matched the average microtubule contact time (T7), but were also conform with the experimentally determined distribution of contact times (see solid line in Fig. 3.3 and the examples in Fig. 3.4). The detailed results for traits T2-T9 are illustrated in appendix B, Fig. B.4.

Fig. 5.11 shows the trajectories of the nucleus and of a microtubule bundle for a simulation run with the reference set of parameters. The nucleus reached the cell center after $\sim 800s$ and then fluctuated only little about the equilibrium position (T2 & T3). As illustrated by the dotted lines, microtubule plus ends contacted the poles for about $75s$ on average. After reaching the poles, microtubules continued to grow only little and soon experienced a catastrophe due to the increased catastrophe rate for slow growing microtubules.
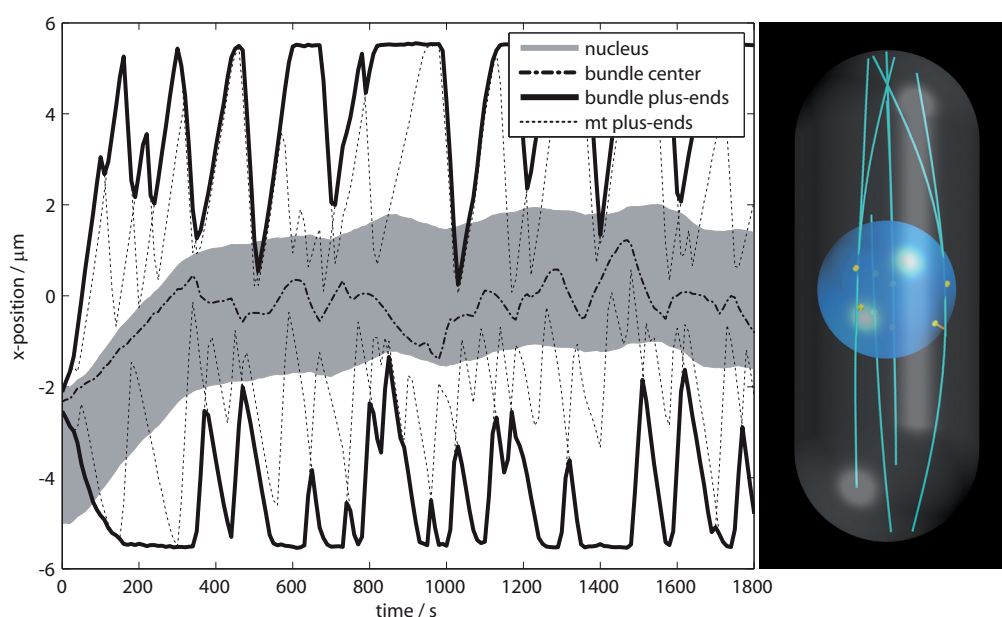
Figure 5.11: Trajectories from a simulation with force dependent growth and catastrophe rates. The simulation was run with the reference set of parameters (see Tab. A.1) and satisfied the nine traits measured in living cells. As indicated by the gray shaded area, the nucleus could successfully be centered (T2 & T3). The dotted lines illustrate that most microtubules reached the cell poles (T5) and that the average contact time of the plus ends with the cell poles satisfied T7.

Overall, we found that simulations with force dependent microtubule dynamics could match the *in vivo* situation without any localized factors. Forces generated by the spatial confinement of the *S. pombe* cortex reduced the growth velocity of microtubules at the cell poles and locally increased the catastrophe rate such that T1-T9 could be fulfilled. To further characterize the force dependent model, we systematically varied all parameters and monitored their influence on the nine traits (see appendix A).

Since our simulations indicated that the cylindrical morphology of fission yeast is sufficient for the proper organization of microtubule bundles, we investigated how cell shape influences the organization of microtubules *in vivo* using mutant cells that cannot maintain a cylindrical cell shape.

5.2 The Relevance of Cell Shape and Force *In Vivo*

In *S. pombe*, forces are generated specifically at the poles due to the cylindrical morphology of the cell. Our simulations suggested that the resulting influence of force on microtubule dynamics, which was demonstrated *in vitro*, is sufficient for proper microtubule organization in living fission yeast cells. This indicated that cell shape is a major determinant of microtubule organization, without the need for localized regulatory factors. To test this possibility *in vivo* we analyzed the behavior of microtubules in cells carrying a temperature sensitive mutation in *pmo25*, a gene required for polarized growth.

5.2.1 Mutants in Pmo25 are Defective in Polarized Growth

Pmo25 is a member of the conserved MO25 protein family which is involved in the regulation of cell polarity (Boudeau et al., 2003; Nelson et al., 2003). In human, MO25 is thought to function as a scaffolding component of the LKB1-STRAD complex and therefore to play a crucial role in the regulation of LKB1 activity and localization (Milburn et al., 2004). LKB1 is a protein kinase that acts as a tumor suppressor and was furthermore shown to be important in the regulation of cell polarity in human (Baas et al., 2004) as well as in flies and nematodes (Martin and Johnston, 2003; Watts et al., 2000). The budding yeast homolog of Pmo25, Hym1, is required for apical bud growth and cell separation (Nelson et al., 2003).

Pmo25 in fission yeast is an essential protein that is involved in polarized growth in interphase and in the separation of daughter cells at cytokinesis (Mendoza et al., 2005). Its sequence is 51% identical to human MO25. The viability of *pmo25Δ* cells was tested using a strain that is heterozygous for the deletion of *pmo25*. Four spores were created from *pmo25+/pmo25Δ* diploid cells but only two of them formed viable colonies. The spores lacking *pmo25* gave rise to round cells that lysed after two or three division cycles (Mendoza et al., 2005). The function of Pmo25 in living cells was investigated using a temperature sensitive mutant named *pmo25-2*. At the restrictive temperature *pmo25-2* cells gradually lost their elongated shape and became oval after $2h$, then mostly spherical after $4-6h$. Furthermore *pmo25-2* cells often went through the cell cycle without finishing cytokinesis and thus exhibited several septa, indicating that Pmo25 is also involved in cell separation. Using a GFP-tagged construct of Pmo25, it was shown that the protein is uniformly distributed throughout the cytoplasm in interphase and localizes to the SPB during mitosis and to the division site at cytokinesis.

Actin patches, which normally localize at the growing poles (Sec. 1.3.2.1), became uniformly distributed over the cell cortex shortly after the temperature shift in *pmo25-2* cells. Yet, they still accumulated at the division site during cytokinesis suggesting that the recruitment of actin to the cytokinetic ring does not require Pmo25 function. Since actin is a general marker of fission yeast growth sites, the depolarization of actin patches in interphase indicates that the growth machinery of the cell is no longer localized at the cell poles, which explains the observation that cells first become oval and then spherical. To determine if Pmo25 is involved in the maintenance or in the initiation of polarized growth, a double mutant was created, containing a temperature sensitive allele of *cdc25*, termed *cdc25-22*. At the restrictive temperature *cdc25-22* cells are blocked in G2 and continue elongating, resulting in abnormally long cells. Like *cdc25-22* cells, *cdc25-22/pmo25-2* double mutants did not enter mitosis at the restrictive temperature but were additionally growing in a depolarized manner. From this it was concluded that Pmo25 has a function in maintaining polarized growth, rather than in the establishment of polarization. Furthermore Pmo25 was shown to act upstream of the proteins Orb6 and Mob2 which are also thought to be involved in the maintenance of polarized growth (Mendoza et al., 2005; Verde et al., 1998; Hou et al., 2003)

Microtubule bundles in spherical cells are no longer parallel but grow in various directions. How-
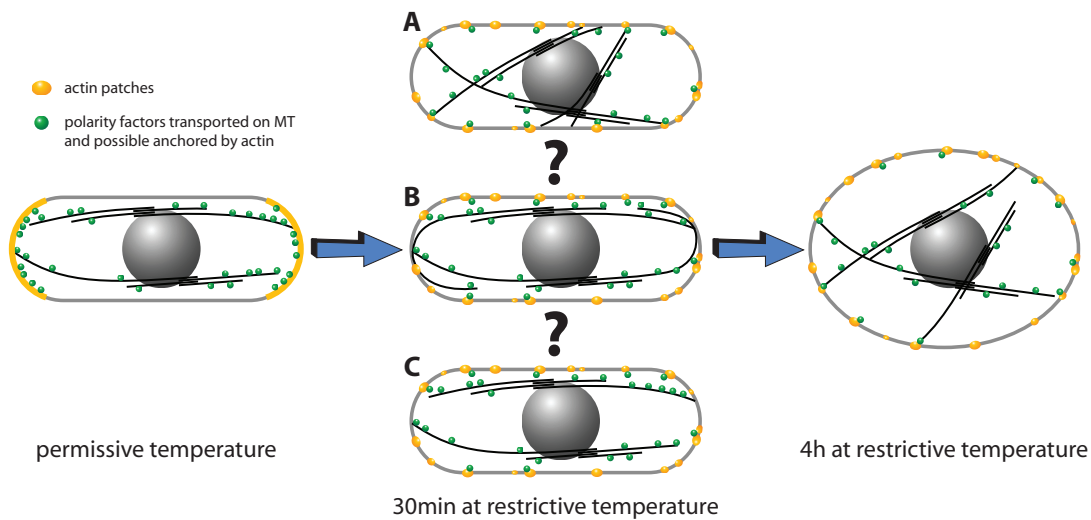
ever, the desorganization of microtubules seems to occur considerably later than the depolarization of actin patches which suggested that microtubule organization depends on cell shape rather than on the localization of polarity markers (Mendoza et al., 2005). To further elucidate the connection between the redistribution of polarity markers, cell shape and microtubule organization we followed the distribution of actin patches and microtubules in *pmo25-2* cells from the time when the cells were shifted to the restrictive temperature until they finally became round.

5.2.2 Microtubule Organization in the Pmo25 Mutant

The organization of microtubule bundles in fission yeast is part of a complicated cycle that regulates cell polarity. Other important factors are the localization of polarity markers like Tea1 and polarized cell growth, which again depends on the localization of actin patches. The most important elements of this polarity cycle are illustrated in Fig. 5.12. The green questionmarks highlight the parts of the cycle that were investigated using the *pmo25-2* temperature sensitive mutant. We first analyzed how microtubules organize in the absence of the polarized growth machinery. As described above, actin patches in *pmo25-2* cells become uniformly distributed over the cortex shortly after shifting the cells to $36°C$, indicating that the growth factors become dispersed all over the cortex. Yet, cell growth is relatively slow and cells remain cylindrical for up to two hours after the temperature shift. In this intermediary state, where cell growth is not anymore restricted to the poles but shape is still normal, we observed the microtubules in cells expressing GFP-α2tub (see methods in appendix D). Three possible scenarios shortly after the temperature shift are illustrated in Fig. 5.13: Firstly, microtubule bundles could become disorganized due to the loss of the polarized growth machinery and of other polarity factors that were possibly anchored by actin. However, this is not very likely since bundles growing at an angle should still be deflected at the cortex and thus align with the cell axis. Secondly, microtubule bundles still align to the cell axis but the catastrophe rate at the poles is not high enough, resulting in curling microtubules. Finally, microtubules stay aligned with the cell axis and do not curl, either because regulatory factors are still present at the poles or because force is sufficient to prevent curling.

We first inspected the loss of polarized growth in *pmo25-2* cells by imaging actin patches labeled with bodipy-phallacidin in fixed cells (see methods in appendix D). As in wild type, actin patches were enriched at cell poles at the permissive temperature (Fig. 5.15C). Yet, within 15 minutes after temperature shift, they became uniformly distributed over the cortex and cells became round within $\sim$4 hours. In contrast to the actin patches, microtubules remained properly organized for more than an hour and did not curl (Fig. 5.15D), which indicated that the polarization of actin patches is not needed for proper microtubule organization. However, we could not rule out the possibility that other polarity factors that affect microtubule dynamics were still present at the poles independently of actin. We therefore followed the organization of microtubule bundles until the cells became almost round. This allowed us to determine if cylindrical cell shape was required to align microtubule bundles along the cell axis or if the possible presence of polarity factors alone could be sufficient for proper microtubule organization. Polarity factors might still be localized at the former poles even in oval or almost round cells, since the cell possesses a memory which is mediated by Tea1, Tea3 and Mod5 (see Sec. 1.3.3 and Fig. 5.12).

Figure 5.12: The polarity cycle in fission yeast. Starting on the left side of the figure, microtubules deliver polarity markers like Tea1 to the cell poles, which are required for the establishment (but not for the maintenance) of polarized growth (see also Sec 1.3.3). Other polarity markers localize to the poles in dependency of Tea1 and microtubules (like for example Tip1), or potentially through other pathways. Actin is not needed for Tea1, Tea3 or Mod5 localization and its influence on other polarity markers is mainly unknown. How such polarity factors are again involved in the organization of microtubules also remains to be investigated. Tea1, Tea3 and Mod5 are found in a complex and form a cycle on their own: Mod5 is responsible for the localization at the plasma membrane, Tea1 for the localization at the poles and Tea3 for the localization at nongrowing poles. Tea1 is furthermore needed for the initiation of actin polymerization while Pmo25 and Orb6 are needed for its maintenance (and maybe initiation) (Pmo25 is thought to function upstream of Orb6). Actin patches are a standard marker of growth sites, and the delocalization of actin results in cells that grow round. The red flash indicates where the experiment interferes with the polarity cycle. Switching off Pmo25 function removes the right half of the graph (see also Fig. 5.14), which allowed us to investigate if microtubules stay organized in the absence of polarized actin patches and polarity factors that depend on actin. Furthermore, the analysis of round cells revealed if cylindrical cell shape is required for proper microtubule organization (green questionmarks). References: [1] Mata and Nurse (1997), [2] Browning et al. (2000), [3] Behrens and Nurse (2002), [4] Snaith et al. (2005), [5] Snaith and Sawin (2003), [6] Sawin and Snaith (2004), [7] Niccoli et al. (2003), [8] Brunner and Nurse (2000), [9] Busch et al. (2004), [10] Martin et al. (2005), [11] Verde et al. (1998), [12] Mendoza et al. (2005)
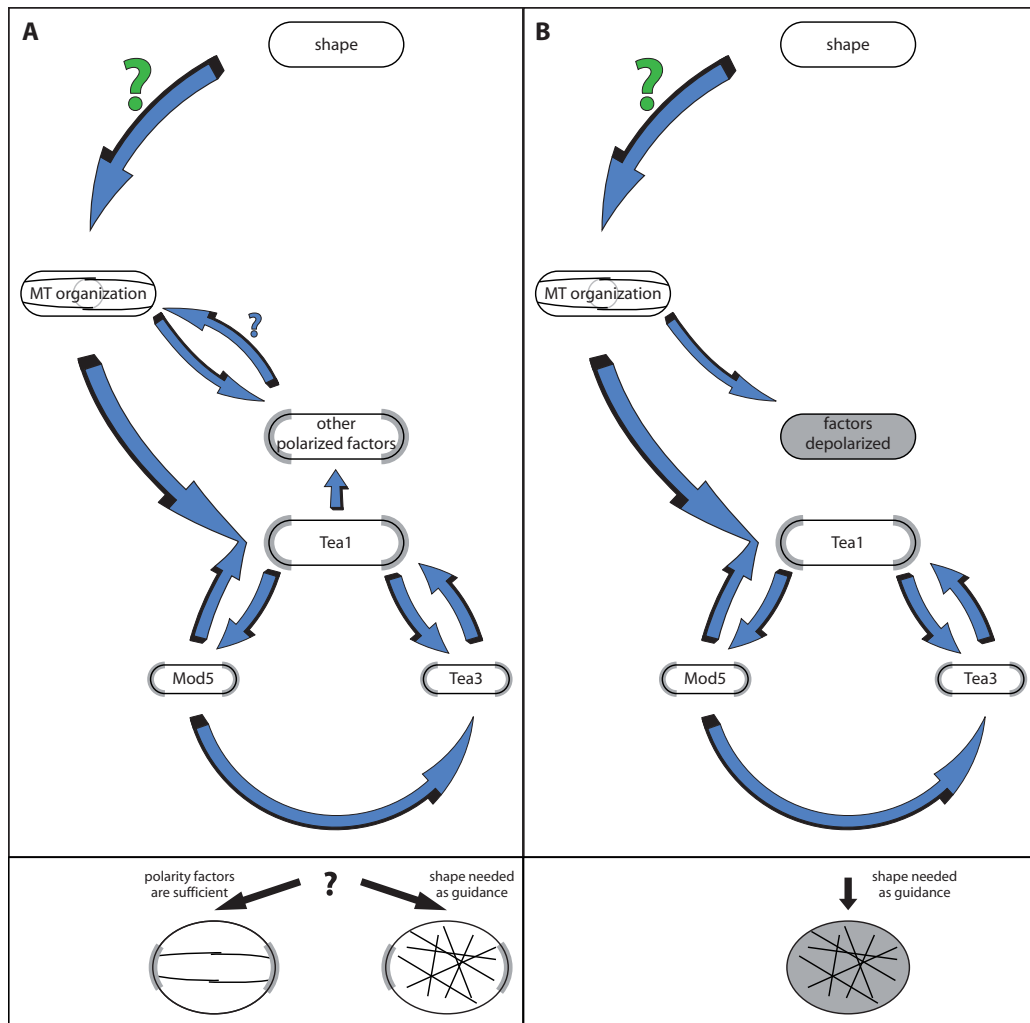
Figure 5.13: Organization of microtubules in cells with depolarized growth machinery. Actin patches are shown in yellow, polarity factors transported along microtubules in green. At the permissive temperature (left side) microtubule bundles align with the cell axis, whereas they are disorganized in cells that grew round after four hours at the restrictive temperature (right side). The *pmo25-2* mutant allowed us to investigate the organization of microtubule bundles in the intermediate state where cell shape is still normal but actin patches are already depolarized. Three possible scenarios are shown in this figure. (A) Microtubule bundles become disorganized as soon as the actin becomes depolarized. (B) Microtubule bundles align with the cell axis but curl at the poles. (C) Bundles stay organized due to cell shape or because of polarity factors that possibly remained at the cell poles independently of actin (see also Fig. 5.14).

We found that the number of cylindrical cells gradually decreased as the cells were growing at the restrictive temperature. The more spherical a cell appeared, the more its microtubule bundles were disorganized. Yet, even when cells started to adopt an ellipsoidal shape microtubule bundles were still properly aligned with the long cell axis. An example is shown at one hour after temperature shift: although the actin was completely depolarized and some cells appeared slightly ellipsoidal (Fig. 5.15C, 1*h*) microtubule bundles remained aligned with the cell axis and did not curl (Fig. 5.15D, 1*h*). Only after two hours microtubule bundles started to become misaligned (Fig. 5.15D, 2*h*) and finally were completely disorganized when the cells were almost round (Fig. 5.15D, 4*h*).

This suggests that cylindrical cell shape is required for the spatial organization of microtubules. Yet, we cannot exclude the possibility that polarity factors other than the actin related growth machinery are involved in regulating microtubule dynamics in cells where shape is still normal. Summarizing, we found that the cylindrical shape is required for the proper alignment of microtubule bundles in fission yeast, but we could not show that shape is also sufficient *in vivo*. However, this was indicated by our simulations with force dependent microtubule dynamics (model 5). To further address this question experimentally it will be necessary to analyze the localization of polarity factors like Tea1 in *pmo25-2* cells. Tea1 Tea3, and Mod5 were shown to localize at the poles independently of actin and Tea1 is furthermore thought to be involved in the removal of Tip1 from microtubule plus ends. Consequently, the regulation of microtubule dynamics via Tip1 might still be functioning, even in *pmo25-2* cells at the restrictive temperature. It would therefore also be interesting to investigate if Tip1 still accumulates at the cell poles. If Tea1, Tea3 and Mod5 are still at the poles, it would be useful to study double mutants of *pmo25* carrying a deletion of *tea1*, or in the ideal case to identify a temperature sensitive mutation of *tea1* that could be combined with *pmo25*. This would allow us to exclude the

influence of many known regulatory factors localizing to the cell poles in interphase.

Apart from that it will be important to analyze not only the organization but also the dynamics of microtubule bundles in *pmo25-2* cells in order to compare it to the nine traits. This might further clarify if force is sufficient to regulate microtubule dynamics in living cells. In any case the shape of *S. pombe* is an essential factor for the organization of microtubules and therefore for the establishment of cell polarity.


Figure 5.14: Interrupting the polarity cycle. After depolarization of the growth machinery, proper microtubule organization might be achieved in two ways: (A) Polarity factors are still present at the poles and regulate microtubule dynamics. When the cell becomes round after a few hours there are again two possible scenarios: Either the polarity factors are sufficient to maintain the organization of microtubule bundles along the cell axis even in spherical cells, or the bundles become disorganized, which indicates that a cylindrical cell shape is required for proper microtubule organization. (B) Polarity factors are absent from the poles and microtubules are organized by cell shape. Microtubules are disorganized when cells become round.

An interesting observation was the apparent depolarization of actin patches in wild type control cells after the shift to $36°C$ (Fig. 5.15A, $15min - 1h$). In contrast to the *pmo25-2* mutant, wild type cells managed to re-establish polarity after two hours. This indicates that the depolarization of actin

in the first place is not due to the mutation of *pmo25* but is caused by the temperature shift alone. Pmo25 might therefore be involved in the re-establishment of polarity after perturbations rather than in its maintenance, as suggested previously (Mendoza et al., 2005).
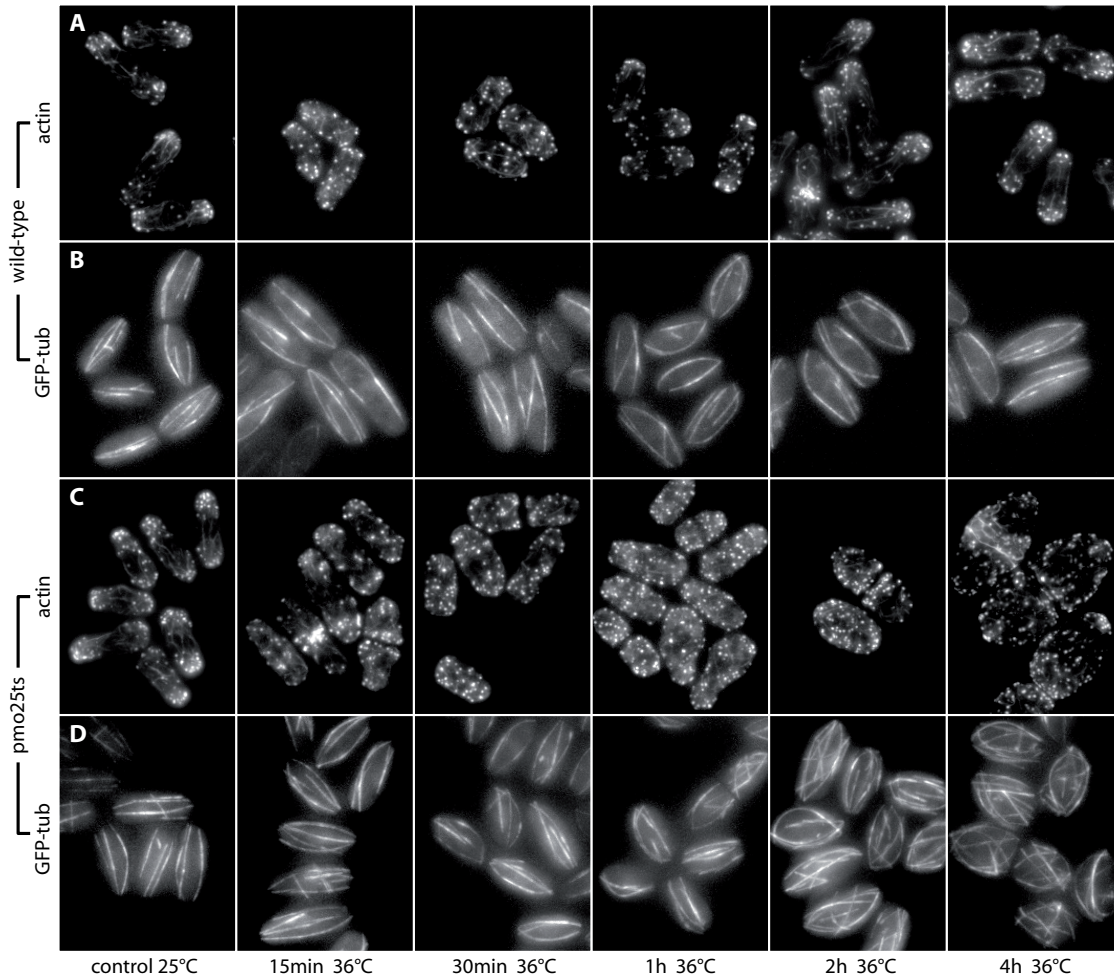
Figure 5.15: Microtubule organization and distribution of actin patches in wild type and *pmo25-2* cells. Microtubule organization was not affected by depolarization of actin patches, and degraded concurrently with cell shape. Wild type (A, B) and *pmo25-2* (C, D) cells were cultured at $25°C$ and then shifted up to the restrictive temperature at $36°C$. Cells were fixed at $25°C$ and $15min$, $30min$, $1h$, $2h$ and $4h$ after the temperature shift. Actin patches were clearly localized to the cell poles, in wild type cells (A) and in *pmo25-2* cells at $25°C$ (C). After $15-30$ minutes at $36°C$ actin patches were uniformly distributed in both cell types. The temperature shift seemed to affect polarization also in the wild type background. After $\sim 1h$ at $36°C$ wild type cells re-established actin polarization, while the mutants remained depolarized. Consequently, after $4h$ *pmo25-2* cells became round, while wild type cells were normal. (B, D) GFP-tubulin was used to image microtubules in cells cultured as described above. Microtubules in wild type cells stayed aligned with the cell axis at all timepoints even when the actin patches were temporarily delocalized. In *pmo25-2* cells, microtubules were oriented normally as long as the cells were cylindrical, even when the actin was depolarized ($15min-1h$). Microtubules were disorganized only when the cells became round after $2-4h$.

5.3 Force Dependent Microtubule Dynamics in Mutant Cells

Our model with force dependent microtubule growth and catastrophes (model 5) could successfully reproduce nine characteristics of the microtubule cytoskeleton in wild type fission yeast cells. To investigate if this model could also match the organization of microtubule bundles in mutant cells, we applied the simulation to study the phenotypes of cells carrying a deletion of the tip tracking proteins Mal3 and Tip1 from the EB1 and Clip-170 families respectively. *tip1* and *mal3* deleted cells are well characterized *in vivo* (see Sec. 1.3.2.3 and 1.2.4.5) and values for the altered dynamic parameters in the mutants are provided by the literature (Busch and Brunner, 2004; Brunner and Nurse, 2000).

The deletion of *mal3* results in a global change of the dynamic parameters (see Tab. 5.2), whereas the deletion of *tip1* results in an increased catastrophe rate only for microtubules touching the cortex in central parts of the cell, and thus locally alters the distribution of catastrophes (see Tab. 5.3). We therefore followed two different strategies to analyze these mutants with the simulation: In the case of *mal3Δ* cells we set the dynamic parameters of the simulation to the values measured in the mutant, in order to verify if we could reproduce the organization of microtubule bundles observed *in vivo* (Sec. 5.3.1). For *tip1Δ* cells, the mechanism how the distribution of catastrophes is changed compared to wild type could not be inferred from the experiments. Consequently, we first had to identify parameters of our model that could possibly reproduce the mutant phenotype. The only parameters that have a local effect on the distribution of catastrophes in model 5 are the ones that are related to force, i.e. the sensitivity to force, f_s, and the catastrophe rate of microtubules at zero growth, $c_{stalled}$. We therefore varied f_s and $c_{stalled}$ to investigate if a change of these two parameters could generate the phenotype observed in *tip1Δ* cells (Sec. 5.3.2).

We found that the phenotype of *tip1* deletion could not be reproduced with the force dependent model, which indicates that the function of Tip1 is not related to the regulation of microtubule response to force. To match the experimental data we therefore introduced an extension of model 5. This extended model suggests a novel mechanism for the regulation of microtubule dynamics by Tip1 in fission yeast.

5.3.1 Simulating the Phenotype of *Mal3* Deletion

Microtubule Dynamics in Mal3Δ Cells.
In cells lacking *mal3* microtubule growth and shrinkage rates are only slightly reduced compared to wild type, but the catastrophe rate of microtubule bundles is increased about twofold (Busch and Brunner, 2004). These additional catastrophes are not restricted to the cell cortex, but about 40% of all bundle catastrophes occur within in the cytoplasm. Furthermore, only $\sim 10\%$ of all bundles are still able to reach the cell poles and the average bundle length[7] is only about half the length of bundles in wild type cells (see Tab. 5.2). If the longest microtubule in a microtubule half-bundle experiences a catastrophe, the whole half-bundle usually shrinks back to the overlap region close to the nucleus (also called iMTOC, see Sec. 1.3.2.2) (Busch and Brunner, 2004). The overlap region remains stable and new microtubules grow out from the iMTOCs after a short pausing time[8]. Events that are equiv-

---

[7]The experimentally measured bundle length always refers to the average projected length of full microtubule bundles, since the absolute length of single microtubules or microtubule half-bundles is difficult to determine by fluorescence microscopy (see also Sec. 3.9 for a discussion of the measurement of the bundle length).

[8] It is not clear, if microtubules that shrink back to the overlap region undergo rescue or if they depolymerize completely and the apparent 'bundle rescues' are caused by different microtubules that are newly nucleated at the iMTOC. Microtubules in interphase fission yeast cells can be nucleated on the nucleus (at the iMTOCs) but also along preexisting microtubules within a bundle (see Sec. 1.3.2.2).

alent to a 'bundle rescue' are therefore largely restricted to the stable overlap zones at the iMTOCs and only rarely occur further away from the nucleus. Since the average lifetime of microtubules in *mal3Δ* cells is considerably shorter than in wild type, bundles shrink back to the overlap region more often. Consequently, the number of apparent bundle rescues is slightly increased from $0.24/min$ to $0.38/min$. This rate furthermore depends on the pausing time between the depolymerization of a bundle and the re-initiation of growth at the iMTOCs, which is about twice as long in *mal3Δ*. From these experimental results it was concluded that Mal3 is a general promoter of microtubule growth, which affects the initiation of growth, i.e the pausing times at the overlap region, as well as its maintenance, i.e. the occurrence of catastrophes. The dynamic parameters of wild type and *mal3Δ* cells are summarized in Tab. 5.2.

	wild type	***mal3Δ***
growth rate	$3.0 \pm 0.6 \mu m/min$	$2.4 \pm 1.1 \mu m/min$
shrinkage rate	$8.5 \pm 2.2 \mu m/min$	$5.6 \pm 1.8 \mu m/min$
bundle catastrophe rate	$0.33/min$	$0.81/min$
fraction of catastrophes at the cortex	more than 95%	$\sim 60\%$
fraction of catastrophes at the cell poles	more than 90%	$\sim 10\%$
average microtubule bundle length	$7.3 \mu m$	$3.6 \mu m$
rate of growth re-initiation after depolymerization back to the overlap zone (apparent bundle rescues at the iMTOC)	$0.24/min$	$0.38/min$
pausing time until re-initiation of growth after complete depolymerization back to the overlap zone	$28 \pm 19 s$	$55 \pm 48 s$

Table 5.2: Quantification of microtubule dynamics in wild type and *mal3Δ* cells. The values shown were measured using strains expressing GFP-tagged α-tubulin from a multicopy plasmid under the control of the nmt1 promoter. All dynamic values were taken from Busch and Brunner (2004) and refer to microtubule bundles rather than single microtubules.

Simulating the Mal3Δ Phenotype

To simulate the phenotype of *mal3* deletion we first adjusted the growth and shrinkage velocities, v_0 and v_s, to match the values measured in the mutant (see Tab. 5.2). We then investigated if increasing the free catastrophe rate, c_0, was sufficient to match the characteristics of the mutant, i.e. the observed distribution of catastrophes and the average microtubule bundle length. All simulations were started with the nucleus at the cell center since simulations with high catastrophe rates failed to center the nucleus within a reasonable amount of time. This is in agreement with the observation that *mal3Δ* cells indeed exhibit defects in nuclear positioning (see Sec. 1.3.2.3). According to the *in vivo* measurements, the catastrophe rate of microtubule bundles in *mal3Δ* cells is about twice as high as the rate in wild type (see Tab. 5.2). However, when we increased c_0 from the reference value $0.005/s$ to $0.01/s$ the effect on the average bundle length and on the distribution of catastrophes was smaller than in the experiment. The average bundle length was only reduced by $\sim 16\%$ compared to more

than a factor two in the mutant (Fig. 5.16C). Almost 70% of all bundle catastrophes still occurred at the cell poles and about 68% at the cortex (Fig. 5.16 A and B). Hence we further increased c_0 until the bundle length dropped by $\sim 50\%$ (from $9.1\mu m$ for 'wild type simulations' with the reference set of parameters down to $4.5\mu m$), which was achieved at $c_0 = 0.03/s$. At this value of the cytoplasmic catastrophe rate about 60% of all bundle catastrophes occurred at the cortex. Furthermore only $\sim 18\%$ of microtubule bundles still reached the cell poles which is in good agreement with the experimental measurements in *mal3Δ* cells. However, we had to increase the cytoplasmic catastrophe rate by a factor six to achieve these results while in *mal3Δ* cells c_0 is only 2.5 times higher than in wild type. The influence of the cytoplasmic catastrophe rate on the distribution of catastrophes and on the bundle length is illustrated in Fig. 5.16.
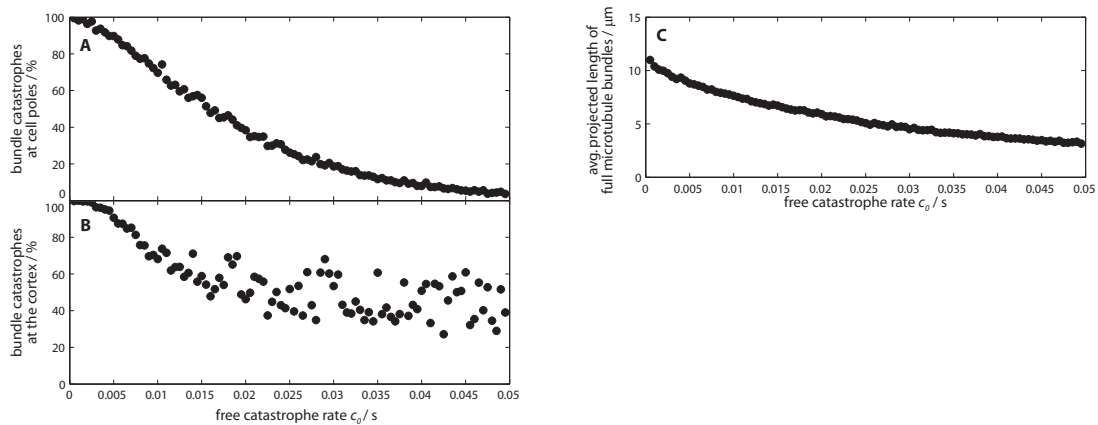
Figure 5.16: Matching the *mal3Δ* phenotype by increasing the cytoplasmic catastrophe rate. The catastrophe rate, c_0, was varied between the reference value $0.005/s$ and $0.05/s$. Corresponding to the mutant, the growth and shrinkage velocities were reduced to $0.04\mu m/s$ and $0.1\mu m/s$ respectively. The number of bundle catastrophes at the poles dropped from more than 90% to 18% for $c_0 = 0.03/s$ (A). At this value about 60% of all catastrophes occurred at the cortex (B), and the average microtubule length was reduced from $\sim 9\mu m$ to $4.49\mu m$ (C). Simulations with $v_0 = 0.04\mu m/s$, $v_s = 0.1\mu m/s$ and $c_0 = 0.03$ therefore resembled the phenotype of *mal3* deletion.

The discrepancy in the increase of c_0 (a factor 2.5 *in vivo* compared to a factor 6 in the simulation) might be due to the pausing of microtubule bundles before they regrow from the iMTOCs (see previous section and footnote 8). In the mutant, microtubule bundles that shrink back to the overlap region pause almost twice as long as in wild type before they start to regrow (see Tab. 5.2). In the simulation, microtubules always regrow immediately if they become shorter than $1\mu m$. If pausing was implemented in the simulation and pausing microtubules were considered with their minimal overlap length of $1\mu m$ for the calculation of the average bundle length, the simulation would probably match the measured values even at lower values of c_0.

The pausing of microtubule bundles at the iMTOCs *in vivo* might be a consequence of the dynamic construction of microtubule bundles, which involves the action of motor proteins and bundling factors as well as nucleation along preexisting microtubules (see Sec. 1.3.2.2). To test this possibility with the simulation, the setup of microtubule bundles would have to be implemented in a more realistic way. If the pauses arise from the dynamic construction of microtubule bundles, implementing this feature in the simulation should reproduce the measured values without any further assumptions. We conclude that simulations with force dependent microtubule dynamics can match the phenotype found in *mal3Δ* cells, if the microtubule growth velocity is reduced as observed *in vivo* and if the cytoplasmic

catastrophe rate is sufficiently increased. The agreement between simulation and experiment might be further enhanced by implementing a more realistic setup of microtubule bundles in the simulation. It should be noted however, that the sensitivity to force is almost irrelevant for the simulation to reproduce *mal3Δ* cells, since microtubules are too short to experience forces at the cell poles.

5.3.2   Simulating the Phenotype of *Tip1* Deletion
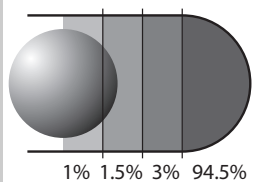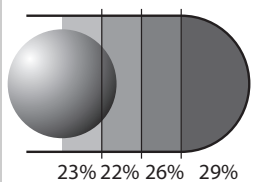
Microtubule Dynamics in Tip1Δ Cells.
The deletion of *tip1* results in a local increase of catastrophes for microtubules that touch the cortex in the central part of the cell (see Sec. 1.3.2.3 for a detailed description of Tip1 function). Microtubules that grow parallel to the cell axis and do not encounter the cortex usually still reach the poles, although such events are rare (only $\sim 30\%$ of all microtubule bundles catastrophe at the poles). In contrast, microtubules that contact the cortex near the cell center are not deflected as in wild type cells, but undergo catastrophe after a short period of sliding. These sliding events last only about $20s$ on average since more than 70% of all microtubule bundles undergo catastrophe before reaching the cell poles. Consequently, catastrophes are almost evenly distributed throughout the length of the cell as shown in Fig. 4.3. Overall, microtubules are $30 - 60\%$ shorter than in wild type cells (see footnote 7) and are found to be less well aligned along the cell axis (Brunner and Nurse, 2000). However, more than 95% of catastrophes still occur at the cortex as in wild type cells. The velocities of microtubule growth and shrinkage are also similar to wild type cells. Summarizing, catastrophes in *tip1Δ* cells occur all over the cortex, while they are restricted to the cell poles in wild type cells (see Tab. 5.3).

Simulating the Tip1Δ Phenotype By Varying the Sensitivity to Force
As demonstrated for the simulations of *mal3Δ* cells, an increase of c_0 results in small fraction of catastrophes at the cortex (Fig. 5.16B) and thus cannot account for the altered distribution of catastrophes in *tip1Δ* cells. However, in model 5 a local increase of the catastrophe rate can occur if microtubules are under compression, for example at the cortex. The forces that are exerted on microtubule plus ends when they slide along central regions of the cortex are relatively low compared to forces at the cell poles. To match the *tip1Δ* phenotype we therefore tried to adjust both the sensitivity to force, f_s, and the catastrophe rate for stalled microtubules, $c_{stalled}$. As for the simulations of *mal3Δ* cells the nucleus was initially placed at the cell center. In the experiments performed by Brunner and Nurse (2000) the fraction of catastrophes was determined in four regions along the cell axis as shown in Fig. 4.3 and in Tab. 5.3. To compare the outcome of the simulations to the *in vivo* measurements we partitioned the cell in a similar way and determined the percentage of bundle catastrophes in each region[9].

We found that increasing the value of $c_{stalled}$ alone could not reproduce the *tip1Δ* phenotype (see the graphs in appendix A.9.3 for the variation of $c_{stalled}$). Indeed, high forces opposing microtubule growth occurred only for long bundles that were compressed between the poles. Consequently, at the standard value of f_s, higher values for $c_{stalled}$ had almost no influence on the catastrophe rate at the center, because $c_{stalled}$ was without effect if the polymerization rate was not reduced. To slow down microtubule growth at the central cortex and thus obtain a higher catastrophe rate we increased the sensitivity to force, i.e. we reduced the value of f_s and varied it logarithmically between $10^{-3}pN$ and the reference value $1.67pN$. It turned out that even for $f_s = 10^{-3}pN$ (i.e. very sensitive microtubules)

---

[9]The area next to the nucleus was defined as region one, followed by regions two and three in the cylindrical cell body and finally the cap region. The three regions in the cylinder all have the same width of $\sim 1.167\mu m$ to cover the whole length of the cell body as defined in the standard set of parameters ($l_{cylinder} = 3.5\mu m$). The length of the cap region corresponds to the radius of the cell, i.e. $2\mu m$. In each region, the catastrophes left and right of the cell center were scored.

	wild type	*tip1Δ*
growth rate	-	similar to wild type
shrinkage rate	-	similar to wild type
bundle catastrophe rate	-	increased
fraction of catastrophes at the cortex	more than 95%	more than 95%
catastrophe distribution along the cell axis	1% 1.5% 3% 94.5%	23% 22% 26% 29%
average microtubule bundle length	—	$30 - 60\%$ shorter on average
contact time at cell poles	$75s$ on average	$40s$ on average
average duration of sliding events	most bundles reach poles	$20s$

Table 5.3: Quantification of microtubule dynamics in wild type and *tip1Δ* cells. The values shown were measured using strains expressing GFP-tagged α-tubulin from a multicopy plasmid under the control of the nmt1 promoter. All dynamic values are taken from Brunner and Nurse (2000) and refer to microtubule bundles rather than single microtubules.

most bundles still reached the cell poles (Fig. 5.17A). The reason was that the forces experienced by microtubules touching the cortex at an angle were only around $0.1pN$ and therefore only had a small effect on the microtubule growth velocity (for comparison: forces at the cell poles are usually between 3 and $5pN$). Furthermore, the maximum catastrophe rate that could be reached if growth was stalled was $0.05/s$. Consequently, increasing f_s alone could not reproduce the traits of *tip1Δ* cells, either.

To test if a higher value for $c_{stalled}$ in combination with increased force sensitivity could reproduce the correct distribution of catastrophes we repeated the variation of f_s with $c_{stalled}$ set to 10^{-6}. With these settings microtubules that stopped growing underwent catastrophe instantaneously. However, as illustrated in Fig. 5.17E, there was still no significant effect on the distribution of catastrophes down to $f_s \approx 0.2pN$. Below this value the forces from the simulated Brownian motion became sufficient to stall the growth of microtubules irrespective of their position[10]. Most microtubules consequently underwent catastrophe in the close proximity of the nucleus. Since the nucleus was initially placed at the cell center and diffused only little during the simulation, most catastrophes were scored at the center (red squares and green diamonds in Fig. 5.17E). However, the results in the regime below $f_s \approx 0.2pN$ have to be regarded as a numerical artifact produced by the simulation due to the way

---

[10] It should be noted that the Brownian forces in the simulation do not correspond to any real physical forces occurring in the cytoplasm. As described in the methods (see Sec. 2.2.2 and footnote 1 in that section), the Brownian forces are calibrated to generate the correct Brownian displacements for a given timestep h. Consequently, the part of the graphs below $10^{-2}pN$ in Figs. 5.17 E-H has to be regarded as a numerical artifact produced by the simulation. For such low values of f_s the simulation does not produce correct results.

Brownian motion is implemented (see footnote 10). We can therefore conclude that the simulation could not reproduce the distribution of catastrophes in *tip1Δ* cells within the range where it generated physically correct results, i.e. down to $f_s \approx 0.2pN$. Values below $0.2pN$ are not physiologically relevant, since microtubules *in vivo* would be destroyed as soon as they encounter any obstacle inside the cytoplasm.

Summarizing, our present model with force dependent microtubule dynamics could not reproduce the distribution of catastrophes in the *tip1Δ* mutant for any values of f_s and $c_{stalled}$. Friction at the cortex might increase the sliding forces of growing microtubule plus ends *in vivo*, which might become relevant in *tip1Δ* cells. This could be tested by implementing cortical friction in the simulation.
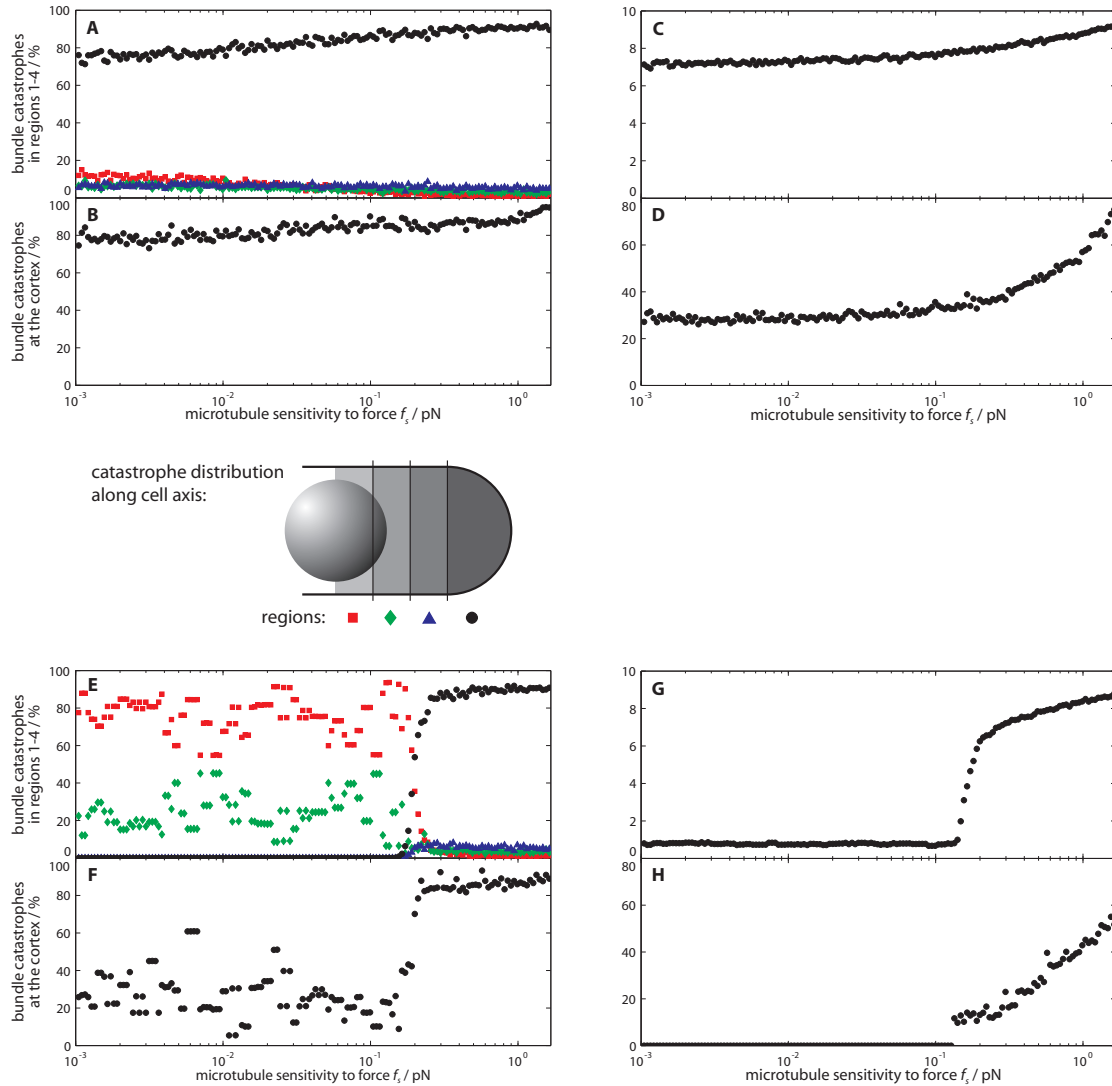
Figure 5.17: Matching the *tip1Δ* phenotype by increasing microtubule sensitivity to force. The sensitivity parameter, f_s, was varied between $10^{-3}pN$ and the reference value $1.67pN$ (low values generate more microtubule catastrophes under force). (A-D): Simulations in the upper graphs were performed with the reference value of $c_{stalled} = 0.05/s$. Even very sensitive microtubules ($f_s = 10^{-3}$) were still able to slide along the cortex and reach the poles (A, black circles), because the catastrophe rate could not exceed $0.05/s$. Most catastrophes therefore occurred in the polar regions (A & B). The bundle length was reduced by only $\sim 22\%$ which did not fit the *in vivo* data. The contact time at the poles was reduced to $1/c_{stalled} \approx 20s$ (D). (E-H): Simulations in the lower graphs were performed with $c_{stalled} = 10^6/s$. The distribution of catastrophes exhibits a sharp transition around $f_s \approx 0.2pN$, where the Brownian forces in the simulation became sufficient to induce catastrophe (E & F). However, the Brownian forces in the simulation do not represent real physical forces and the part of the graphs below $0.2pN$ has to be considered as a numerical artifact (see text). Above that value the distribution of catastrophes changed only little with f_s, indicating that sliding forces were not sufficient to induce catastrophes at central parts of the cortex.

Catastrophes at the Cortex - An Extension of Force Dependent Microtubule Dynamics

The main characteristic of *tip1Δ* cells is that microtubules undergo catastrophe when they contact the cortex. A possible mechanism involves a catastrophe promoting factor localized all over the cell cortex. In this case the function of Tip1 would be to protect microtubule tips from this catastrophe promoting activity. Microtubules touching the cortex would not be affected as long as Tip1 accumulates at microtubule plus ends. Only at the poles where Tip1 is removed from microtubule tips (the removal possibly involves Tea1, see Sec. 1.3.2.3), the catastrophe promoting factor could affect microtubule dynamics. In contrast, in a *tip1Δ* cell such a factor would act on all microtubules that contact the cortex irrespective of the distance to the pole, while microtubules growing in the cytoplasm could still reach the poles.
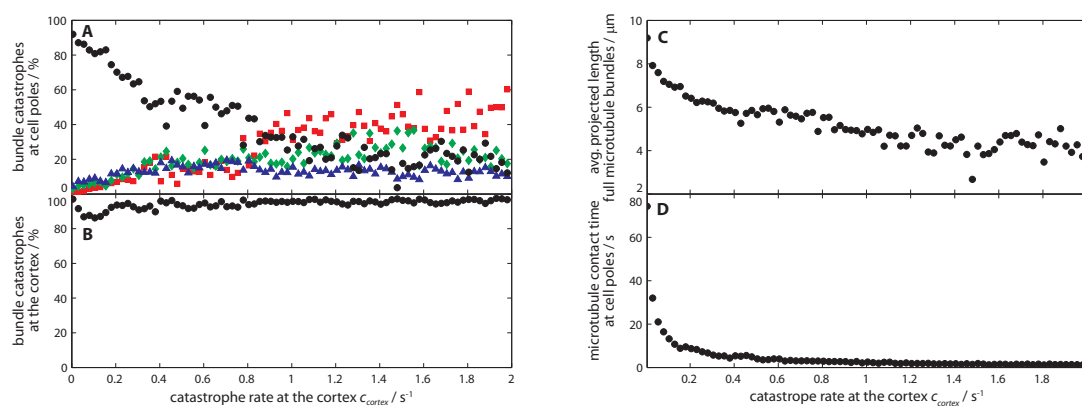
Figure 5.18: Variation of the cortical catastrophe rate in the extended force model. The cortical catastrophe rate, c_{cortex}, was varied between the cytoplasmic rate, c_0, and $2/s$. With increasing c_{cortex} more bundle catastrophes occurred in region one close to the nucleus (A, red squares), while less microtubules reached the poles, resulting in a decrease of the average length of microtubule bundles (C). Almost all catastrophes occurred at the cortex for any value of c_{cortex} (B). The best fit was obtained for $c_{cortex} \approx 0.9/s$, where bundle catastrophes were almost equally distributed along the cell axis (A). However, this rate resulted in microtubule contact times at the poles that were significantly lower than the $\sim 40s$ measured *in vivo* (D).

To test this possibility we modified our model with force dependent microtubule dynamics and added a parameter c_{cortex} that determines the catastrophe rate for microtubules that touch the cortex anywhere[11]. An important feature of this model is that the cortex still does not carry any positional information since the cortical catastrophe rate at the poles is not different from the remaining parts of the cortex. The positional information to discriminate between the poles and central parts of the cell is still only generated by force. This extended model is equivalent to the standard force model if $c_{cortex} = c_0$. We systematically varied c_{cortex} between the cytoplasmic rate and $2/s$ to test if we could reproduce the *tip1Δ* phenotype. The best match was obtained for $c_{cortex} \approx 0.9/s$ (Fig. 5.18). Bundle catastrophes were almost evenly distributed along the cell axis, with 33% at the poles and 35%, 18% and 14% in regions one to three respectively. Furthermore, 96% of all bundles underwent catastrophe at the cortex and the average bundle length dropped to $4.97\mu m$ which is about 55% of the bundle length obtained with the standard set of parameters. The only result that did not conform with

---

[11]For microtubules that contacted the cortex the probability to undergo catastrophe was set to c_{cortex} if $c_{cortex} > c_{stalled}$. If c_{cortex} was lower than $c_{stalled}$, we used $c_0 = c_{cortex}$ for the basal catastrophe rate, which could then be increased up to $c_{stalled}$ under force, just as in the standard force model (see Sec. 2.2.7 for the implementation).

the *in vivo* measurements was the microtubule contact time with the cell poles, which was $2.72s$ in the simulation compared to $\sim 40s$ in the experiments. Similarly, microtubules that touched the cortex close to the cell center rapidly experienced catastrophe in the simulation while they were sliding along the cortex for about $20s$ *in vivo*.

The low contact times were a direct consequence of the high cortical catastrophe rate that was needed to redistribute catastrophes equally along the cell axis. The reason why we had to use $c_{cortex} = 0.9/s$ became evident from watching the replay of the simulation. In the beginning, microtubules were randomly oriented on the nucleus and frequently contacted the cortex at the cell center where they rapidly underwent catastrophe. However, after a while, the bundles became oriented along the cell axis and microtubules barely touched the central cortex anymore. The cortical catastrophe rate had to be that high to ensure that the few microtubules that still contacted the cortex at the cell center rapidly underwent catastrophe. This situation is different from what is observed *in vivo*. In *tip1Δ* cells microtubules frequently contact the cortex when they grow out from the nucleus. The reason might be again that the simulation did not correctly reproduce the pausing of microtubule bundles at the iMTOCs before the re-initiation of growth from the overlap regions (see also the discussion of the *mal3Δ* phenotype in section 5.3.1 and footnote 8). *In vivo*, short microtubule bundles diffuse on the nucleus and orient randomly before they regrow, resulting in an increased number of bundles that encounter the cortex. The turnover of microtubule bundles in living cells, which results from the dynamic construction of microtubule bundles from MAPs and motors, is probably essential for this reorientation (see Sec. 1.3.2.2). To reproduce the organization of microtubule bundles in *tip1Δ* cells including the observed microtubule contact times, it might therefore be necessary to implement a more realistic setup of microtubule bundles in the simulation.

Another possibility is to modify the catastrophe inducing mechanism. We assumed that Tip1 protects microtubule plus ends from a catastrophe promoting activity at the cortex. It might as well be, that Tip1 prevents the binding of a catastrophe promoting factor which is normally located at the cortex but is transferred to microtubule plus ends when they contact the cortex. Such a factor would only become active when a microtubule touches the cortex but it would continue to act on the plus end, even if the microtubule already lost contact. The function of Tip1 in this model would not be to protect the plus tips from catastrophes directly, but to prevent the binding of the catastrophe promoting factor. For microtubules sliding along the cortex this would not make a difference compared to the previous model. However, microtubules that only shortly touch the cortex and then loose contact (for example because the bundle rotates due to the pushing of another microtubule at the opposite end of the bundle) would be affected if they picked up this factor[12]. In the simulation, such a model could be realized easily by defining a higher catastrophe rate for microtubules that contacted the cortex for a certain amount of time. For example, the catastrophe rate of microtubules that contacted the cortex for more than a second could be set to $\sim 0.05/s$ to reproduce the average sliding time of $20s$. This might allow the simulation to reproduce the correct distribution of microtubule catastrophes and at the same time match the contact times measured *in vivo*.

We conclude that the extended force model can reproduce all but one feature of *tip1Δ* cells, which is the contact time of microtubules at the poles and the sliding along the central cortex. The inability to match the longer contact and sliding times might result from the static setup of microtubule bundles in the simulation that does not allow reorientation of short bundles. To match the *tip1Δ* phenotype it is necessary to implement dynamic bundle construction. Another possibility is provided by the modified model explained above which was not yet implemented, or by a combination of both ideas.

---

[12]In living cells, such events are difficult to distinguish from continuous sliding along the cortex. To test this model it would be necessary to determine the frequency of short contacts in the simulation.

Chapter 6

Discussion and Outlook

As described before, microtubule bundles are essential for the regulation of cell polarity in interphase fission yeast cells. Using an approach which combined computer simulations and experiments we investigated how microtubule dynamic instability is regulated to generate the organization of microtubules observed *in vivo*. The computational model allowed us to to identify the minimal set of components and assumptions that was required to properly adjust microtubule dynamics. To decide if the simulation correctly reproduced the behavior of living cells, we compared its output to several characteristics that were determined *in vivo*. For this comparison, nine traits (T1-T9) were chosen that could be quantified experimentally. The output of the simulation was processed to be directly comparable to the *in vivo* measurements. For example, the observation of fluorescently labeled α-tubulin only provided the full length of microtubule bundles projected on the z-direction (T9). Consequently, the length of microtubule bundles in the simulation was also projected on the z-direction to resemble the *in vivo* measurement.

Quantitative data for the first six traits could be obtained from the literature, whereas values for T7-T9 were not available. We therefore recorded time series of living *S. pombe* cells expressing fluorescently labeled α2tub to determine the distribution of microtubule contact times with the cell poles (T7), the number of half-bundles touching the cell poles (T8) and the distribution of microtubule bundle length (T9). Our measurements revealed that microtubules contacted the cell poles for about $66s$ on average. The distribution of contact times exhibited a local maximum at about $60s$. Furthermore, the average total length of microtubule bundles was about 70% of the cell length, and between three to four half-bundles (i.e. about 50%) contacted a cell pole at any time (see chapter 3). To determine the size of the nucleus, cells were transformed with a plasmid encoding for a GFP-tagged marker of nuclear and plasma membranes. We found that the nucleus occupies about 75% of the cell diameter, indicating that the mobility of the nucleus is considerably affected by the flow of the cytoplasm (see appendix A.4).

Five Models for Microtubule Dynamic Instability
Five different models for the regulation of microtubule dynamic instability were implemented in the computer simulation. In our first model microtubule dynamics was independent of the position of microtubule plus ends, tubulin concentration and force (model 1, independent dynamics). This model demonstrated that microtubule dynamics needs to be regulated at the cell poles to reproduce the organization of microtubule bundles observed in living cells, as was also suggested earlier in the field. Several mechanisms have been proposed how such regulation might occur *in vivo*, including the effects of tubulin concentration (model 2), localized regulatory factors (model 3) and forces acting on microtubule plus ends (model 4 & 5). In model 1 and 2 the dynamics of microtubule plus ends is

independent of their position, whereas model 3 assumes a localized catastrophe promoting activity at the cell poles. In model 4 and 5 local effects on microtubule dynamics arise from general physical properties of microtubules in connection with the cylindrical shape of the *S. pombe* cortex.

Further analysis of model 1 revealed that it was unable to fulfill two important traits at the same time. Microtubules were either too short to fulfill T5 which states that more than 90% of all microtubule bundles reach the cell poles, or they became too long and curled around the poles, violating T4. This behavior was caused by the exponential distribution, $p(L) = \lambda e^{-\lambda L}$, of microtubule length in this model. The requirement that 90% of all microtubule bundles reach the cell poles imposes a minimum for the average length, $\langle L \rangle = 1/\lambda$, while T4 imposes a maximum (see Sec. 4.1.3). Fulfilling T5 therefore implies to fail T4 and vice versa. This clearly demonstrated the need for a different regulation of microtubule dynamics in order to adjust the distribution of microtubule length.

It was suggested that the amount of free tubulin available for polymerization might be exactly regulated in living cells, such that microtubules are prevented from becoming too long. To test if this is sufficient to reproduce the behavior of microtubule bundles *in vivo*, we expanded model 1 by one parameter which specified a maximum, Σ_{MT}^{0}, for the total length of all microtubules in the simulation. In this model, the velocity of microtubule growth was proportional to $\Sigma_{MT}^{0} - \Sigma_{MT}$, where Σ_{MT} is the sum of the current microtubule length (see chapter 4). However, we found that the results were similar to model 1. Since microtubule catastrophes were stochastic, single microtubules often became very long while the others were short and thus curled at the poles, failing T4. To fulfill T4 the maximum total microtubule length had to be reduced such that only very few microtubules could still reach the poles, failing T5. We did not investigate the effect of an additional increase of the catastrophe rate in this model. However, it is very unlikely that this would significantly enhance the situation since it would not localize microtubule catastrophes to the cell poles.

Summarizing, global regulation of microtubule dynamics failed to adjust microtubule length to cell length, which made it impossible to comply with T4 and T5 at the same time. The simulation allowed us to test a wide range of different values for the dynamic parameters of model 1 and 2. We therefore conclude that global regulation of microtubule dynamics for example by equally distributed MAPs and +TIPs cannot properly adjust microtubule length and is therefore unlikely to be the only determinant of microtubule organization *in vivo*.

Evidence for the local regulation of microtubule dynamics was found in cells that were deleted of the microtubule plus end tracking protein Tip1. Tip1 is thought to protect microtubules from catastrophes at central parts of the cell cortex, whereas it is removed in a Tea1 dependent mechanism at the cell poles (Brunner and Nurse, 2000). Effectively, this results in a higher catastrophe rate specifically at the cell poles. To test if this is sufficient for the proper organization of microtubule bundles we implemented a model with a locally increased catastrophe rate in the simulation (localized catastrophes). We found that a model with localized catastrophes solved the problem of adjusting microtubule length to cell length, and simulations complied with the first six traits measured in living cells. But, due to the high catastrophe rate, microtubules contacted the poles only shortly before they underwent catastrophe, which is in conflict with the observation that microtubules touch the poles for about $66s$ on average *in vivo* (T7). Furthermore, the distribution of contact times was exponential unlike the *in vivo* distribution which has a maximum at $\sim 60s$. The duration of microtubule contacts with the poles is an important feature of microtubule organization in living cells which is related to the regulation of cell polarity. In wild type cells microtubules deposit polarity markers like Tea1 and Tip1 at the cell poles, a function that might be severely impaired if microtubules touch the cell poles only shortly. This would for example be the case if the polarity markers are delivered by molecular motors. A longer contact would then lead to a higher concentration of marker proteins deposited at the poles. To allow longer contact times in the simulation, the catastrophe rate at the poles would have

to be decreased which would again result in curling microtubules. A solution to this problem would be to use a slightly lower catastrophe rate at the poles and at the same time slow down the growth velocity of microtubules that contact the cell ends. Indeed it was observed in living cells that the polymerization rate of microtubules contacting the cell poles is lower than for microtubules growing in the cytoplasm (Tran et al., 2001; Loïodice et al., 2005). Very recent results furthermore indicate that the CLASP Peg1 is required for the decrease of microtubule growth at the poles (Grallert et al., 2006), but it remains unclear how this protein is involved in this function.

The additional assumption that microtubule polymerization slows down if microtubules touch the cell poles could be easily implemented on top of model 3. However, this would mean to introduce an additional mechanism that is not well understood *in vivo* and that at the same time makes the simulation more complicated. Furthermore, simulations would still exhibit an exponential distribution of contact times which does not match our measurements in living cells. For any model used in this study it would probably be possible to invent additional parameters to improve the outcome of simulations. However, we were looking for the most simple model that required the lowest number of assumptions to reproduce the nine traits measured in living cells. Therefore, instead of imposing the slowdown of microtubule growth at the cell poles, we implemented the experimental finding that microtubule polymerization slows down if forces are opposing the direction of microtubule growth (model 4) (Dogterom and Yurke, 1997). Performing simulations with model 4 we found that the growth velocity of microtubules decreased specifically at the cell poles. High forces occurred only for microtubule bundles that spanned the whole cell length and were compressed between the two poles. This illustrated that the cylindrical shape of fission yeast was sufficient to locally slow down microtubule growth without the need of additional cell end factors.

The difference between the two approaches (model 3 and model 4) is that model 3 assumes that the cell poles are chemically different from other parts of the cortex, although the model cannot explain why this should be the case. In model 4 the different behavior of microtubule plus ends at the cell poles arises from an intrinsic property of microtubules that is the same for all microtubules irrespective of their position, i.e. microtubule sensitivity to force. No *a priori* knowledge about the cell poles is required, the local effect is caused solely by the cylindrical shape of the *S. pombe* cortex. Model 4 therefore represents a far more general approach that also has greater predictive power since it could be applied to other cell shapes as well.

Simulations with force dependent growth could fulfill the first seven traits. However, instead of being too short as in the previous model, the average microtubule contact time with the cell poles was now about three to four times too long because microtubule growth almost stalled at the cell ends. Hence, the number of half-bundles touching the cell poles at any time (T8) and the average total length of microtubule bundles (T9) were higher than measured *in vivo*. This demonstrated that the slowdown of growth alone was not sufficient but that a higher catastrophe rate at the poles was needed as well in order to fulfill the nine traits of living cells.

Measurements *in vitro* have shown that slow growing microtubules have a higher catastrophe rate (Janson et al., 2003). Adding this experimental finding to our model we found that such simulations indeed fulfilled all of the nine traits. Our simulations therefore suggested that forces generated by the spatial confinement of the *S. pombe* cortex are sufficient to adjust microtubule dynamics at the cell poles and that a localized regulatory activity is not required. The parameters used for the working simulations corresponded to the values that were determined by measurements in living cells and *in vitro*. The model with force dependent microtubule dynamics is especially appealing, because positional information is generated solely from the intrinsic global properties of microtubules in connection with cell shape. The fact that microtubules can organize independently of cell end factors is remarkable, as it indicates how the cell may recover from depolarization.

Dependence of Microtubule Organization on Cell Shape In Vivo

To investigate how the organization of microtubules correlates with cell shape we analyzed cells with a temperature sensitive mutation in *pmo25*. In these cells the growth machinery rapidly depolarizes at the restrictive temperature and cells grow round within $\sim 4h$. We found that microtubules aligned with the cell axis as long as the cells were clearly cylindrical. Only when the cells obtained a more spherical morphology after more than two hours at the restrictive temperature, microtubules became disorganized. The experiment demonstrated that the cylindrical morphology of the cortex is required for the alignment of microtubule bundles with the cell axis *in vivo*. It did not show however, if a cylindrical shape is also sufficient since it is unclear if other polarity factors remained at the cell poles independently of actin and of the growth machinery. Possible candidates are Tea1, Tea3 and Mod5 which were shown to localize to the poles even in the absence of actin (Sawin and Snaith, 2004; Snaith et al., 2005). These might again recruit other proteins to the poles that regulate microtubule dynamics.

If such factors are still properly localized even in round cells, they are not sufficient to maintain normal microtubule organization as shown by our experiment. Summarizing we can therefore state that cylindrical cell shape is required for the alignment of microtubule bundles along the cell axis. Whether it is also sufficient *in vivo* remains to be investigated, but our simulations with model 5 suggest that this is indeed the case. One possibility for an experimental verification would be to reconstitute the system *in vitro* using cylindrical chambers containing the proteins needed for the dynamic bundle construction.

Another important factor is the localization of Tea1, Tea3 and Mod5 in the *pmo25* mutant. If Tea1 was still present at the poles after the temperature shift, this would indicate that the regulation of microtubule dynamics by Tip1 and maybe other factors might still be functioning (Tea1 has a possible role in the removal of Tip1 from microtubule plus ends at the cell poles, see Sec. 5.2.2 for further suggestions). To further elucidate the question if Tip1 is removed from microtubule plus ends in the *pmo25* mutant it would also be useful to study not only the spatial orientation of microtubule bundles but also the dynamic parameters that determine the nine traits. Such parameters, like for example microtubule contact times with the poles, would then have to be compared to the corresponding values in wild type cells that were treated the same way, i.e. cells that were shifted to a higher temperature shortly before the measurement.

Simulation of Mutant Cells With Force Dependent Microtubule Dynamics

To further characterize our model with force dependent microtubule dynamics we investigated, if the simulation could reproduce the microtubule related phenotypes found in *mal3Δ* and *tip1Δ* cells. In *mal3Δ* cells microtubules are overall shorter and exhibit an increased number of catastrophes. We found that microtubule dynamics in *mal3Δ* cells could be matched by increasing the cytoplasmic catastrophe rate in the simulation. In *tip1Δ* cells, microtubules undergo catastrophe shortly after touching the cortex not only at the cell poles but also in central regions of the cell. This phenotype could not be reproduced by simulations with force dependent microtubule dynamics, because catastrophes caused by force occurred almost exclusively at the cell poles. Forces opposing the direction of microtubule growth were high only for microtubule bundles that were compressed between the two poles. The forces that occurred during the sliding of microtubule plus ends along the cortex in central regions of the cell were too low to significantly slow down microtubule growth and did therefore not affect the catastrophe rate. Even when we increased the sensitivity of microtubules to force we could not reproduce the distribution of catastrophes measured in *tip1Δ* cells.

The forces experienced by sliding microtubules *in vivo* might be higher than in the simulation due to friction and obstacles in the cytoplasm like mitochondria or vacuoles. A model that includes friction might therefore be able to reproduce the observed distribution of microtubule catastrophes.

However, this would implicate that the removal of Tip1 causes microtubules to become hypersensitive to force which is not very likely since the value of the force sensitivity, f_s, used for the simulation of wild type cells was experimentally determined *in vitro* with pure tubulin. Yet it would be possible that other proteins affect the stability of microtubule plus ends in the absence of Tip1 which might create a difference between the *in vivo* value of f_s and the value measured *in vitro*. It therefore cannot be excluded that friction might be important.

Consequently, we tested an extended model with a higher catastrophe rate imposed on microtubules that touched the cortex anywhere along the cell axis. The biological interpretation of such a model is that Tip1 has a hypothetical function in the protection of microtubule plus ends from a catastrophe promoting activity that is localized all over the cortex (Brunner and Nurse, 2000). The deletion of *tip1* would consequently remove this protection against catastrophes. We found that this model could indeed reproduce most features of *tip1Δ* cells apart from the contact time of microtubules with the cortex which was too low in the simulations. The reason for this discrepancy might be that microtubules in the simulation only rarely contacted the cortex in central regions of the cell once they became aligned with the cell axis. In living cells, microtubule bundles exhibit constant turnover which causes them to reorient and to encounter the cortex more often (see discussion in Sec. 5.3.2). To match the phenotype of *tip1Δ* cells including the contact times it might therefore be necessary to implement the dynamic constructions of microtubule bundles in the simulation.

The idea of a catastrophe promoting factor at the cortex can be developed further to explain some other interesting experimental observations. In wild type cells, Mal3 is gradually removed from microtubule plus ends at the cell poles about $80s$ before the occurrence of catastrophe (Busch and Brunner, 2004) which corresponds to the average contact time of microtubules with cortex (T7). In contrast, Mal3 stays bound to growing microtubules that slide along the central cortex. This suggests that Mal3 removal at the poles is caused either by the slow down of microtubule growth or by some other factor that prevents the binding of Mal3 to microtubule plus ends. Experimental measurements indicated that the accumulation of Mal3 at microtubule plus ends is independent of the polymerization rate which favors the second possibility (Busch and Brunner, 2004).

Moreover, Mal3 also disappears prior to catastrophe from microtubules that contact the central cortex in *tip1Δ* cells. This means that in *tip1Δ* cells microtubules (or Mal3) loose the ability to discriminate between central parts of the cortex and the cell poles. As described before, Mal3 inhibits microtubule catastrophes. In the context of the extended model proposed above, it is therefore possible that the catastrophe promoting activity at the cortex is mediated by a factor that binds to microtubule plus ends and competes with the binding of Mal3. This would explain the observation of Mal3 removal from microtubule plus ends at the cortex in *tip1Δ* cells as well as Mal3 removal at the cell poles in wild type. The function of Tip1 would then be to prevent the binding of this potential factor to microtubule plus ends. This model is appealing because it is simple but still explains most observations in wild type cells as well as in the *tip1Δ* and *mal3Δ* mutants. Furthermore, it does not postulate the existence of unknown factors that directly regulate microtubule dynamics but only the existence of a protein that binds to microtubule plus ends and thus prevents the accumulation of other +TIPs like Mal3. Another intriguing property of this model is that such a factor could not be identified by screening for interaction partners of Tip1 and Mal3 since it is not required to bind either of these proteins. It would probably also not be identified in a screen for proteins that affect microtubule dynamics since its deletion in wild type cells would have no effect, apart from a possibly longer contact time at the poles or a slightly increased number of curling microtubules. However, at the present time this model is purely hypothetical and further experiments would be needed to check if it has any relevance *in vivo*. A possible candidate for such a factor should localize to the cortex and possibly cause microtubule curling upon deletion. Its deletion should furthermore rescue the *tip1Δ* phenotype.

Conclusions and Outlook

Using computer simulations we demonstrated that the main characteristics of microtubule behavior in interphase fission yeast cells can be explained, if the effect of force antagonizing microtubule polymerization is taken into consideration. Our model suggests that the localized activity of regulatory proteins is not required to trigger catastrophes at the cell poles. It rather indicates that the intrinsic physical properties of microtubules in connection with the specific cell shape of *S. pombe* are sufficient for the proper organization of microtubule bundles. Our experiments with *pmo25* mutants confirmed that cell shape is essential for the alignment of microtubule bundles with the cell axis. Furthermore, the simulation of mutant phenotypes in *mal3Δ* and *tip1Δ* cells lead to the proposal of a novel hypothesis how Tip1 might function *in vivo* to discriminate between central parts of the cortex and the cell poles. Our model suggests that Tip1 protects microtubule plus ends from a catastrophe promoting factor localized at the cell cortex. Selected removal of Tip1 at the cell poles (involving for example Tea1 or force) could thus assist force in triggering catastrophes at cell ends. To verify if the proposed mechanism is relevant *in vivo* it will be necessary to identify the hypothesized catastrophe promoting activity in living fission yeast cells.

Recent experimental observations in cells where the nucleus was displaced to a cell pole by centrifugation apparently contradicted our model with force dependent microtubule dynamics (model 5). It was described that the microtubules on the side of the nucleus close to a pole (the proximal end) seemed to be more stable than the microtubules facing the other pole (the distal end) (Daga et al., 2006). In model 5, microtubules at the proximal end that are involved in pushing the nucleus back to the cell center, are expected to exhibit more catastrophes than the ones that grow unhindered through the cytoplasm towards the distal end. Indeed our simulation showed this type of behavior. However, the new experimental results are not necessarily incompatible with the force model if one takes into account the possible effects of regulatory MAPs in living cells. It has been shown that molecular motors from the kinesin 8 family depolymerize microtubules in a length dependent manner (Varga et al., 2006) in budding yeast. In fission yeast the two kinesins Klp5 and Klp6 were also shown to depolymerize microtubules (West et al., 2001). It is therefore possible that in the experiment Klp5 and Klp6 induced catastrophe of the long microtubules facing the distal end, while the short microtubules on the proximal side were not affected. Such a mechanism might cover the increase of the catastrophe rate due to force and thus explain the experimental observations.

The simulation has been a valuable tool to test different models of microtubule dynamic instability in fission yeast. To further analyze force as an essential determinant of microtubule organization, it can now be extended to include microtubule associated proteins like Klp5 and Klp6 to match recent experimental observations. To make the model more realistic it will be necessary to implement the dynamic construction of microtubule bundles from MAPs and motors (Janson et al., 2007). The simulation could then be used to study microtubule dynamics and organization in mutant cells that exhibit defects in microtubule bundling and in the spatial distribution of bundles, which often give rise to bent and T-shaped cells (Fig. 6.1). To study morphogenesis it would furthermore be necessary to implement the transport of polarity factors along microtubules. This would allow us to study the positive feedback between cell shape and microtubule organization where the position of growth factors is determined by microtubules which are again organized by cell shape as demonstrated in this study. Expanding the simulation will clear the way for a more systematic approach towards the understanding of morphogenesis.
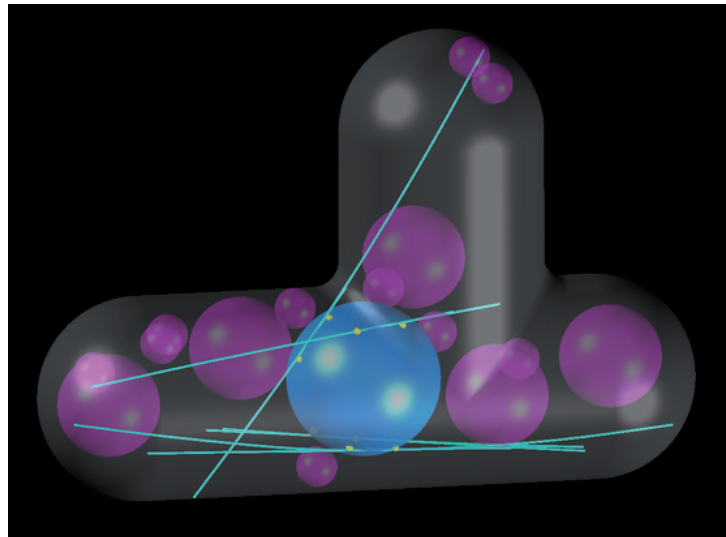
Figure 6.1: Simulation of a Tee-shaped cell. In the future, the simulation can be used to study the organization of microtubules in mutants with altered morphologies.

Appendix A

Parameters of the Simulation

The input parameters of the simulation can be categorized into three groups (see Tab. A.1):

1. The first group comprises parameters that directly correspond to physical properties of the simulated objects. Values for these parameters were determined experimentally, either in wild type cells, e.g. the growth velocity of microtubules, or *in vitro*, e.g. the catastrophe rate for stalled microtubules.

2. The second group contains parameters that have not been measured experimentally, e.g. the rigidity of the plasma membrane, or parameters that describe elements of the simulation that were simplified compared to the *in vivo* situation. Examples for the latter case are the assembly of microtubule bundles and the connection of bundles to the nucleus. Both are static in our model whereas they are dynamic in reality. These parameters are calibrated to represent the conditions *in vivo*.

3. The last group of parameters is related to the numerical methods used to calculate the motion of objects in the system, e.g. the integration time step h. These parameters should ideally not have any influence on the results, and are chosen accordingly.

We selected a reference parameter set corresponding to a wild type cell under standard laboratory conditions (see Tab. A.1). In the model with force dependent microtubule dynamics (model 5), simulations run with these parameters fulfilled T1-T9 consistently. To probe the system, parameters were varied one by one while keeping the others at their reference value. These variations were performed in model 5 and allowed us to predict the influence of each parameter on microtubule organization and on the nine traits. The most interesting results are presented in the following paragraphs. For each parameter we furthermore describe how the reference value was chosen according to our own *in vivo* measurements, previously published data or theoretical considerations.

A.1   Cell Size

The shape of the *S. pombe* cortex is idealized as a cylinder closed by half-sphere caps. Two parameters characterize this shape: the half-length $l_{cylinder}$ of the cylinder and the cell radius r_{cell}. Since the cylinder is closed by half-spheres, the cap radius is equal to the cylinder radius and the resulting total cell length is $l_{cell} = 2(l_{cylinder} + r_{cell})$.

Wild type *S. Pombe* grow from 7 to $14\mu m$ in length (Tran et al., 2001) while maintaining a constant diameter of $\sim 4\mu m$. We therefore used $r_{cell} = 2\mu m$ and $l_{cylinder} = 3.5\mu m$ to simulate a cell with

Parameter	Symbol	Value	
Physical			
Cortex and Cytoplasm			
cell radius	r_{cell}	$2\,\mu m$	
half-length of cell body	$l_{cylinder}$	$3.5\,\mu m$	(total cell length is $11\mu m$)
stiffness of the cortex	k_{cortex}	$100\,pN/\mu m$	
effective viscosity of the cytoplasm	η_{cell}	$0.9\,pN\,s/\mu m^2$	
Nucleus			
radius	$r_{nucleus}$	$1.5\,\mu m$	
mobility of anchoring buoys	μ^S	$0.1\,\mu m/pN\,s$	
membrane repulsive elasticity	k_{steric}	$10\,pN/\mu m$	
stiffness of mt-nucleus links	k_{link}	$10\,pN/\mu m$	
Microtubules			
flexural rigidity of MTs	κ_{mt}	$30\,pN\mu m^2$	
free growth velocity	v_0	$0.05\,\mu m/s$	($3\mu m/min$, varied in Fig. 2)
shrinkage velocity	v_s	$0.15\,\mu m/s$	($9\mu m/min$, negative in the simulation)
free catastrophe rate	c_0	$0.005\,/s$	($0.3/min$, varied in Fig. 2)
sensitivity to force	f_s	$1.67\,pN$	
catastrophe rate for stalled mt	$c_{stalled}$	$0.05\,/s$	($3/min$)
Microtubule Bundles			
number of bundles	N_{bundle}	4	
number of MTs per bundle	N_{mt}	4	
width of the overlap region	$l_{overlap}$	$1\,\mu m$	
stiffness of mt-bundling links	k_{bundle}	$1000\,pN/\mu m$	
Numerical			
time step	h	$10\,ms$	
convergence threshold	ψ	0.1	
MT segmentation length	ρ	$0.5\,\mu m$	

Table A.1: Parameters of the simulation and reference values. The reference values of "Physical"parameters are set according to measurements in wild type cells or *in vitro*, as described in the text. "Numerical" parameters control the discretization and the numerical solver. They are chosen to solve the equations of motion with sufficient precision.
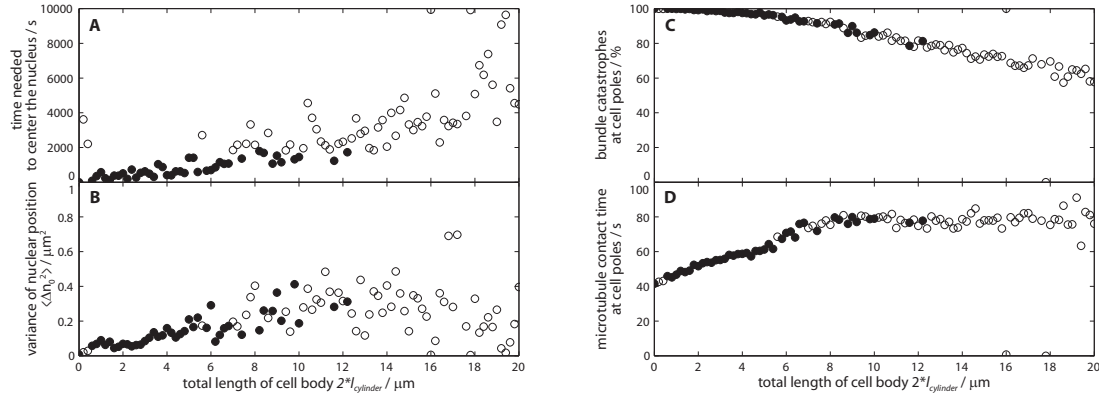
Figure A.1: Variation of the cell length via the central cylinder $l_{cylinder}$. (A and B) The variation of the nuclear position $\langle n_0 \rangle$ increases as less microtubules reach the cell ends and more catastrophes occur in the central cylinder of the cell. (C) Curling of microtubules is effectively prevented even in short cells. (D) Due to higher bending forces for short microtubules contact times decrease in short cells (see text).

an average length of $11\mu m$. Varying $l_{cylinder}$ allowed us to predict how the nine traits change *in vivo* as the cell grows. As expected, less microtubules reached the cell ends in longer cells (T5, Fig. A.1B). Yet even in very short cells ($l_{cylinder} \approx 0$), the forces at microtubule plus ends were sufficient to prevent curling (T4, Fig. A.1C). Since less microtubules contacted the cortex in long cells, the variance of the nuclear position increased (T3, Fig.A.1A). Interestingly, microtubule bundles aligned along the cell axis (T1) even for very short cells (up to $l_{cylinder} = 0.1\mu m$) within three minutes of simulation time. For round cells ($l_{cylinder} = 0$) however, the orientation of microtubule bundles was random. The contact time of microtubules with the cell ends (T7) decreased for shorter cells (Fig. A.1D), which was caused by the higher critical buckling force for short microtubules. Our predictions about the dependency of the nine traits on cell length could now also be verified *in vivo*.

A.2   Stiffness of the Cortex

At the level of light microscopy microtubule pushing forces do not deform the cortex, which is covered by a rigid cell wall. Below this scale the elastic properties of the cortex and its response to force are unknown. In the simulation the cortex is represented by a harmonic potential (see Sec. 2.2.5). Therefore its elasticity k_{cortex} directly relates microtubule polymerization forces to the distance by which a microtubule can protrude from the cell body. Using a stiffness of $k_{cortex} = 100pN\mu m^{-1}$ microtubules stick out from the cortex by less than $\sim 100nm$ at a typical microtubule polymerization force of $\sim 5pN$. Protrusions that small are not detectable by light microscopy and hence correctly represent the steadiness of the cell wall observed *in vivo*.

Varying the stiffness logarithmically between 10^{-1} and $10^3 pN\mu m^{-1}$ showed that there was almost no effect on the nine traits for higher values of k_{cortex} (Fig. A.2) which would therefore also be suitable to use. Incidentally, the simulation became numerically unstable for $k_{cortex} > 3\cdot 10^3 pN/\mu m$. Nevertheless, higher values could be used with a smaller integration time step h.
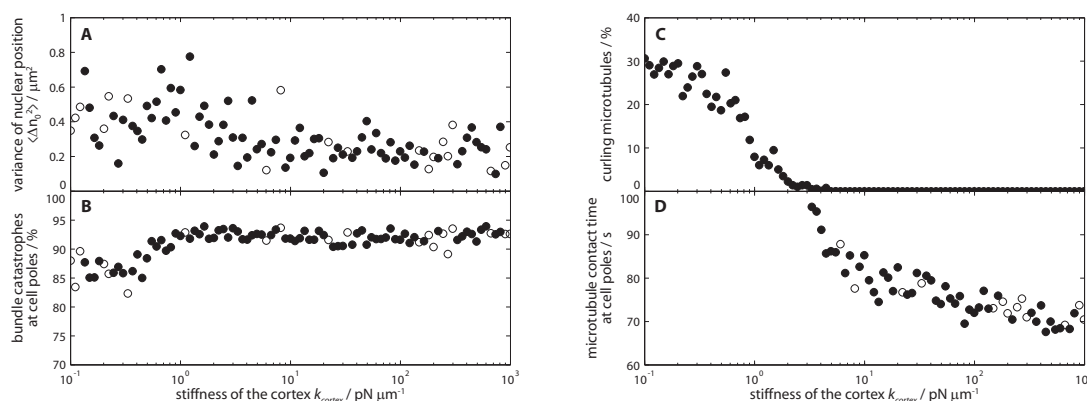
Figure A.2: Variation of the stiffness of the cortex k_{cortex}. Above $k_{cortex} = 10pN\mu m^{-1}$ microtubules were properly confined and most traits were unaffected by the choice of this parameter. Only the contact time (T7) was slightly higher for lower values of k_{cortex}, because microtubules could effectively grow longer before catastrophe was induced by the confinement. For $k_{cortex} < 10pN/\mu m$ microtubules protruded visibly from the cortex and started to curl around the cell poles (T4) (C). Consequently, less bundle catastrophes occurred at the poles (T5) and the variance of the nuclear position (T3) was slightly higher (A and B). Filled symbols denote simulations where the nucleus could be centered within 30min, i.e. T2 was fulfilled. Empty symbols depict simulations where centering took longer. Since the measurement of T3, T5, T6 and T7 started only when the nucleus crossed the cell center (see chapter 3), these traits were effectively measured over a shorter time period in such simulations.

A.3   Viscosity of the Cytoplasm

The viscoelastic properties of the *S. pombe* cytoplasm were investigated by observing the motion of lipid granules of radius $150nm$ in living yeast cells (Tolić-Nørrelykke et al., 2004). It was shown that the granules exhibit subdiffusive behavior at time scales between 10^{-4} and $10^{2}s$ which is thought to be caused by the presence of polymer networks and membranous structures. Above $1s$ however, some granules diffused normally (see Fig.3 in Tolić-Nørrelykke et al., 2004). At this time scale, we used Stokes's law together with the Einstein-Smoluchowski relation, to estimate the effective viscosity of the cytoplasm. Since the particles are small compared to the radius of the cell the effects of lubrication flow were neglected in this calculation. From Fig. 3 in Tolić-Nørrelykke et al. (2004) we determined a mean square displacement of $\langle \Delta r^2 \rangle = 10^{-2} \mu m^2$ at a time lag of $1s$, which results in an effective viscosity of $\eta \approx 0.9 pN s/\mu m^2$, i.e. $900\times$ water. For simplicity, we assumed a purely viscous behavior of the cytoplasm in our model and used this value for all our simulations.

To study the influence of this parameter on the nine traits we varied the viscosity between 10^{-3} (i.e. the viscosity of water) and $10^{2}pN s/\mu m^2$. The only characteristic affected by the viscosity was the positioning of the nucleus (Fig. A.3). For values above $2pN s/\mu m^2$ the nucleus could not be centered anymore within the time measured in wild type cells (T2). Lowering the viscosity increased the variance of the nuclear position.

A.4   Radius of the Nucleus

Because of the lubrication flow between the nucleus and the cortex the mobility of the nucleus is highly sensitive to the size of the gap $r_{cell} - r_{nucleus}$. Changing $r_{nucleus}$ from $1.5\mu m$ to $1.6\mu m$
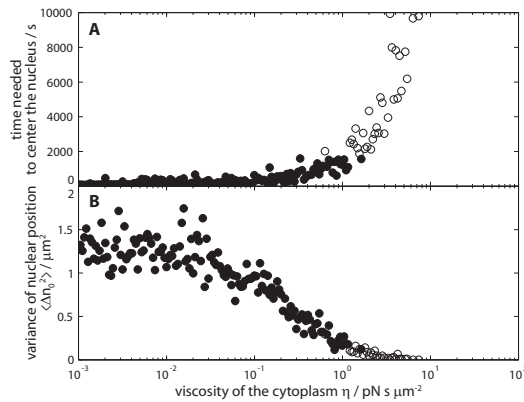
Figure A.3: Variation of the cytoplasmic viscosity η. Out of the nine traits, only the positioning of the nucleus was affected for values between $10^{-3} pN\,s\,\mu m^{-2}$ and $10^{2} pN\,s\,\mu m^{-2}$. (A) Above $\eta = 2pNs\mu m^{-2}$ the nucleus could not be centered anymore within 30 minutes (T2). (B) Simulations with low viscosity exhibited a large variance of the nuclear position $\langle \Delta n_0^2 \rangle$ (T3). For an explanation of symbols see Fig. A.2.
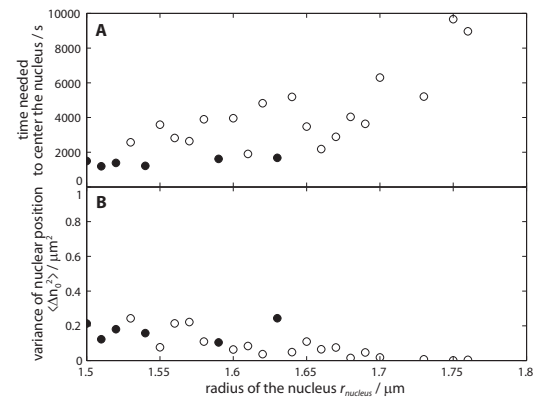
Figure A.4: Variation of the nuclear radius $r_{nucleus}$. Only the positioning of the nucleus was affected (T2 & T3). The smaller the gap between the nucleus and the cortex the harder it becomes for the cytoplasm to pass through the gap (see Sec. 2.2.4.1) and for the nucleus to move. For $r_{nucleus} > 1.65\mu m$ the nucleus was not centered anymore within the time observed in wild type cells (T2). For an explanation of symbols see Fig. A.2.

reduces the predicted mobility by a factor 2 (see Sec. 2.2.4.1). Consequently we determined the relative size of the gap *in vivo*, using wild type cells transformed with pD817, a plasmid encoding for
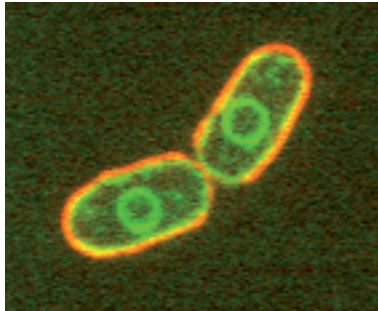
Figure A.5: Measuring the size of the cell and the nucleus. The image shows a maximum projection of the central slices from a z-stack ($\Delta z = 0.5\mu m$). The plasma membrane and the nucleus are shown in green, the cortex in red.

GFP-cytochrome P450 reductase to label nuclear and plasma membranes. Additionally, cells were incubated with TRITC-lectin to label the cell cortex from the outside (Fig. A.5). Images were taken with a spinning disc confocal microscope. The radius of the nucleus was determined from maximum projections by fitting a circle to the GFP-signal. A circular Hough transformation was used to automatically detect the nuclei and measure their radii. To determine the size of the cell the plasma membrane and the cortex were fitted to the shape of an idealized pombe cell, i.e. a rectangle closed by two half-circles. A Gauss-Newton method was implemented to minimize the geometric distance to the cell outline. The average of the two short half-axis was then used for the cell radius. The fitting was done semi-automatically with custom macros in Matlab. We found $r_{nucleus}/r_{cell} \approx 0.75$, i.e. $r_{nucleus} = 1.5\mu m$ for $r_{cell} = 2\mu m$ ($n = 56$ cells).

We varied the radius of the nucleus between 1.5 and $2.0\mu m$. As for the viscosity of the cytoplasm, the only characteristic influenced was the positioning of the nucleus (T2 & T3) (Fig. A.4). The variance of the nuclear position decreased for larger radii (T3) until centering failed within the time observed in wild type cells (T2).

A.5   Mobility of "Buoys" in the Nuclear Membrane

Little is known about the identity of the molecules involved in anchoring microtubule bundles to the nucleus. Possible candidates are Mia1p (Zheng et al., 2006) and Mto2p (Janson et al., 2005). To estimate the mobility of the anchoring points in the simulation, we therefore considered the Spindle Pole Body (SPB) which is the most prominent of the microtubule anchors *in vivo*. In interphase the SPB is embedded in the nuclear membrane with one microtubule bundle usually being attached to it. In electron microscopy it is observed as an oblate ellipsoid with a thickness of $h = 90nm$ and a radius of $r = 90nm$ (Ding et al., 1997). These dimensions can be used to calculate its mobility in the membrane using the Saffman-Dellbrück equation (Saffman and Delbrück, 1975) which describes the mobility of a cylindrical object in a thin membrane surrounded by a viscous fluid:

$$\mu^s = \frac{1}{4\pi\eta_{nucleus} h} \left(\ln \frac{\eta_{nucleus} h}{\eta_{cell} r} - \gamma \right) \tag{A.1}$$

where γ is Euler's constant and $\eta_{nucleus}$ is the viscosity of the nuclear membrane. Assuming that $\eta_{nucleus} \sim 10 \cdot \eta_{cell}$, we find $\mu^S \sim 0.17 \mu m/pN\, s$. In wild type cells the mobility of the SPB is most likely further delimited by the chromosomes being attached to the nucleoplasmic face of the SPB. Therefore we used $\mu^S = 0.1 \mu m/pN\, s$ in our simulations, and found that varying μ^S up to three orders of magnitude in each direction had no effect on T2-T9. Only if $\mu^S < 10^{-2} \mu m/pN\, s$, microtubule bundles took significantly longer to orient than in wild type cells (T1). This was partly compensated by the elasticity of the microtubule-nucleus links, which allowed microtubule bundles to align partially even if the buoys did not move.
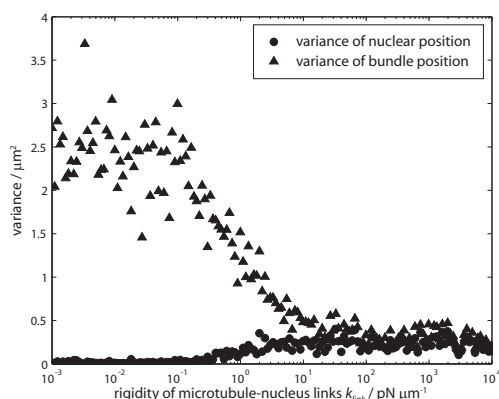
Figure A.6: Variation of the link stiffness k_{link}. The motion of microtubule bundles and the nucleus is uncoupled for $k_{link} < 10^{-1} pN/\mu m$ (the bundles move independently of the nucleus, which remains mostly immobile). For $k_{link} > 10^2 pN/\mu m$, they move together with a variance of $\sim 0.2 \mu m^2$.

A.6   Microtubule-Nucleus Steric Interaction

To prevent microtubule bundles from entering the nucleus, the simulation includes a repulsive interaction between the nucleus and any part of a microtubule entering it. This interaction is modeled as a repulsive harmonic potential of stiffness k_{steric}. Technically, the repulsion is independent of the links between the nucleus and microtubule bundles. Yet, we set $k_{steric} = k_{link}$ since both interactions are mediated by the elastic nuclear membrane *in vivo*. Varying k_{steric} over several orders of magnitude (even setting $k_{steric} = 0$) revealed that this parameter does not influence any of the nine traits.

A.7   Stiffness of Microtubule-Nucleus Links

In vivo the nucleus visibly deforms as it is being pushed by the attached microtubule bundles (Daga et al., 2006; Tran et al., 2001; Janson et al., 2005). For this reason the motion of the nucleus and its bundles is thought to be coupled softly. Forces transmitted on the nucleus are attenuated, but

nevertheless determine its motion at long time scales. The deformations can reach $\sim 1\mu m$ (Daga et al., 2006) and are driven by microtubule polymerization, which produces forces in the range of $\sim 5pN$ per microtubule. We therefore used a value of $k_{link} = 10pN/\mu m$ to match the magnitude of the deformations observed in living cells.

To examine the influence of k_{link}, it was varied between 10^{-3} and $10^4 pN/\mu m$. The nucleus was initially placed at the cell center to be able to study the system at low values of k_{link} where re-centering would fail otherwise. Two regimes for the relative motion of microtubule bundles and the nucleus were found (Fig. A.6). Interestingly, the value used to match the deformations observed *in vivo* is at the onset of the transitional region between the two regimes.

A.8 Microtubule Dynamics

A.8.1 Free Growth Velocity

Experimental values for the average growth velocity v_0 of free microtubules in *S. pombe* (i.e. in the cytoplasm without opposing force) range from 0.032 to $0.06\mu m/s$ (Tran et al., 2001; Janson et al., 2005; Busch et al., 2004). For the reference set of parameters we used a medial value $v_g = 0.05\mu m/s$. Theoretically, the average length of microtubules with independent dynamics is v_0/c_0 (assuming microtubules do not rescue within the cytoplasm). Consequently, v_0 has a strong influence on the nine traits and was varied for each of the three models of dynamic instability.

A.8.2 Shrinkage Velocity

Measured values for the shrinkage velocity v_s of microtubules in *S. pombe* range from $0.07\mu m/s$ (Drummond and Cross, 2000) to $0.21\mu m/s$ (Loïodice et al., 2005). We chose a medial value of $0.15\mu m/s$ (the shrinkage velocity is specified as a negative speed in the simulation). However, since the length distribution of microtubules does not depend on v_s in the absence of rescues, we did not expect this parameter to influence the nine traits.

To confirm this we varied the shrinkage rate between 0 and $0.5\mu m/s$ and indeed found no effect for values above $0.05\mu m/s$. Only at very slow shrinkage velocities the variance of the nuclear position increased slightly (Fig. A.7), because microtubules spent an increasing amount of time shrinking. This effectively decreased the frequency of microtubule pushing events. Yet, this effect is unlikely to be relevant *in vivo*.
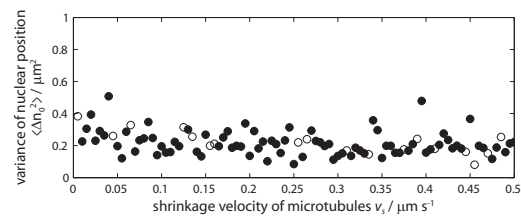
Figure A.7: Variation of the shrinkage velocity v_s. The variance of the nuclear position $\langle \Delta n_0^2 \rangle$ increases slightly for very slow shrinkage velocities. For an explanation of symbols see Fig. A.2.

A.8.3 Free Catastrophe Rate

The free catastrophe rate c_0 defines the probability of catastrophe for microtubules which are not influenced by position or force, i.e. microtubules which grow unhindered in the cytoplasm. *In vivo* measurements of c_0 are complicated for the following reasons: Firstly, only catastrophes of the longest microtubules within a bundle can so far be registered, since shorter microtubules are difficult to detect by light microscopy. Secondly the rates measured this way usually include catastrophes that occurred

at the cell poles, e.g. $c \approx 0.005/s$ (Tran et al., 2001; Busch and Brunner, 2004) and therefore possibly contain catastrophes that were induced locally.

However, an upper bound for the free catastrophe rate can be obtained theoretically from the requirement of microtubule bundles to fulfill trait T5 (90% of all microtubule bundles reach the cell poles). Since microtubule dynamics within a bundle are not correlated, we can deduce the length distribution of bundles for the case of independent dynamics analytically (see Sec. 4.1.2). From this, we can estimate the fraction of bundles that grow long enough to reach the cell poles when the nucleus is centered (see Sec. 4.1.3). The dashed lines in the plots in section 5.1 indicate the result: if c_0 is below this line T5 should be fulfilled, which was confirmed by the simulation. With 2 microtubules per half-bundle, $c_0 < 0.0063/s$ ($0.38/min$) is needed at $v_0 = 0.05\mu m/s$. We therefore used $c_0 = 0.005/s$ for the reference set of parameters.

A.8.4   Rescue Rate

Shrinking microtubules in *S.pombe* are not observed to undergo rescue within the cytoplasm (Tran et al., 2001). Accordingly the cytoplasmic rescue rate is set to zero in the simulation.

A.9   Microtubule Response to Force

Microtubule behavior under force is influenced by three parameters: The flexural rigidity κ_{mt} which defines bending, the sensitivity to force f_s, which affects the assembly rate and $c_{stalled}$, which controls the increase of the catastrophe rate.
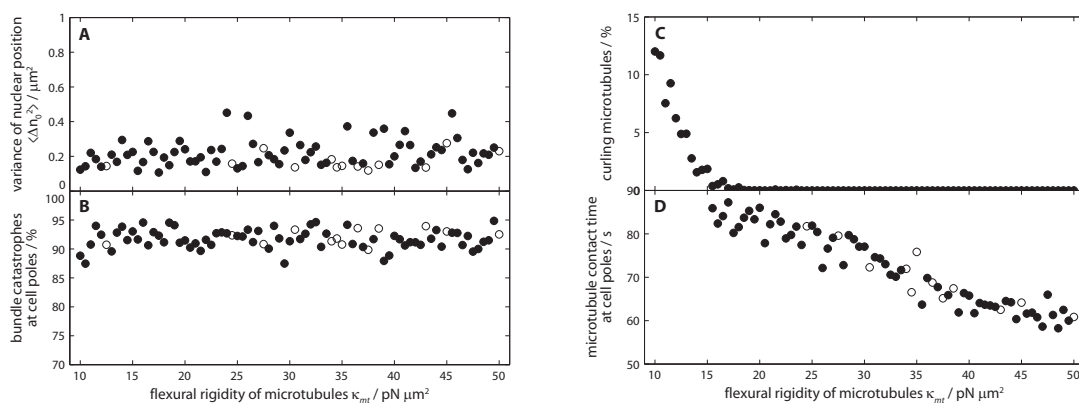
Figure A.8: Variation of the flexural rigidity κ_{mt} of microtubules. (A, B) The variance of the nuclear position and the location of catastrophes are not affected by κ_{mt}. (C) Flexible microtubules curl more easily. (D) Stiff microtubules have lower contact times (see text). For an explanation of symbols see Fig. A.2.

### A.9.1   Flexural Rigidity of Microtubules

The flexural rigidity of microtubules κ_{mt} determines how microtubules bend under compressive forces. *In vitro* measurements range from $5pN\mu m^2$ (Gittes et al., 1993) up to $40pN\mu m^2$ (Dogterom and Yurke, 1997). We used $\kappa_{mt} = 30pN\mu m^2$. The effective bending elasticity of microtubule bundles can be higher than just the sum of their individual microtubules, if the microtubules cannot slide

relative to each other longitudinally. In *S. pombe* however, microtubules sometimes bend away from the rest of the bundle and therefore do not seem to be tightly linked outside of the overlap zone. Accordingly, microtubules in the simulation are not connected outside of this region.

Varying the flexural rigidity in the simulation we found that the variance of the nuclear position and the distribution of catastrophes were not affected, if κ_{mt} was between 10 and $50 pN\mu m^2$ (Fig. A.8A and B). Only for very flexible fibers ($\kappa_{mt} < 15 pN\mu m^2$) the number of catastrophes at the cell poles decreased due to curling, which is generally facilitated for more flexible microtubules (Fig. A.8C). Microtubules did not curl for $\kappa_{mt} > 25 pN\mu m^2$. Furthermore, microtubule contact times at the cell poles were lower for stiffer microtubules (Fig. A.8D), due to the increasing confinement forces opposing microtubule growth. Higher forces consequently lead to a higher catastrophe rate in the force dependent model.

A.9.2 Sensitivity to Force

The parameter f_s defines the exponential dependence of the growth velocity v_g on force (see eq. 2.14). The value used in the simulation was measured using pure tubulin (Dogterom and Yurke, 1997). In these experiments the normalized force f/κ_{mt} was determined from the shape of microtubules, assuming they behave like homogeneous elastic rods (Landau and Lifshitz, 1986). Plotting the growth velocity v_g against f/κ_{mt} uncovered an exponential relationship, which was fitted using 3 parameters A, B and C to $v_g = A\, exp(C\, f/\kappa_{mt}) - B$. Combining the published value of $C = 18 \pm 4\mu m^2$ (Dogterom and Yurke, 1997), with our chosen flexural rigidity $\kappa_{mt} = 30 pN\mu m^2$ provided $f_s = \kappa_{mt}/C = 1.67 pN$.
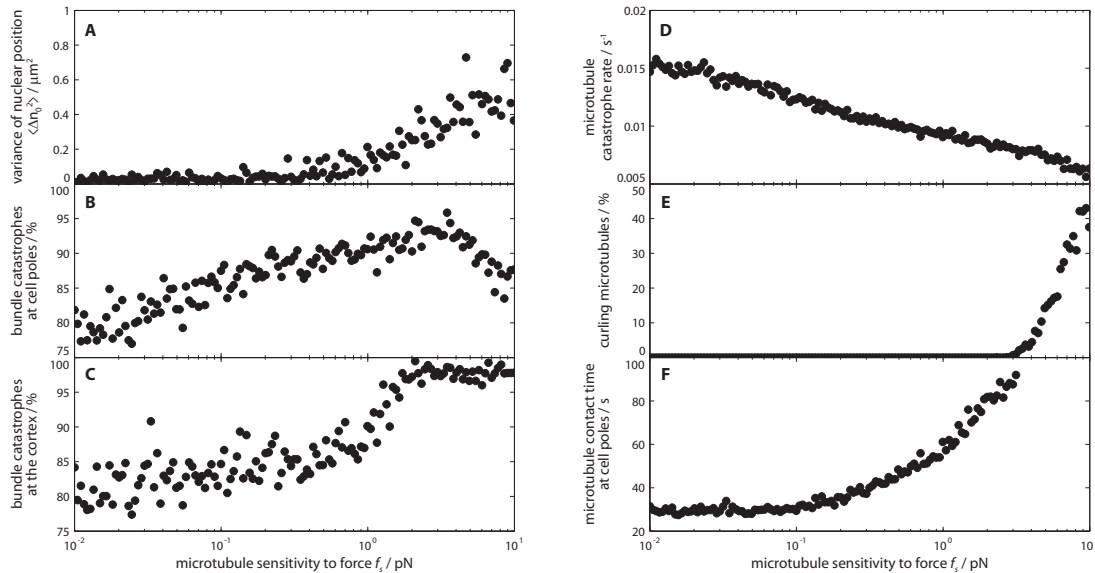

Figure A.9: Variation of microtubule sensitivity to force f_s. Microtubules that are insensitive to force (high f_s) continue polymerizing at the cell poles leading to (A) a higher variance of the nuclear position; (E) a higher number of curling microtubules and (F) an increase of the the contact time. More sensitive microtubules (low f_s) have more catastrophes (D). Very sensitive microtubules catastrophe even before reaching the cortex (B and C).

In the simulation f_s was varied between 10^{-2} and $10 pN$. The nucleus was initially placed at the center to be able to explore the behavior of the system for very sensitive microtubules (low f_s). We

found that the variance of the nuclear position increased for more stable microtubules (higher f_s) (Fig. A.9A). The contact time at the cell poles became longer (Fig. A.9F) as microtubules were less affected by force and catastrophes occurred later. For $f_s > 3pN$ the increase of the catastrophe rate due to force (Fig. A.9D) was not sufficient anymore to stop microtubules from curling around cell poles (Fig. A.9E). Consequently the amount of catastrophes at the poles decreased as microtubules curled and grew back towards the nucleus (Fig. A.9B). Interestingly, the value measured, $f_s = 1.67pN$, is located in the intermediate region where microtubules neither curl nor catastrophe due to Brownian motion.

A.9.3   Catastrophe Rate for Stalled Microtubules

In vitro, rapidly growing microtubules have a higher lifetime (Janson et al., 2003), following a simple linear relationship (see part B). If microtubule growth is stalled completely by an opposing force ($v_g = 0$), catastrophe is observed within $24s$ on average. This value was shown to be independent of tubulin concentration (Janson et al., 2003), which suggests that it can be applied for *S. pombe* even if the tubulin concentration is unknown. We thus used $c_{stalled} = 0.05/s$.
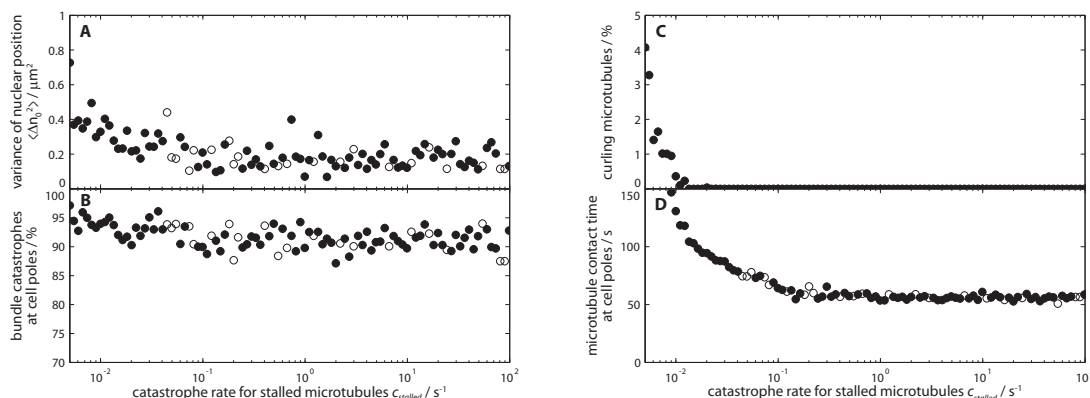
Figure A.10: Variation of the catastrophe rate for stalled microtubules $c_{stalled}$. If the catastrophe rate of slow growing microtubules did not increase sufficiently, microtubules contacted the cell poles for a long time (D) and eventually started to curl (C). Consequently the position of the nucleus exhibited a greater variance (A). The value determined *in vitro*, $c_{stalled} = 0.042s^{-1}$, was sufficient to stop microtubule curling. For an explanation of symbols see Fig. A.2.

We varied $c_{stalled}$ logarithmically between the cytoplasmic rate c_0 and $10^5 s^{-1}$. For $c_{stalled} < 0.02 s^{-1}$ microtubules curled around the cell poles (Fig. A.10C). Notably, simulations with $c_{stalled} \approx c_0$ demonstrated that the slow-down of microtubule polymerization alone was not sufficient to stop microtubules from curling at the poles and to stably center the nucleus. The increase of the catastrophe rate induced by force was needed to fulfill traits T1-T9.
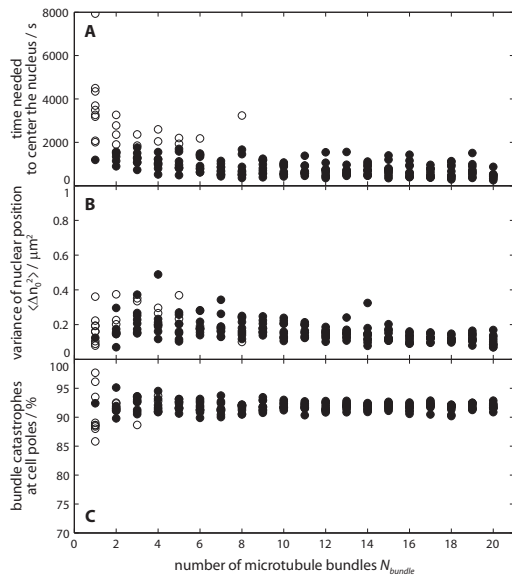
A.10   Microtubule Bundles

A.10.1   Number of Bundles

Wild type cells contain between 3 and 5 microtubule bundles (Tran et al., 2001; Janson et al., 2005; Loïodice et al., 2005). We used $N_{bundle} = 4$ and varied it between 1 and 20, keeping the number
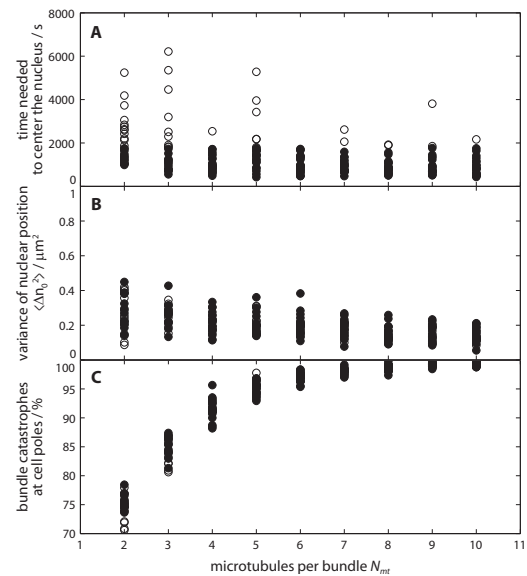
of microtubules per bundle, N_{mt}, constant. We found that nuclear centering proceeded faster and was more accurate for higher values of N_{bundle} (Fig. A.11 A and B), because more microtubules were available for pushing. Furthermore, increasing either N_{bundle} or N_{mt} had similar effects on the centering time and the variance of the nucleus (see Figs. A.11 A and B, A.12 A and B and the discussion of N_{mt} below), due to the fact that the dynamics of microtubules within a bundle were mostly uncorrelated in the simulation. While the motion of the nucleus therefore rather depended on the total number of microtubules ($N_{bundle} \cdot N_{mt}$), other characteristics were more sensitive to the bundle structure (see below).

A.10.2   Bundle Structure

The structure of simulated microtubule bundles is specified by the number of microtubules per bundle N_{mt}, the width of the overlap zone $l_{overlap}$ and the stiffness k_{bundle} of the connections (Fig. 2.2). Experimentally, the number of microtubules per bundle was first determined from images of cells labeled with GFP-tubulin. From the stepwise increase in fluorescence intensity it was estimated that $N_{mt} = 2$ or 3 (Tran et al., 2001). Recent data from electron tomography revealed that the bundle associated to the Spindle Pole Body (SPB) contains more microtubules (5.7 ± 1.5) than the remaining ones (3.25 ± 2.5) (Höög et al., 2007).

Figure A.11: Variation of the number of microtubule bundles N_{bundle}. Centering of the nucleus was (A) faster and (B) more accurate with a higher number of microtubule bundles, while the location of bundle catastrophes (C) was almost unaffected. Ten simulations were run for each value of N_{bundle}. For an explanation of symbols see Fig. A.2.

Figure A.12: Variation of the number of microtubules per bundle N_{mt}. A high number of microtubules per bundle reduced (A) the centering-time and (B) the variance of the nuclear position $\langle \Delta n_0^2 \rangle$. (C) Bundles which contained more microtubules became longer and were more likely to catastrophe at the cell poles. Ten simulations were run for each value of N_{mt}. For an explanation of symbols see Fig. A.2.

For simplicity, all bundles in the simulation were constructed equally using $N_{mt} = 4$ (2 microtubules facing each side). As described in the previous paragraph, increasing N_{mt} facilitated the centering

of the nucleus by increasing the total number of microtubules (Fig. A.12 A and B). Yet, changing
the number of microtubules per bundle alters the spacial distribution of bundle catastrophes (see Fig.
4.1) in contrast to N_{bundle} (Figs. A.11 C, A.12 C). Since the average length of microtubule bundles
increased with the number of microtubules per bundle (equation 4.9), the percentage of catastrophes
in the cell caps increased as well.

The width of the overlap can be determined by imaging cells labeled with GFP-tubulin. Analyzing
again the stepwise increase in the fluorescence signal results in an overlap length of $0.84 \pm 0.29 \mu m$
(Tran et al., 2001). More direct measurements of the antiparallel bundling protein Ase1p-GFP give
$1.4 \pm 0.5 \mu m$ (Loïodice et al., 2005). We chose a medial value of $l_{overlap} = 1 \mu m$. Varying this
parameters between 0.1 and $2 \mu m$ we found no significant effect on any of the traits.

In wild type cells, separation of microtubule bundles is very rare ($0.06/min$) Carazo-Salas and
Nurse (2006) and was therefore neglected in the simulation. On the contrary, bundles do not fall apart
under their own polymerization force even when they push at both cell poles. In the simulation, stiff
links ($k_{bundle} = 1000 pN/\mu m$) were used to simulate the bundling proteins, e.g. Ase1p, which is
thought to crosslink antiparallel microtubules Loïodice et al. (2005). Higher values of k_{bundle} gave
identical results.

A.11   Numerical Parameters

Several parameters are specific to the numerical solver and to the discretization of microtubules, and
should not influence the outcome of the simulation. Lower values for these parameters lead to more
accurate results but also require a higher number of calculations and therefore slow down the simula-
tion. To choose an appropriate set of values we looked at the behavior of the nine traits (T1-T9) upon
modifications of the integration time step h, the microtubule segment length ρ and the convergence
criteria ψ.
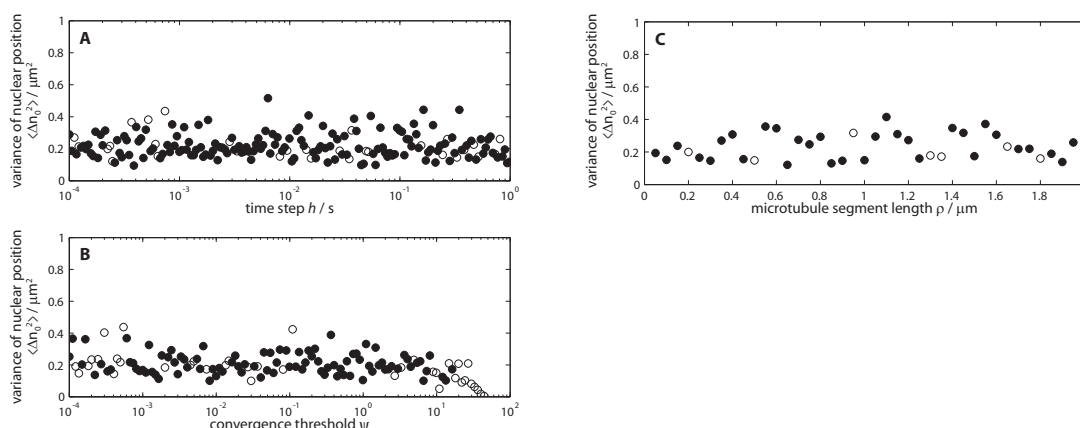
Figure A.13: Variation of numerical parameters. The variance of the nuclear position $\langle \Delta n_0^2 \rangle$ is
shown representative for the nine traits as a function of the integration time-step h (A), the convergence
criteria ψ (B) and the segment length ρ (C). The results of the simulation became inconsistent for $\psi > 10$
($\psi = 0.1$ was used in this study). The implicit integration method performed well in our simulations,
even at large time-steps. For an explanation of symbols see Fig. A.2.

The most important parameter is the integration time step h. By virtue of the implicit integration
scheme (Nédélec, 2002) the simulation was numerically stable even at $h = 1s$. Varying h between
$10^{-4}s$ and $1s$ showed no effect on any of the nine traits (Fig. A.13A). We thus used $h = 0.01s$ in this

study. The parameter ρ defines the distance between the points that are used to calculate the bending of microtubules (Nédélec, 2002). Varying ρ from $0.1\mu m$ to $2\mu m$ did not change the result of the simulation (Fig. A.13C) and $\rho = 0.5\mu m$ was used for all simulations. The convergence threshold ψ of the numerical solver (Nédélec, 2002) was set to 0.1 to minimize the influence on the nine traits (Fig. A.13B). These tests guaranteed that the errors associated with the numerical calculations were low enough for the purpose of our study.

Appendix B

Results of the Variation of v_0 and c_0 for Traits T2 - T9
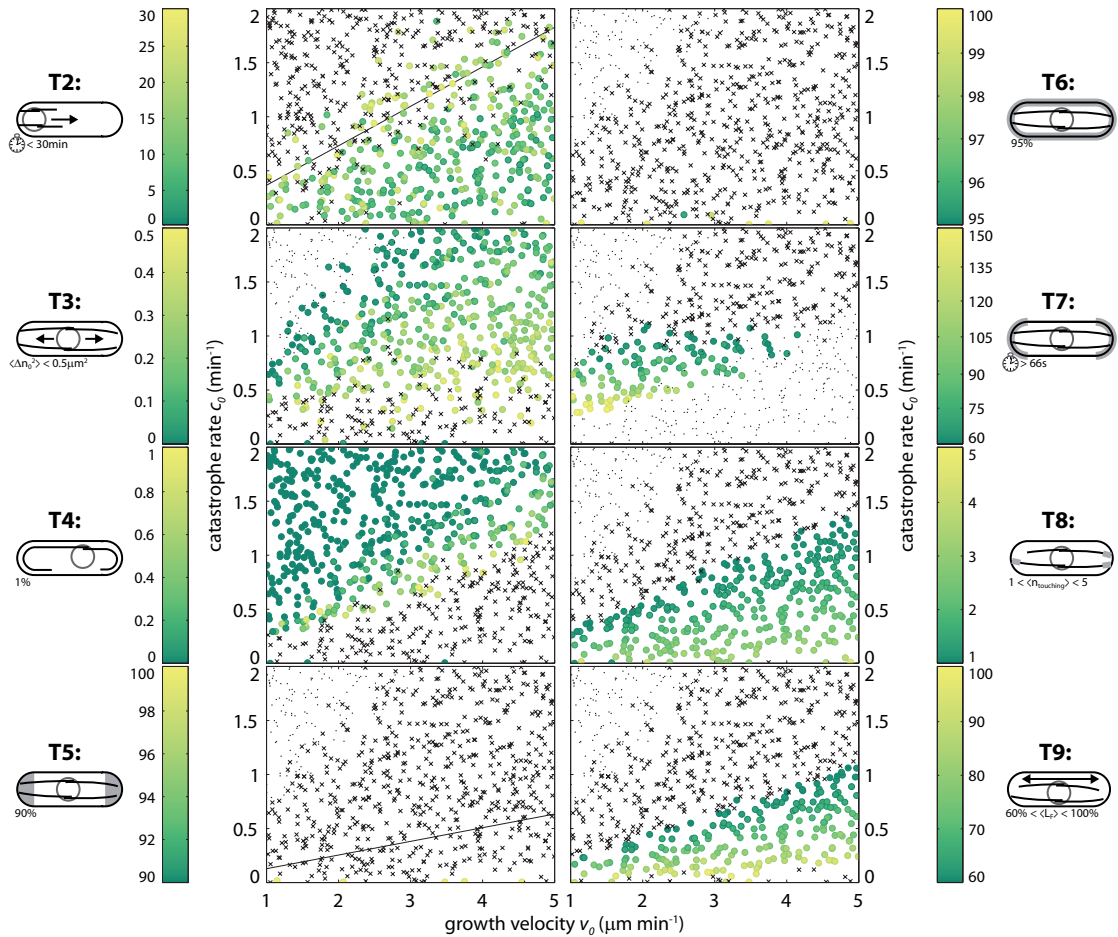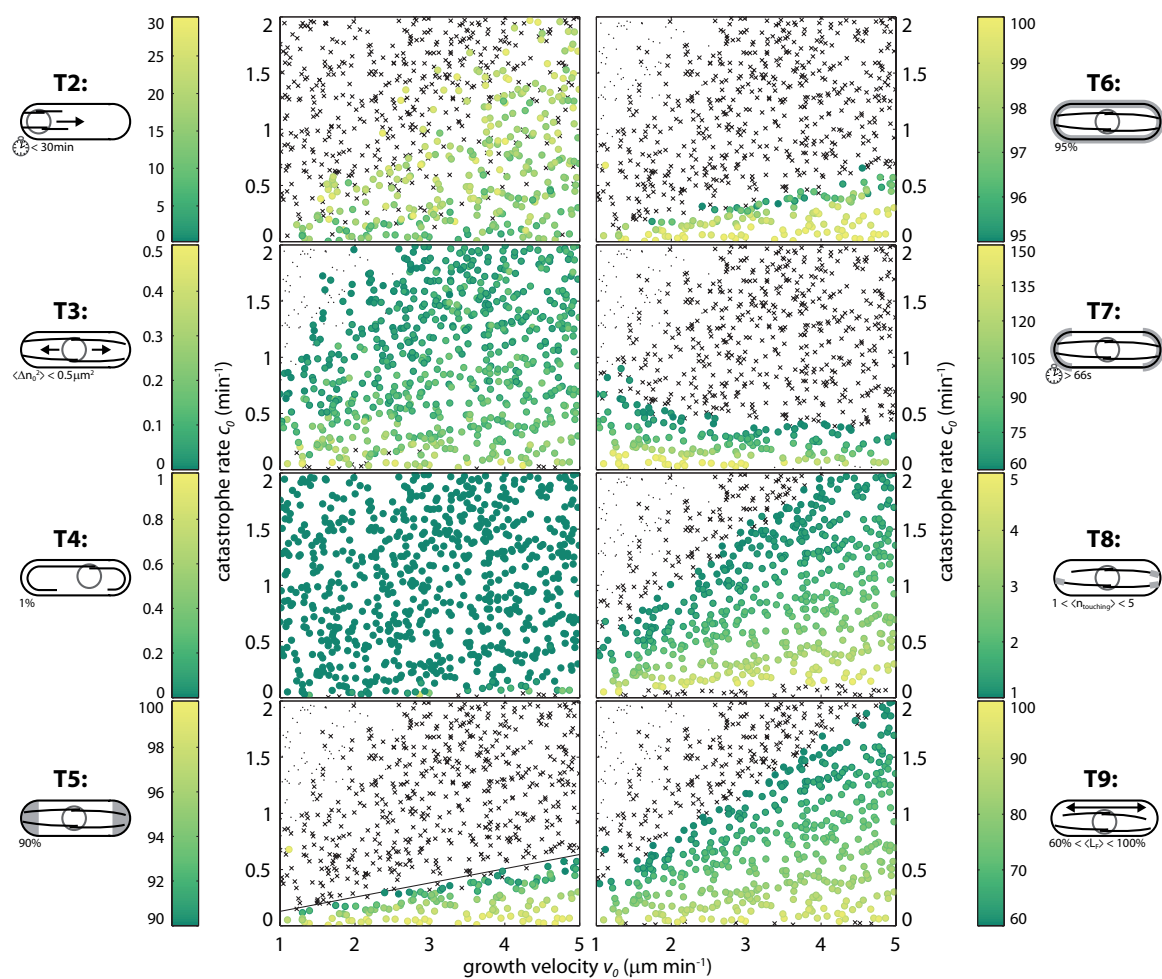

Figure B.1: Evaluation of the traits T2-T9 for simulations with limited tubulin concentration. Circles depict simulations that fulfilled the corresponding trait while crosses mark the ones that failed. In some cases, traits T3 and T5 - T9 could not be evaluated, since the measurement of these traits only includes values after the nucleus reached the cell center. If microtubules were not able to push the nucleus to the center within simulation time, T3 and T5 - T9 were marked by dots. Furthermore, microtubule contact times (T7) could not be determined for microtubules curling around the cell poles. All simulations were performed with $\Sigma_{MT}^0 = 80\mu m$.
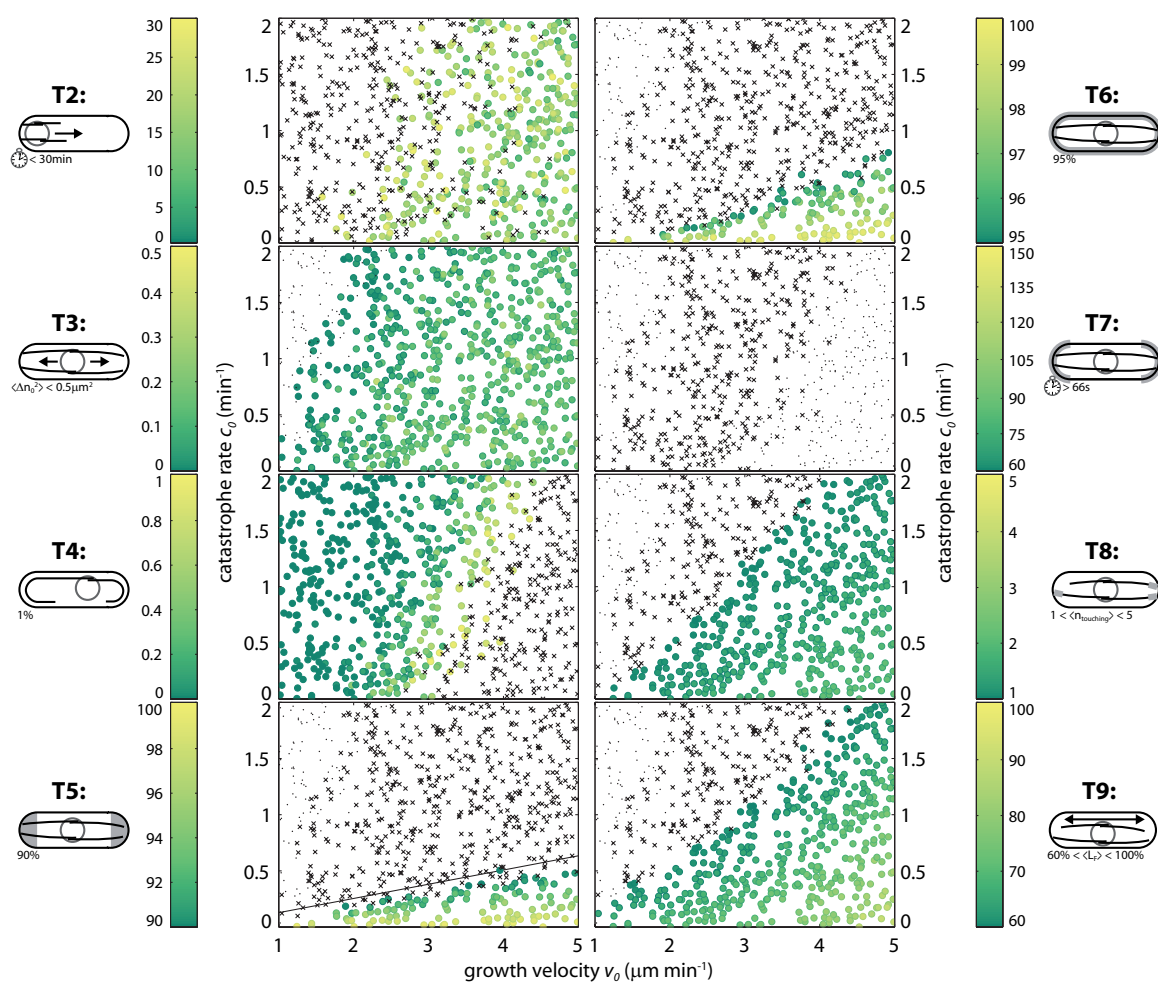
Figure B.2: Evaluation of the traits T2-T9 for simulations with localized catastrophes. The meaning of symbols is as explained in the caption of Fig. B.1. All simulations were performed with $c_{cortex} = l_{cylinder}$ and $c_{poles} = 0.05s^{-1}$.
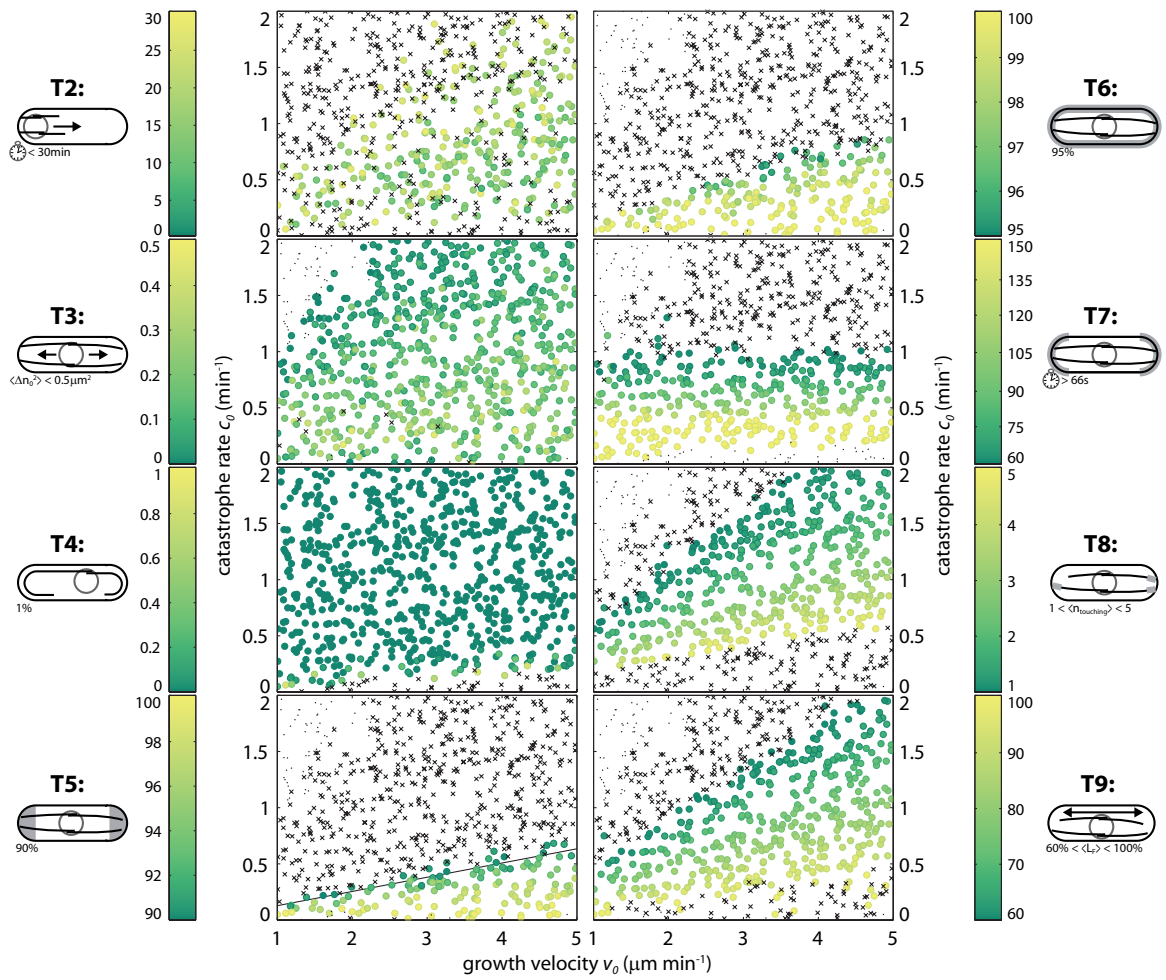
Figure B.3: Evaluation of the traits T2-T9 for simulations with force dependent growth velocity. The meaning of symbols is as explained in the caption of Fig. B.1. All simulations were performed with $f_s = 1pN$.

Figure B.4: Evaluation of the traits T2-T9 for simulations with force dependent growth and catastrophes. The meaning of symbols is as explained in the caption of Fig. B.1. All simulations were performed with the reference set of parameters (see Tab. A.1).

Appendix C

The Distribution of Microtubule Length for Independent Dynamics

C.1 Average Microtubule Length

The average growth velocity, J, for a population of microtubules with independent dynamics (model 1) is given by equation (4.3). This result can be obtained either by solving the differential equations (4.2) (see Verde et al. (1992); Dogterom and Leibler (1993) for further information) or from the following considerations: for given catastrophe and rescue rates, c and r, the average waiting time for the occurrence of the next transition event is just the inverse of the rate. The average time a microtubule spends growing or shrinking is therefore

$$
\begin{aligned}
t_g &= c^{-1} \\
t_s &= r^{-1}.
\end{aligned}
\tag{C.1}
$$

The total average lifetime of a microtubule, i.e. one cycle of growth and shrinkage, is the sum $t_g + t_s = c^{-1} + r^{-1}$. Consequently, the fraction of its total lifetime that a microtubule spends growing or shrinking is given by

$$
\begin{aligned}
\xi_g &= \frac{t_g}{t_g + t_s} = \frac{r}{c + r} \\
\xi_s &= \frac{t_s}{t_g + t_s} = \frac{c}{c + r}
\end{aligned}
\tag{C.2}
$$

respectively, which is equivalent to the fraction of growing and shrinking microtubules in the population. From this it follows directly that the average growth velocity, i.e. the flux of the microtubule length, is

$$
J = \xi_g v_g - \xi_s v_s = \frac{v_g r - v_s c}{c + r},
\tag{C.3}
$$

and the average microtubule length is $\langle L \rangle = Jt$. As described in section 4.1, this is only true in the regime of unbounded microtubule growth. For bounded growth ($J < 0$) one has consider the renucleation of microtubules after complete disassembly, which leads to a constant steady state length.

C.2   Length Distribution In the Bounded Regime

In the regime of bounded growth the average microtubule length, $\langle L \rangle$, reaches a steady state given by equation (4.4). Since the distribution of microtubule length does not change in time, the differential equations (4.2) for the distribution of growing and shrinking microtubule plus ends simplify to

$$
\begin{aligned}
\frac{\partial p_g}{\partial x} &= -\frac{c}{v_g}p_g + \frac{r}{v_g}p_s \\
\frac{\partial p_s}{\partial x} &= -\frac{c}{v_s}p_g + \frac{r}{v_s}p_s.
\end{aligned}
\tag{C.4}
$$

This system of ordinary differential equations can be solved with standard methods, if appropriate boundary conditions are applied. Assuming that

$$
\lim_{x\to\infty} p_g(x) = 0, \qquad \lim_{x\to\infty} p_s(x) = 0
$$

and

$$
\int_0^\infty p_g(x) + p_s(x) = 1
\tag{C.5}
$$

one gets

$$
\begin{aligned}
p_g(x) &= \frac{\lambda}{1 + \frac{v_g}{v_s}}e^{-\lambda x} \\
p_s(x) &= \frac{\lambda}{1 + \frac{v_s}{v_g}}e^{-\lambda x}, \qquad \text{with } \lambda = \langle L \rangle^{-1} = \frac{v_s c - v_g r}{v_g v_s}.
\end{aligned}
\tag{C.6}
$$

The total fraction of microtubule plus ends at x is simply the sum of $p_g(x)$ and $p_s(x)$ and is therefore exponentially distributed as described in section 4.1:

$$
p(x) = p_g(x) + p_s(x) = \lambda e^{-\lambda x}
\tag{C.7}
$$

With equation (C.7) the average microtubule length is

$$
\langle L \rangle = \int_0^\infty x \cdot p(x)dx = \frac{1}{\lambda}.
\tag{C.8}
$$

Appendix D

Experimental Materials & Methods

D.1 Yeast Strains and Media

Unless otherwise stated cells were grown in liquid EMM2 medium at 25°C with standard procedures. For actin staining, wild type (972) and pmo25-79 strains were used. For microtubule live imaging we used wild type and pmo25-79 strains expressing endogenous α2tub N-terminally tagged with GFP and expressed under control of the nmt1 promoter (kind gift of Y.Hiraoka).

D.2 Actin Staining

The method to stain actin was modified from Arai et al. (1998). WT and pmo25-79 cells were grown in YE5S at 25°C and then shifted to 36°C. Cells were fixed at the time-points indicated (Fig. 3) in pre-warmed 3% paraformaldehyde (PFA) (Electron Microscopy Sciences #15710, EM-grade) and 0.24M sorbitol for $30min$ as described in Arai et al. (1998). For the staining, a $2\mu l$ cell pellet was resuspended in $50\mu l$ PEMBAL and incubated with $15\mu l(0.2u/\mu l)$ bodipy-phallacidin (Molecular Probes, B607) for $30min$ at room temperature and then washed 3 times with PEMBAL. Cells were examined under a Zeiss Axiovert 200M microscope using a 100x oil-immersion objective (Zeiss Plan Apochromat, 1.4 NA). Z-stacks were acquired with a spacing of $100nm$ and maximum projections were generated using ImageJ (`http://rsb.info.nih.gov/ij/`).

D.3 Time-Course of Cells Expressing GFP-tubulin

Cells were grown in YE5S at 25°C, shifted to 36°C and then mounted on pre-warmed, lectin (Sigma, L2380) coated slides. Cells were imaged immediately on a microscope (see specifications above) equipped with an environmental chamber (EMBL workshop) equilibrated at 36°C.

D.4 Time-Lapse Imaging and Image Analysis

To determine microtubule contact times, cells expressing GFP-α2tub were mounted on Matek dishes (P35G-1.5-10C) using lectin (Sigma, L2380) and imaged alive on a PerkinElmer Ultraview RS spinning-disc confocal microscope with a 100x oil-immersion objective (Zeiss Plan Neofluar, 1.3 NA). Z-stacks ($0.5\mu m$ steps) covering the full cell volume were acquired every $3sec$. Movies of maximum projections were analyzed and correlated with movies of all single confocal planes using ImageJ to determine the contact point and contact time of microtubules at the cortex of cell poles (see T7 in chapter 3).

Bibliography

F. J. Ahmad, Y. He, K. A. Myers, T. P. Hasaka, F. Francis, M. M. Black and P. W. Baas. Effects of dynactin disruption and dynein depletion on axonal microtubules. *Traffic* **7**, 524–537 (2006).

A. Akhmanova, C. C. Hoogenraad, K. Drabek, T. Stepanova, B. Dortland, T. Verkerk, W. Vermeulen, B. M. Burgering, C. I. D. Zeeuw, F. Grosveld and N. Galjart. Clasps are CLIP-115 and -170 associating proteins involved in the regional regulation of microtubule dynamics in motile fibroblasts. *Cell* **104**, 923–935 (2001).

A. Akhmanova and C. C. Hoogenraad. Microtubule plus-end-tracking proteins: mechanisms and functions. *Curr Opin Cell Biol* **17**, 47–54 (2005).

J. Al-Bassam, R. S. Ozer, D. Safer, S. Halpain and R. A. Milligan. MAP2 and tau bind longitudinally along the outer ridges of microtubule protofilaments. *J Cell Biol* **157**, 1187–1196 (2002).

B. Alberts, A. Johnson, J. Lewis, M. Raff, K. Roberts and P. Walter. *Molecular Biology of The Cell*. Garland Science (2002).

L. Amos and A. Klug. Arrangement of subunits in flagellar microtubules. *J Cell Sci* **14**, 523–549 (1974).

R. Arai, K. Nakano and I. Mabuchi. Subcellular localization and possible function of actin, tropomyosin and actin-related protein 3 (Arp3) in the fission yeast Schizosaccharomyces pombe. *Eur J Cell Biol* **76**, 288–295 (1998).

R. Arai and I. Mabuchi. F-actin ring formation and the role of F-actin cables in the fission yeast Schizosaccharomyces pombe. *J Cell Sci* **115**, 887–898 (2002).

I. Arnal, E. Karsenti and A. A. Hyman. Structural transitions at microtubule ends correlate with their dynamic properties in Xenopus egg extracts. *J Cell Biol* **149**, 767–774 (2000).

I. Arnal, C. Heichette, G. S. Diamantopoulos and D. Chrétien. CLIP-170/tubulin-curved oligomers coassemble at microtubule ends and promote rescues. *Curr Biol* **14**, 2086–2095 (2004).

J. M. Askham, K. T. Vaughan, H. V. Goodson and E. E. Morrison. Evidence that an interaction between EB1 and p150(Glued) is required for the formation and maintenance of a radial microtubule array anchored at the centrosome. *Mol Biol Cell* **13**, 3627–3645 (2002).

N. Ausmees, J. R. Kuhn and C. Jacobs-Wagner. The bacterial cytoskeleton: an intermediate filament-like function in cell shape. *Cell* **115**, 705–713 (2003).

A. F. Baas, L. Smit and H. Clevers. LKB1 tumor suppressor protein: PARtaker in cell polarity. *Trends Cell Biol* **14**, 312–319 (2004).

P. W. Baas, C. V. Nadar and K. A. Myers. Axonal transport of microtubules: the long and short of it. *Traffic* **7**, 490–498 (2006).

F. A. Barr and J. Egerer. Golgi positioning: are we looking at the right MAP? *J Cell Biol* **168**, 993–998 (2005).

R. Behrens and P. Nurse. Roles of fission yeast tea1p in the localization of polarity factors and in organizing the microtubular cytoskeleton. *J Cell Biol* **157**, 783–793 (2002).

J. D. Beinhauer, I. M. Hagan, J. H. Hegemann and U. Fleig. Mal3, the fission yeast homologue of the human APC-interacting protein EB-1 is required for microtubule integrity and the maintenance of cell form. *J Cell Biol* **139**, 717–728 (1997).

V. Berlin, C. A. Styles and G. R. Fink. BIK1, a protein required for microtubule function during mating and mitosis in Saccharomyces cerevisiae, colocalizes with tubulin. *J Cell Biol* **111**, 2573–2586 (1990).

L. Blanchoin and T. D. Pollard. Hydrolysis of ATP by polymerized actin depends on the bound divalent cation but not profilin. *Biochemistry* **41**, 597–602 (2002).

J. Boudeau, A. F. Baas, M. Deak, N. A. Morrice, A. Kieloch, M. Schutkowski, A. R. Prescott, H. C. Clevers and D. R. Alessi. MO25alpha/beta interact with STRADalpha/beta enhancing their ability to bind, activate and localize LKB1 in the cytoplasm. *EMBO J* **22**, 5102–5114 (2003).

H. Browning, J. Hayles, J. Mata, L. Aveline, P. Nurse and J. R. McIntosh. Tea2p is a kinesin-like protein required to generate polarized growth in fission yeast. *J Cell Biol* **151**, 15–28 (2000).

H. Browning, D. D. Hackney and P. Nurse. Targeted movement of cell end factors in fission yeast. *Nat Cell Biol* **5**, 812–818 (2003).

D. Brunner and P. Nurse. CLIP170-like tip1p Spatially Organizes Microtubular Dynamics in Fission Yeast. *Cell* **102**, 695–704 (2000).

W. Bu and L.-K. Su. Characterization of functional domains of human EB1 family proteins. *J Biol Chem* **278**, 49721–49731 (2003).

P. M. Bungay and H. Brenner. The Motion of a Closely-Fitting Sphere in a Fluid-Filled Tube. *Int J Multiphase Flow* **1**, 25–56 (1973).

K. S. Burbank and T. J. Mitchison. Microtubule dynamic instability. *Curr Biol* **16**, R516–R517 (2006).

R. G. Burns. Alpha-, beta-, and gamma-tubulins: sequence comparisons and structural constraints. *Cell Motil Cytoskeleton* **20**, 181–189 (1991).

K. E. Busch and D. Brunner. The microtubule plus end-tracking proteins mal3p and tip1p cooperate for cell-end targeting of interphase microtubules. *Curr Biol* **14**, 548–559 (2004).

K. E. Busch, J. Hayles, P. Nurse and D. Brunner. Tea2p Kinesin Is Involved in Spatial Microtubule Organization by Transporting Tip1p on Microtubules. *Dev Cell* **6**, 831–843 (2004).

M. Caplow, R. Ruhlen, J. Shanks, R. A. Walker and E. D. Salmon. Stabilization of microtubules by tubulin-GDP-Pi subunits. *Biochemistry* **28**, 8136–8141 (1989).

M. Caplow, R. L. Ruhlen and J. Shanks. The free energy for hydrolysis of a microtubule-bound nucleotide triphosphate is near zero: all of the free energy for hydrolysis is stored in the microtubule lattice. *J Cell Biol* **127**, 779–788 (1994).

R. E. Carazo-Salas and P. Nurse. Self-organization of interphase microtubule arrays in fission yeast. *Nat Cell Biol* **8**, 1102–1107 (2006).

R. E. Carazo-Salas, C. Antony and P. Nurse. The kinesin Klp2 mediates polarization of interphase microtubules in fission yeast. *Science* **309**, 297–300 (2005).

R. Carballido-López. The bacterial actin-like cytoskeleton. *Microbiol Mol Biol Rev* **70**, 888–909 (2006).

M. F. Carlier. Actin polymerization and ATP hydrolysis. *Adv Biophys* **26**, 51–73 (1990).

M. F. Carlier and D. Pantaloni. Binding of phosphate to F-ADP-actin and role of F-ADP-Pi-actin in ATP-actin polymerization. *J Biol Chem* **263**, 817–825 (1988).

P. Carvalho, J. S. Tirnauer and D. Pellman. Surfing on microtubule ends. *Trends Cell Biol* **13**, 229–237 (2003).

P. Carvalho, M. L. Gupta, M. A. Hoyt and D. Pellman. Cell cycle control of kinesin-mediated transport of Bik1 (CLIP-170) regulates microtubule stability and dynein activation. *Dev Cell* **6**, 815–829 (2004).

L. Cassimeris. Accessory protein regulation of microtubule dynamics throughout the cell cycle. *Curr Opin Cell Biol* **11**, 134–141 (1999).

L. Cassimeris, D. Gard, P. T. Tran and H. P. Erickson. XMAP215 is a long thin molecule that does not increase microtubule stiffness. *J Cell Sci* **114**, 3025–3033 (2001).

L. Cassimeris. The oncoprotein 18/stathmin family of microtubule destabilizers. *Curr Opin Cell Biol* **14**, 18–24 (2002).

M. Caudron, G. Bunt, P. Bastiaens and E. Karsenti. Spatial coordination of spindle assembly by chromosome-mediated signaling gradients. *Science* **309**, 1373–1376 (2005).

L. Chang and R. D. Goldman. Intermediate filaments mediate cytoskeletal crosstalk. *Nat Rev Mol Cell Biol* **5**, 601–613 (2004).

D. Chrétien and R. H. Wade. New data on the microtubule surface lattice. *Biol Cell* **71**, 161–174 (1991).

D. Chrétien, F. Metoz, F. Verde, E. Karsenti and R. H. Wade. Lattice defects in microtubules: protofilament numbers vary within individual microtubules. *J Cell Biol* **117**, 1031–1040 (1992).

D. Chrétien, S. D. Fuller and E. Karsenti. Structure of growing microtubule ends: two-dimensional sheets close into tubes at variable rates. *J Cell Biol* **129**, 1311–1328 (1995).

D. Chrétien, J. M. Kenney, S. D. Fuller and R. H. Wade. Determination of microtubule polarity by cryo-electron microscopy. *Structure* **4**, 1031–1040 (1996).

R. Cooke. The role of the bound nucleotide in the polymerization of actin. *Biochemistry* **14**, 3250–3256 (1975).

C. R. Cowan and A. A. Hyman. Asymmetric cell division in C. elegans: cortical polarity and spindle positioning. *Annu Rev Cell Dev Biol* **20**, 427–453 (2004).

R. A. Crowther and M. Goedert. Abnormal tau-containing filaments in neurodegenerative diseases. *J Struct Biol* **130**, 271–279 (2000).

R. R. Daga and F. Chang. Dynamic positioning of the fission yeast cell division plane. *Proc Natl Acad Sci U S A* **102**, 8228–8232 (2005).

R. R. Daga, A. Yonetani and F. Chang. Asymmetric microtubule pushing forces in nuclear centering. *Curr Biol* **16**, 1544–1550 (2006).

A. Dammermann, A. Desai and K. Oegema. The minus end in sight. *Curr Biol* **13**, R614–R624 (2003).

L. Dehmelt and S. Halpain. The MAP2/Tau family of microtubule-associated proteins. *Genome Biol* **6**, 204 (2005).

A. Desai and T. J. Mitchison. Microtubule polymerization dynamics. *Annu Rev Cell Dev Biol* **13**, 83–117 (1997).

A. Desai, S. Verma, T. J. Mitchison and C. E. Walczak. Kin I kinesins are microtubule-destabilizing enzymes. *Cell* **96**, 69–78 (1999).

G. S. Diamantopoulos, F. Perez, H. V. Goodson, G. Batelier, R. Melki, T. E. Kreis and J. E. Rickard. Dynamic localization of CLIP-170 to microtubule plus ends is coupled to microtubule assembly. *J Cell Biol* **144**, 99–112 (1999).

R. Ding, R. R. West, D. M. Morphew, B. R. Oakley and J. R. McIntosh. The spindle pole body of Schizosaccharomyces pombe enters and leaves the nuclear envelope as the cell cycle proceeds. *Mol Biol Cell* **8**, 1461–1479 (1997).

M. Dogterom and S. Leibler. Physical Aspects of the Growth and Regulation of Microtubule Structures. *Phys Rev Lett* **70**, 1347–1350 (1993).

M. Dogterom and B. Yurke. Measurement of the Force-Velocity Relation for Growing Microtubules. *Science* **278**, 856–860 (1997).

M. Dogterom, J. W. J. Kerssemakers, G. Romet-Lemonne and M. E. Janson. Force generation by dynamic microtubules. *Curr Opin Cell Biol* **17**, 67–74 (2005).

K. Döhner, C.-H. Nagel and B. Sodeik. Viral stop-and-go along microtubules: taking a ride with dynein and kinesins. *Trends Microbiol* **13**, 320–327 (2005).

D. R. Drummond and R. A. Cross. Dynamics of interphase microtubules in *Schizosaccharomyces pombe*. *Curr Biol* **10**, 766–775 (2000).

D. Dujardin, U. I. Wacker, A. Moreau, T. A. Schroer, J. E. Rickard and J. R. D. Mey. Evidence for a role of CLIP-170 in the establishment of metaphase chromosome alignment. *J Cell Biol* **141**, 849–862 (1998).

A. Ebneth, R. Godemann, K. Stamer, S. Illenberger, B. Trinczek and E. Mandelkow. Overexpression of tau protein inhibits kinesin-dependent trafficking of vesicles, mitochondria, and endoplasmic reticulum: implications for Alzheimer's disease. *J Cell Biol* **143**, 777–794 (1998).

R. Egel, editor. *The Molecular Biology of Schizosaccharomyces pombe*. Springer (2004).

D. W. Ehrhardt and S. L. Shaw. Microtubule dynamics and organization in the plant cortical array. *Annu Rev Plant Biol* **57**, 859–875 (2006).

Elbaum, K. F. D and Libchaber. Buckling microtubules in vesicles. *Phys Rev Lett* **76**, 4078–4081 (1996).

H. P. Erickson and E. T. O'Brien. Microtubule dynamic instability and GTP hydrolysis. *Annu Rev Biophys Biomol Struct* **21**, 145–166 (1992).

C. Faivre-Moskalenko and M. Dogterom. Dynamics of microtubule asters in microfabricated chambers: The role of catastrophes. *Proc Natl Acad Sci* **99**, 16788–16793 (2002).

B. Feierbach and F. Chang. Roles of the fission yeast formin for3p in cell polarity, actin cable formation and symmetric cell division. *Curr Biol* **11**, 1656–1665 (2001).

R. Fodde, J. Kuipers, C. Rosenberg, R. Smits, M. Kielman, C. Gaspar, J. H. van Es, C. Breukel, J. Wiegant, R. H. Giles and H. Clevers. Mutations in the APC tumour suppressor gene cause chromosomal instability. *Nat Cell Biol* **3**, 433–438 (2001).

R. Fodde. The multiple functions of tumour suppressors: it's all in APC. *Nat Cell Biol* **5**, 190–192 (2003).

Y. Gachet and J. S. Hyams. Endocytosis in fission yeast is spatially associated with the actin cytoskeleton during polarised cell growth and cytokinesis. *J Cell Sci* **118**, 4231–4242 (2005).

S. Gadde and R. Heald. Mechanisms and molecules of the mitotic spindle. *Curr Biol* **14**, R797–R805 (2004).

N. Galjart. CLIPs and CLASPs and cellular dynamics. *Nat Rev Mol Cell Biol* **6**, 487–498 (2005).

N. Galjart and F. Perez. A plus-end raft to control microtubule dynamics and function. *Curr Opin Cell Biol* **15**, 48–53 (2003).

Y. Q. Gao, W. Yang and M. Karplus. A structure-based model for the synthesis and hydrolysis of ATP by F1-ATPase. *Cell* **123**, 195–205 (2005).

M. L. Garcia and D. W. Cleveland. Going new places using an old MAP: tau, microtubules and human neurodegenerative disease. *Curr Opin Cell Biol* **13**, 41–48 (2001).

E. C. Garner, C. S. Campbell and R. D. Mullins. Dynamic instability in a DNA-segregating prokaryotic actin homolog. *Science* **306**, 1021–1025 (2004).

B. Gigant, P. A. Curmi, C. Martin-Barbey, E. Charbaut, S. Lachkar, L. Lebeau, S. Siavoshian, A. Sobel and M. Knossow. The 4 Å X-ray structure of a tubulin:stathmin-like domain complex. *Cell* **102**, 809–816 (2000).

B. Gigant, C. Wang, R. B. G. Ravelli, F. Roussi, M. O. Steinmetz, P. A. Curmi, A. Sobel and M. Knossow. Structural basis for the regulation of tubulin by vinblastine. *Nature* **435**, 519–522 (2005).

F. Gittes, B. Mickey, J. Nettleton and J. Howard. Flexural rigidity of microtubules and actin filaments measured from thermal fluctuations in shape. *J Cell Biol* **120**, 923–934 (1993).

J. M. Glynn, R. J. Lustig, A. Berlin and F. Chang. Role of bud6p and tea1p in the interaction between actin and microtubules for the establishment of cell polarity in fission yeast. *Curr Biol* **11**, 836–845 (2001).

G. Goshima, F. Nédélec and R. D. Vale. Mechanisms for focusing mitotic spindle poles by minus end-directed motor proteins. *J Cell Biol* **171**, 229–240 (2005).

P. Graceffa and R. Dominguez. Crystal structure of monomeric actin in the ATP state. Structural basis of nucleotide-dependent actin dynamics. *J Biol Chem* **278**, 34172–34180 (2003).

A. Grallert, C. Beuter, R. A. Craven, S. Bagley, D. Wilks, U. Fleig and I. M. Hagan. S. pombe CLASP needs dynein, not EB1 or CLIP170, to induce microtubule instability and slows polymerization rates at cell tips in a dynein-dependent manner. *Genes Dev* **20**, 2421–2436 (2006).

A. C. Groen, L. A. Cameron, M. Coughlin, D. T. Miyamoto, T. J. Mitchison and R. Ohi. XRHAMM functions in ran-dependent microtubule nucleation and pole formation during anastral spindle assembly. *Curr Biol* **14**, 1801–1811 (2004).

O. J. Gruss, R. E. Carazo-Salas, C. A. Schatz, G. Guarguaglini, J. Kast, M. Wilm, N. L. Bot, I. Vernos, E. Karsenti and I. W. Mattaj. Ran induces spindle assembly by reversing the inhibitory effect of importin alpha on TPX2 activity. *Cell* **104**, 83–93 (2001).

I. M. Hagan. The fission yeast microtubule cytoskeleton. *J Cell Sci* **111 (Pt 12)**, 1603–1612 (1998).

I. Hayashi and M. Ikura. Crystal structure of the amino-terminal microtubule-binding domain of end-binding protein 1 (EB1). *J Biol Chem* **278**, 36430–36434 (2003).

J. Hayles and P. Nurse. A journey into space. *Nat Rev Mol Cell Biol* **2**, 647–656 (2001).

R. Heald. A dynamic duo of microtubule modulators. *Nat Cell Biol* **2**, E11–E12 (2000).

R. Heald, R. Tournebize, T. Blank, R. Sandaltzopoulos, P. Becker, A. Hyman and E. Karsenti. Self-organization of microtubules into bipolar spindles around artificial chromosomes in Xenopus egg extracts. *Nature* **382**, 420–425 (1996).

B. T. Helfand, L. Chang and R. D. Goldman. The dynamic and motile properties of intermediate filaments. *Annu Rev Cell Dev Biol* **19**, 445–467 (2003).

E. R. Hildebrandt and M. A. Hoyt. Mitotic motors in Saccharomyces cerevisiae. *Biochim Biophys Acta* **1496**, 99–116 (2000).

P. J. Hollenbeck and W. M. Saxton. The axonal transport of mitochondria. *J Cell Sci* **118**, 5411–5419 (2005).

T. E. Holy, M. Dogterom, B. Yurke and S. Leibler. Assembly and positioning of microtubule asters in microfabricated chambers. *Proc Natl Acad Sci U S A* **94**, 6228–6231 (1997).

S. Honnappa, C. M. John, D. Kostrewa, F. K. Winkler and M. O. Steinmetz. Structural insights into the EB1-APC interaction. *EMBO J* **24**, 261–269 (2005).

J. L. Höög, C. Schwartz, A. T. Noon, E. T. O'toole, D. N. Mastronarde, J. R. McIntosh and C. Antony. Organization of interphase microtubules in fission yeast analyzed by electron tomography. *Dev Cell* **12**, 349–361 (2007).

H. Hotani and T. Horio. Dynamics of microtubules visualized by darkfield microscopy: treadmilling and dynamic instability. *Cell Motil Cytoskeleton* **10**, 229–236 (1988).

M.-C. Hou, D. J. Wiley, F. Verde and D. McCollum. Mob2p interacts with the protein kinase Orb6p to promote coordination of cell polarity with cell cycle progression. *J Cell Sci* **116**, 125–135 (2003).

W. D. Howard and S. N. Timasheff. GDP state of tubulin: stabilization of double rings. *Biochemistry* **25**, 8292–8300 (1986).

A. W. Hunter, M. Caplow, D. L. Coy, W. O. Hancock, S. Diez, L. Wordeman and J. Howard. The kinesin-related protein MCAK is a microtubule depolymerase that forms an ATP-hydrolyzing complex at microtubule ends. *Mol Cell* **11**, 445–457 (2003).

A. A. Hyman, S. Salser, D. N. Drechsel, N. Unwin and T. J. Mitchison. Role of GTP hydrolysis in microtubule dynamics: information from a slowly hydrolyzable analogue, GMPCPP. *Mol Biol Cell* **3**, 1155–1167 (1992).

M. E. Janson, M. E. d. Dood and M. Dogterom. Dynamic instability of microtubules is regulated by force. *J Cell Biol* **161**, 1029–1034 (2003).

M. E. Janson, T. G. Setty, A. Paoletti and P. T. Tran. Efficient formation of bipolar microtubule bundles requires microtubule-bound gamma-tubulin complexes. *J Cell Biol* **169**, 297–308 (2005).

M. E. Janson, R. Loughlin, I. Loïodice, C. Fu, D. Brunner, F. J. Nédélec and P. T. Tran. Crosslinkers and motors organize dynamic microtubules to form stable bipolar arrays in fission yeast. *Cell* **128**, 357–368 (2007).

T. Kamasaki, R. Arai, M. Osumi and I. Mabuchi. Directionality of F-actin cables changes during the fission yeast cell cycle. *Nat Cell Biol* **7**, 916–917 (2005).

M. Kirschner and T. Mitchison. Beyond self-assembly: from microtubules to morphogenesis. *Cell* **45**, 329–342 (1986).

A. Kis, S. Kasas, B. Babić, A. J. Kulik, W. Benoît, G. A. D. Briggs, C. Schönenberger, S. Catsicas and L. Forró. Nanomechanics of microtubules. *Phys Rev Lett* **89**, 248101 (2002).

Y. Komarova, G. Lansbergen, N. Galjart, F. Grosveld, G. G. Borisy and A. Akhmanova. EB1 and EB3 control CLIP dissociation from the ends of growing microtubules. *Mol Biol Cell* **16**, 5334–5345 (2005).

Y. A. Komarova, I. A. Vorobjev and G. G. Borisy. Life cycle of MTs: persistent growth in the cell interior, asymmetric transition frequencies and effects of the cell boundary. *J Cell Sci* **115**, 3527–3539 (2002).

E. D. Korn, M. F. Carlier and D. Pantaloni. Actin polymerization and ATP hydrolysis. *Science* **238**, 638–644 (1987).

A. Krebs, K. N. Goldie and A. Hoenger. Structural rearrangements in tubulin following microtubule formation. *EMBO Rep* **6**, 227–232 (2005).

L. Kreplak, H. Bär, J. F. Leterrier, H. Herrmann and U. Aebi. Exploring the mechanical behavior of single intermediate filaments. *J Mol Biol* **354**, 569–577 (2005).

T. Krouglova, J. Vercammen and Y. Engelborghs. Correct diffusion coefficients of proteins in fluorescence correlation spectroscopy. Application to tubulin oligomers induced by Mg2+ and Paclitaxel. *Biophys J* **87**, 2635–2646 (2004).

M. Kurachi, M. Hoshi and H. Tashiro. Buckling of a single microtubule by optical trapping forces: direct measurement of microtubule rigidity. *Cell Motil Cytoskeleton* **30**, 221–228 (1995).

L. D. Landau and E. M. Lifshitz. *Theory of Elasticity*. Pergamon Press (1986).

G. Lansbergen, Y. Komarova, M. Modesti, C. Wyman, C. C. Hoogenraad, H. V. Goodson, R. P. Lemaitre, D. N. Drechsel, E. van Munster, T. W. J. Gadella, F. Grosveld, N. Galjart, G. G. Borisy and A. Akhmanova. Conformational changes in CLIP-170 regulate its binding to microtubules and dynactin localization. *J Cell Biol* **166**, 1003–1014 (2004).

C. J. Lawrence, R. K. Dawe, K. R. Christie, D. W. Cleveland, S. C. Dawson, S. A. Endow, L. S. B. Goldstein, H. V. Goodson, N. Hirokawa, J. Howard, R. L. Malmberg, J. R. McIntosh, H. Miki, T. J. Mitchison, Y. Okada, A. S. N. Reddy, W. M. Saxton, M. Schliwa, J. M. Scholey, R. D. Vale, C. E. Walczak and L. Wordeman. A standardized kinesin nomenclature. *J Cell Biol* **167**, 19–22 (2004).

L. Lee, J. S. Tirnauer, J. Li, S. C. Schuyler, J. Y. Liu and D. Pellman. Positioning of the mitotic spindle by a cortical-microtubule capture mechanism. *Science* **287**, 2260–2262 (2000).

D. Liakopoulos, J. Kusch, S. Grava, J. Vogel and Y. Barral. Asymmetric loading of Kar9 onto spindle poles and microtubules ensures proper spindle alignment. *Cell* **112**, 561–574 (2003).

L. A. Ligon, S. S. Shelly, M. K. Tokito and E. L. F. Holzbaur. Microtubule binding proteins CLIP-170, EB1, and p150Glued form distinct plus-end complexes. *FEBS Lett* **580**, 1327–1332 (2006).

I. Loïodice, J. Staub, T. G. Setty, N.-P. T. Nguyen, A. Paoletti and P. T. Tran. Ase1p organizes antiparallel microtubule arrays during interphase and mitosis in fission yeast. *Mol Biol Cell* **16**, 1756–1768 (2005).

R. K. Louie, S. Bahmanyar, K. A. Siemers, V. Votin, P. Chang, T. Stearns, W. J. Nelson and A. I. M. Barth. Adenomatous polyposis coli and EB1 localize in close proximity of the mother centriole and EB1 is a functional component of centrosomes. *J Cell Sci* **117**, 1117–1128 (2004).

E. M. Mandelkow, E. Mandelkow and R. A. Milligan. Microtubule dynamics and microtubule caps: a time-resolved cryo-electron microscopy study. *J Cell Biol* **114**, 977–991 (1991).

J. Marks, I. M. Hagan and J. S. Hyams. Growth polarity and cytokinesis in fission yeast: the role of the cytoskeleton. *J Cell Sci Suppl* **5**, 229–241 (1986).

S. G. Martin and F. Chang. Dynamics of the formin for3p in actin cable assembly. *Curr Biol* **16**, 1161–1170 (2006).

S. G. Martin and D. S. Johnston. A role for Drosophila LKB1 in anterior-posterior axis formation and epithelial polarity. *Nature* **421**, 379–384 (2003).

S. G. Martin, W. H. McDonald, J. R. Yates and F. Chang. Tea4p links microtubule plus ends with the formin for3p in the establishment of cell polarity. *Dev Cell* **8**, 479–491 (2005).

J. Mata and P. Nurse. tea1 and the microtubular cytoskeleton are important for generating global spatial order within the fission yeast cell. *Cell* **89**, 939–949 (1997).

E. K. McCarthy and B. Goldstein. Asymmetric spindle positioning. *Curr Opin Cell Biol* **18**, 79–85 (2006).

D. McCollum, A. Feoktistova, M. Morphew, M. Balasubramanian and K. L. Gould. The Schizosaccharomyces pombe actin-related protein, Arp3, is a component of the cortical actin cytoskeleton and interacts with profilin. *EMBO J* **15**, 6438–6446 (1996).

S. J. McConnell and M. P. Yaffe. Intermediate filament formation by a yeast protein essential for organelle inheritance. *Science* **260**, 687–689 (1993).

R. Melki, S. Fievez and M. F. Carlier. Continuous monitoring of Pi release following nucleotide hydrolysis in actin or tubulin assembly using 2-amino-6-mercapto-7-methylpurine ribonucleoside and purine-nucleoside phosphorylase as an enzyme-linked assay. *Biochemistry* **35**, 12038–12045 (1996).

M. Mendoza, S. Redemann and D. Brunner. The fission yeast MO25 protein functions in polar growth and cell separation. *Eur J Cell Biol* **84**, 915–926 (2005).

B. Mickey and J. Howard. Rigidity of microtubules is increased by stabilizing agents. *J Cell Biol* **130**, 909–917 (1995).

H. Miki, M. Setou, K. Kaneshiro and N. Hirokawa. All kinesin superfamily protein, KIF, genes in mouse and human. *Proc Natl Acad Sci U S A* **98**, 7004–7011 (2001).

H. Miki, Y. Okada and N. Hirokawa. Analysis of the kinesin superfamily: insights into structure and function. *Trends Cell Biol* **15**, 467–476 (2005).

C. C. Milburn, J. Boudeau, M. Deak, D. R. Alessi and D. M. F. van Aalten. Crystal structure of MO25 alpha in complex with the C terminus of the pseudo kinase STE20-related adaptor. *Nat Struct Mol Biol* **11**, 193–200 (2004).

R. K. Miller, S. D'Silva, J. K. Moore and H. V. Goodson. The CLIP-170 orthologue Bik1p and positioning the mitotic spindle in yeast. *Curr Top Dev Biol* **76**, 49–87 (2006).

J. M. Mitchison and P. Nurse. Growth in cell length in the fission yeast Schizosaccharomyces pombe. *J Cell Sci* **75**, 357–376 (1985).

T. Mitchison and M. Kirschner. Dynamic instability of microtubule growth. *Nature* **312**, 237–242 (1984).

A. Mogilner and G. Oster. The polymerization ratchet model explains the force-velocity relation for growing microtubules. *Eur Biophys J* **28**, 235–242 (1999).

C. A. Moores and R. A. Milligan. Lucky 13-microtubule depolymerisation by kinesin-13 motors. *J Cell Sci* **119**, 3905–3913 (2006).

M. Moritz and D. A. Agard. Gamma-tubulin complexes and microtubule nucleation. *Curr Opin Struct Biol* **11**, 174–181 (2001).

J. L. Morrell, M. Morphew and K. L. Gould. A mutant of Arp2p causes partial disassembly of the Arp2/3 complex and loss of cortical actin function in fission yeast. *Mol Biol Cell* **10**, 4201–4215 (1999).

E. E. Morrison, B. N. Wardleworth, J. M. Askham, A. F. Markham and D. M. Meredith. EB1, a protein which interacts with the APC tumour suppressor, is associated with the microtubule cytoskeleton throughout the cell cycle. *Oncogene* **17**, 3471–3477 (1998).

F. Motegi, R. Arai and I. Mabuchi. Identification of two type V myosins in fission yeast, one of which functions in polarized cell growth and moves rapidly in the cell. *Mol Biol Cell* **12**, 1367–1380 (2001).

N. Mücke, L. Kreplak, R. Kirmse, T. Wedig, H. Herrmann, U. Aebi and J. Langowski. Assessing the flexibility of intermediate filaments by atomic force microscopy. *J Mol Biol* **335**, 1241–1250 (2004).

T. Müller-Reichert, D. Chrétien, F. Severin and A. A. Hyman. Structural changes at microtubule ends accompanying GTP hydrolysis: information from a slowly hydrolyzable analogue of GTP, guanylyl (alpha,beta)methylenediphosphonate. *Proc Natl Acad Sci U S A* **95**, 3661–3666 (1998).

M. Nakamura, X. Z. Zhou and K. P. Lu. Critical role for the EB1 and APC interaction in the regulation of microtubule polymerization. *Curr Biol* **11**, 1062–1067 (2001).

F. Nédélec. Computer simulations reveal motor properties generating stable antiparallel microtubule interactions. *J Cell Biol* **158**, 1005–1015 (2002).

B. Nelson, C. Kurischko, J. Horecka, M. Mody, P. Nair, L. Pratt, A. Zougman, L. D. B. McBroom, T. R. Hughes, C. Boone and F. C. Luca. RAM: a conserved signaling network that regulates Ace2p transcriptional activity and polarized morphogenesis. *Mol Biol Cell* **14**, 3782–3803 (2003).

T. Niccoli, M. Arellano and P. Nurse. Role of Tea1p, Tea3p and Pom1p in the determination of cell ends in Schizosaccharomyces pombe. *Yeast* **20**, 1349–1358 (2003).

E. Nogales, S. G. Wolf and K. H. Downing. Structure of the alpha beta tubulin dimer by electron crystallography. *Nature* **391**, 199–203 (1998).

E. Nogales and H.-W. Wang. Structural mechanisms underlying nucleotide-dependent self-assembly of tubulin and its relatives. *Curr Opin Struct Biol* **16**, 221–229 (2006).

C. E. Oakley and B. R. Oakley. Identification of gamma-tubulin, a new member of the tubulin super-family encoded by mipA gene of Aspergillus nidulans. *Nature* **338**, 662–664 (1989).

E. T. O'Brien, E. D. Salmon, R. A. Walker and H. P. Erickson. Effects of magnesium on the dynamic instability of individual microtubules. *Biochemistry* **29**, 6648–6656 (1990).

D. J. Odde. Chromosome capture: take me to your kinetochore. *Curr Biol* **15**, R328–R330 (2005).

J. B. Olmsted and G. G. Borisy. Ionic and nucleotide requirements for microtubule polymerization in vitro. *Biochemistry* **14**, 2996–3005 (1975).

Ott, Magnasco, Simon and Libchaber. Measurement of the persistence length of polymerized actin using fluorescence microscopy. *Phys Rev E* **48**, R1642–R1645 (1993).

L. R. Otterbein, P. Graceffa and R. Dominguez. The crystal structure of uncomplexed actin in the ADP state. *Science* **293**, 708–711 (2001).

F. Pampaloni, G. Lattanzi, A. Jonás, T. Surrey, E. Frey and E.-L. Florin. Thermal fluctuations of grafted microtubules provide evidence of a length-dependent persistence length. *Proc Natl Acad Sci U S A* **103**, 10248–10253 (2006).

D. Pantaloni, C. L. Clainche and M. F. Carlier. Mechanism of actin-based motility. *Science* **292**, 1502–1506 (2001).

J. D. Pardee and J. A. Spudich. Mechanism of K+-induced actin assembly. *J Cell Biol* **93**, 648–654 (1982).

D. A. Parry and P. M. Steinert. Intermediate filaments: molecular architecture, assembly, dynamics and polymorphism. *Q Rev Biophys* **32**, 99–187 (1999).

R. J. Pelham and F. Chang. Role of actin polymerization and actin cables in actin-patch movement in Schizosaccharomyces pombe. *Nat Cell Biol* **3**, 235–244 (2001).

F. Perez, G. S. Diamantopoulos, R. Stalder and T. E. Kreis. CLIP-170 highlights growing microtubule ends in vivo. *Cell* **96**, 517–527 (1999).

P. Pierre, J. Scheel, J. E. Rickard and T. E. Kreis. CLIP-170 links endocytic vesicles to microtubules. *Cell* **70**, 887–900 (1992).

P. Pierre, R. Pepperkok and T. E. Kreis. Molecular characterization of two functional domains of CLIP-170 in vivo. *J Cell Sci* **107 (Pt 7)**, 1909–1920 (1994).

W. H. Press, S. A. Teukolsky, W. T. Vettering and B. P. Flannery. *Numerical Recipes in C++*. Cambridge University Press (2002).

D. Pruyne, M. Evangelista, C. Yang, E. Bi, S. Zigmond, A. Bretscher and C. Boone. Role of formins in actin assembly: nucleation and barbed-end association. *Science* **297**, 612–615 (2002).

K. Radtke, K. Döhner and B. Sodeik. Viral interactions with the cytoskeleton: a hitchhiker's guide to the cell. *Cell Microbiol* **8**, 387–400 (2006).

R. B. G. Ravelli, B. Gigant, P. A. Curmi, I. Jourdain, S. Lachkar, A. Sobel and M. Knossow. Insight into tubulin regulation from a complex with colchicine and a stathmin-like domain. *Nature* **428**, 198–202 (2004).

S. L. Reck-Peterson, A. Yildiz, A. P. Carter, A. Gennerich, N. Zhang and R. D. Vale. Single-molecule analysis of dynein processivity and stepping behavior. *Cell* **126**, 335–348 (2006).

M. Rehberg and R. Gräf. Dictyostelium EB1 is a genuine centrosomal component required for proper spindle formation. *Mol Biol Cell* **13**, 2301–2310 (2002).

J. E. Rickard and T. E. Kreis. Identification of a novel nucleotide-sensitive microtubule-binding protein in HeLa cells. *J Cell Biol* **110**, 1623–1633 (1990).

J. E. Rickard and T. E. Kreis. Binding of pp170 to microtubules is regulated by phosphorylation. *J Biol Chem* **266**, 17597–17605 (1991).

K. Riehemann and C. Sorg. Sequence homologies between four cytoskeleton-associated proteins. *Trends Biochem Sci* **18**, 82–83 (1993).

V. I. Rodionov and G. G. Borisy. Microtubule treadmilling in vivo. *Science* **275**, 215–218 (1997).

A. Roll-Mecak and R. D. Vale. Making more microtubules by severing: a common theme of noncentrosomal microtubule arrays? *J Cell Biol* **175**, 849–851 (2006).

M. A. Rould, Q. Wan, P. B. Joel, S. Lowey and K. M. Trybus. Crystal structures of expressed non-polymerizable monomeric actin in the ADP and ATP states. *J Biol Chem* **281**, 31909–31919 (2006).

C. I. Rubin and G. F. Atweh. The role of stathmin in the regulation of the cell cycle. *J Cell Biochem* **93**, 242–250 (2004).

P. G. Saffman and M. Delbrück. Brownian motion in biological membranes. *Proc Natl Acad Sci U S A* **72**, 3111–3113 (1975).

L. Sandblad, K. E. Busch, P. Tittmann, H. Gross, D. Brunner and A. Hoenger. The Schizosaccharomyces pombe EB1 homolog Mal3p binds and stabilizes the microtubule lattice seam. *Cell* **127**, 1415–1424 (2006).

K. E. Sawin and P. Nurse. Regulation of Cell Polarity by Microtubules in Fission Yeast. *J Cell Biol* **142**, 457–471 (1998).

K. E. Sawin and H. A. Snaith. Role of microtubules and tea1p in establishment and maintenance of fission yeast cell polarity. *J Cell Sci* **117**, 689–700 (2004).

K. E. Sawin, P. C. C. Lourenco and H. A. Snaith. Microtubule nucleation at non-spindle pole body microtubule-organizing centers requires fission yeast centrosomin-related protein mod20p. *Curr Biol* **14**, 763–775 (2004).

J. Scheel, P. Pierre, J. E. Rickard, G. S. Diamantopoulos, C. Valetti, F. G. van der Goot, M. Häner, U. Aebi and T. E. Kreis. Purification and analysis of authentic CLIP-170 and recombinant fragments. *J Biol Chem* **274**, 25883–25891 (1999).

A. Schepis, B. Schramm, C. A. M. de Haan and J. K. Locker. Vaccinia virus-induced microtubule-dependent cellular rearrangements. *Traffic* **7**, 308–323 (2006).

E. Schiebel. gamma-tubulin complexes: binding to the centrosome, regulation and microtubule nucleation. *Curr Opin Cell Biol* **12**, 113–118 (2000).

S. C. Schuyler and D. Pellman. Microtubule "plus-end-tracking proteins": The end is just the beginning. *Cell* **105**, 421–424 (2001).

K. Schwartz, K. Richards and D. Botstein. BIM1 encodes a microtubule-binding protein in yeast. *Mol Biol Cell* **8**, 2677–2691 (1997).

Y.-L. Shih and L. Rothfield. The bacterial cytoskeleton. *Microbiol Mol Biol Rev* **70**, 729–754 (2006).

H. A. Snaith and K. E. Sawin. Fission yeast mod5p regulates polarized growth through anchoring of tea1p at cell tips. *Nature* **423**, 647–651 (2003).

H. A. Snaith, I. Samejima and K. E. Sawin. Multistep and multimode cortical anchoring of tea1p at cell tips in fission yeast. *EMBO J* **24**, 3690–3699 (2005).

V. Snell and P. Nurse. Genetic analysis of cell morphogenesis in fission yeast–a role for casein kinase II in the establishment of polarized growth. *EMBO J* **13**, 2066–2074 (1994).

Y. H. Song and E. Mandelkow. Recombinant kinesin motor domain binds to beta-tubulin and decorates microtubules with a B surface lattice. *Proc Natl Acad Sci U S A* **90**, 1671–1675 (1993).

Y. H. Song and E. Mandelkow. The anatomy of flagellar microtubules: polarity, seam, junctions, and lattice. *J Cell Biol* **128**, 81–94 (1995).

M. Srayko, E. T. O'toole, A. A. Hyman and T. Müller-Reichert. Katanin disrupts the microtubule lattice and increases polymer number in C. elegans meiosis. *Curr Biol* **16**, 1944–1949 (2006).

S. V. Strelkov, H. Herrmann and U. Aebi. Molecular architecture of intermediate filaments. *Bioessays* **25**, 243–251 (2003).

L. K. Su, M. Burrell, D. E. Hill, J. Gyuris, R. Brent, R. Wiltshire, J. Trent, B. Vogelstein and K. W. Kinzler. APC binds to the novel protein EB1. *Cancer Res* **55**, 2972–2977 (1995).

L. G. Tilney, J. Bryan, D. J. Bush, K. Fujiwara, M. S. Mooseker, D. B. Murphy and D. H. Snyder. Microtubules: evidence for 13 protofilaments. *J Cell Biol* **59**, 267–275 (1973).

J. S. Tirnauer and B. E. Bierer. EB1 proteins regulate microtubule dynamics, cell polarity, and chromosome stability. *J Cell Biol* **149**, 761–766 (2000).

J. S. Tirnauer, E. O'Toole, L. Berrueta, B. E. Bierer and D. Pellman. Yeast Bim1p promotes the G1-specific dynamics of microtubules. *J Cell Biol* **145**, 993–1007 (1999).

J. S. Tirnauer, J. C. Canman, E. D. Salmon and T. J. Mitchison. EB1 targets to kinetochores with attached, polymerizing microtubules. *Mol Biol Cell* **13**, 4308–4316 (2002)a.

J. S. Tirnauer, S. Grego, E. D. Salmon and T. J. Mitchison. EB1-microtubule interactions in Xenopus egg extracts: role of EB1 in microtubule stabilization and mechanisms of targeting to microtubules. *Mol Biol Cell* **13**, 3614–3626 (2002)b.

I. M. Tolić-Nørrelykke, E.-L. Munteanu, G. Thon, L. Oddershede and K. Berg-Sørensen. Anomalous Diffusion in Living Yeast Cells. *Phys Rev Lett* **93**, 78102 (2004).

R. Tournebize, A. Popov, K. Kinoshita, A. J. Ashford, S. Rybina, A. Pozniakovsky, T. U. Mayer, C. E. Walczak, E. Karsenti and A. A. Hyman. Control of microtubule dynamics by the antagonistic activities of XMAP215 and XKCM1 in Xenopus egg extracts. *Nat Cell Biol* **2**, 13–19 (2000).

P. T. Tran, L. Marsh, V. Doye, S. Inoué and F. Chang. A Mechanism for Nuclear Positioning in Fission Yeast Based on Microtubule Pushing. *J Cell Biol* **153**, 397–411 (2001).

R. D. Vale and R. J. Fletterick. The design plan of kinesin motors. *Annu Rev Cell Dev Biol* **13**, 745–777 (1997).

R. D. Vale and R. A. Milligan. The way things move: looking under the hood of molecular motor proteins. *Science* **288**, 88–95 (2000).

R. D. Vale, T. S. Reese and M. P. Sheetz. Identification of a novel force-generating protein, kinesin, involved in microtubule-based motility. *Cell* **42**, 39–50 (1985).

R. D. Vale. The molecular motor toolbox for intracellular transport. *Cell* **112**, 467–480 (2003).

V. Varga, J. Helenius, K. Tanaka, A. A. Hyman, T. U. Tanaka and J. Howard. Yeast kinesin-8 depolymerizes microtubules in a length-dependent manner. *Nat Cell Biol* **8**, 957–962 (2006).

R. J. Vasquez, D. L. Gard and L. Cassimeris. XMAP from Xenopus eggs promotes rapid plus end assembly of microtubules and rapid microtubule polymer turnover. *J Cell Biol* **127**, 985–993 (1994).

K. T. Vaughan. TIP maker and TIP marker; EB1 as a master controller of microtubule plus ends. *J Cell Biol* **171**, 197–200 (2005).

C. Vedrenne and H.-P. Hauri. Morphogenesis of the endoplasmic reticulum: beyond active membrane expansion. *Traffic* **7**, 639–646 (2006).

F. Verde, M. Dogterom, E. Stelzer, E. Karsenti and S. Leibler. Control of microtubule dynamics and length by cyclin A- and cyclin B-dependent kinases in Xenopus egg extracts. *J Cell Biol* **118**, 1097–1108 (1992).

F. Verde, J. Mata and P. Nurse. Fission yeast cell morphogenesis: identification of new genes and analysis of their role during the cell cycle. *J Cell Biol* **131**, 1529–1538 (1995).

F. Verde, D. J. Wiley and P. Nurse. Fission yeast orb6, a ser/thr protein kinase related to mammalian rho kinase and myotonic dystrophy kinase, is required for maintenance of cell polarity and coordinates cell morphogenesis with the cell cycle. *Proc Natl Acad Sci U S A* **95**, 7526–7531 (1998).

R. H. Wade, D. Chrétien and D. Job. Characterization of microtubule protofilament numbers. How does the surface lattice accommodate? *J Mol Biol* **212**, 775–786 (1990).

C. E. Walczak, I. Vernos, T. J. Mitchison, E. Karsenti and R. Heald. A model for the proposed roles of different microtubule-based motor proteins in establishing spindle bipolarity. *Curr Biol* **8**, 903–913 (1998).

R. A. Walker, E. T. O'Brien, N. K. Pryer, M. F. Soboeiro, W. A. Voter, H. P. Erickson and E. D. Salmon. Dynamic instability of individual microtubules analyzed by video light microscopy: rate constants and transition frequencies. *J Cell Biol* **107**, 1437–1448 (1988).

R. A. Walker, S. Inoué and E. D. Salmon. Asymmetric behavior of severed microtubule ends after ultraviolet-microbeam irradiation of individual microtubules in vitro. *J Cell Biol* **108**, 931–937 (1989).

B. J. Wallar and A. S. Alberts. The formins: active scaffolds that remodel the cytoskeleton. *Trends Cell Biol* **13**, 435–446 (2003).

G. Wallon, J. Rappsilber, M. Mann and L. Serrano. Model for stathmin/OP18 binding to tubulin. *EMBO J* **19**, 213–222 (2000).

Y. L. Wang. Exchange of actin subunits at the leading edge of living fibroblasts: possible role of treadmilling. *J Cell Biol* **101**, 597–602 (1985).

P. Watson, R. Forster, K. J. Palmer, R. Pepperkok and D. J. Stephens. Coupling of ER exit to microtubules through direct interaction of COPII with dynactin. *Nat Cell Biol* **7**, 48–55 (2005).

J. L. Watts, D. G. Morton, J. Bestman and K. J. Kemphues. The C. elegans par-4 gene encodes a putative serine-threonine kinase required for establishing embryonic asymmetry. *Development* **127**, 1467–1475 (2000).

A. Wegner. Head to tail polymerization of actin. *J Mol Biol* **108**, 139–150 (1976).

R. R. West, T. Malmstrom, C. L. Troxell and J. R. McIntosh. Two related kinesins, klp5+ and klp6+, foster microtubule disassembly and are required for meiosis in fission yeast. *Mol Biol Cell* **12**, 3919–3932 (2001).

S. Westermann, H.-W. Wang, A. Avila-Sakar, D. G. Drubin, E. Nogales and G. Barnes. The Dam1 kinetochore ring complex moves processively on depolymerizing microtubule ends. *Nature* **440**, 565–569 (2006).

C. Wiese and Y. Zheng. Microtubule nucleation: gamma-tubulin and beyond. *J Cell Sci* **119**, 4143–4153 (2006).

A. Wilde and Y. Zheng. Stimulation of microtubule aster formation and spindle assembly by the small GTPase Ran. *Science* **284**, 1359–1362 (1999).

T. Z. Win, Y. Gachet, D. P. Mulvihill, K. M. May and J. S. Hyams. Two type V myosins with non-overlapping functions in the fission yeast Schizosaccharomyces pombe: Myo52 is concerned with growth polarity and cytokinesis, Myo51 is a component of the cytokinetic actin ring. *J Cell Sci* **114**, 69–79 (2001).

T. Wittmann, A. Hyman and A. Desai. The spindle: a dynamic assembly of microtubules and motors. *Nat Cell Biol* **3**, E28–E34 (2001).

T. Wittmann and A. Desai. Microtubule cytoskeleton: a new twist at the end. *Curr Biol* **15**, R126–R129 (2005).

H. Xiao, P. Verdier-Pinard, N. Fernandez-Fuentes, B. Burd, R. Angeletti, A. Fiser, S. B. Horwitz and G. A. Orr. Insights into the mechanism of microtubule stabilization by Taxol. *Proc Natl Acad Sci U S A* **103**, 10166–10173 (2006).

M. P. Yaffe, D. Harata, F. Verde, M. Eddison, T. Toda and P. Nurse. Microtubules mediate mitochondrial distribution in fission yeast. *Proc Natl Acad Sci U S A* **93**, 11664–11668 (1996).

A. Yamashita, M. Sato, A. Fujita, M. Yamamoto and T. Toda. The roles of fission yeast ase1 in mitotic cell division, meiotic nuclear oscillation, and cytokinesis checkpoint signaling. *Mol Biol Cell* **16**, 1378–1395 (2005).

A. Yildiz and P. R. Selvin. Kinesin: walking, crawling or sliding along? *Trends Cell Biol* **15**, 112–120 (2005).

K. H. Yoon, M. Yoon, R. D. Moir, S. Khuon, F. W. Flitney and R. D. Goldman. Insights into the dynamic properties of keratin intermediate filaments in living epithelial cells. *J Cell Biol* **153**, 503–516 (2001).

M. Yoon, R. D. Moir, V. Prahlad and R. D. Goldman. Motile properties of vimentin intermediate filament networks in living cells. *J Cell Biol* **143**, 147–157 (1998).

L. Zheng, C. Schwartz, L. Wee and S. Oliferenko. The Fission Yeast Transforming Acidic Coiled Coil-related Protein Mia1p/Alp7p Is Required for Formation and Maintenance of Persistent Microtubule-organizing Centers at the Nuclear Envelope. *Mol Biol Cell* **17**, 2212–2222 (2006).

Y. Zheng, M. L. Wong, B. Alberts and T. Mitchison. Nucleation of microtubule assembly by a gamma-tubulin-containing ring complex. *Nature* **378**, 578–583 (1995).

J. Zumbrunn, K. Kinoshita, A. A. Hyman and I. S. Näthke. Binding of the adenomatous polyposis coli protein to microtubules increases microtubule stability and is regulated by GSK3 beta phosphorylation. *Curr Biol* **11**, 44–49 (2001).

Acknowledgements